# Investigation of $M$Fe$_2$O$_4$ ($M$ = Fe, Co, Ni, Cu, Zn) Spinels as Conversion Type Model Systems for Rechargeable Lithium-Ion Batteries

PhD dissertation

M.Tech. Geethu Balachandran

TECHNISCHE
UNIVERSITÄT
DARMSTADT

# Ehrenwörtliche Erklärung

Ich erkläre hiermit ehrenwörtlich, dass ich die vorliegende Arbeit selbstständig angefertigt habe. Sämtliche aus fremden Quellen direkt oder indirekt übernommenen Gedanken sind als solche kenntlich gemacht.

Die Arbeit wurde bisher keiner anderen Prüfungsbehörde vorgelegt und noch nicht veröffentlicht.

Darmstadt, den 16. 07. 2018

# Investigation on $MFe_2O_4$ ($M$ = Fe, Co, Ni, Cu, Zn) Spinels as Conversion Type Model Systems for Rechargeable Lithium-Ion Batteries

Vom Fachbereich Material- und Geowissenschaften

der Technische Universität Darmstadt

zur Erlangung des akademischen Grades

**Doktor-Ingenieur**

(Dr.-Ing.)

genehmigte Dissertation

von

Geethu Balachandran M.Tech.

geboren in Nilambur, India

1. Prüfer : Prof. Dr. rer. nat. Horst Hahn
   Technische Universität Darmstadt (TUD)
2. Prüfer : Prof. Dr. rer. nat. Helmut Ehrenberg
   Karlsruhe Institut für Technologie (KIT)

Tag der Einreichung : 16/07/2018

Tag der mündlichen Prüfung : 21/12/2018

Darmstadt 2018

D 17

Geethu Balachandran: Investigation of $M$Fe$_2$O$_4$ ($M$ = Fe, Co, Ni, Cu, Zn) Spinels as Conversion Type Model Systems for Rechargeable Lithium-Ion Batteries
Darmstadt, Technische Universität Darmstadt,
Year thesis published in TUprints 2019
Date of the viva voce 21.12.2018

# Contents

# Abbreviations

Å ..... Angstrom

°C ..... degree Celsius

C ..... capacity

C-rate ..... charge/discharge rate

CV ..... Cyclic Voltammetry

DMC ..... Dimethyl carbonate

DSC ..... Differential Scanning Calorimetry

DW ..... Debye-Waller

EOD ..... End of Discharge

EOC ..... End of Charge

EC ..... Ethylene Carbonate

eV ..... electron volt

FT ..... Fourier Transform

GeV ..... Giga electron volt

h ..... hours

keV ..... kilo electron volt

LCF ..... Linear combination fitting

Li ..... Lithium

LIBs ..... Lithium Ion Batteries

NMP ..... N-Methylpyrrolidone

MSPD ..... Material Science Powder Diffraction

PVdF ..... Polyvinylidene fluoride

r ..... interatomic distance

SEI ..... Solid Electrolyte Interphase

SEM ..... Scanning electron microscopy

SRPD ..... Synchrotron Radiation Powder Diffraction

t ..... time

TG ..... Thermogravimetry

V ..... volume

XANES ..... X-ray absorption near edge spectroscopy

XAS ..... X-ray absorption spectroscopy

XRD ..... X-ray diffraction

λ ..... Lambda, wavelength of X-radiation

Additional abbreviations used for the materials

| | |
|---|---|
| CFO-800 | $CoFe_2O_4$ material annealed at 800 °C |
| NFO-800 | $NiFe_2O_4$ material annealed at 800 °C |
| FO-600 | $Fe_3O_4$ material annealed at 600 °C |
| FO-800 | $Fe_3O_4$ material annealed at 800 °C |
| ZFO-800 | $ZnFe_2O_4$ material annealed at 800 °C |

# List of Figures

# List of Tables

# Abstract

Anode materials with high specific capacity, long service life, short charging times, high energy density and low cost should be used to meet the current requirements for lithium-ion batteries. By fine-tuning the low cost and environmentally friendly transition metal oxides, which react through a conversion mechanism with lithium, higher energy density lithium ion devices could be achieved. Despite the promising properties shown by the conversion electrodes, their commercial application is dented by factors such as rather complex phase transitions, voltage hysteresis which affects the efficiency, additional capacity resulting from electrolyte decomposition and interfacial storage and poor cycling stability of pristine materials due to contact loss and reduced electrical conductivity. Therefore, to fully understand all these parameters, even deeper knowledge of the conversion reaction pathways than currently available is still required.

In the current study, spinel type mixed-transition metal ferrites, $M$Fe$_2$O$_4$ ($M$ = Fe, Co, Ni, Cu and Zn) were investigated as conversion type model systems for LIB anodes to elucidate the influence of partial substitution of Fe in the structure, Fe$_3$O$_4$, with different 3d-cations. The phase formation and microstructure development during the first charge-discharge process were investigated using combined *in situ* synchrotron powder diffraction and X-ray absorption spectroscopy techniques. During the irreversible initial discharge, a two phase mechanism is observed. Both main phase and lithiated phase crystallize in $Fd\bar{3}m$ space group, however, in the lithiated phase the atoms occupying 8a tetrahedral sites are displaced to 16c octahedral sites together with the intercalation of lithium into 16c and 8a sites. With further lithiation crystalline material transforms to an amorphous and inhomogeneous product

consisting of metallic nanoparticles in a $Li_2O$ matrix. During the following charge process metal nanoparticles are converted to binary oxides different from the parent material.

# Chapter 1 - Introduction

Renewable energy resources have become the subject of political, economic and scientific interest in recent years because of the limited availability of fossil fuels and increase of greenhouse gas emissions. Addressing this major problem of our times necessitates changes in the current energy infrastructure. Energy storage systems with high storage capacity, long service life, short charging times, high energy density and low cost, are required in order to keep up with the growing demands. In the recent discussions about diesel engine driving bans in some major German cities, various ideas about the future of the automobile, particularly with regard to electrically powered vehicles have attracted public attention. However, a general-purpose solution is very difficult to implement for all requirements, including entertainment electronics and the advancing e-mobility. The form of the energy storage medium has to be adapted to the respective application. For example, battery systems have already been successfully used for stationary storage of electric energy as energy buffers for stabilizing power networks in pilot projects, whose capacity can be easily scaled up. However, these storage systems in some cases are not suitable for mobile applications.

One of today's most promising ways of storing electrical energy are lithium-ion batteries (LIBs), due to their high energy and power densities as well as relatively good cycling stability[1]. M. S. Whittingham demonstrated a fast rechargeable lithium metal/$TiS_2$ cell at *Exxon Research and Engineering laboratory* and paved way for the rechargeable battery business[2]. In 1981, Goodenough replaced $TiS_2$ with layered $LiCoO_2$ as high energy cathode material[3]. Later in 1983, they further developed low cost manganese spinel cathode materials ($LiMnO_2$)[4]. It was considered as the breakthrough for the commercialization of layered oxide cathode materials $LiMO_2$ (M= Ni, Co, Mn). LIBs have emerged as the most desirable device

to meet the demands in portable electronic devices or in electrically operated vehicles and they soon outperformed the competition with a leading overall market share of more than 63% worldwide[5,6] as shown in ***Figure 1***. This explains why they receive intense attention at both fundamental and applied levels.

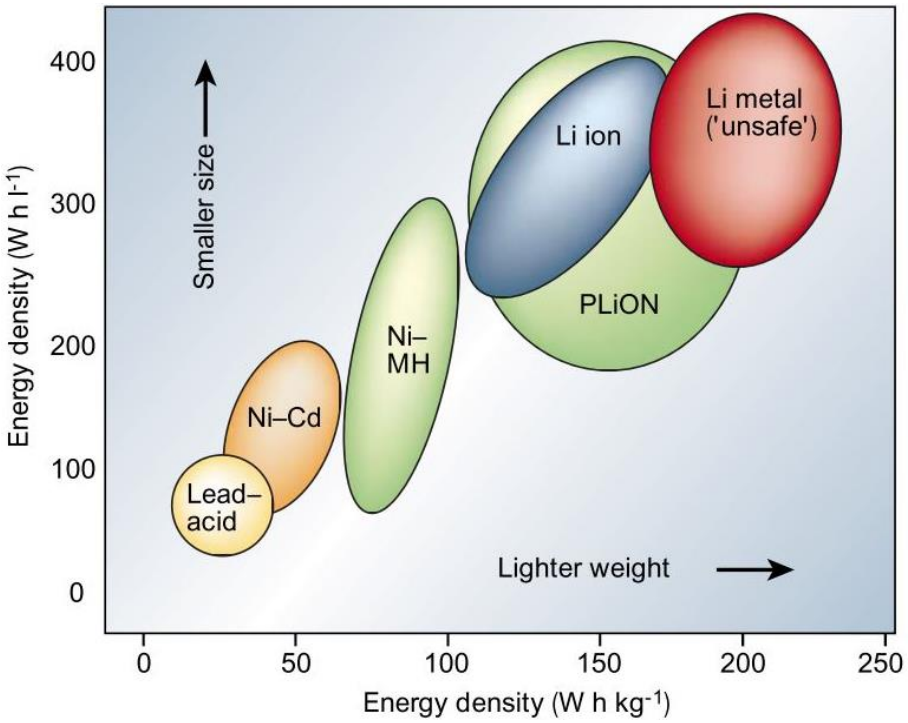


***Figure 1*** *– Comparison of the different battery technologies in terms of volumetric and gravimetric energy densities*[6].

Lithium ion and electron transport during discharging in a Li-ion cell is illustrated in ***Figure 2***. Note that for a lithium-ion battery, anode (negative electrode) and cathode (positive electrode) are defined for their state during discharge. The lithium ions move through the electrolyte from anode to the cathode while electrons travel through the electric circuit. The separator is a porous membrane which plays a critical role of separating the cathode from the anode but allows ions to flow through it.

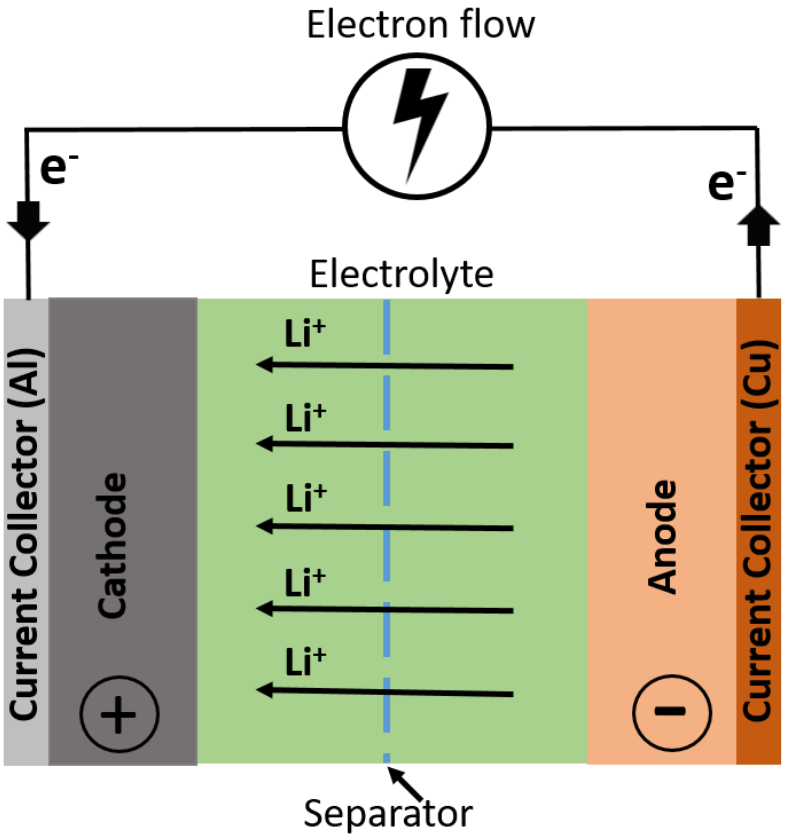


***Figure 2** – Transport of electrons and $Li^+$ ions during discharging in a Li-ion cell.*

The commercialization of lithium metal batteries was dented due to safety issues and drew the attention of researchers and stake holders to come up with a better battery technology[7]. As an alternative for the lithium metal anode, graphite was found with the idea of having an identical layered structure with the ability to reversibly store lithium[8–10]. The intercalation/de-intercalation mechanism facilitated the lithium ion conduction between anode and cathode using a solid organic electrolyte[11]. Graphite can intercalate one lithium ion per six carbon atoms, resulting in a stoichiometry of $LiC_6$. The achievable capacity is about 372 mAh $g^{-1}$, which is somewhat higher than that for most cathode materials[1]. After Yoshino's safety demonstration to show the safety advantage of $LiCoO_2$/graphite over lithium metal anode based batteries[12], Sony commercialized the lithium ion batteries in 1991. This cell setup reached a potential exceeding 3.6 V and an energy density in the range of around 120-150 Whkg$^{-1}$. The high cell potential is attainable due to the low operating potential of a graphite

anode of 0.2 to 0.6 V vs $Li^+/Li$. Additionally, layered graphite is cheap, possesses high capacity, reversibility and interfacial stability[13]. However, the capacity of graphite is limited by the number of available lattice sites in the hexagonal $sp^2$ graphite structure[14] and, therefore, cannot be further increased. Additionally, when graphite electrodes are used as anodes, the lithium intercalation potential reaches values near 0.0 V vs. $Li^+/Li$. The deposition of highly reactive metallic lithium ("lithium plating") can occur at such a low potential and is a serious safety concern.

Usually in a LIB, anode materials should be used in a capacity excess, compared to the cathode material for safety reasons. Hence, using a high capacity anode material would be helpful to reduce the cell size and thereby result in a production cost reduction. Anode materials which are free from lithium plating as well as possessing a high capacity should be used for future lithium-ion batteries. ***Figure 3*** shows various anode materials with respect to their electrochemical potential against lithium and their theoretically achievable capacity. As observed from ***Figure 3***, graphite has only a very low specific capacity compared to other available anode materials. The highest capacities are achieved by alloying materials. Silicon is probably the best known and well researched material in this class. With a theoretical specific capacity of about 4200 mAh $g^{-1}$, its capacity even exceeds that of pure lithium. However, the decrease in capacity during cycling and increase in the internal resistance caused by large volume changes upon lithium insertion and extractions has been found to be a limiting issue for Si anodes[15].

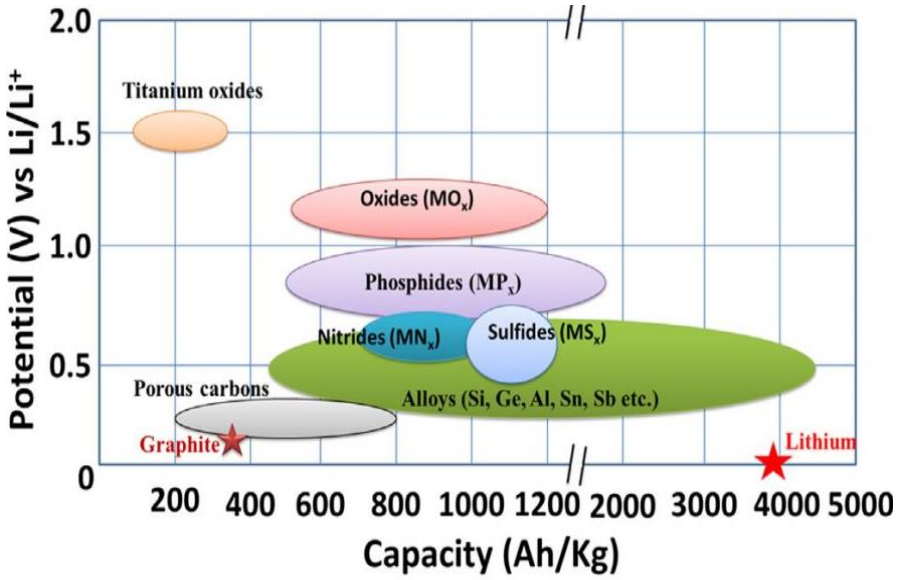


***Figure 3*** *– Schematic illustration of active anode materials for the next generation of lithium-ion batteries. Potential vs. $Li^+/Li$ and the corresponding capacity density are shown*[16].

Conversion materials find a prominent place as good anode materials with specific capacities of 600-1200 mAh $g^{-1}$[17–20]. Such a large specific capacity is achieved through a conversion reaction in which more than one electron transfer occurs per transition metal ion compared to commonly used intercalation compounds. Conversion compounds of interest include oxides, hydrides, nitrides, sulfides, and fluorides[21–28] of which the reaction potentials span a wide range depending on the electronegativity of the anion. For metal oxides operating via conversion reaction, the initial discharge involves the reduction of the transition metals into a composite material consisting of metallic nanoparticles (2-8 nm) dispersed in an amorphous $Li_2O$ matrix. Upon the following charge, the metal particles are re-oxidized. However, the structure and composition of thus formed nanostructured metal oxides may be different compared to the pristine oxide (***Figure 4***).

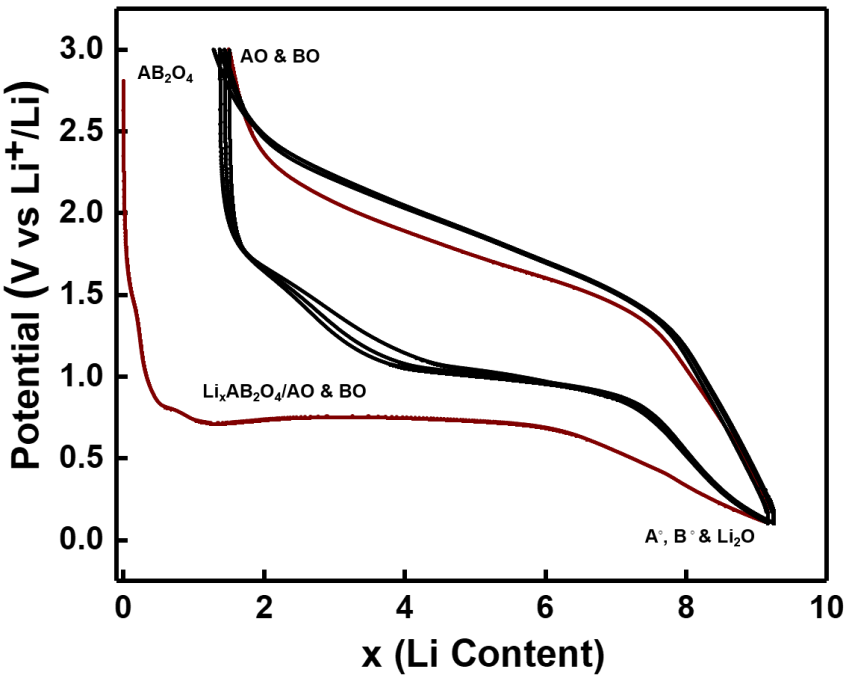


***Figure 4*** *– Voltage versus Li content profile of the first four cycles for conversion electrode material $Fe_3O_4$, measured against Li counter electrode. Different processes that occur during this complex reaction are indicated at appropriate voltages.*

Mixed-transition metal oxides containing $A_xB_{3-x}O_4$ spinel structured oxides such as ferrites ($AFe_2O_4$, A = Mn, Co, Ni, Cu, Zn, Mg and Ca), manganites ($AMn_2O_4$, A = Co, Ni, and Zn) and cobaltites ($ACo_2O_4$, A = Fe, Mn, Cu, Ni, Zn) have shown interesting electrochemical properties as LIB anodes[29]. Iron oxide has received much attention in recent times due to its very high theoretical capacity, low cost and environmental benignity[30–32]. How so ever, Mixed-transition metal oxides exhibit higher electrical conductivity than simple transition metal oxides owing to the relatively low activation energy for electron transfer between cations. By fine-tuning the low cost and environmentally friendly transition metal iron oxides which react through a conversion mechanism with lithium, higher energy density lithium ion devices could be achieved.

Despite the promising properties shown by the conversion electrodes, their commercial application is strongly handicapped by factors such as rather complex phase transitions, voltage hysteresis which in turn affects the efficiency, additional capacity resulting from

electrolyte decomposition and interfacial storage and poor cycling stability of pristine materials due to contact loss and less electrical conductivity. Therefore, to fully understand all these parameters, even deeper knowledge of the conversion reaction pathways than currently available is still required.

## 1.1. Motivation and Aim of Work

The general scheme of the conversion reaction leading to the formation of metal clusters and $Li_2O$ at the end of the first discharge is well established. However, only few studies about the evolution of the structure during initial discharge are available. Prior to the formation of the metal clusters and $Li_2O$, phase transitions related to the lithium insertion can occur and the local structure thus formed at the end of the first discharge may strongly depend on the reaction pathway. In addition to the initial structure, parameters such as initial particle size and charge-discharge rate may also have impact on the reaction pathway.

$Fe_3O_4$ is one of the most investigated transition metal oxides as conversion anode. Numerous attempts were made to improve the electrochemical performance by material modification and by partial substitution of Fe with other transition metals such as Co, Ni, Cu, Zn, Mn, Mg etc. However, it is still not clear if the partial substitution of Fe by other transition metals leads to better performance characteristics. At the same time, the comparison of the difference in the electrochemical reaction mechanism owing to the partial substitution of Fe with other transition metals are also not reported.

*In situ* investigations have proven extremely insightful for better understanding the electrochemical reaction mechanism in different electrode materials for LIBs. However, the most commonly used structural investigation method such as powder X-ray diffraction are only partially suitable for investigating the nanoscale products of the conversion reaction.

Even during the first discharge, with increasing lithiation, amorphization of the material occurs which is accompanied by the formation of metal nanoclusters, hardly detectable by diffraction techniques. Whereas, X-ray absorption spectroscopy (XAS) can give element specific information about various atoms present in the material. Furthermore, materials to be investigated by XAS do not require long range order; therefore, this method is highly appropriate and informative to study local nanostructures formed during operation of conversion-type materials. However, these studies are often performed *ex situ* with electrodes obtained from the cells at different states of charge.

In the current study, the phase transformation and microstructure development during the first discharge-charge process were investigated using combined *in situ* synchrotron powder diffraction and X-ray absorption spectroscopy techniques. An attempt was made to establish a direct relationship between electrochemical performance and structural properties of $M$Fe$_2$O$_4$, $M$ = Fe, Co, Ni, Cu and Zn, mixed-spinel structured conversion electrodes to formulate a general electrochemical mechanism.

# Chapter 2 - Experimental

## 2.1. Synthesis of Metal Ferrites

The electrochemical properties of various metal ferrites are strongly dependent on the synthesis route which determines the particle size, morphology and the surface chemistry of the same. Therefore, while choosing a synthesis route it is highly important to have a fine control over the reaction pathways. The commonly used solid state routes do not allow a fine control over the reaction pathways during the process which results in impurity phases as well as of wide particle size distributions. However, wet chemical routes are suitable alternatives due to the fact that at low temperatures they yield products with smaller particle sizes. The most commonly used wet-synthesis routes are self-combustion synthesis, solvothermal and hydrothermal synthesis, sol–gel, reverse micelle synthesis, polyol assisted synthesis and co-precipitation[33–38]. Co-precipitation is a simple and environmental friendly synthesis route, where the metal-ion precursors are generally precipitated in alkaline solution at a temperature 75–80 °C. Even though it demands strict control of the precipitation condition, it is one of the most adopted methods for the synthesis of nanocrystalline transition metal ferrites in large quantity.

Prior to the adaption of the final synthesis method to all investigated samples, both co-precipitation and inverse co-precipitation were applied for the synthesis of $CoFe_2O_4$. Iron(II) acetate [$Fe(C_2H_3O_2)_2$], cobalt(II) acetate tetrahydrate [$Co(C_2O_2H_3)_2(H_2O)_4$] and sodium hydroxide [NaOH] were used for the synthesis and were purchased from Alfa Aesar, Germany. In normal co-precipitation, anhydrous iron acetate (0.4 M, 50 mL) and cobalt acetate tetrahydrate (0.2 M, 50 mL) were mixed in doubly distilled deionized water and sodium hydroxide solution (1 M, 50 mL) was added dropwise with vigorous stirring under

air. Whereas, in the inverse co-precipitation method the metal acetates were added to sodium hydroxide solution drop wise with vigorous stirring under air. After the complete addition, the temperature was maintained at 80 °C for 1 hour. The obtained metal hydroxide precipitates were centrifuged at 6000 rpm for 15 min and washed three times with deionized water to remove the remaining excess NaOH. The metal hydroxide precipitates were then transferred into a drying oven and were dried at 85 °C overnight. The mixtures were then ground in a mortar, calcined at 800 °C, for obtaining crystalline metal ferrite samples, at a heating rate of 400 °C $h^{-1}$ for 4 hours in air, and then cooled to room temperature without any explicit temperature control. The obtained substances were again ground into a very fine powder.

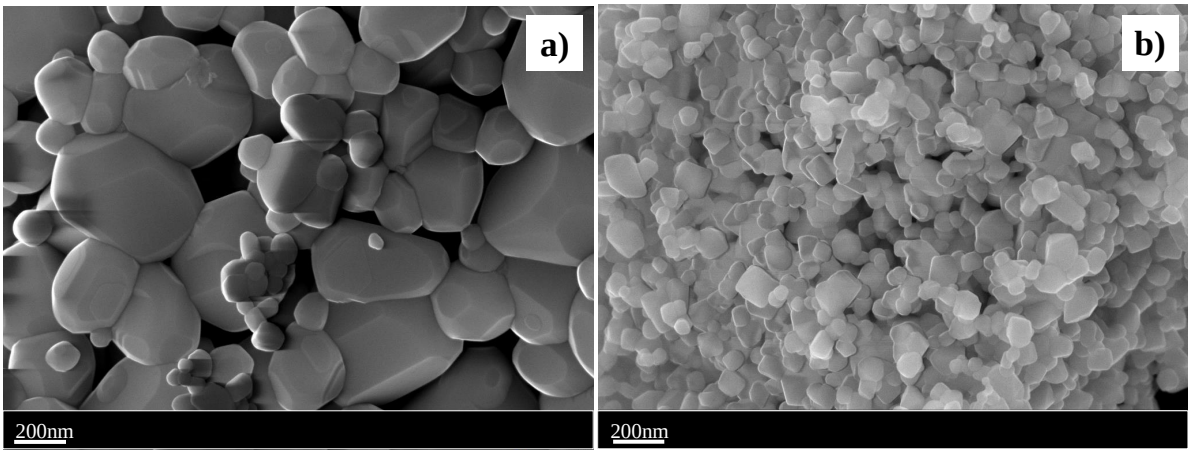


***Figure 5** – SEM images of $CoFe_2O_4$ annealed at 800 °C synthesized by normal co-precipitation (a) and inverse co-precipitation (b).*

***Figure 5*** shows the SEM images of $CoFe_2O_4$ synthesized by normal co-precipitation (***Figure 5***a) and inverse co-precipitation (***Figure 5***b). The addition of the salt solution to NaOH, not vice versa, seem to be more favourable for the nuclei formation during precipitation, which in turn helps to obtain smaller and uniform particles[39]. The material synthesized through normal co-precipitation has a particle size range varying from 50 nm to 500 nm whereas inverse co-precipitation synthesized material have much smaller particles in the range of 30-70 nm. Therefore, inverse co-precipitation is selected for further material

synthesis, taking into consideration that a smaller particle size is better for a more reversible conversion reaction[18,40].

Synthesis of $NiFe_2O_4$, $CuFe_2O_4$ and $ZnFe_2O_4$ were carried out with the same inverse co-precipitation procedure as for $CoFe_2O_4$ but by using Nickel(II) acetate tetrahydrate $[Ni(C_2O_2H_3)_2(H_2O)_4]$, Copper(II) acetate monohydrate $[Cu(CO_2CH_3)_2(H_2O)]$ and Zinc acetate dehydrate $[Zn(C_2O_2H_3)_2(H_2O)_2]$ as precursors.

For the synthesis of $Fe_3O_4$ (magnetite), ferrous ($Fe^{2+}$) and ferric ($Fe^{3+}$) chloride were used as precursors and the reaction solution/mixture was bubbled with argon in order to avoid the oxidation of $Fe^{2+}$ in the solution and, therefore, formation of both maghemite, $\gamma$-$Fe_2O_3$, and hematite, $\alpha$-$Fe_2O_3$. In addition, the obtained precipitates were calcined in Argon.

All the chemicals used for the synthesis were purchased from Alfa Aesar, Germany; of analytical grade and were used without further purification.

## 2.2. Electrochemical Characterization

The electrochemical characterization was carried out in an electrochemical cell, which is basically a two electrode cell.

### 2.2.1. Components of Electrochemical Test Cell

The electrochemical cell consists of three main components:

#### I. Electrode

In this work, the electrochemical tests were carried out using electrodes containing two different ratios of active material, conductive agent and binder. The electrodes were prepared either by mixing 80 % (w/w) of active material, 10 % (w/w) SUPER C65 carbon (TIMCAL)

which is used as conductive agent and 10 % (w/w) polyvinylidenefluoride (Solef PVdF 6020 binder, Solvay) in N-methyl-2-pyrrolidone (NMP, Sigma-Aldrich) to prepare a slurry or by mixing 60 % (w/w) of active material, 20 % (w/w) SUPER C65 carbon and 20 % of carboxy methyl cellulose (CRT 2000 PA 07 from DOW) and styrene-butadiene rubber (MTI Corporation) mixture as binder (CMC:SBR in 1:1 ratio) dissolved in distilled water. The electrode compositions will be here after named as 80:10:10 and 60:20:20. The obtained slurry was coated on copper foil. Depending upon the type of electrochemical test, the wet thickness of the coating was adjusted to 175 µm or 300 µm. The prepared electrode sheets were dried at 100 °C in air. After drying, electrode discs were punched out with 12 mm diameter (***Figure 6***(left)). Prior to test cell assembling, the electrodes were re-dried in a vacuum oven for one hour. The active mass loading is 2-3 mg and 4-5 mg, respectively for 175 µm and 300 µm thick coatings. The electrodes for *in situ* diffraction experiments were prepared by pressing the 60:20:20 ratio of electrode mixture on 8 mm Ø copper mesh with a pressure of 4 tons. The copper mesh was made with a 4 mm hole in the middle so as to avoid the high intensity copper reflections (***Figure 6*** (Right)).

***Figure 6 –*** *Electrode mixture coated on copper foil with punched out 12 mm holes (left) and pressed on copper mesh (right).*

Depending upon the test cells, lithium metal foils of different thicknesses and diameters were used as counter electrode. For the in-house *in situ* cell design[41], a lithium metal foil (Alfa

Aesar, 99.9 %) with 0.75 mm thickness and 10 mm diameter and the for custom-made CR2025 *in situ* coin cells[42], lithium metal foil (MTI Corporation, 99.9%) with 0.45 mm thickness and 15.6 mm diameter were used as the counter electrodes. Both cells were custom-made and developed in the working group.

### II. Electrolyte

In this work, the electrochemical cells were made with LP30 Selectipur® electrolyte (1M $LiPF_6$ in EC: DMC = 1:1) supplied from Merck. The electrolyte was used as received. The electrolyte was opened and stored inside an Ar-filled glovebox where the humidity was maintained below 1 ppm.

### III. Separator

A separator is placed between the working and counter electrodes to prevent the short circuit inside the cell. For conventional test cells, a glass microfiber filter supplied from Whatmann® (GF/D 70mm Ø) with 12 mm diameter was used as separator. For the coin cells, the Celgard® trilayer PP/PE/PP battery separator with 16 mm diameter was used.

## 2.2.2. Electrochemical Cell Layout

Electrochemical experiments were mainly carried out in CR2032 type normal coin-half-cells. The cells were assembled in an Ar-filled glove box with lithium foil (MTI Corporation) as anode, LP30 as electrolyte and Celgard (16 mm Ø) as separator. *In situ* investigations were carried out in two different types of cells depending on the measurement set up. Some of the *in situ* measurements were carried out in in-house *in situ* coin cell whereas others were done in CR2032 and CR2025 type *in situ* coin cells as shown in ***Figure 7***.

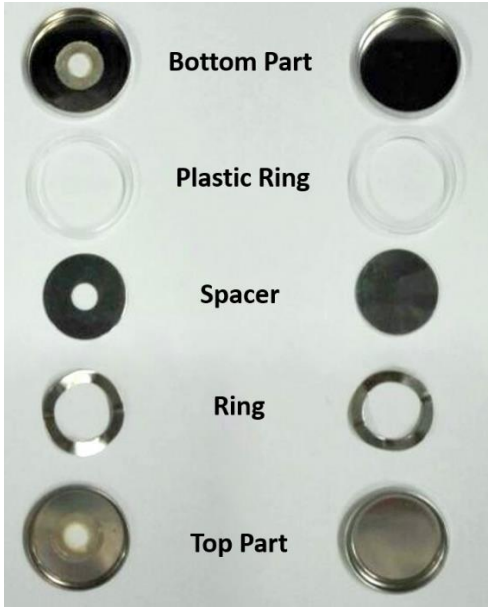


***Figure 7** – Cell parts of in situ (left) and normal coin cell (right).*

Both *in situ* cells were custom made with 4-5 mm beam entrance windows covered with glass , Kapton© (polyimide film) or glassy carbon, developed in our working group[41,42]. For diffraction studies, the *in situ* coincell bottom part is also covered with a copper foil with 17 mm Ø which is fixed firmly using the plastic ring to make sure the electrode has good contact with the cell parts. The cell windows were sealed with Kapton (Good Fellow, 8mm Ø and 0.075 mm thick) or glass (Thermo Scientific 8 mm Ø and 0.16 mm) fixed with a high density polyethylene foil by heating up to 180 °C. The overall diameter of the window is 8 mm and the cell is built in such a way that there is a hole of 4-5 mm in the center which facilitates the penetration of beam through the cell.

## 2.2.3. Electrochemical Cycling Techniques

The electrochemical tests were performed using a multichannel potentiostat, VMP (Bio-Logic Science Instruments, France) by a computer controlled EC-Lab program. The cells were placed in a temperature controlled climate chamber at 25 °C. The obtained data were analyzed using the program EC-Lab. For LIBs, CC-CV (constant current, constant voltage) is the universally accepted charging method. A constant current is applied through the cell

until a specified voltage is reached. In that point, the charging changes to constant voltage which is maintained across the battery terminals until it drops to a sufficiently low value and the charge is terminated. In this study, the electrochemical experiments were done either by controlling the cell potential (potentiostatic mode) or the current flow (galvanostatic mode).

## I. Cyclic Voltammetry

The cyclic voltammetry (CV) measures the electrical current that develops in an electrochemical cell during scanning the potential between two given values at a fixed rate. The CV experiments are usually performed in three-electrode setup, but it is not uncommon to estimate the electrochemical activity regions for lithium ion battery materials using a two-electrode cell. In this case the working electrode is the material under investigation, and lithium serves as both, reference and counter electrode. In this work, a two-electrode setup was used. The cyclic voltammogramms for different materials were obtained at 0.1 mV $s^{-}1$ in the voltage range of 0.1 V to 3.0 V vs. $Li^{+}/Li$.

## II. Galvanostatic Cycling (GCPL)

For Galvanostatic Cycling with Potential Limitation (GCPL), a potential limitation is set between working and counter electrode and the change of potential during cycling (charged-discharged) in this range is recorded by applying a constant current. The current is usually represented as the C-rate. Which is the time frame for either a full charge or discharge where *C* denotes the theoretical or nominal charge capacity (Ah) of a cell or battery. The results of Galvanostatic cycling are usually presented as E (voltage) versus t (time), specific capacity (mAh $g^{-1}$) or lithium content in the working electrode. Therefore, galvanostatic cycling gives information about the cycling stability and performance of a battery. In this work, the current rate was kept constant (C/10 i.e., the current corresponds to the value which is necessary to

utilize the theoretical capacity of the material during 10 hours) during charging and discharging for analyzing cycling stability performances.

## 2.3. X-Ray Diffraction

X-ray diffraction (XRD) is one the most efficient and widely used techniques for phase identification of a crystalline material and can provide information on unit cell dimensions and microstructure. It is based on the constructive interference of monochromatic X-rays and a crystalline sample. The condition for diffraction is described by Bragg's Law:

$$2d \sin\theta = n\lambda$$

where d is the spacing between the scattering planes in the lattice, θ is the angle between incoming beam and scattering plane of the crystal and λ is the wavelength of the incoming beam.

By analyzing the diffraction patterns, the structural information including phase fraction, lattice parameters, atomic positions, occupation numbers, lattice strain and crystallite size are obtained. The Rietveld method using the Fullprof software package was used for the structure analysis of the diffraction patterns[43].

Some *ex situ* powder X-ray diffraction experiments were performed on a STOE STADI/P laboratory powder diffractometer (Mo-$K_{\alpha 1}$ radiation). All the *in situ* electrochemical cycling experiments and most of the *ex situ* measurements for pristine samples were done at high resolution synchrotron radiation power diffraction (SRPD) beam lines as the Materials Science and Powder Diffraction Beamline (MSPD) at ALBA and the high-resolution powder diffraction beamline (P02.1) at PETRA-III, DESY.

## 2.3.1. Laboratory Diffractometer

The laboratory diffractometer is a STOE STADI/P powder diffractometer (***Figure 8***) equipped with a Dectris MYTHEN 1K linear silicon strip detector and curved Ge 111 double crystal monochromator yielding pure $K_{\alpha 1}$ radiation ($\lambda$=0.7093Å). The molybdenum tube gives relatively good flux and its $K_{\alpha 1}$ emission energy is 17.5 keV. The diffraction patterns for pristine samples were collected by filling the samples in 0.5 mm Ø borosilicate capillaries.

***Figure 8*** *– Instrumental set up of the Molybdenum (laboratory) diffractometer.*

## 2.3.2. Material Science and Powder Diffraction Beamline, ALBA

ALBA is a 3rd generation synchrotron light facility, the newest source in the Mediterranean area with 3 GeV electron beam energy. The MSPD beamline operates at

energies between 8 and 50 keV and it has a superconducting wiggler as an insertion device. The beamline is equipped with a Mythen1D position sensitive detector, a MAD26 high resolution detector and Si 111 double crystal monochromator for powder diffraction. Approximately half of the *in situ* synchrotron radiation powder diffraction (SRPD) measurements for the materials under investigation were carried out at MSPD, ALBA using the energy of 30 keV (λ = 0.413486 Å)[44]. A 8-cell *in situ* sample holder and *in situ* coincells[42] were mounted onto a rotatable frame controlled by a motor (***Figure 9***) which allows the positioning and consecutive measurement of multiple electrochemical cells which are cycled by connecting to a VMP potentiostat. The horizontal beam size was 3mm and the beam is slightly focused in the vertical direction to ~0.3mmwith an exposure time of 40 s per pattern.

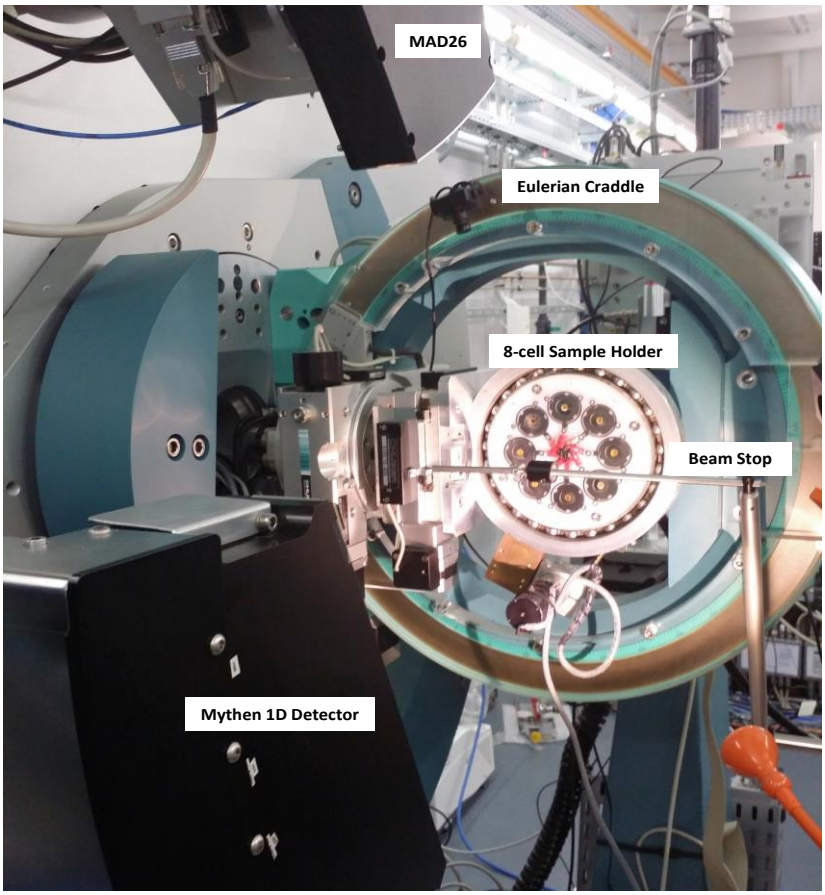


***Figure 9*** *– Instrumental set up of the MSPD beamline at ALBA, Barcelona with in situ 8-Cell sample holder set up installed.*

## 2.3.3. High Resolution Powder Diffraction Beamline (P02.1-PETRA III)

PETRA III is the high brilliance 3rd generation synchrotron radiation source at DESY (Deutsches Elektronen-Synchrotron). The P02.1 beamline operates at a fixed energy of 60 keV (λ = 0.207 Å) and exhibits low divergence, small energy bandwidth and relatively high flux.

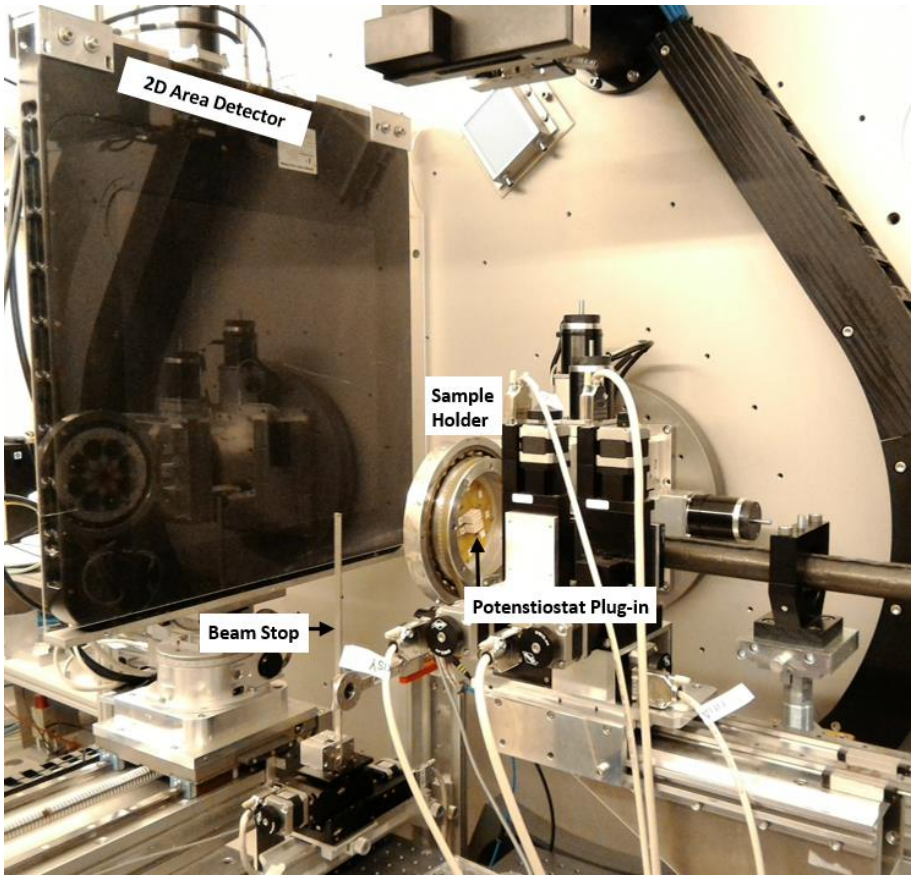


***Figure 10*** *– Instrumental set up of the P02.1 at PETRA III, DESY, Hamburg with in situ 8-Cell sample holder set up installed.*

The beamline is equipped with a dispersive high resolution double crystal Laue monochromator with diamond 111 and silicon 111 crystals for powder X-ray diffraction (***Figure 10***). During measurements, the beam size was set to 0.75x0.75 $mm^2$ and the sample to detector distance was 1600 mm. The diffraction patterns were collected using a 2D flat panel detector (Perkin Elmer XRD1621). The obtained 2D images were integrated to 1D

diffraction patterns using the X-ray image processing program Fit2D[45]. All *in situ* SRPD measurements were done using the 8-cell sample holder[42] and *in situ* coin cells. The diffraction patterns for pristine samples were collected by filling the samples in 0.5 mm Ø borosilicate capillaries.

## 2.4. Scanning Electron Microscopy

A scanning electron microscope (SEM) produces the sample image using an electron beam which scans the surface of the sample. The electrons are scattered by the sample atoms producing various signals that can be used to obtain information about the surface topography and composition.

The morphology investigations of initial powders were performed by using a Zeiss Supra 55 scanning electron microscope with primary electron energies of 5 and 15 keV and an in-lens detector. The measured particle size was calculated by using the SmartTiffV2 software.

## 2.5. Thermogravimetry and Differential Scanning Calorimetry Analysis

Thermogravimetry (TG) and Differential Scanning Calorimetry (DSC) analyses were simultaneously used to analyze the thermal behavior of the materials. The simultaneous application of TG-DSC on one sample at a time yields more information due to identical test conditions. By varying temperature with time, TGA measures the change of sample mass with temperature. DSC measures the difference in the amount of heat required to increase the temperature of a sample and suitable reference as a function of temperature.


***Figure 11 –*** *Simultaneous TG-DSC instrument* STA 449 C (Netzsch, Germany) installed inside Ar-filled glovebox. *Inset shows the sample holder and heating element.*

TG-DSC measurements were carried out using a Model STA 449 C (Netzsch, Germany) analyzer (***Figure 11***). In this work, the thermal behavior was detected over the temperature range from room temperature to 1000°C by scanning at a fixed heating rate of 5 °C/min. Both sample and reference crucibles were made of alumina. 10 mg of powders were used for the measurements. Prior to the actual measurements, calibration was done. The complete measurement setup was installed in an Argon filled glove box and the experimental atmosphere is controlled with different gas inlets.

## 2.6. X-Ray Absorption Spectroscopy

XAS measures the variation of the intensity of the absorption coefficient as a function of the incident X-ray energy which can be used for studying oxidation states as well as local coordination of an absorbing atom. It follows the Beer-Lambert's law of absorption, when an X-ray beam is transmitted through a sample, the linear absorption coefficient (μ) can be given as follows:

$$I_T = I_0 \exp(-\mu t)$$

$$\mu t = \ln (I_0/I_T)$$

where $I_0$ is the intensity of the incident X-rays on the sample, t is the thickness of the sample, $I_T$ is the intensity of transmitted X-rays through the sample.

An XAS spectrum is characterized by three regions: the pre-edge region, X-ray absorption near edge (XANES) region and the extended X-ray absorption fine structure (EXAFS) region. Analysis of the pre-edge regions is used to determine the local structure of first-row transition metals. The XANES region, which extends from approximately -20 eV below the absorption edge of an element to about 100 eV above the edge, is characterized by the multiple scattering of the photoelectron with the surrounding atom. The line shape of the XANES depends on the formal valence of the atom, coordination environment and extent of filling of the excited state. The EXAFS region, which extends from about 100 eV to as much as 1000 eV above the edge, gives the local coordination environment around the absorbing atom. This region characterized by the single scattering of the photoelectron with the surrounding atoms and get back scattered due to relatively large kinetic energy. Analyzing the EXAFS oscillations can give information on the number and distance of the surrounding atoms. (***Figure 12***).

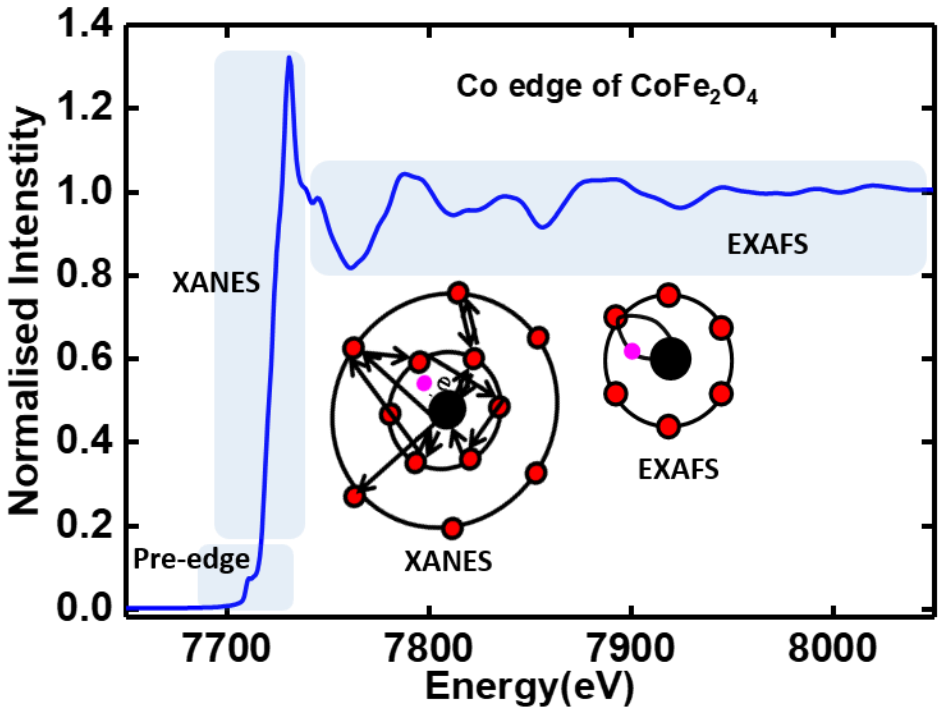


***Figure 12** – The Co K edge XAS spectra of $CoFe_2O_4$.*

XANES spectra of different materials at pristine and different discharge and charge states are compared to the reference material to determine the oxidation state of the absorbing atom. The XAS measurements were carried out for all pristine materials and *in situ* XAS studies were carried out for $MFe_2O_4$ (M = Fe, Co, Ni, Zn) materials at Fe, Co, Ni and Zn K edges. During *in situ* measurements, to get the information about the different phase fractions, linear combination fitting (LCF) analysis is done on the XANES region using different reference materials. The Fourier transform of the experimental EXAFS data is done using the IFEFFIT and FEFF[46] to relate the electrochemical mechanism to its local structure.

XAS experiments were carried out in a synchrotron radiation facility to have a high X-ray flux to obtain good signal-to-noise data in a reasonable time frame. Also a broad spectral range of up to 1000 eV at uniformly high flux during a single scan can be achieved by using intense and tunable X-rays with high stability in flux, energy, and beam position. *In situ* and *ex situ* XAS measurements were carried out at the XAS beamline at Angströmquelle

Karlsruhe (ANKA) and at the high-energy XAS beamline (P65) at PETRA-III EXTENSION, DESY. *In situ* measurements were done using 300 µm thick coated electrodes on copper foil, cut into 12 mm discs. For *ex situ* measurements of the reference materials, about 10 mg of pristine material was uniformly mixed with carboxy methyl cellulose in a mortar and pressed with 8 tons into a pellet. This dilution is performed so as to obtain the optimum edge jump for the XAS spectra.

## 2.6.1. Angströmquelle Karlsruhe – XAS Beamline

The XAS beamline at ANKA, Karlsruhe, provides reasonably high flux. The spectra were recorded in transmission geometry with conventional step scan mode at different edges during electrochemical cycling. ***Figure 13*** shows the layout of the XAS beamline at ANKA with the two-cell sample holder using in-house *in situ* cells. To get reasonably good transmission spectra, especially at the Fe edge, the glass window from one side of the *in situ* cell was replaced by a 500 µm-thin glassy carbon window.

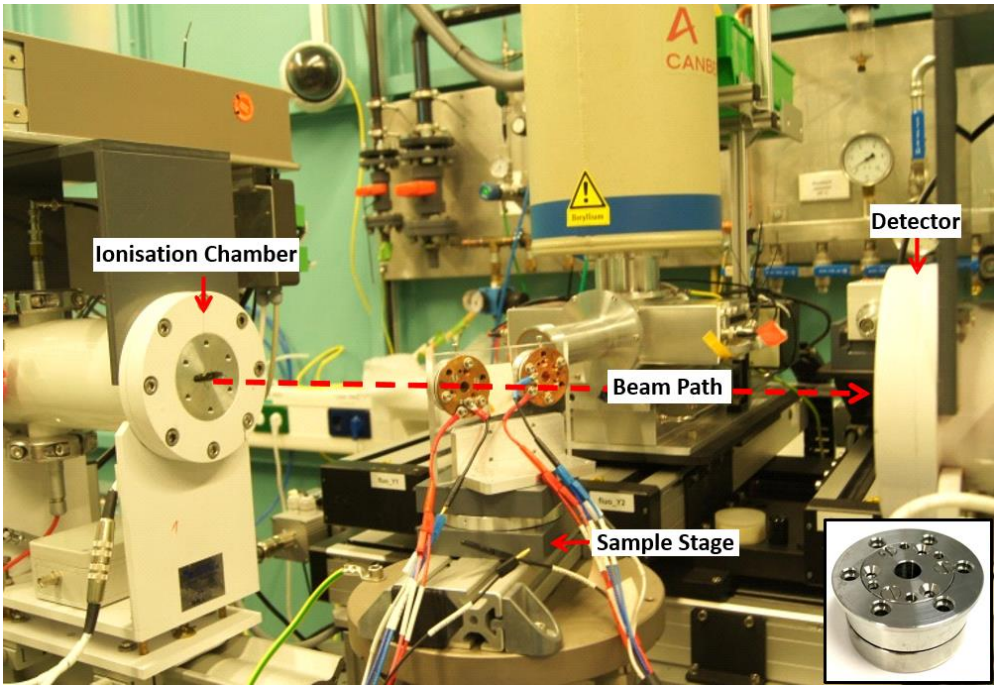


***Figure 13*** *– The layout of the XAS beamline at ANKA. Inset is an* in-house *in situ cell.*

The *in situ* cells were placed in the sample stage and aligned separately. The sample stage was moved automatically to shift between the samples. In order to measure different edges in one run, the double-crystal fixed exit monochromator equipped with Si 111 crystals as well as the ionization chamber (IC Spec Ionization Chamber, Oxford) were optimized for the specified edge. To detect the fluorescence signal, a five-element germanium detector (Ultra-LEGe Detector) was used. The positions of the electrochemical test cells and the energy ranges were all synchronized to facilitate the simultaneous *in situ* measurement of two samples at two different edges. To obtain reasonable time resolution, quick-EXAFS measurements were performed with a scan rate of 5 min per spectrum.

### 2.6.2. High-Energy XAS Beamline (P65-PETRA III Extension)

The P65 XAS Beam line provides a relatively large beam (0.5x1 $mm^2$) and with a 11 period undulator delivering a maximum monochromatic photon flux of $2*10^{12}$ $s^{-1}$ at 9 keV. ***Figure 14*** shows a photograph of the P65 XAS beamline at PETRA III Extension with 8-cell sample holder using *in situ* coin cells. The *in situ* cells were placed in the sample holder on the sample stage and aligned separately. The sample stage was aligned and moved automatically with the help of a motor to change between the samples. Even though 8 cells could be measured at a time, for a reasonable quality of the data, a maximum of 4 cells were used considering multiple edges and a scan rate of 10-11 minutes for each spectrum. The P65 beamline is equipped with the double-crystal fixed exit monochromator equipped with Si 111 crystals, 7 pixel HPGe energy dispersive detector, Si-PIPS diodes and a 11 period mini-undulator. X-ray absorption spectroscopy in both transmission and fluorescence modes were performed.

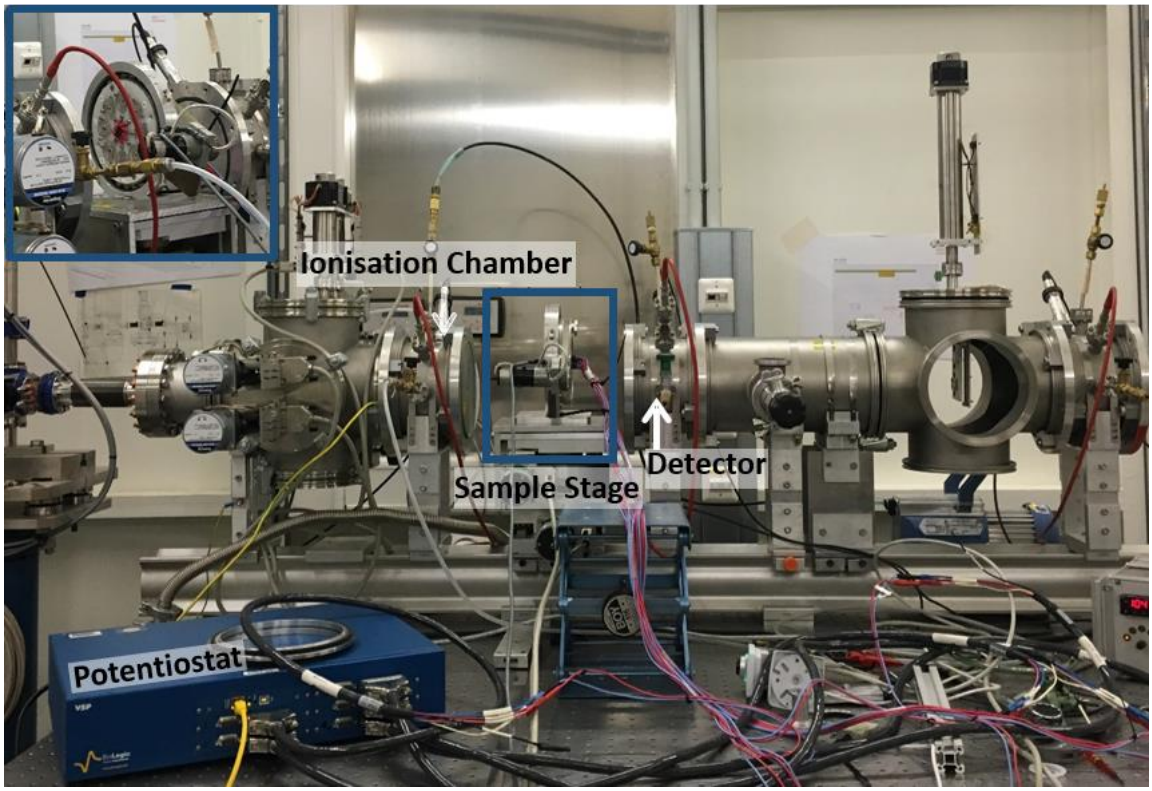


***Figure 14 –*** *The photograph of P65 XAS beamline at PETRA III Extension.*

The spectra were processed by using the Demeter software package based on IFEFFIT and FEFF[46]. For each edge and for each sample, the fitting parameter involved a unique amplitude reduction factor $S_0^2$, which accounts for the relaxation of all the other electrons in the absorbing atom to the hole in the core level and an overall energy parameter ($E_0$). Moreover, each shell corresponding to an edge or sample was associated with a unique temperature factor or EXAFS Debye–Waller (DW) factors and interatomic distance parameters (r). All the EXAFS fittings were carried out in the k range of 2–12 $Å^{-1}$and r range of 1–3 Å.

# Chapter 3 - Results and Discussions

## 3.1. Characterization of As-Prepared Materials

The characterization of the 3d transition metal ferrites, $MFe_2O_4$ ($M$ = Fe, Co, Ni, Cu, Zn) synthesized by an inverse co-precipitation procedure was done using various techniques. A detailed structural investigation was performed using powder X-ray diffraction. The morphology of the synthesized materials was analyzed using scanning electron microscopy. The thermal properties were investigated using thermogravimetry and differential scanning calorimetry studies and oxidation state and local co-ordination environment were measured using X-ray absorption spectroscopy.

### 3.1.1. Thermogravimetric Analyses of $MFe_2O_4$ ($M$ = Fe, Co, Ni, Cu, Zn)

In order to understand the temperature dependent reactions occurring in the synthesized materials, the metal hydroxides or the precipitates obtained after the centrifugation of the co-precipitation products were subjected to TG-DSC analysis. The TG-DSC curves obtained for the samples are shown in ***Figure 15*** below.

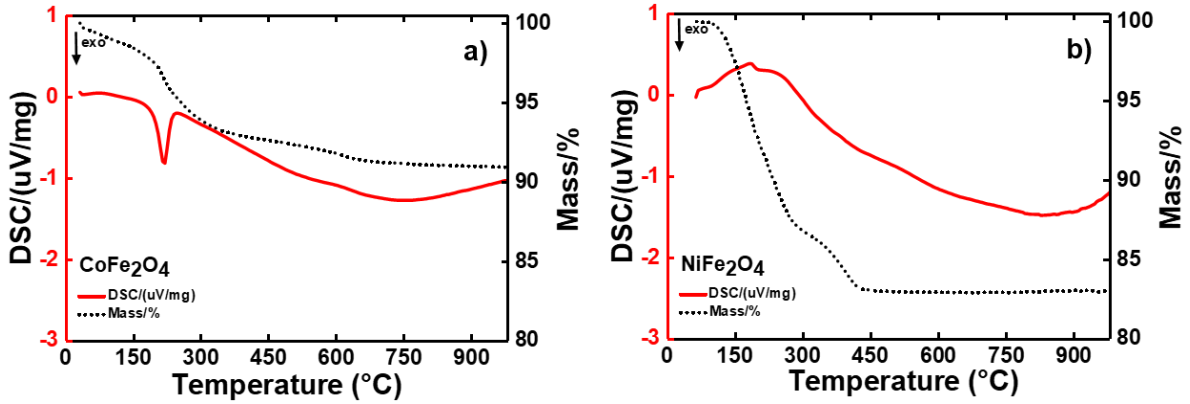

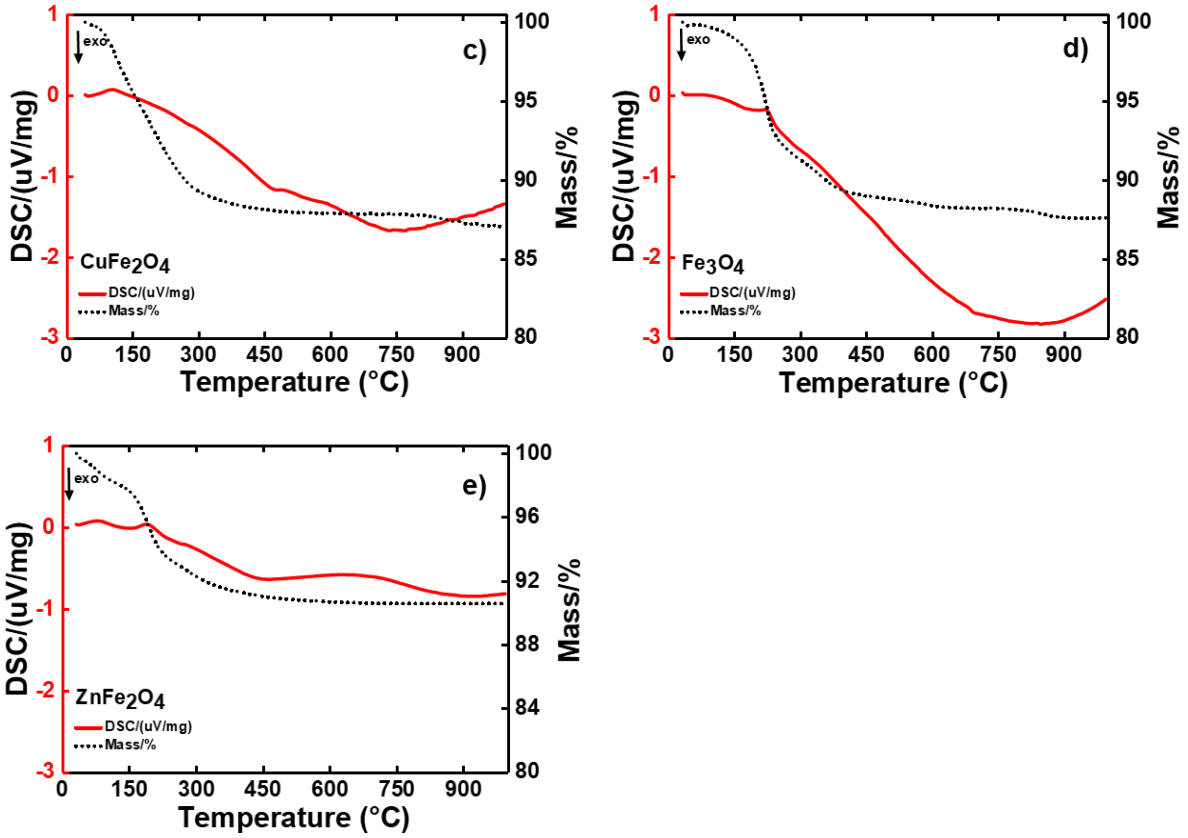


***Figure 15** – TG (Black dotted lines) and DSC curves (red lines) at a rate of 5 °C/ min, for $CoFe_2O_4$ (a), $NiFe_2O_4$ (b), $CuFe_2O_4$ (c), $Fe_3O_4$ (d) and $ZnFe_2O_4$ (e) measured in air atmosphere and for $Fe_3O_4$ in Argon atmosphere.*

The initial weight loss and the endothermic peak occurring in the DSC below 150 °C for all materials corresponds to the evaporation of water from the surface of the material[47,48]. For $CoFe_2O_4$, the exothermic peak at 220 °C is resulting from the decomposition of the transition metal hydroxide (which is obtained after the precipitation) as well as remains of water traces and organics[49].

An accelerated mass loss in the TG curve occurs below 300-450 °C. It can be ascribed to the decomposition of residual organic compounds. In $ZnFe_2O_4$, there is no obvious mass loss above 500 °C in the TG-DSC curves, indicating the formation of final $ZnFe_2O_4$ nanoparticles[50]. Also for $NiFe_2O_4$, the TGA curve is almost flat, i.e., there is no weight loss and no endothermic and exothermic peaks are observed in DSC above 450 °C which indicates the formation of pure $NiFe_2O_4$. In $NiFe_2O_4$, there is no significant phase transition.

In $Fe_3O_4$, the weight loss tends to be constant above 450 °C until 700 °C. Between 700 °C and 870 °C, the presence of an exothermic peak is due to the oxidation of $Fe_3O_4$ with a slight increase in the weight. For $CuFe_2O_4$, the DSC curve of the precursor sample shows an exothermic peak from around 630 °C to 870 °C with an increase in weight in the TG curve which may correspond to a solid-state reaction between CuO and $Fe_2O_3$ and formation of $CuFe_2O_4$[51].

Therefore, the initial weight losses up to 300 °C could involve decomposition of the transition metal hydroxide (which is obtained after the precipitation) as well as remains of water traces. No significant weight loss was observed above 450-500 °C in most cases, where the spinel ferrites were completely formed and, hence, shows a similar behavior among different ferrites. Therefore, to understand the relationship between annealing temperature of the sample to material properties and electrochemical performance, two different temperatures were chosen: 600 °C and 800 °C.

### 3.1.2. Structural Characterization of $M$Fe$_2$O$_4$ ($M$ = Fe, Co, Ni, Cu, Zn)

The spinels with general formula $(A^{2+})_{tet}[2B^{3+}]_{oct}(O^{2-})_4$ crystallize in the cubic system (space group $Fd\bar{3}m$) with cubic close-packed oxide anions and cations A and B occupying 1/8 of the tetrahedral and 1/2 of the octahedral sites[52,53]. Among the spinel oxides, the ferrite system are known for the variations in cation distribution over the tetragonal and octahedral sites.

Depending upon the degree of inversion, $x$ which is the fraction of the divalent metal cations in octahedral sites in $(A_{1-x}B_x)_{Tet}[A_xB_{2-x}]_{Oct}O_4$, the spinels can be classified into three different categories. (i) Normal spinels ($x$ = 0), the tetrahedral and octahedral sites are occupied by divalent and trivalent cations, respectively. (ii) Inverse spinels ($x$ = 1), the divalent cations occupy the octahedral sites and trivalent cations occupy both tetrahedral and octahedral sites.

(iii) Partially inverse spinel, the divalent and trivalent cations are distributed at both tetrahedral and octahedral sites. However, the cation distribution not only depends on the electronic configuration and valence state of the metals, but also varies with the synthesis conditions. ***Figure 16*** shows the crystal structure of inverse spinel $NiFe_2O_4$ sample.

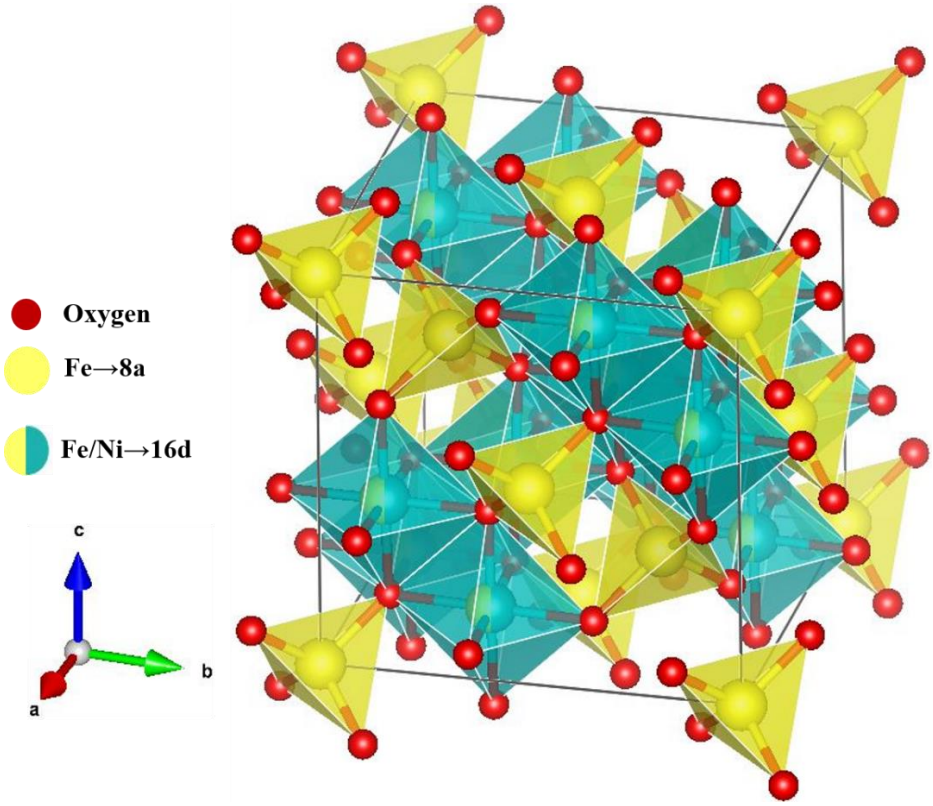


***Figure 16*** *– Crystal structure of inverse spinel $NiFe_2O_4$.*

To determine the spinel structure and cation distribution of 3d transition metal ferrites, $MFe_2O_4$ (*M* = Fe, Co, Ni, Cu, Zn), in the current study calcined at different temperatures, X-ray diffraction was carried out. The Rietveld analysis results of these materials are presented below.

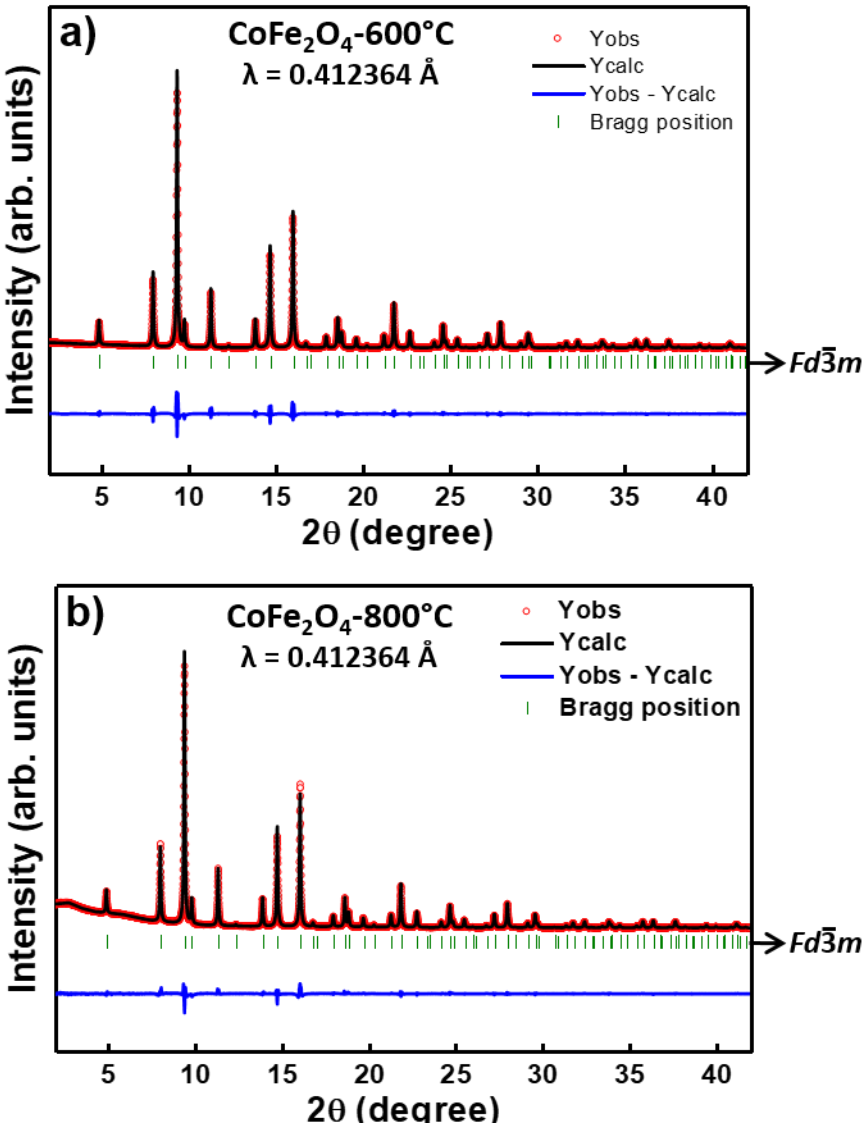


***Figure 17*** *– Rietveld refinement results based on synchrotron diffraction patterns of as prepared $CoFe_2O_4$ annealed at 600 °C (a) and 800 °C (b) measured in 0.5 mm capillaries.*

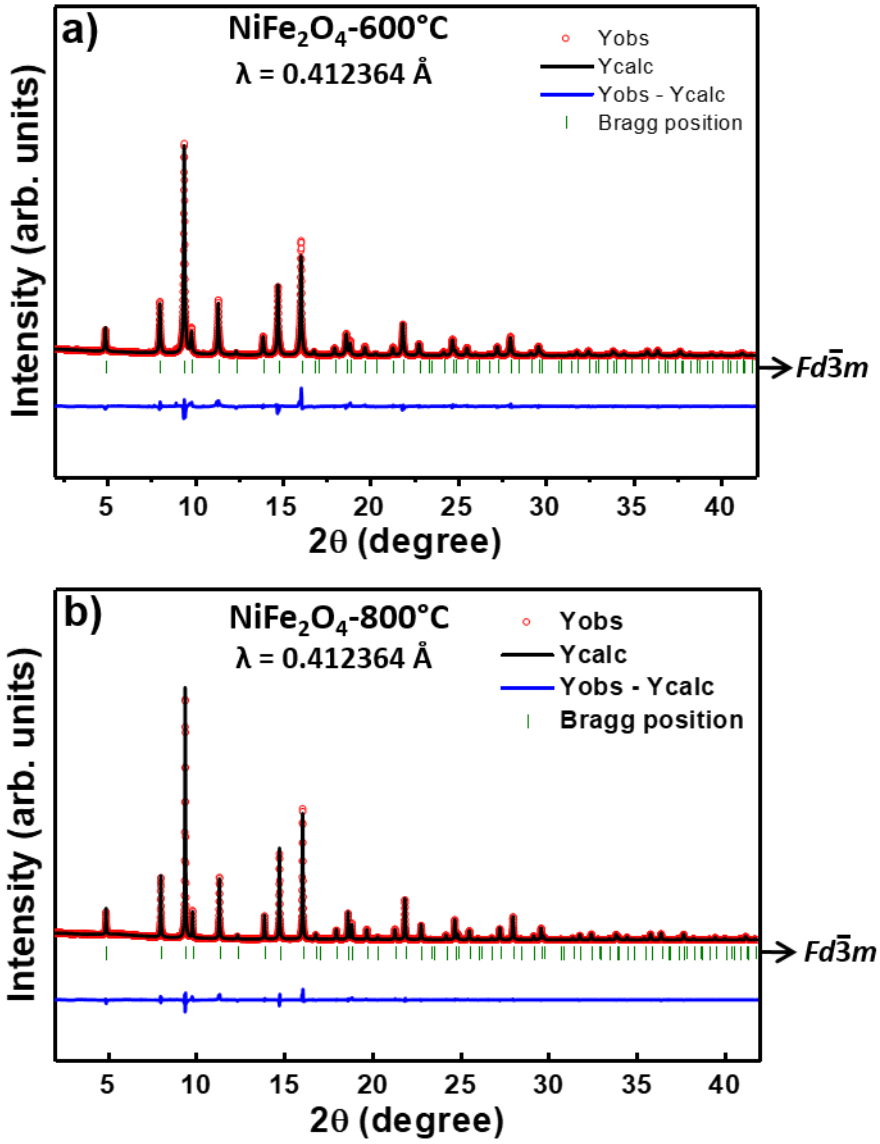


***Figure 18*** *– Rietveld refinement results based on synchrotron diffraction patterns of as prepared $NiFe_2O_4$ annealed at 600 °C (a) and 800 °C (b) measured in 0.5 mm capillaries.*

***Figure 17*** and ***Figure 18*** show the Rietveld analysis results of $CoFe_2O_4$ and $NiFe_2O_4$ annealed at 600 °C and 800 °C. Both $CoFe_2O_4$ and $NiFe_2O_4$ samples were phase pure at the two different temperatures. The most accurate fit of the experimental pattern was achieved while considering $NiFe_2O_4$ as inverse cubic spinel (space group $Fd\bar{3}m$) and $CoFe_2O_4$ as partially inverse[54] cubic spinel structure (space group $Fd\bar{3}m$). However, due to the similarity in the atomic form factor of Co, Ni and Fe, the precise determination of the cation distribution by means of X-ray diffraction is difficult.

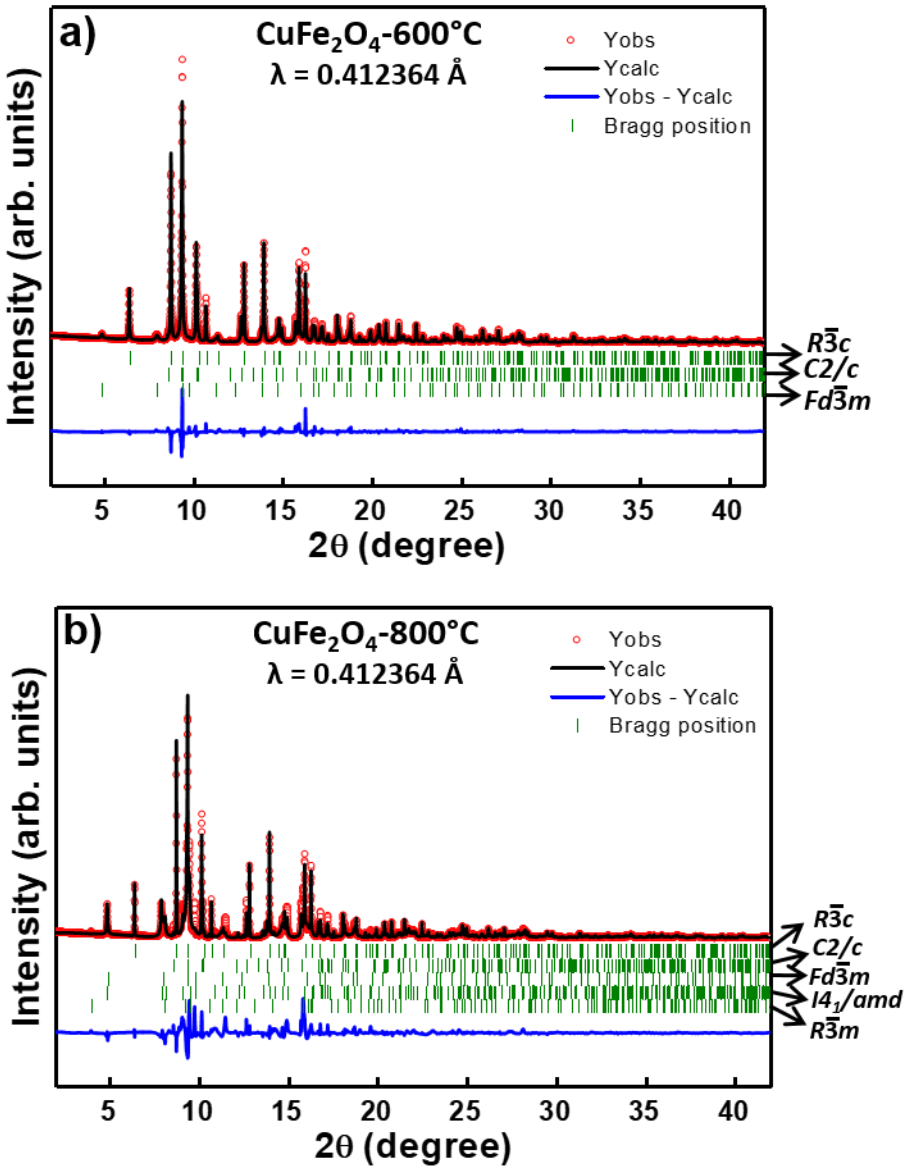


***Figure 19*** *– Rietveld refinement results based on synchrotron diffraction patterns of as prepared $CuFe_2O_4$ annealed at 600 ° C (a) and 800 °C (b) measured in 0.5 mm capillaries.*

Rietveld analysis of $CuFe_2O_4$ annealed at 600 °C and 800 °C revealed the presence of multiple phases in both cases. At 600 °C, 58.5 ± 0.3 % of $Fe_2O_3$ (space group $R\bar{3}c$), 26.6 ± 0.2 % of CuO (space group C 2/c) and 15± 0.2 % of inverse spinel $CuFe_2O_4$ (space group $Fd\bar{3}m$) were present as seen from ***Figure 19***. Whereas at 800 °C, 25 ± 0.5 % of $Fe_2O_3$ (space group $R\bar{3}c$), 16.4 ± 0.4 % of CuO (space group C 2/c), 51.9 ± 1.4 % of inverse spinel $CuFe_2O_4$ (space group $Fd\bar{3}m$), 2.9 ± 0.1 % of $CuFe_2O_4$ (space group $I4_1/amd$) and 3.9 ± 0.9

% of $CuFeO_2$ (space group $R\bar{3}m$) were present. Similar phases were observed by Gruner *et al.*,[38] and Adam *et al.*,[55] for the Cu-Fe-O system. With increasing temperature, $CuFe_2O_4$ with $I4_1/amd$ space group appears together with the formation of $R\bar{3}m$ $CuFeO_2$.

Magnetite ($Fe_3O_4$) is one of the well-studied spinel structures in which Fe is known to exist in mixed valence states. The tetrahedral 8a (A) sites are solely occupied by $Fe^{3+}$ ions and the octahedral 16d (B) sites are occupied by a mixture of $Fe^{2+}$ and $Fe^{3+}$ ions[56,57] in the $AB_2O_4$ spinel lattice. In the current study, the inverse spinel $Fe_3O_4$ (space group $Fd\bar{3}m$, ICSD record: 26410) is phase pure at 600 °C and a majority of this phase decomposes into FeO (space group $Fm\bar{3}m$, ICSD record: 31081) at 800 °C (***Figure 20***). Phase transformations of $Fe_3O_4$ into FeO and metallic iron is reported in literature when heated in inert atmosphere[58–60] but no such metallic phase is observed in the current study. Also the multiple impurity reflections seen around 3.4°, 3.9°, 4.3°, 5.2° and 6.3° 2θ angles in $Fe_3O_4$-800 °C cannot be assigned to any known phase from the database.

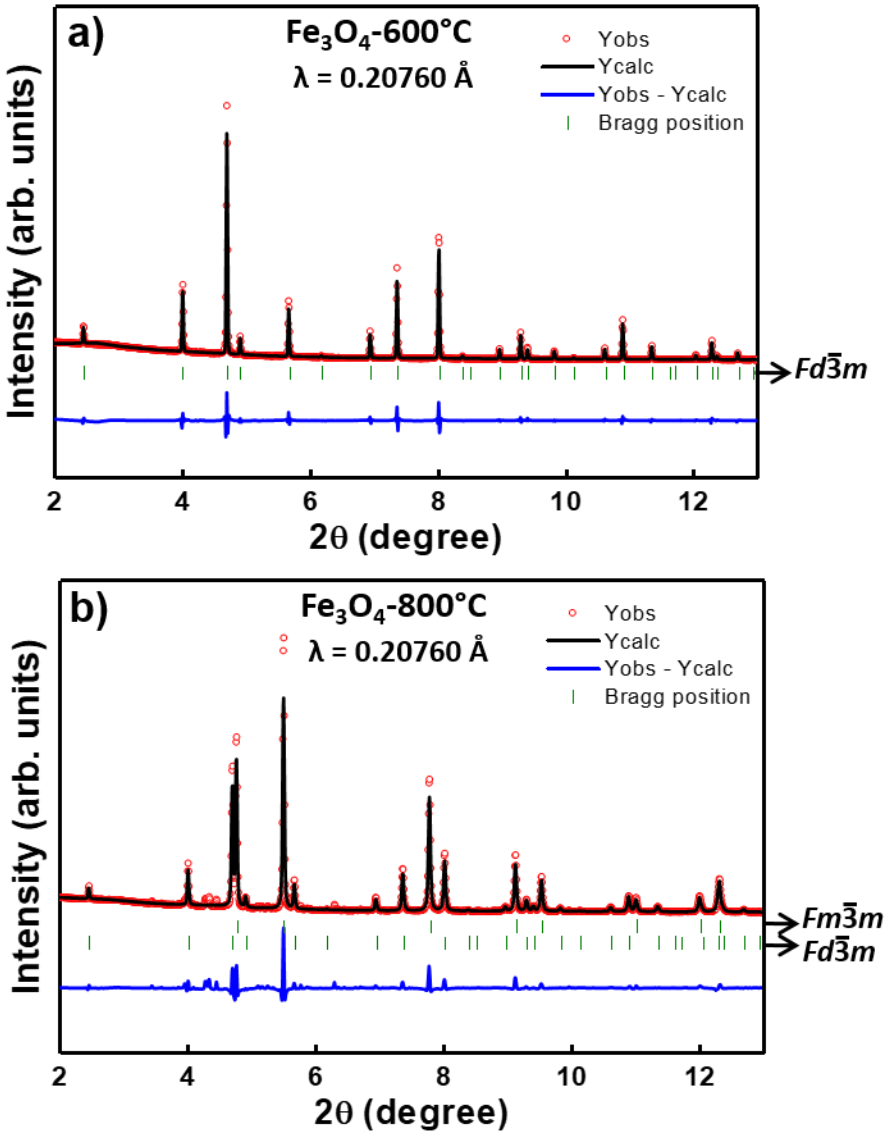


***Figure 20*** *– Rietveld refinement results based on synchrotron diffraction patterns of as prepared $Fe_3O_4$ annealed at 600 ° C (a) and 800 °C (b) measured in 0.5 mm capillaries.*

The Rietveld analysis based on the obtained synchrotron diffraction patterns for pristine samples, ZFO-600 and ZFO-800 (***Figure 21***) shows that the materials have an inverse spinel structure. ZFO-600 with an average particle size of 86 nm shows a higher degree of inversion compared to ZFO-800 with an average particle size of 140 nm which agrees with the previously reported studies on zinc ferrite nanoparticles[61,62].

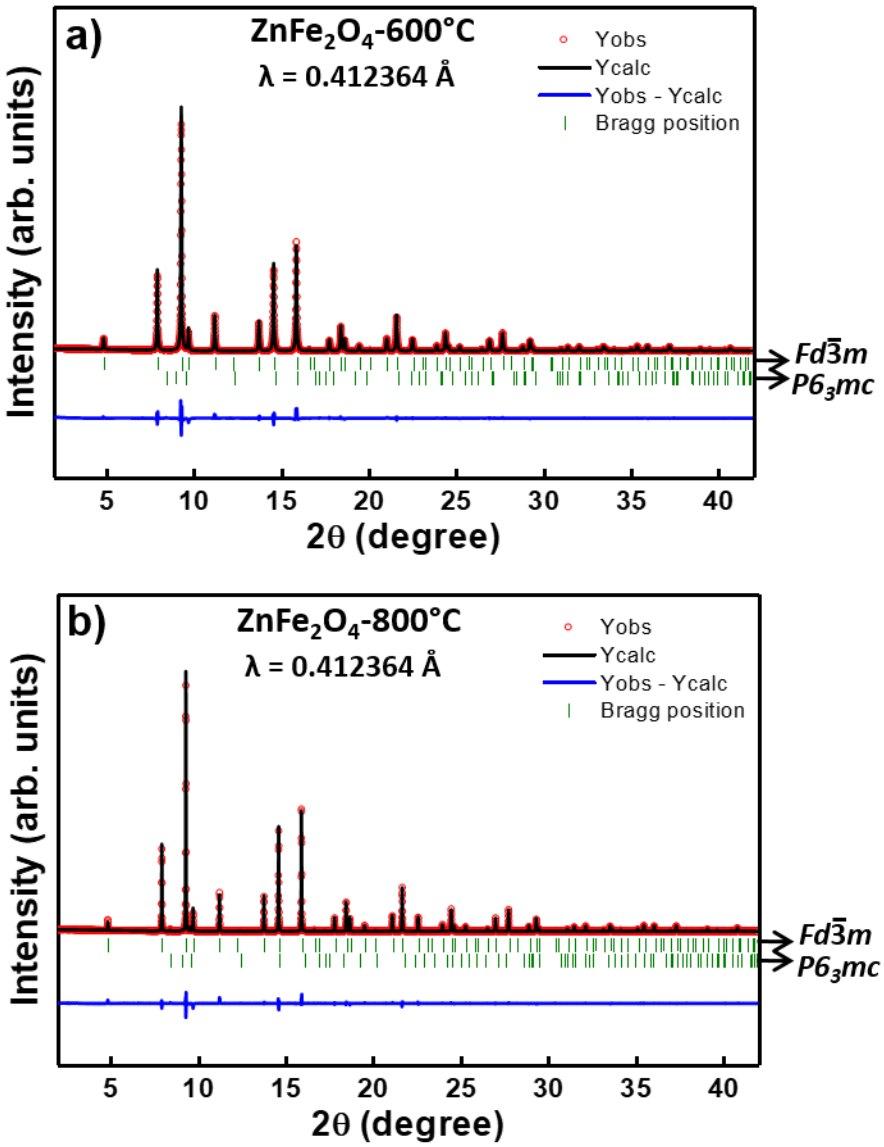


***Figure 21** – Rietveld refinement results based on synchrotron diffraction patterns of as prepared $ZnFe_2O_4$ annealed at 600 °C (a) and 800 °C (b) measured in 0.5 mm capillaries.*

For all the above spinel ferrite samples, the oxygen position parameter lies within the normal limit of 0.25 and 0.27. The summary of the Rietveld analysis of different electrode materials with observed phases, phase ratios, space group and lattice constants are given in ***Table 1***.

***Table 1 - Summary of Rietveld refinement.***

| Sample | Phase | Phase Content (wt %) | Space Group | Lattice Parameter (Å) |
|---|---|---|---|---|

| | | | | |
|---|---|---|---|---|
| $CoFe_2O_4$-600 °C | $CoFe_2O_4$ | 100 | $Fd\bar{3}m$ | $a$=$b$=$c$= 8.3765(2) |
| $CoFe_2O_4$-800 °C | $CoFe_2O_4$ | 100 | $Fd\bar{3}m$ | $a$=$b$=$c$= 8.3725(1) |
| $NiFe_2O_4$-600 °C | $NiFe_2O_4$ | 100 | $Fd\bar{3}m$ | $a$=$b$=$c$= 8.3449(3) |
| $NiFe_2O_4$-800 °C | $NiFe_2O_4$ | 100 | $Fd\bar{3}m$ | $a$=$b$=$c$= 8.3408(1) |
| $CuFe_2O_4$-600 °C | $Fe_2O_3$ | 58.45 | $R\bar{3}c$ | $a$=$b$= 5.0369(1)<br>$c$= 13.7534(7) |
| | CuO | 26.57 | $C2/c$ | $a$= 4.6889(5)<br>$b$= 3.4219(3)<br>$c$= 3.42194(5) |
| | $CuFe_2O_4$ | 14.98 | $Fd\bar{3}m$ | $a$=$b$=$c$= 8.386(3) |
| $CuFe_2O_4$-800 °C | $CuFe_2O_4$ | 51.86 | $Fd\bar{3}m$ | $a$=$b$=$c$= 8.364(5) |
| | $Fe_2O_3$ | 25.01 | $R\bar{3}c$ | $a$=$b$= 5.0380(4)<br>$c$= 13.749(1) |
| | CuO | 16.36 | $C2/c$ | $a$= 4.6879(9)<br>$b$= 3.4248(7)<br>$c$= 5.133(1) |
| | $CuFeO_2$ | 3.92 | $R\bar{3}c$ | $a$=$b$= 2.998(3)<br>$c$= 17.69(3) |
| | $CuFe_2O_4$ | 2.85 | $I4_1/amd$ | $a$=$b$= 5.819(1)<br>$c$= 8.693(3) |
| $Fe_3O_4$-600 °C | $Fe_3O_4$ | 100 | $Fd\bar{3}m$ | $a$=$b$=$c$= 8.3920(1) |
| | FeO | 62.02 | $Fm\bar{3}m$ | $a$=$b$=$c$= 4.3248(3) |

| | | | | |
|---|---|---|---|---|
| $Fe_3O_4$-800 °C | $Fe_3O_4$ | 37.98 | $Fd\bar{3}m$ | $a$=$b$=$c$= 8.3930(7) |
| $ZnFe_2O_4$-600 °C | $ZnFe_2O_4$ | 99.86 | $Fd\bar{3}m$ | $a$=$b$=$c$= 8.4431(1) |
| | ZnO | 0.14 | $P6_3mc$ | $a$=$b$= 3.236(3)<br>$c$= 5.28(1) |
| $ZnFe_2O_4$-800 °C | $ZnFe_2O_4$ | 98.85 | $Fd\bar{3}m$ | $a$=$b$=$c$= 8.44356(5) |
| | ZnO | 1.15 | $P6_3mc$ | $a$=$b$= 3.2498(2)<br>$c$= 5.2022(7) |

### 3.1.3. Morphological Characterization of $M$Fe$_2$O$_4$ ($M$ = Fe, Co, Ni, Cu, Zn)

SEM images of 3d transition metal ferrites, $MFe_2O_4$ (M = Fe, Co, Ni, Cu, Zn) calcined at 600 °C and 800 °C are presented in ***Figure 22***. The particles annealed at 600 °C exhibit a smaller particle size compared to those annealed at 800 °C. In the case of $Fe_3O_4$ this is most pronounced. ***Table 2*** shows the particle size for each material at different annealing temperatures.

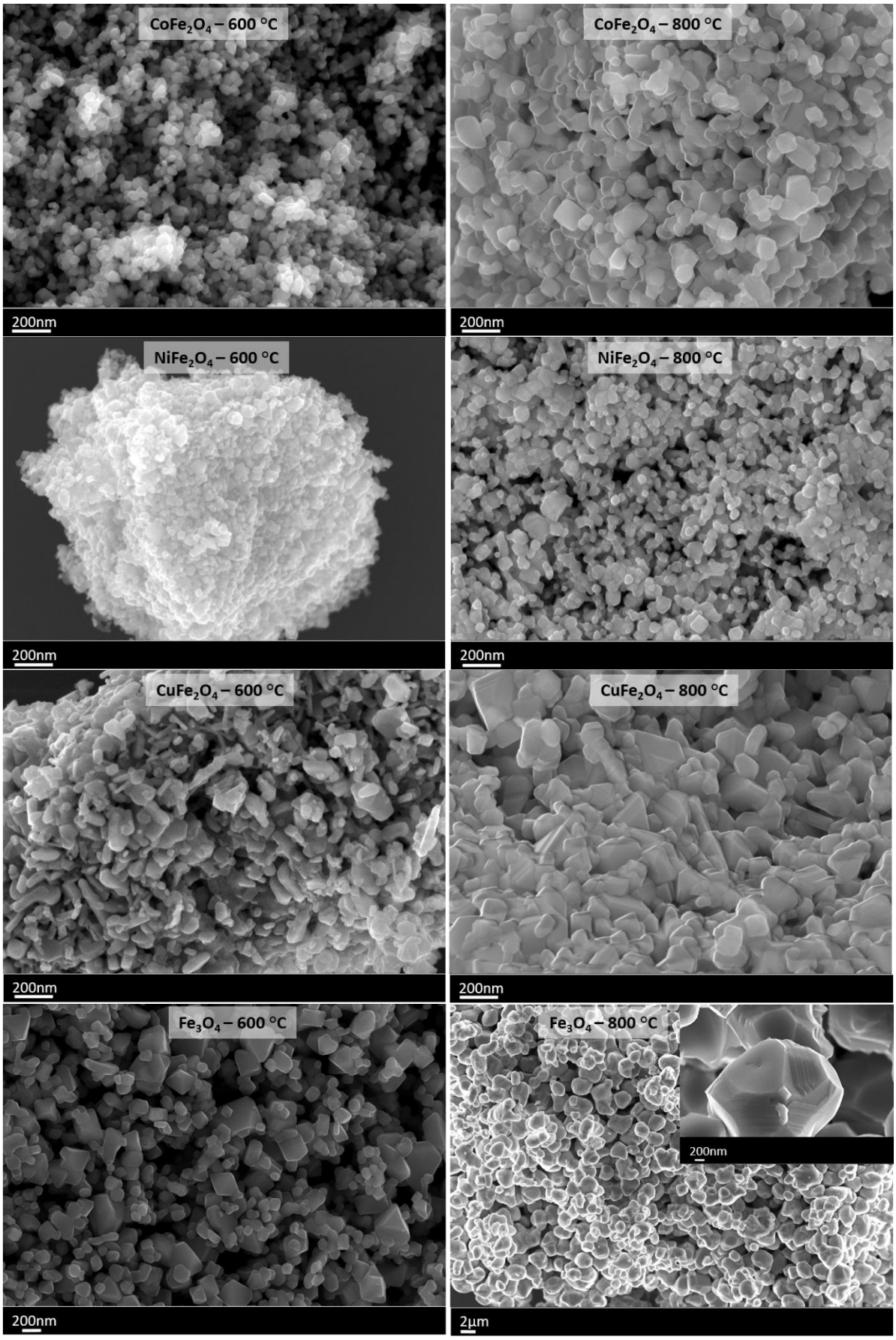
$CoFe_2O_4$ – 600 °C
200nm
$CoFe_2O_4$ – 800 °C
200nm
$NiFe_2O_4$ – 600 °C
200nm
$NiFe_2O_4$ – 800 °C
200nm
$CuFe_2O_4$ – 600 °C
200nm
$CuFe_2O_4$ – 800 °C
200nm
$Fe_3O_4$ – 600 °C
200nm
$Fe_3O_4$ – 800 °C
200nm
2µm

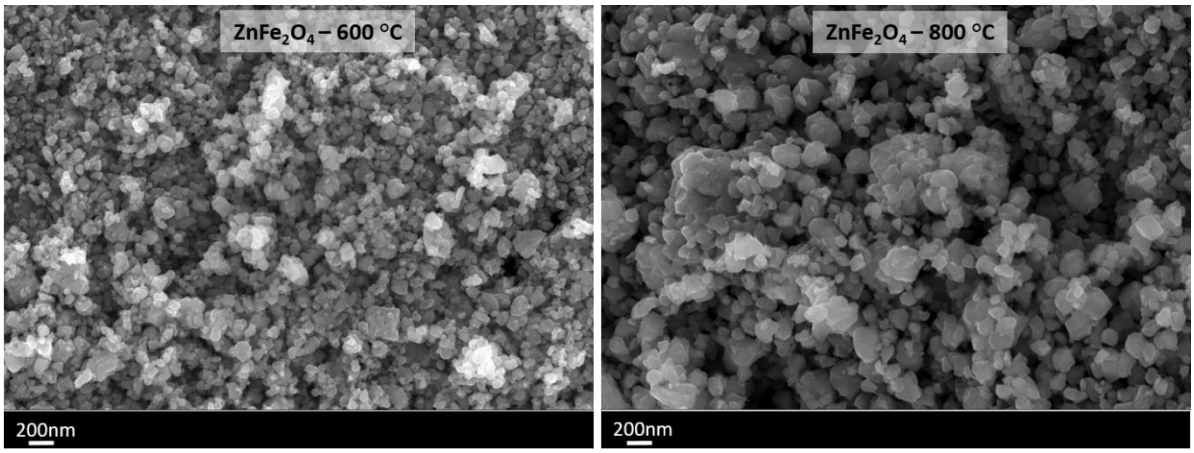


***Figure 22 –*** *SEM images of $MFe_2O_4$ (M = Co, Ni, Fe, Cu, Zn) annealed at 600 °C and 800 °C.*

***Table 2 - Particle size of 3d transition metal ferrites, $MFe_2O_4$ (M = Fe, Co, Ni, Cu, Zn) calcined at 600 °C and 800 °C determined by SEM.***

| Sample | Annealing Temperature | |
|---|---|---|
| | **600 °C** | **800 °C** |
| $CoFe_2O_4$ | 38±2 nm | 70±21 nm |
| $NiFe_2O_4$ | 27±15 nm | 52±19 nm |
| $Fe_3O_4$ | 111±47 nm | 1.73±0.62 µm |
| $CuFe_2O_4$ | 47±20 nm | 89±24 nm |
| $ZnFe_2O_4$ | 43±12 nm | 82±35 nm |

## 3.1.4.Oxidation State and Local Coordination Environment of *M*$Fe_2O_4$ (*M* = Fe, Co, Ni, Cu, Zn)

The 3d transition metal ferrites annealed at 800 °C were investigated by X-ray absorption spectroscopy to understand the oxidation state and local co-ordination environment in the pristine state.

XANES regions of the Fe K edge of both, $CoFe_2O_4$ and $NiFe_2O_4$, are compared with reference materials FeO and $Fe_2O_3$ (***Figure 23***). It can be seen that the edge position of both samples overlap with the edge position of the $Fe_2O_3$ sample and, therefore, in both ferrite samples, Fe has a formal valence state of $Fe^{3+}$ as in the case of $Fe_2O_3$. Also it was observed that the Fe K edge XANES region line shapes of both, $CoFe_2O_4$ and $NiFe_2O_4$, are comparatively similar which suggest that the local coordination of Fe in both the samples is almost identical.

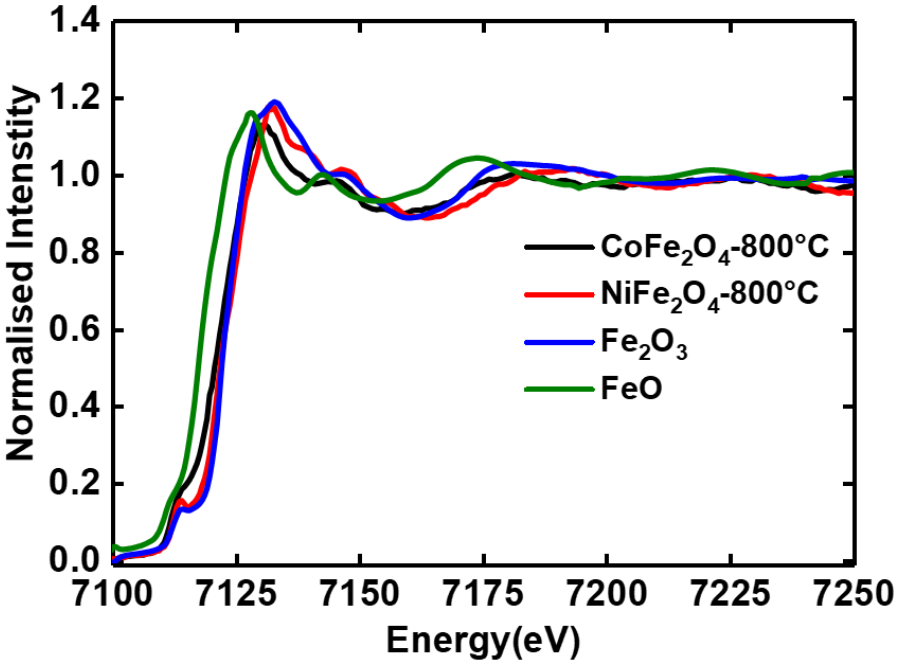


***Figure 23*** *– The Fe K edge XANES region for both $CoFe_2O_4$ and $NiFe_2O_4$ annealed at 800 °C.*

Similarly, by comparing the XANES region at Co and Ni edges with that of the corresponding reference materials (CoO and NiO) (***Figure 24a*** and ***b***), a former or pristine oxidation state of +2 can be assigned to both elements.

The XANES K edge spectra of 3d transition metals are characterized by a pre-edge and a main edge feature which provides the oxidation state and site symmetry of the absorbing atom. The pre-edge arises from the 1s → 3d dipole transitions that are forbidden by dipole selection rules and, therefore, only shows a weak intensity. The main edge is caused by the 1s → 4p orbital mixing or direct quadrupolar coupling. A detailed investigation of

nanoparticulate ferrites are previously reported by Nilsen et al.[63] The position and intensity of the pre-edge are sensitive to the local symmetry of the absorbing metal. From the previous studies it is clear that the pre-edge feature is more intense for a non-centrosymmetric tetrahedral iron (III) environment than for a centrosymmetric octahedral and for an inverse spinel the pre-edge intensity is approximately a weighted average of the tetrahedral and octahedral intensities.

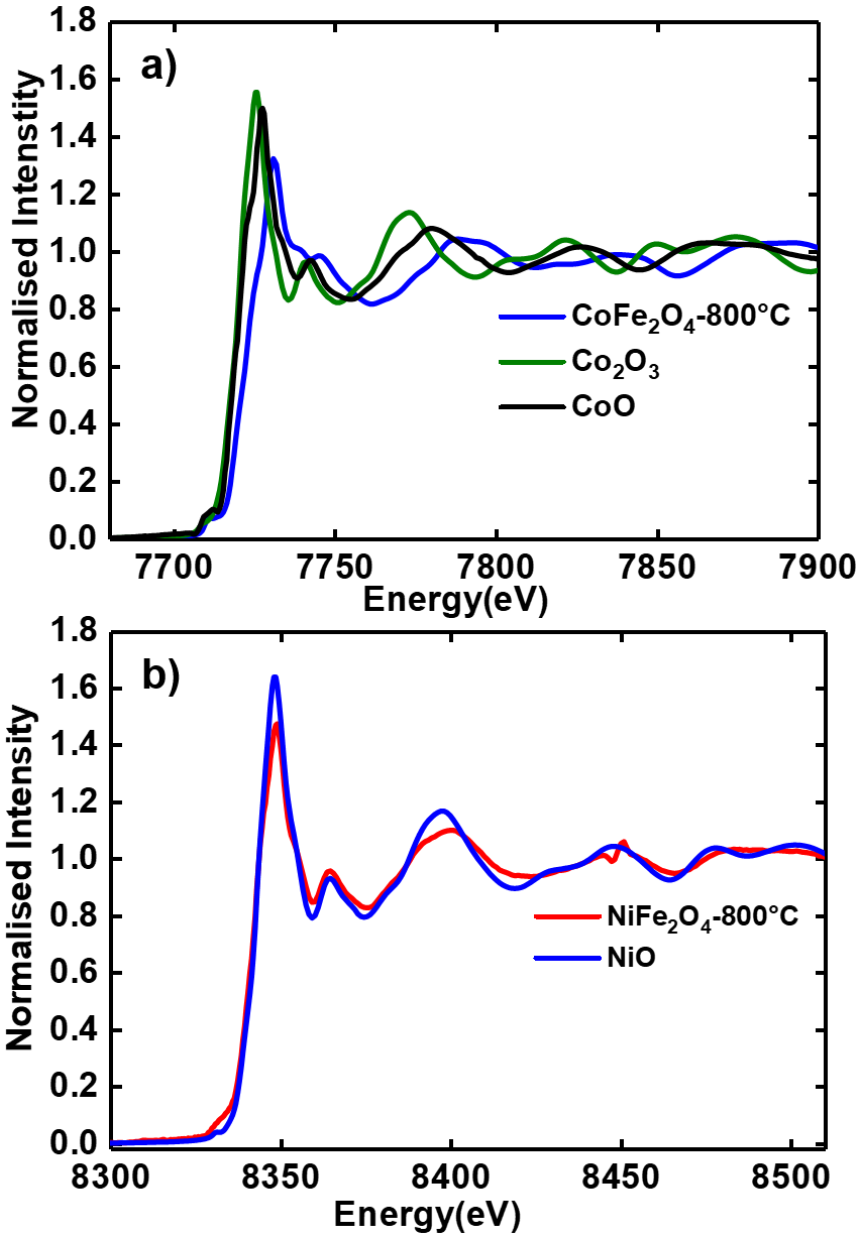


***Figure 24** – The Co (a) and Ni (b) K edge XANES region for $CoFe_2O_4$ and $NiFe_2O_4$ annealed at 800 °C.*

Therefore, the pre-edge features of the Fe K edge around 7113-7115 eV suggests the occupancy of $Fe^{3+}$ in both, tetrahedral and octahedral sites, for both $CoFe_2O_4$ and $NiFe_2O_4$. However, the pre-edge peak of the Ni K edge around 8332 eV is very weak compared to Fe and Co edges at 7711 eV in both the samples. This is because in $NiFe_2O_4$, Ni has an octahedral coordination in the inverse spinel and Fe is both octahedrally and tetrahedrally coordinated. Whereas, in the partially inverse spinel $CoFe_2O_4$, both, Fe and Co, are at tetrahedral and octahedral sites, which results in a corresponding pre-edge feature.

It is interesting to investigate $Fe_3O_4$ annealed at 600 °C and 800 °C using X-ray absorption spectroscopy due to the different crystallographic phases as observed by X-ray diffraction. ***Figure 25*** shows the XANES region of the Fe K edge of $Fe_3O_4$ samples annealed at 600 °C (***Figure 25****a*) and 800 °C (***Figure 25b***) compared with reference materials FeO, $Fe_2O_3$ and Fe metal foil. $Fe_3O_4$ has two Fe atoms existing in +3 and one in +2 oxidation states. Analyzing the XANES region, we can see that the edge position of $Fe_3O_4$-600 °C overlaps with the edge position of the $Fe_2O_3$ sample. Hence, Fe has a former/pristine valence state of $Fe^{3+}$ as in the case of $Fe_2O_3$. However, there is a slight shift of the edge to lower energy which also is an indication for the presence of Fe in +2 oxidation state. Whereas, the edge position of $Fe_3O_4$-800 °C overlaps with the edge position of the reference FeO spectra where Fe is in +2 Oxidation state. The higher amount of $Fe^{2+}$ in $Fe_3O_4$-800 °C comparing to $Fe_3O_4$-600 °C as revealed by XANES agrees very well with the results of XRD analysis, where FeO was identified as a main phase in $Fe_3O_4$-800 °C. The pre-edge feature of the Fe K edge around 7112 eV is much more pronounced in $Fe_3O_4$-600 °C material compared to $Fe_3O_4$-800 °C.

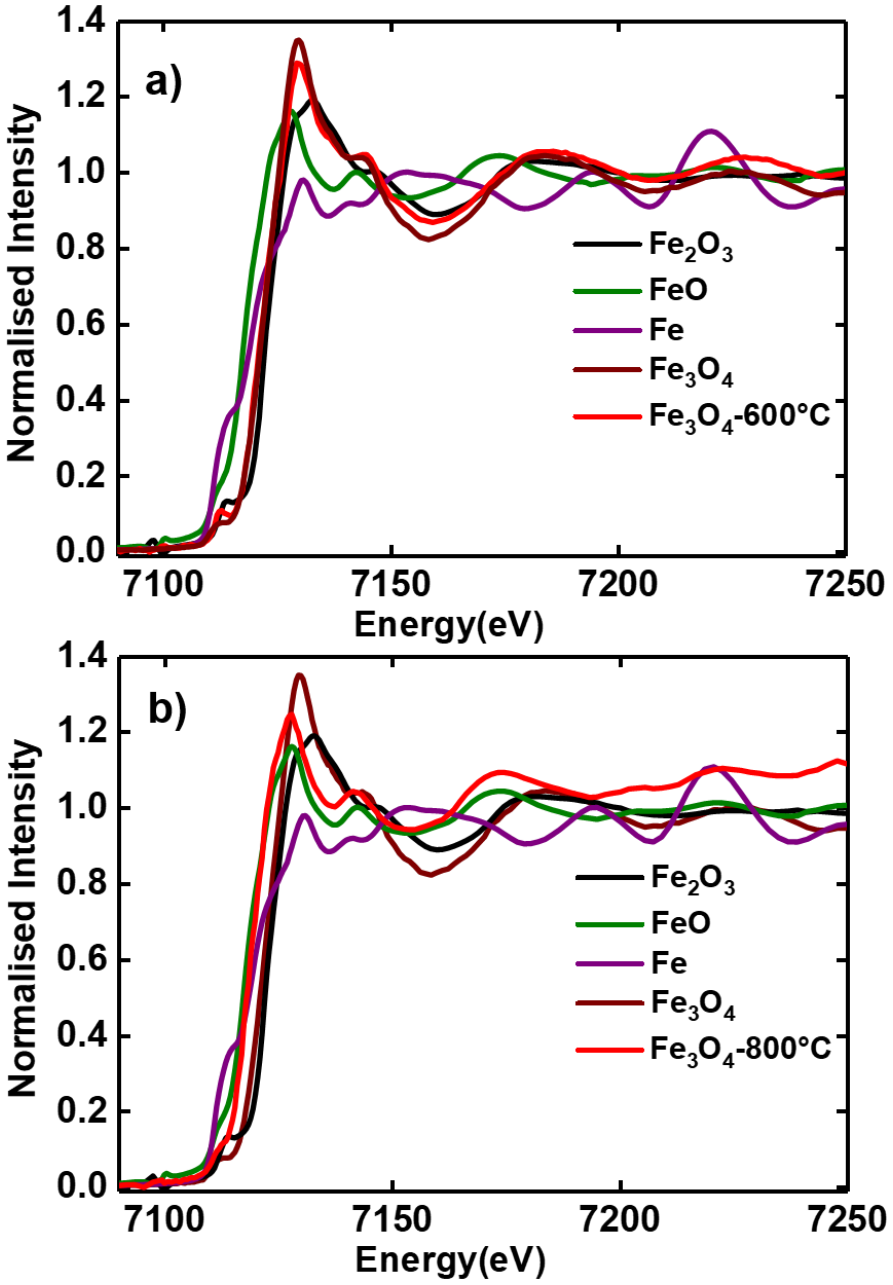


***Figure 25** – The Fe K edge XANES region for $Fe_3O_4$ annealed at 600 °C (a) and 800 °C (b).*

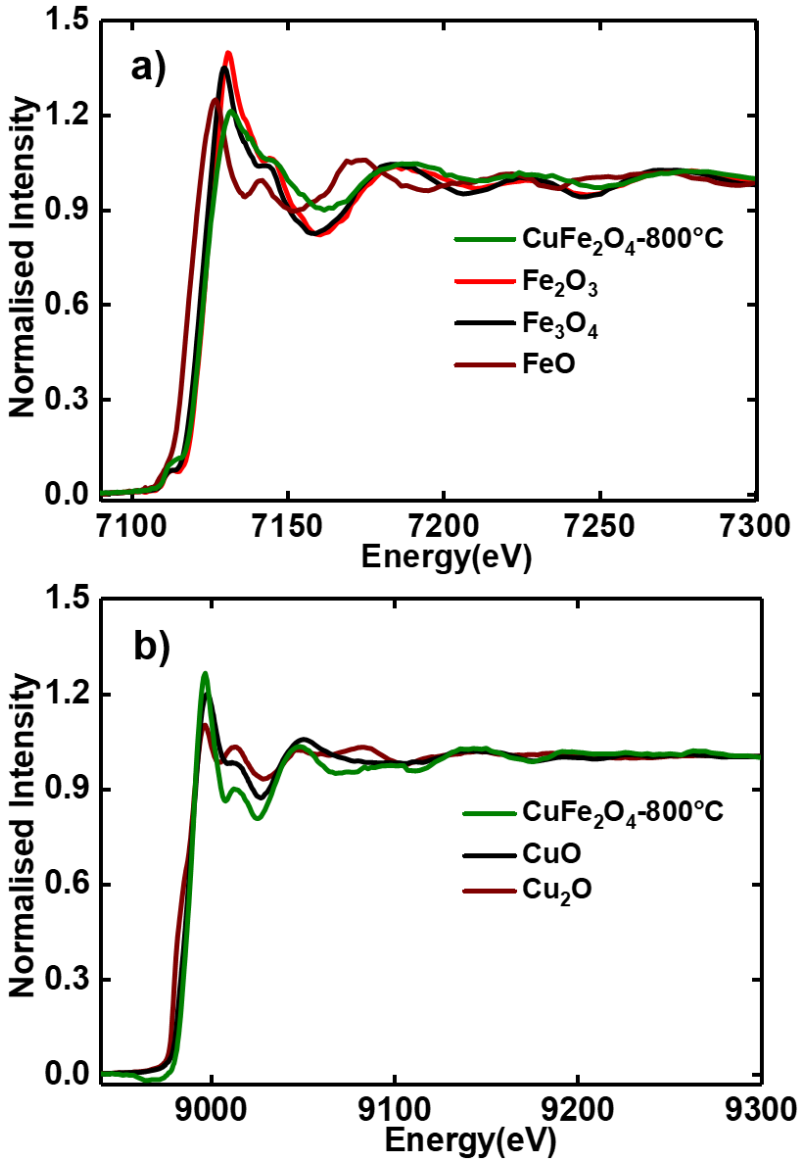


***Figure 26** – The Fe (a) and Cu (b) K edge XANES region for $CuFe_2O_4$ annealed at 800 °C.*

The comparison of Fe and Cu K edges of $CuFe_2O_4$-800 °C with the reference materials is given in ***Figure 26a*** and ***b***. Even though the X-ray diffraction analysis gets complicated with increasing number of phases, the X-ray absorption finger printing technique is rather easy if the same element present in different phases exists in different oxidation states. From XRD analysis, $CuFe_2O_4$-800 °C exists as a mixture of 25.01 % of $Fe_2O_3$ (space group $R\bar{3}c$), 16.36 % of CuO (space group C 2/c), 51.86 % of inverse spinel $CuFe_2O_4$ (space group $Fd\bar{3}m$), 2.85 % of $CuFe_2O_4$ (space group $I4_1/amd$) and 3.92 % of $CuFeO_2$ (space group $R\bar{3}m$). In all

these compounds Fe exists in +3 oxidation state and Cu in +2 except in $CuFeO_2$ where Cu exists in +1 state (One should also consider that there is only a very small amount of $CuFeO_2$ in the whole mixture). The Fe K edge overlaps with $Fe_2O_3$ and the Cu K edge with CuO which confirms the oxidation state of +3 of Fe and +2 oxidation state of Cu in $CuFe_2O_4$-800 °C. A Pre-edge feature is observed for the Fe Kedge at 7113 eV.

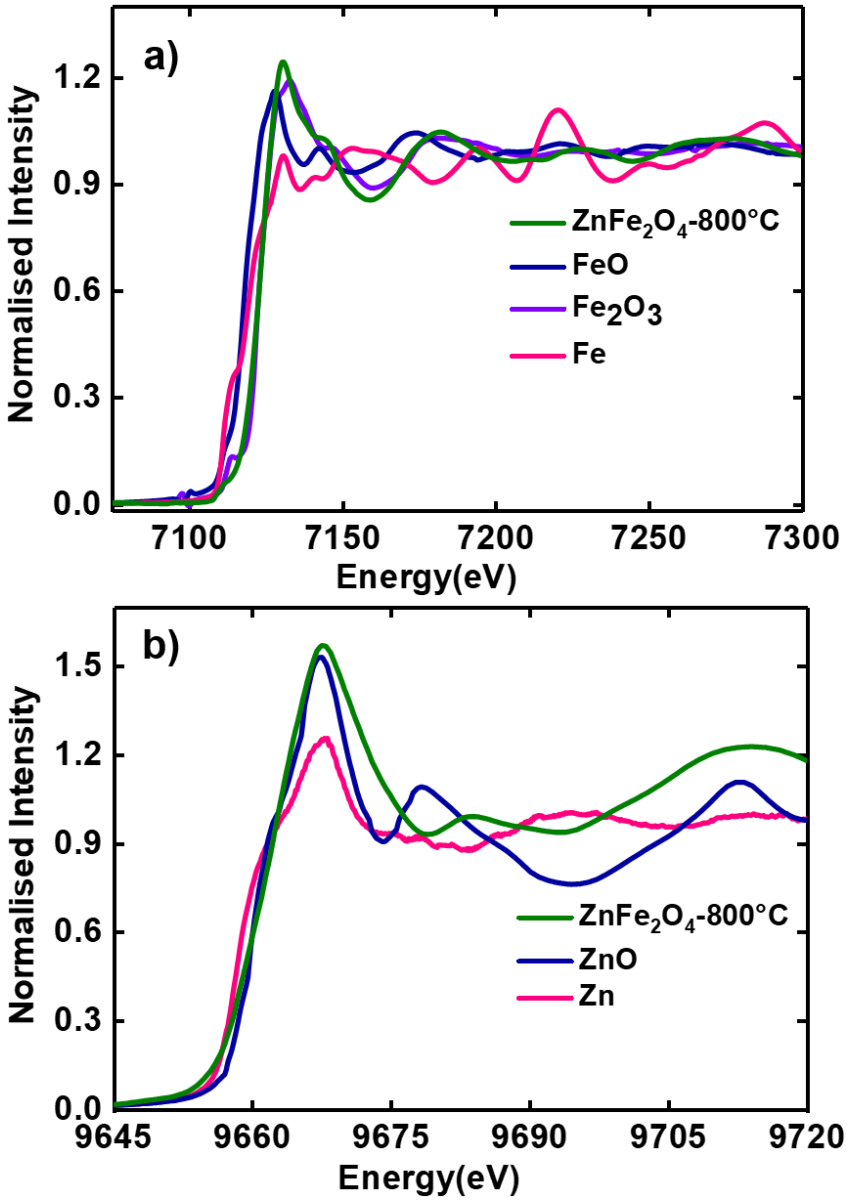


***Figure 27** – The Fe (a) and Zn (b) K edge XANES region for $ZnFe_2O_4$ annealed at 800 °C.*

In $ZnFe_2O_4$-800 °C, the oxidation states of Zn and Fe are +2 and +3, respectively, when compared with the reference materials as shown in ***Figure 27***. Fe K edge shows a pre-edge feature at 7110.64 eV. However, no pre-edge feature is observed for the Zn K edge. The average oxidation state of various transition metals in pristine $MFe_2O_4$ ($M$ = Fe, Co, Ni and Cu) is summarized in ***Table 3*** using X-ray absorption spectroscopy.

***Table 3 - The average oxidation state of pristine 3d transition metal ferrites.***

| Sample | K edge | |
|---|---|---|
| | **Fe K edge** | **Co/Ni/Cu/Zn K edge** |
| $CoFe_2O_4$-800 | +3 | +2 |
| $NiFe_2O_4$-800 | +3 | +2 |
| $Fe_3O_4$-600 | +2/+3 | |
| $Fe_3O_4$-800 | +2/+3 | |
| Cu $Fe_2O_4$-800 | +3 | +2 |
| $ZnFe_2O_4$-800 | +3 | +2 |

## 3.2. Electrochemical Performance of $MFe_2O_4$ (M = Fe, Co, Ni, Cu, Zn)

The electrochemical behavior of pristine 3d transition metal ferrites, $MFe_2O_4$ ($M$ = Fe, Co, Ni, Cu, Zn), was investigated in half-cells using CR2032 type coin cells as described in section 2.2.1. The working electrodes were normally prepared by mixing the active material with SUPER C65 carbon and binder, coated on copper foil and the counter electrode is lithium metal. To check the reproducibility, three cells were tested for each type of measurement. In order to enhance the electrochemical performance, the electrode compositions as well as electrode preparation techniques were optimized and then applied to all electrodes.

### 3.2.1. Factors Affecting Electrochemical Cycling Stability

There are different factors influencing the electrochemical performance of the conversion anode materials and the parameters chosen for this work are described below:

#### I. Annealing Temperature

The ferrite samples annealed at 600°C and 800°C were cycled between 0.1 to 3.1 V for 50 cycles at a C-rate of C/10 so as to obtain a first comparison on their cycling stability and specific capacities. The electrode composition of 80:10:10 with PVdF as binder has been chosen for these measurements and the electrode preparation was performed as explained in the section 2.2.1. The difference in the electrochemical cycling behavior for various materials are shown below.

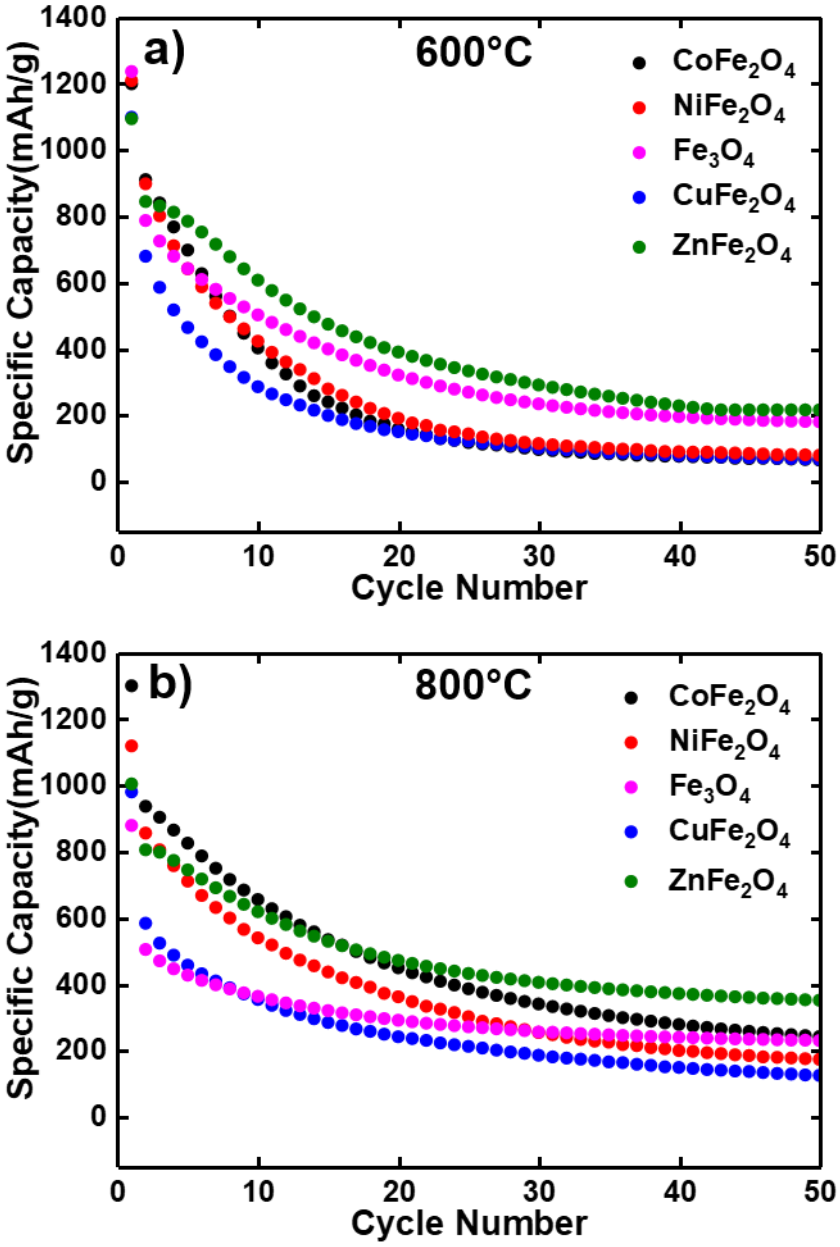


***Figure 28** – The cycling stability $MFe_2O_4$ (M = Fe, Co, Ni, Cu and Zn) annealed at 600 °C (a) and 800 °C (b) with an electrode composition of 80:10:10 cycled between 0.1 to 3.1 V at a C-rate of C/10 for 50 cycles.*

The difference in specific capacity over 50 cycles for different materials calcined at different temperatures is tabulated in ***Table 4*** and ***Table 5***. Capacity retention calculation is done by considering the specific capacity at the 20$^{th}$ cycle as first cycle, since the system starts giving stable results at this point. The initial capacity for all metal ferrites were slightly higher than the theoretical value. The additional capacity could be due to electrode/electrolyte

interphases (solid-electrolyte interphase, polymer/gel-like film), additional $Li^+$ accommodation through reactions with grain boundary phases in nanostructures, interfacial $Li^+$ accommodation along with charge separation at phase boundaries[64]. After the initial loss, the capacity value gets stabilized by the 20th cycle.

***Table 4 - The difference in specific capacity over 50 cycles for different materials calcined at 600 °C***

| **Sample** | **Initial Capacity-1st cycle (mAh $g^{-1}$)** | **Initial Capacity-2nd cycle (mAh $g^{-1}$)** | **Specific Capacity after 50 cycles (mAh $g^{-1}$)** | **Capacity Retention after 50 cycles (%)** |
|---|---|---|---|---|
| $CoFe_2O_4$ | 1200 | 911 | 65 | 41 |
| $NiFe_2O_4$ | 1210 | 899 | 79 | 41 |
| $Fe_3O_4$ | 1238 | 788 | 180 | 56 |
| $CuFe_2O_4$ | 1100 | 680 | 67 | 44 |
| $ZnFe_2O_4$ | 1095 | 845 | 216 | 55 |

***Table 5 - The difference in specific capacity over 50 cycles for different materials calcined at 800 °C.***

| **Sample** | **Initial Capacity-1st cycle (mAh $g^{-1}$)** | **Initial Capacity-2nd cycle (mAh $g^{-1}$)** | **Specific Capacity after 50 cycles (mAh $g^{-1}$)** | **Capacity Retention after 50 cycles (%)** |
|---|---|---|---|---|
| $CoFe_2O_4$ | 1302 | 938 | 243 | 54 |
| $NiFe_2O_4$ | 1120 | 856 | 174 | 48 |
| $Fe_3O_4$ | 880 | 505 | 231 | 79 |

| | | | | |
|---|---|---|---|---|
| $CuFe_2O_4$ | 981 | 581 | 126 | 52 |
| $ZnFe_2O_4$ | 1095 | 845 | 352 | 74 |

The X-ray diffraction and consecutive Rietveld analysis of the pristine materials annealed at 600°C and 800°C, accounts for an increase in crystallinity as well as changes in crystal structure and unit cell parameters with respect to the calcination temperature. The crystallinity and particle size are known to have a strong influence on the conversion materials performance[65–67]. Here, the ferrite samples annealed at 800°C show better cycling stability compared to that of the samples annealed at 600°C. It seems that high crystallinity and bigger particle size of the materials are beneficial for retaining capacity during cycling. The better capacity retention, with increasing particle size was also reported for $Fe_3O_4$[68]. On the other hand, the optimal particle size of the materials is very likely to be material dependent[66,67].

## II. Electrode Composition and Electrode Pressing

The electrode engineering for conversion-type materials with respect to active material, conductive carbon and binder ratio is crucial since the electrode undergoes huge volume changes upon cycling. To choose the most efficient composition, the electrodes were prepared in three different ratios, 80:10:10, 60:20:20 and 60:30:10 of active material, carbon and binder respectively. These experiments were carried out with commercially available $CuFe_2O_4$ (***Figure 29***).

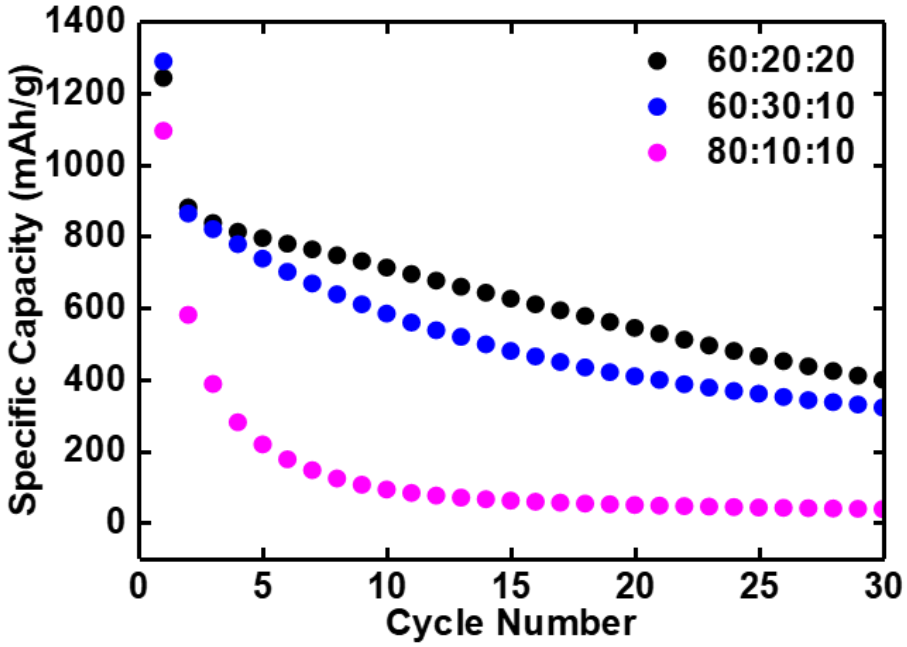


***Figure 29*** *– The cycling performance of commercial $CuFe_2O_4$ electrodes prepared with different ratio of electrode components cycled between 0.1 to 3.1 V at a C-rate of C/10 for 20 cycles.*

Electrodes with 60:20:20 and 60:30:10 ratios of active material, carbon and binder respectively, show better specific capacities (399 and 321 mAh $g^{-1}$) and capacity retention (45% and 37%) after 30 cycles compared to the electrode with 80:10:10 ratio (37 mAh $g^{-1}$ and 6%, Capacity retention calculation is done by considering the specific capacity using the 2$^{nd}$ cycle as first cycle). The enhancement of the performance upon increasing carbon and binder content is most probably due to more stable conduction network formed in the electrode bulk and increased adhesion properties in conversion electrodes. It helps the particles to stay connected within the electrode mixture and to the current collector upon cycling. Therefore, the formation of the electrochemically inactive areas due to loss of electrical contact can be suppressed. Three electrodes of each ratio were tested to check the reproducibility. The electrode with 60:20:20 ratio showed the best performance among the three ratios and hence was used hereafter for all following experiments.

Also the effect of pressing the electrodes at different pressures (5 tons and 8 tons) was studied using commercial $CuFe_2O_4$ electrodes. The accelerated fading of capacity was

observed for pressed electrodes in comparison to the unpressed ones (***Figure 30***). This effect is quite surprising, since the pressing might help to keep the electrical contact between particles. The possible explanation can be hindered electrolyte access for the denser electrodes, especially after several cycles.

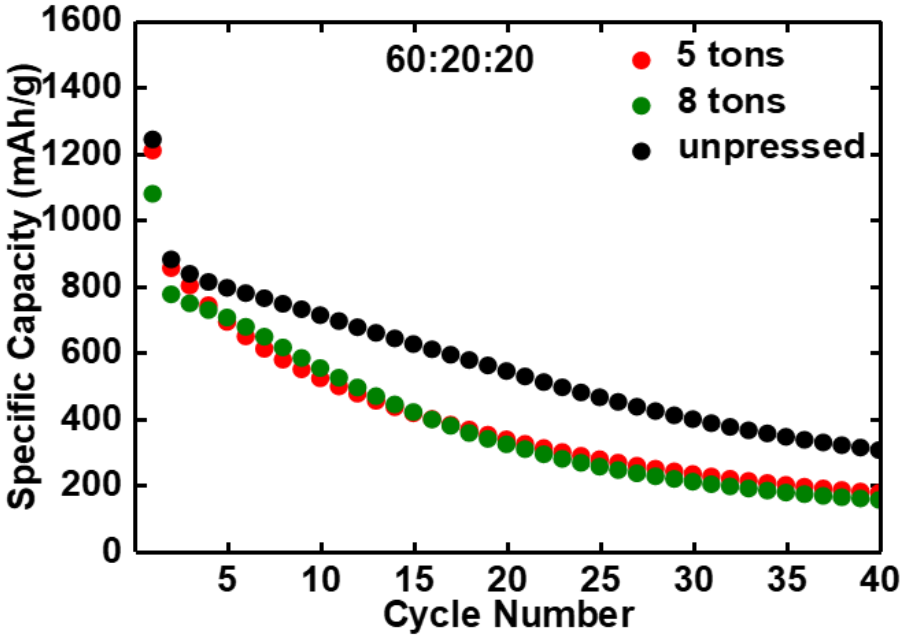


***Figure 30*** *– The cycling performance of commercial* $CuFe_2O_4$ *of electrode composition of 60:20:20 with and without pressing the electrode, cycled between 0.1 to 3.1 V at a C-rate of C/10 for 40 cycles.*

As concluded from the above studies, the samples annealed at 800°C were selected for further electrochemical investigations with an electrode composition, 60:20:20 (without any pressing) for the comparison of electrochemical performance among all synthesized ferrites.

***Figure 31*** shows the improvement in capacity retention by using 60:20:20 electrode composition without pressing of electrodes.

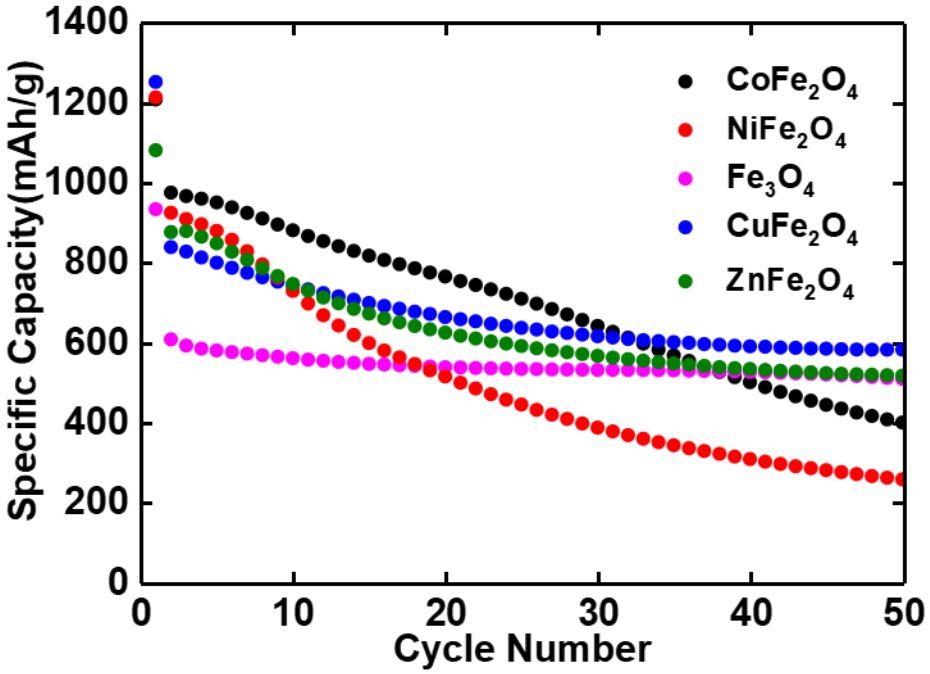


***Figure 31*** *– The cycling stability* $MFe_2O_4$ (*M* = Fe, Co, Ni, Cu and Zn) *annealed at 800 °C with an electrode composition of 60:20:20 cycled between 0.1 to 3.1 V at a C-rate of C/10 for 50 cycles.*

***Figure 31*** shows the capacity retention after 50 cycles for $MFe_2O_4$ (*M* = Fe, Co, Ni, Cu and Zn) electrode materials annealed at 800°C cycled between 0.1 to 3.1 V at a C-rate of C/10 with 60:20:20 electrode mixture ratio. Capacity retention calculation is done by considering the specific capacity using the $20^{th}$ cycle as first cycle. It is interesting to see how the partial substitution of Fe in $Fe_3O_4$ with other transitions metals such as Co, Ni, Cu and Zn influences the electrochemical performance in lithium ion half cells. $CoFe_2O_4$ and $NiFe_2O_4$ show rather high discharge capacities in the initial cycles, which decrease drastically with further cycling. Among these, $CoFe_2O_4$ shows better performance, which retains a discharge capacity of 400 mAh $g^{-1}$ after 50 cycles whereas the capacity of $NiFe_2O_4$ drops to 258 mAh $g^{-1}$g. For $CuFe_2O_4$ and $ZnFe_2O_4$, the most significant decrease in capacity was observed up to approximately 35 cycles, but after that both materials demonstrate stable performance with a capacity of approximately 500 mAh $g^{-1}$.

*Table 6 - The specific capacity over 50 cycles for different electrode materials annealed at 800 °C with electrode compositions 80:10:10 and 60:20:20.*

| Sample | Electrode Composition | | | | | |
|---|---|---|---|---|---|---|
| | 80:10:10 | | | 60:20:20 | | |
| | Initial Capacity-1st cycle (mAh $g^{-1}$) | Specific Capacity after 50 cycles (mAh $g^{-1}$) | Capacity Retention after 50 cycles (%) | Initial Capacity-1st cycle (mAh $g^{-1}$) | Specific Capacity after 50 cycles (mAh $g^{-1}$) | Capacity Retention after 50 cycles (%) |
| $CoFe_2O_4$ | 1302 | 243 | 54 | 1209 | 400 | 52 |
| $NiFe_2O_4$ | 1120 | 174 | 48 | 1215 | 258 | 50 |
| $Fe_3O_4$ | 880 | 231 | 79 | 934 | 509 | 94 |
| $CuFe_2O_4$ | 981 | 126 | 52 | 1253 | 582 | 88 |
| $ZnFe_2O_4$ | 1095 | 352 | 74 | 1082 | 517 | 83 |

Hence, from the above findings it is evident that the chemical composition (binary vs. ternary) and the type of the additional metal in the ternary ferrites have a strong impact on the electrochemical performance. The comparison of ternary oxides and binary $Fe_3O_4$ is complicated by the fact, that the $Fe_3O_4$-800 sample has a significant amount of FeO, which has lower theoretical capacity (744 mAh $g^{-1}$) compared to the capacity of $Fe_3O_4$ (924 mAh $g^{-1}$) or ternary oxides. However, one can see that $Fe_3O_4$ demonstrates a more stable cycling behavior than ternary oxides. Among them, Cu and Zn ferrites show less degradation upon cycling in comparison to Co and Ni compounds. These differences may result from the different structural rearrangements occurring upon initial discharge and, therefore, different microstructure formed in the initial cycles. At the same time, the type of metal nanoparticles formed at the end of discharge may have strong impact on the character of parasitic reactions

occurring in the electrochemical cell. Therefore, the degradation phenomena may proceed to different extent depending on the element composition.

## III. Binder

Binder plays an important role among the electrode components acting as an effective agent that adheres the electrode components together among themselves and also with the current collector. PVdF is the most commonly used binder due to its high electrochemical stability and adhesive capacity. However, NMP is used as solvent to dissolve PVdF. NMP is a volatile solvent which is highly hazardous in terms of safety and pollution issues and also requires very high humidity control during the manufacturing of electrodes.

Recently, a combination of water soluble, CMC/SBR binders were widely used for negative electrodes[69,70] including conversion type systems[71–74], due to their higher flexibility, stronger binding force, better heat resistance and lower cost compared to PVdF. CMC/SBR binders help in retaining the capacity for longer cycles by maintaining better electrical contact between electrode, current collector and conducting agent and also to minimize the electrode-electrolyte side reactions.

Herein in this work, $CoFe_2O_4$-800 °C and $NiFe_2O_4$-800 °C electrodes, which showed highest specific capacities but rapid capacity fading using PVdF binder, were prepared using CMC/SBR binder to understand the effect of binder on electrochemical performance. The electrode mixture ratio is chosen to be 60:20:20 (60 % (w/w) of active material, 20 % (w/w) SUPER C65 carbon and 20 % of carboxy methyl cellulose and styrene-butadiene rubber mixture as binder (CMC:SBR in 1:1 ratio) dissolved in distilled water) to compare the same using already investigated PVdF binder (***Figure 32*** and ***Table 7***). The optimized weight ratio of CMC:SBR was chosen to be 1:1 from a previous investigation of Zhang *et al.*,[71].

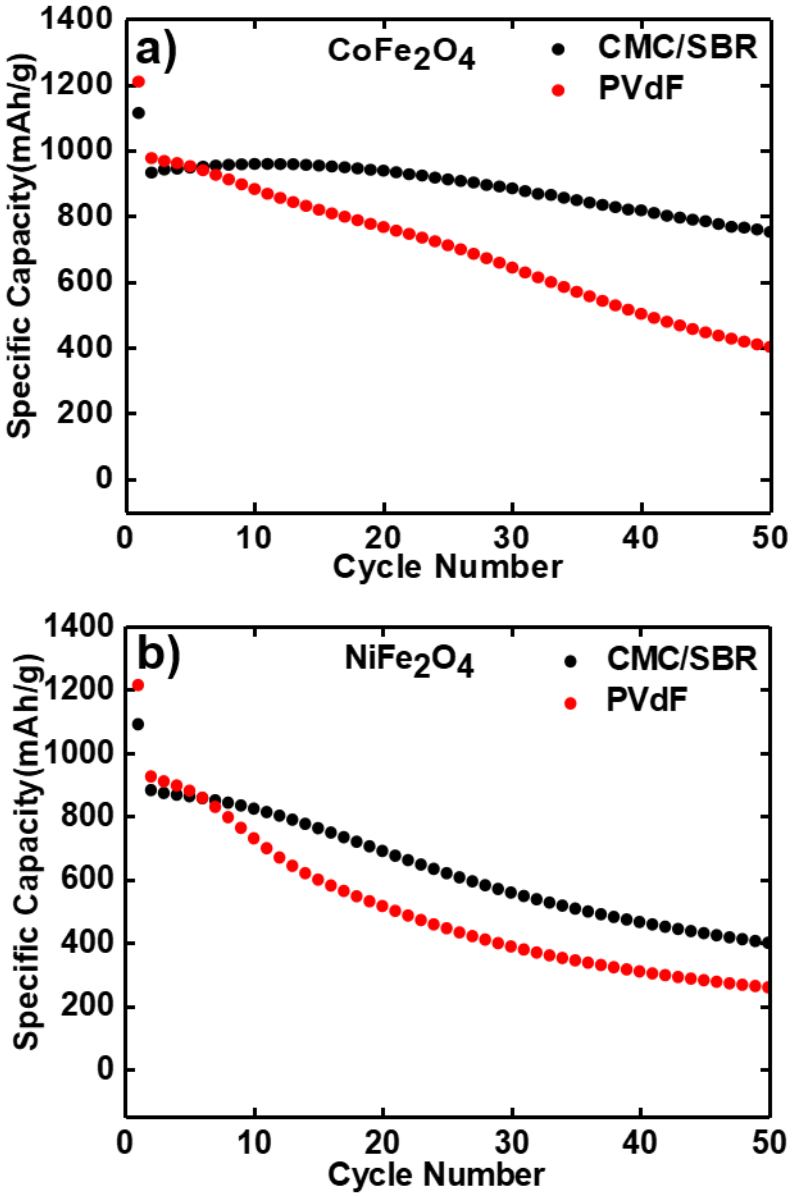


***Figure 32** – The cycling stability of $CoFe_2O_4$ (a) and $NiFe_2O_4$ (b) annealed at 800°C with an electrode composition of 60:20:20 using PVdF and CMC/SBR binder cycled between 0.1 to 3.1 V at a C-rate of C/10 for 50 cycles.*

The initial discharge capacities of both materials are higher than the theoretical values due to the formation of a solid-electrolyte interface (SEI). Moreover, the initial discharge capacities of $CoFe_2O_4$-800°C and $NiFe_2O_4$-800°C are higher for PVdF binder than for CMC/SBR binder. Hence, CMC/SBR binder seems to reduce the SEI Formation and the side reactions in the initial and subsequent cycles. The carboxylic group present in the CMC/SBR binder forms strong hydrogen bonds and hence enhances the binding strength within the

anode materials whereas the PVdF is bonded through weak Van der Waals forces[73]. Even though the CMC/SBR binder shows better capacity retention, cobalt ferrite has less capacity loss than nickel ferrite with both, PVdF and CMC/SBR binders.

***Table 7 - The difference in specific capacities for $CoFe_2O_4$-800 °C and $NiFe_2O_4$-800 °C using PVdF and CMC/SBR binders.***

| Sample | Effect of Binder | | | | | |
|---|---|---|---|---|---|---|
| | Initial Specific Capacity ($mAh\ g^{-1}$) | | Specific Capacity after 50 Cycles ($mAh\ g^{-1}$) | | Capacity Retention after 50 cycles (%) | |
| | PVdF | CMC/SBR | PVdF | CMC/SBR | PVdF | CMC/SBR |
| $CoFe_2O_4$ | 1209 | 1113 | 400 | 751 | 52 | 80 |
| $NiFe_2O_4$ | 1215 | 1091 | 258 | 400 | 50 | 58 |

## 3.2.2. Cyclic Voltammetry

Cyclic voltammetry has been conducted to determine the electrochemically active potential regions of the electrode materials. The electrochemical cells were cycled in the voltage window of 0.1 to 3.1 V with a scan rate of 0.1 $mVs^{-1}$.

The cyclic voltammetry results obtained for $CoFe_2O_4$ and $NiFe_2O_4$ cycled between 0.1 and 3.1 V at a scan rate of 0.1 $mVs^{-1}$ for 30 cycles are shown in ***Figure 33***. The characteristic feature of the CV curves is the significant difference between the first and subsequent cycles, which is well known for conversion-type electrode materials. This is very well seen in the ***Figure 33***. A sharp cathodic peak was observed in the first cycle at around 0.57 V for $CoFe_2O_4$ and at 0.58 V for $NiFe_2O_4$, corresponding to the reduction of transition-metal ions to the metallic state and formation of $Li_2O$.

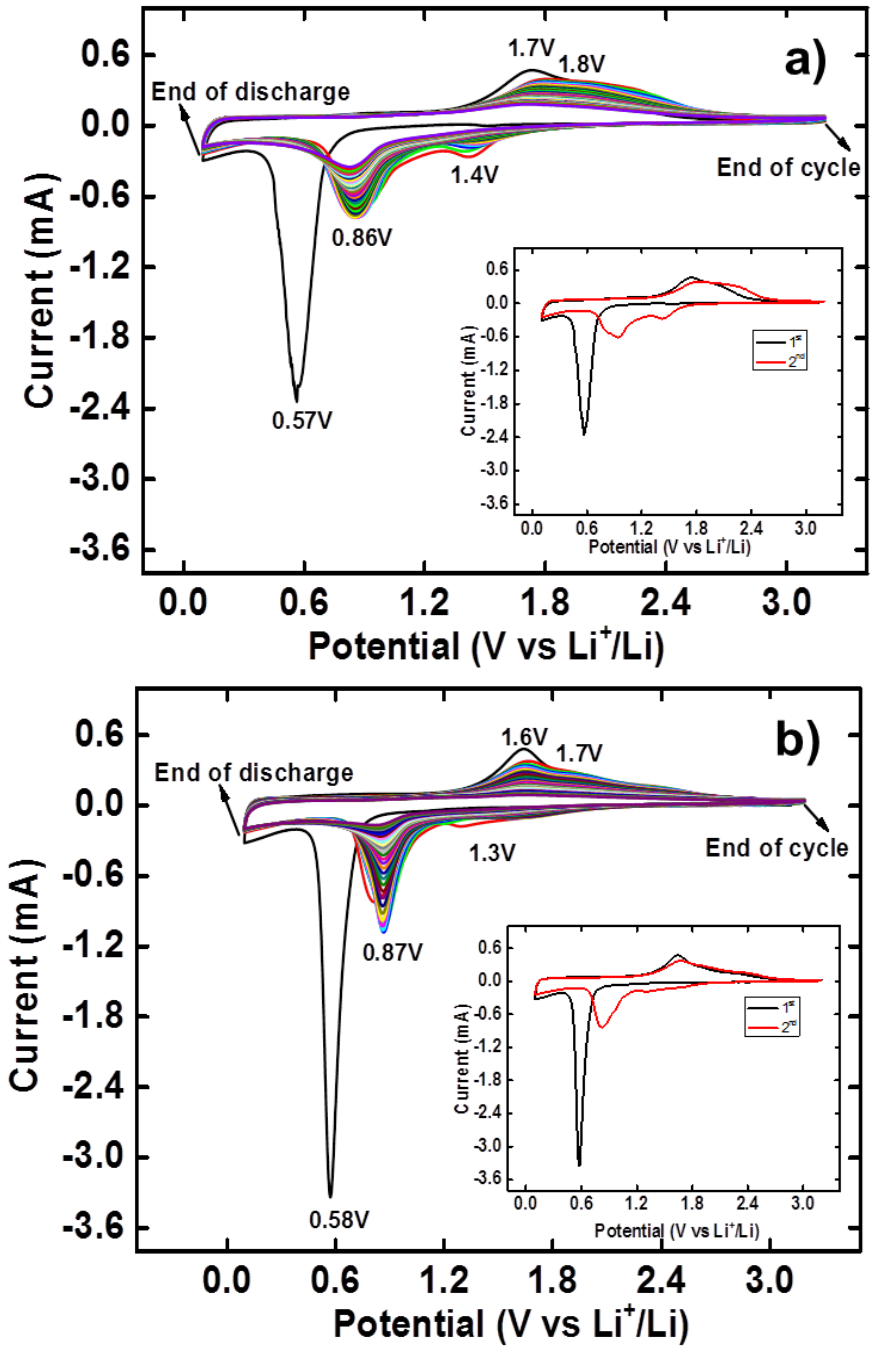


***Figure 33*** *– The cyclic voltammetry results obtained for $CoFe_2O_4$ (a) and $NiFe_2O_4$ (b) annealed at 800 °C cycled between 0.1 and 3.1 V at a scan rate of 0.1 $mVs^{-1}$ for 30 cycles. Inset shows the first and second cycle for both materials.*

The increase in cathodic current at the end of discharge may indicate the reduction of the electrolyte, promoted by the presence of metal nanoparticles. The anodic part in the first cycle consists of two peaks, which are not very well resolved. These peaks are usually attributed to the oxidation of metal nanoparticles; nevertheless, at the end of this process, the

spinel structure of the initial compound may not be restored. Upon second discharge, two cathodic peaks were observed at 0.86 and 1.4 V for $CoFe_2O_4$ and at 0.83 and 1.3 V for $NiFe_2O_4$, respectively. After the first cycle, the peak current and the integrated area of the anodic peak were decreased which indicates the capacity loss during the charging process.

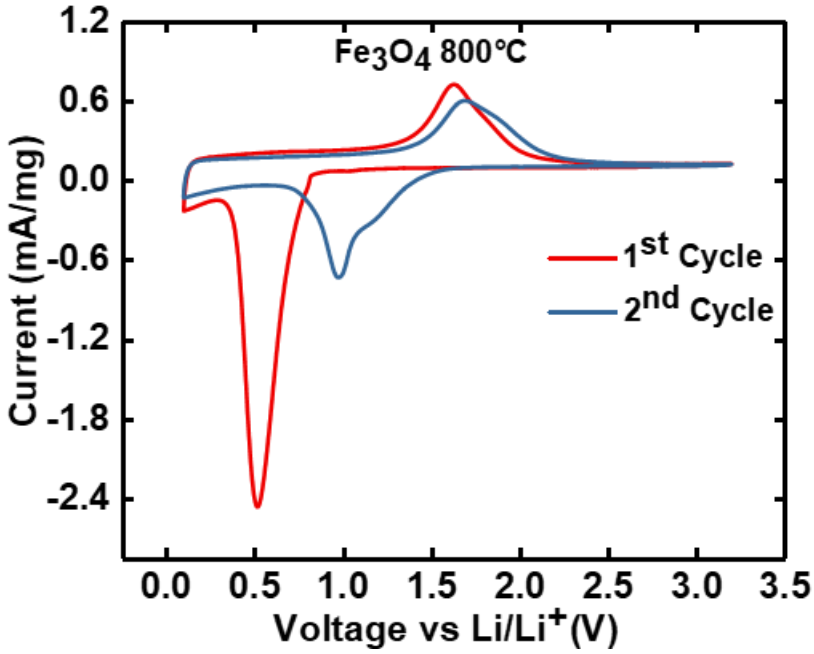


***Figure 34*** *– The cyclic voltammetry results obtained for $Fe_3O_4$ annealed at 800 °C cycled between 0.1 and 3.1 V at a scan rate of 0.1 $mVs^{-1}$ for first two cycles.*

The cyclic voltammetry of $Fe_3O_4$ for the first two cycles in the voltage window between 0.1 and 3.1 V at a scan rate of 0.1 $mVs^{-1}$ is shown in ***Figure 34***. In accordance with previous reports in the literature for $Fe_3O_4$ based electrode materials[75–79], the significant cathodic peak at 0.51 V during the first discharge process could be assigned to the reduction of $Fe^{3+}$ and $Fe^{2+}$ to metallic Fe and the decomposition of the electrolyte. The anodic peak present at 1.62 V, corresponds to reversible oxidation of metallic Fe into the corresponding oxide. In the subsequent cycles, the cathodic and anodic peaks shift to 0.97 V and 1.70 V, respectively.

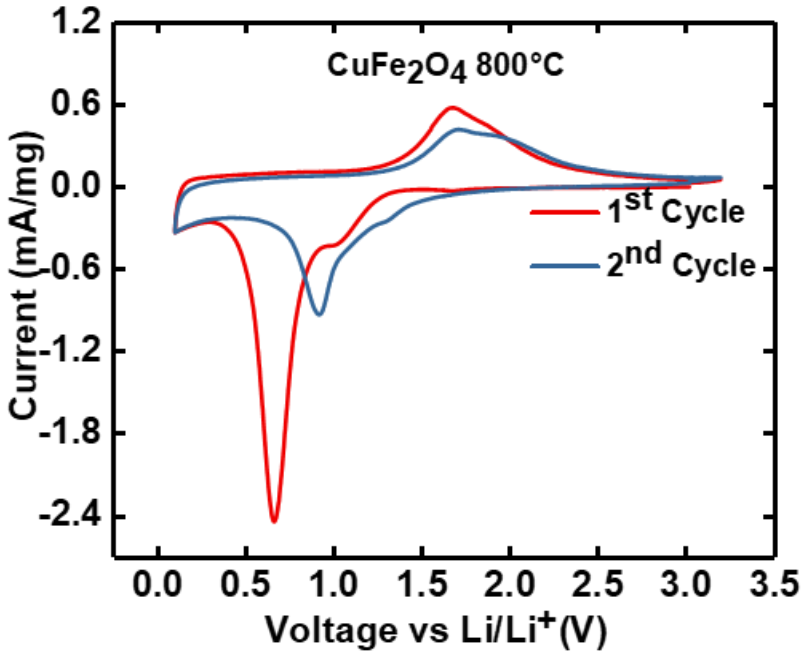


***Figure 35** – The cyclic voltammetry results obtained for $CuFe_2O_4$ annealed at 800 °C cycled between 0.1 and 3.1 V at a scan rate of 0.1 $mVs^{-1}$ for first two cycles.*

The CV curves for the first two cycles of $CuFe_2O_4$ annealed at 800°C are shown in ***Figure 35***. During the first discharge/lithiation reaction, a broad peak at 0.6 V with an onset at 1.1 V is seen which could be attributed to the decomposition of the $CuFe_2O_4$ structure into metallic Cu and Fe nanoparticles in an amorphous matrix of $Li_2O$ and also the formation of SEI. Some previous reports also assigned the onset peak to the formation of a stable intermediate $Li_xCuFe_2O_4$[80,81], where x is the amount of lithium inserted into the material. The peaks around 1.67 and 1.95 V in the charge process could be assigned to the oxidation of metallic Cu and Fe nanoparticles to their corresponding binary oxides. In the corresponding cycle, the discharge peaks at 0.9 V and the broad peak around 1.3 V were attributed to the reduction of the binary oxides and the formation of the SEI membrane, respectively. The shift of the discharge peak to the higher voltage of 0.9 V in comparison to the first discharge indicates a change in the reaction mechanism in the second cycle. The anodic peak with the shoulder corresponds to the reversible oxidations of metals to binary iron and copper oxides as previously reported for $CuFe_2O_4$ anode materials[80–83].

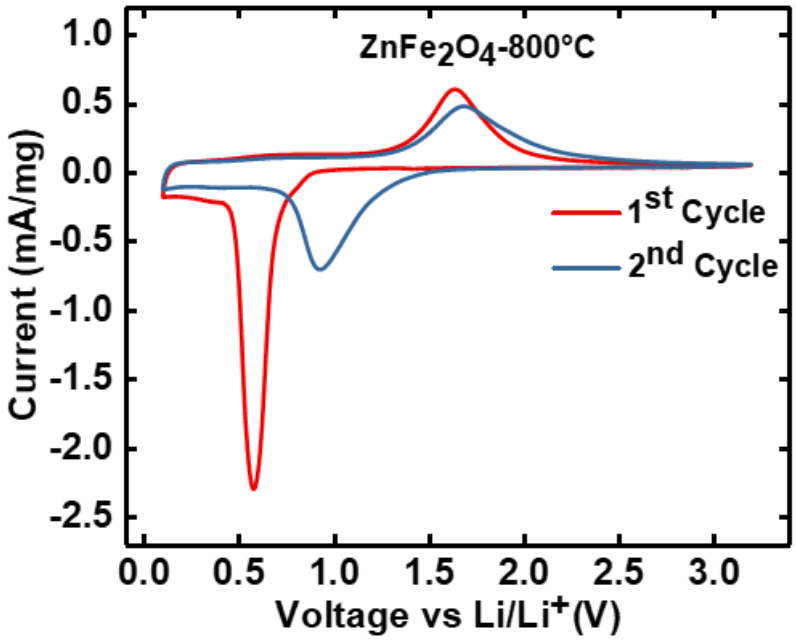


***Figure 36*** *– The cyclic voltammetry results obtained for $ZnFe_2O_4$ annealed at 800 °C cycled between 0.1 and 3.1 V at a scan rate of 0.1 $mVs^{-1}$ for first two cycles.*

***Figure 36*** shows the first and second CV cycles of the $ZnFe_2O_4$-800 °C electrode. As reported previously[34,71,84,85], the tiny cathodic spike at 0.82 V in the first reduction is attributed to $Li^+$ intercalation into $ZnFe_2O_4$ and the large spiky irreversible peak at 0.578 V corresponds to the conversion reaction of lithiated $ZnFe_2O_4$ into metallic Zn and Fe together with the SEI formation. The weak peak at 0.35 V accounts for the LiZn alloy formation. In the corresponding anodic scan, the initial broad oxidation peak at the very beginning corresponds to the de-alloying of LiZn and the one at 1.63 V could be assigned to the oxidation of metallic Fe and Zn into binary oxides together with the decomposition of $Li_2O$. In the second cycle, a shift of the cathodic peak to a higher voltage of 0.924 V was observed. The ZnO presented as an admixture in the $ZnFe_2O_4$-800°C material is expected to be also electrochemically active in the studied voltage range. As observed by Li *et al.*,[86] the cathodic peak for ZnO should be at 0.5-0.6 V and the anodic peak at 1.5 V. Therefore, if the ZnO in the studied $ZnFe_2O_4$-800°C is electrochemically active, the peaks from ZnO overlap with those from the main phase and a clear distinction of the two phases from the CV is not possible.

It is noteworthy that, after the first cycle, in all electrode materials, the cathodic and anodic peaks shift to higher potentials, followed by a decrease in peak intensity. This confirms the irreversibility of the redox reactions together with a parasitic reaction such as SEI formation. Also the electrochemically active regions could be identified.

## 3.3. Elucidation of the Electrochemical Reaction Mechanism in $M$Fe$_2$O$_4$ ($M$ = Ni, Co) Conversion-Type Negative Electrode Model Systems by using *in situ* X-ray Absorption Spectroscopy

Chen and Greenblatt[87] firstly reported the lithium insertion into spinel ferrites and its use as cathode materials for lithium-ion batteries. After that in 2002, R. Alcántara together with P. Lavela and J. L. Tirado for the first time used $NiFe_2O_4$ as active electrode material against lithium metal in test cells where they studied the changes in oxidation state and magnetic order of Fe atoms during electrochemical reaction[88]. Due to the availability of appropriate $^{57}Co$ and $^{57}Fe$ source and the favorable Debye-temperatures, Mossbauer spectroscopy has been extensively used to investigate $CoFe_2O_4$ and $NiFe_2O_4$ as negative electrode systems in Li-ion batteries[35,89–92]. However, these studies are often performed *ex situ* with electrodes obtained from the cells at different states of charge. Moreover, Mossbauer spectroscopy can only access the chemical information around the Fe nuclei. X-ray absorption spectroscopy (XAS) can give element specific information about the various atoms present in the material. Furthermore, materials investigated by XAS do not require long range order; therefore, this method is highly informative for the study of local nanostructures formed during operation of conversion-type materials.

Here, *in situ* XAS is applied to get an insight in the mechanism of the initial reduction of different metal ferrites $M$Fe$_2$O$_4$ ($M$ = Co, Ni) in the electrochemical cell against lithium metal anode. The co-precipitation synthesized $CoFe_2O_4$ and $NiFe_2O_4$ annealed at 800 °C were chosen for XAS studies due to better electrochemical performances compared to their counterparts annealed at 600 °C as shown in ***Figure 30***. The expected overall electrochemical reactions during the first discharge (1) and subsequent charge (2) are given below:

$$CoFe_2O_4/NiFe_2O_4 + 8Li^+ + 8e^- \rightarrow 4Co/Ni + 2Fe + 4Li_2O \quad (1)$$

$$Co/Ni + 2Fe + 4Li_2O \rightarrow CoO/NiO + Fe_2O_3 + 8Li^+ + 8e^- \quad (2)$$

The SEM images of $CoFe_2O_4$ and $NiFe_2O_4$ are displayed in ***Figure 22***, from which the average particles size was estimated to be 70±21.00 nm for $CoFe_2O_4$ and 52±19 nm for $NiFe_2O_4$. The cyclic voltammetry (CV) results obtained for both anode materials; $CoFe_2O_4$ and $NiFe_2O_4$ between 0.1-3.1 V at a scan rate of 0.1 $mVs^{-1}$ are shown in ***Figure 33***. The characteristic feature of the CV curves is the significant difference between first and subsequent cycles, which is well known for conversion type electrodes.

## 3.3.1. Oxidation state and local coordination elucidation

***Figure 37*** shows voltage versus Li composition curves for $CoFe_2O_4$ and $NiFe_2O_4$ obtained during *in situ* XAS experiment (a) or during cell cycling to prepare the electrodes for *ex situ* characterization after one complete charge-discharge cycle (b). Due to the complex construction of in-house *in situ* cell, the inserted Li amount is lower in case of the *in situ* experiments.

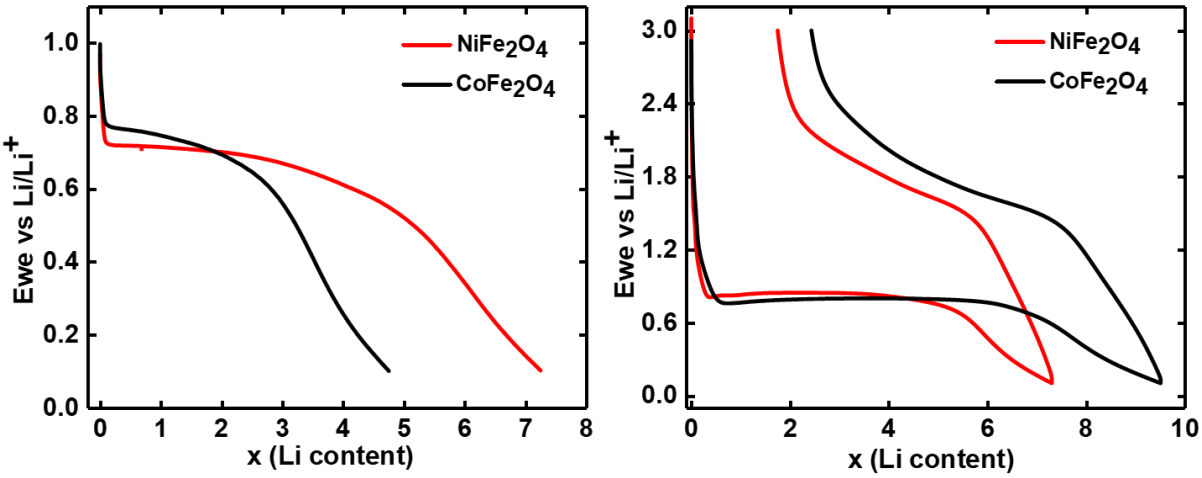


***Figure 37*** – *The x (Li content) versus voltage curve for $CoFe_2O_4$ and $NiFe_2O_4$ for a) in situ and b) ex situ XAS measurements at a C-rate of C/10.*

In order to obtain direct information about the oxidation states of Fe, Co/Ni in $CoFe_2O_4$ and $NiFe_2O_4$, the XANES (X-ray absorption near edge structure) regions of the XAS spectra of the samples at the Fe and Co/Ni K edges were compared with the XANES regions obtained from XAS spectra of different reference materials. The XANES region which extends from approximately -20 eV below the absorbing edge to 100 eV above the edge of an XAS spectrum, is often used in a qualitative way. Therefore, the edge position and line shape obtained from the reference materials are compared to any unknown sample, and information also about the oxidation state and to a certain extent, coordination environment of the absorbing atom can be extracted.

By comparing the XANES region obtained at the Fe K edge (***Figure 23***), it can be seen that the edge position of both samples overlap with the edge position of the $Fe_2O_3$ sample which was measured as the reference. Therefore, Fe has a formal valence state of $Fe^{3+}$. Moreover, it can also be seen that the Fe K edge XANES region line shape of both, $CoFe_2O_4$ and $NiFe_2O_4$, are identical. Therefore, the local coordination of Fe in both the samples is almost identical. Similarly, by comparing the XANES region at Co and Ni edges with that (***Figure 24***) of the corresponding reference materials (CoO and NiO), a formal oxidation state of +2 can be assigned to both elements. The pre-edge features of the Fe K edge suggests the occupancy of $Fe^{3+}$ to be in both tetrahedral and octahedral sites for both $CoFe_2O_4$ and $NiFe_2O_4$ which is similar to the $Fe_3O_4$ reference material with an inverse spinel structure. However, the pre-edge peak at the Ni K edge is very weak compared to Fe and Co edges in both the samples. This is because in $NiFe_2O_4$, Ni coordinates octahedrally in the inverse spinel structure and Fe is both, octahedrally and tetrahedrally coordinated. Whereas in partially inverse $CoFe_2O_4$, both Fe and Co are in tetrahedrally and octahedrally coordinated sites which results in a corresponding pre-edge feature.

The *in situ* measurements for both $CoFe_2O_4$ and $NiFe_2O_4$ at Fe, Co, and Ni edges revealed edge shifts and changes in the XANES line shapes, which may be assigned to an oxidation state change as well as coordination changes around the absorbing atoms (***Figure 38***).

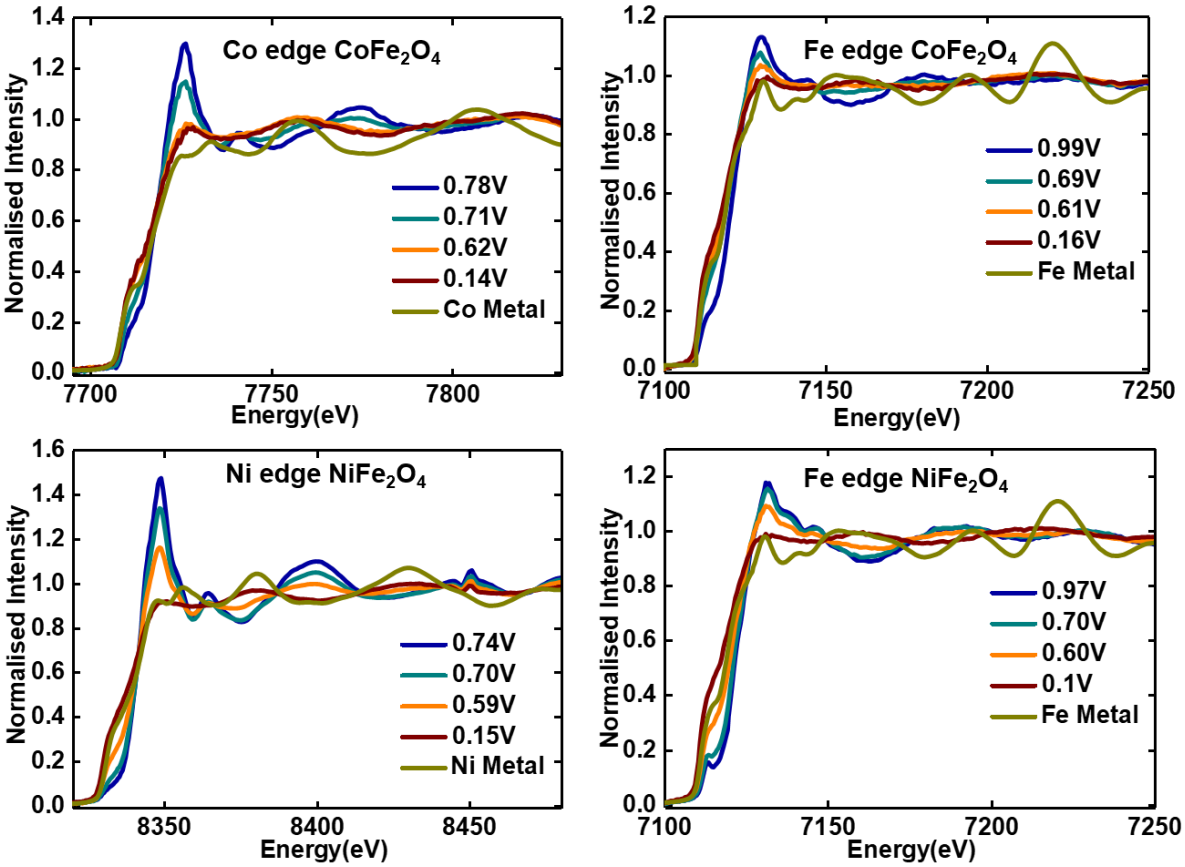


***Figure 38** – In situ XANES region obtained for $CoFe_2O_4$ and $NiFe_2O_4$.*

It is expected during the conversion reaction that the ferrite materials can transform into their respective oxides and to metallic states. Coexistence of different phases can complicate the EXAFS analysis; therefore, to get the information about the different phase fractions, linear combination fitting (LCF) analysis was done on the XANES region at selected potentials. Reference materials such as $Fe_3O_4$, $Fe_2O_3$, FeO and Fe metal foil were used for LCF analysis at the Fe K edge. For the LCF fitting at Co and Ni edges, CoO, Co metal, NiO and Ni metal spectra were used as references. From the LCF analysis for both $CoFe_2O_4$ and $NiFe_2O_4$ at the Fe K edge, an increase in the Fe metal fraction was observed with

electrochemical reduction. Moreover, a small fraction of the FeO component could also be fitted during the LCF analysis indicating the formation of $Fe^{2+}$ during reduction. At the end of discharge, only a contribution from metallic Fe was observed at the Fe K edge. Similarly, at Co and Ni edges, a coexistence of the metal oxide and the metallic phase was observed during discharging. A complete transformation into metallic Co and Ni was detected at the end of discharge for $CoFe_2O_4$ and $NiFe_2O_4$, respectively. The LCF fitting results are summarized in ***Table 8*** and ***Table 9***.

***Table 8 - LCF fitting results at Fe K edge for $CoFe_2O_4$ and $NiFe_2O_4$ at different potentials. Contributions from each reference material at different potentials are tabulated.***

| Sample | Potential vs. $Li^+/Li$ | Contribution from $Fe_2O_3$ | Contribution from FeO | Contribution from Fe |
|---|---|---|---|---|
| $CoFe_2O_4$ | 0.69 V<br>0.61 V<br>0.16 V | 0.30<br>0.20<br>0.06 | 0.20<br>0.15<br>0.10 | 0.50<br>0.65<br>0.84 |
| $NiFe_2O_4$ | 0.70 V<br>0.60 V<br>0.44 V<br>0.1 V | 0.77<br>0.44<br>0.12 | 0.06<br>0.16<br>0.15 | 0.23<br>0.50<br>0.72<br>0.85 |

***Table 9 - LCF fitting results at Co/Ni K edge for $CoFe_2O_4$ and $NiFe_2O_4$ at different potentials. Contributions from each reference material at different potentials are tabulated.***

| Sample | Potential | Contribution from CoO/NiO | Contribution from Co/Ni |
|---|---|---|---|

| | | | |
|---|---|---|---|
| $CoFe_2O_4$ | 0.71 V<br>0.6 V<br>0.16 V | 0.6<br>0.16<br>0.06 | 0.4<br>0.84<br>0.94 |
| $NiFe_2O_4$ | 0.70 V<br>0.59 V<br>0.44 V<br>0.1 V | 0.72<br>0.38<br>0.06 | 0.28<br>0.62<br>0.94<br>1 |

The formation of metallic clusters for all the transition elements can also be qualitatively inferred from the real space ("R space"). The Fourier transform (FT) of the EXAFS part of the spectrum reveals one single peak around 2.3 Å, which corresponds to the next neighbor distances of the respective metallic species. Note that at all the edges the relative FT amplitude decreased during electrochemical reduction (***Figure 39***). This effect can be attributed to the formation of metallic nano domains during the conversion reaction. However, during the discharge, the FT peak at 3 Å corresponding to the tetrahedrally and octahedrally coordinated 3d transition metals decreases drastically from the very beginning of lithiation which could be caused by the displacement of the transition metal from the tetrahedral site to vacant octahedral sites.

EXAFS data at all edges were analyzed at the end of discharge based on the structure model of a pure metal to verify the formation of metallic nanodomains during conversion reaction. EXAFS analyses of the pure fcc-metal foils yield coordination numbers of 12. However, from the *in situ* measurements, the coordination numbers for all metal-metal shells were considerably lower at the end of discharge, confirming the formation of nano metallic domains or clusters. Moreover, the exact size of the formed nanoparticles cannot be deduced from the EXAFS analyses, summarized in ***Table 10*** for the end of discharge (between 0.1 V and 0.2 V vs. $Li^+/Li$).

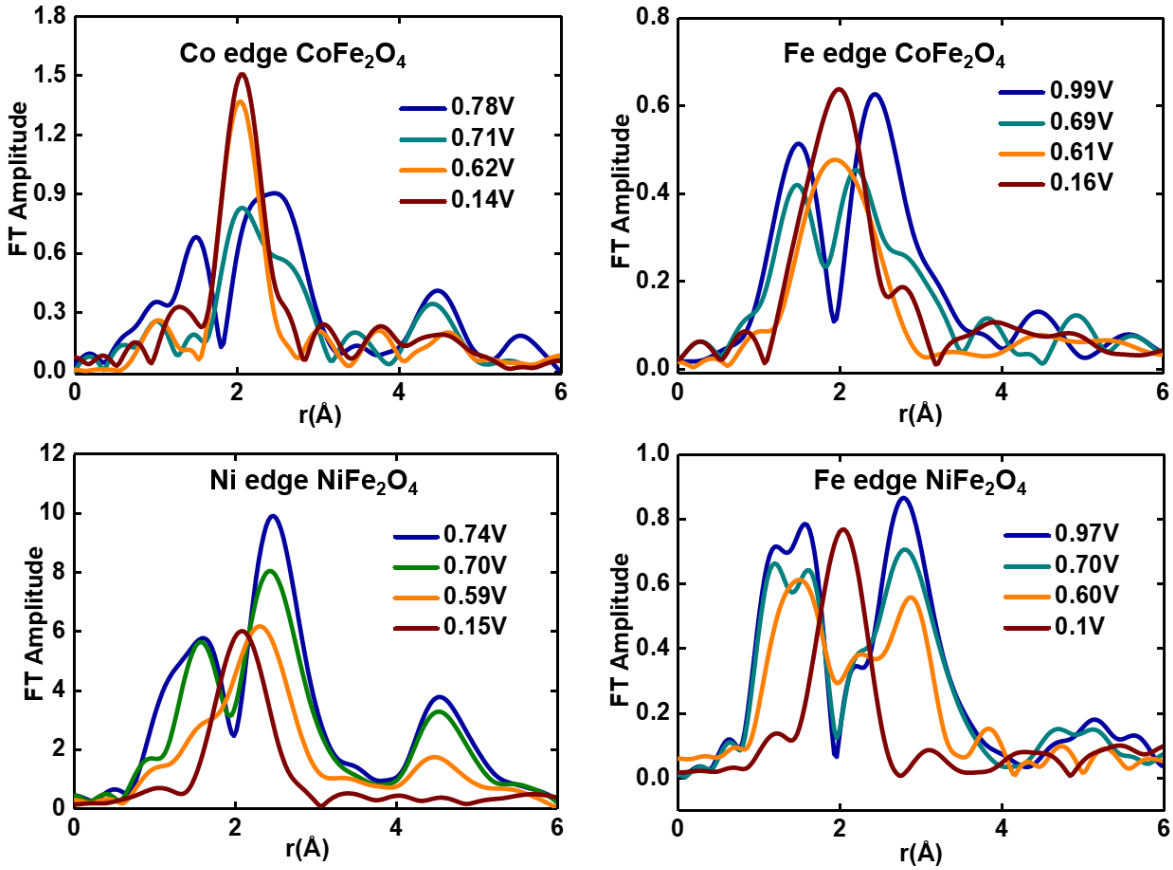


***Figure 39*** *– In situ FT spectra obtained for $CoFe_2O_4$ and $NiFe_2O_4$.*

***Table 10 - EXAFS fitting results at the end of discharge. Coordination number (N), distance between the nearest neighbor (r) and Debye Waller factors (DW) are fitted and the results are tabulated. Amplitude reduction factors, which is a fitting parameter for many electron excitations at the absorbing atom, were obtained from reference materials and are fixed during the fitting.***

| Edge | Sample | Coordination Number (N) | Interatomic distance (r Å) | Debye Waller factor ($Å^2$) |
|---|---|---|---|---|
| Fe | $CoFe_2O_4$ | (Fe-Fe ) 2.4 | (Fe-Fe) 2.41(2) | (Fe-Fe) 0.005(2) |
| Fe | $NiFe_2O_4$ | (Fe-Fe) 4.3 | (Fe-Fe) 2.44(1) | (Fe-Fe) 0.013(1) |
| Co | $CoFe_2O_4$ | (Co-Co) 4.9 | (Co-Co) 2.41(2) | (Co-Co) 0.009(2) |
| Ni | $NiFe_2O_4$ | (Ni-Ni) 7.1 | (Ni-Ni) 2.44(1) | (Ni-Ni) 0.020(2) |

Finally, electrodes obtained at the end of the first cycle were subjected to *ex situ* XAS to get more information about the reversibility of the conversion of metallic phases formed at the end of first discharge to metal oxides. For both $CoFe_2O_4$ and $NiFe_2O_4$ samples, it can be seen that the XANES line shape at the Fe edge for the pristine samples as well as the samples after first cycle were almost identical (***Figure 40***).

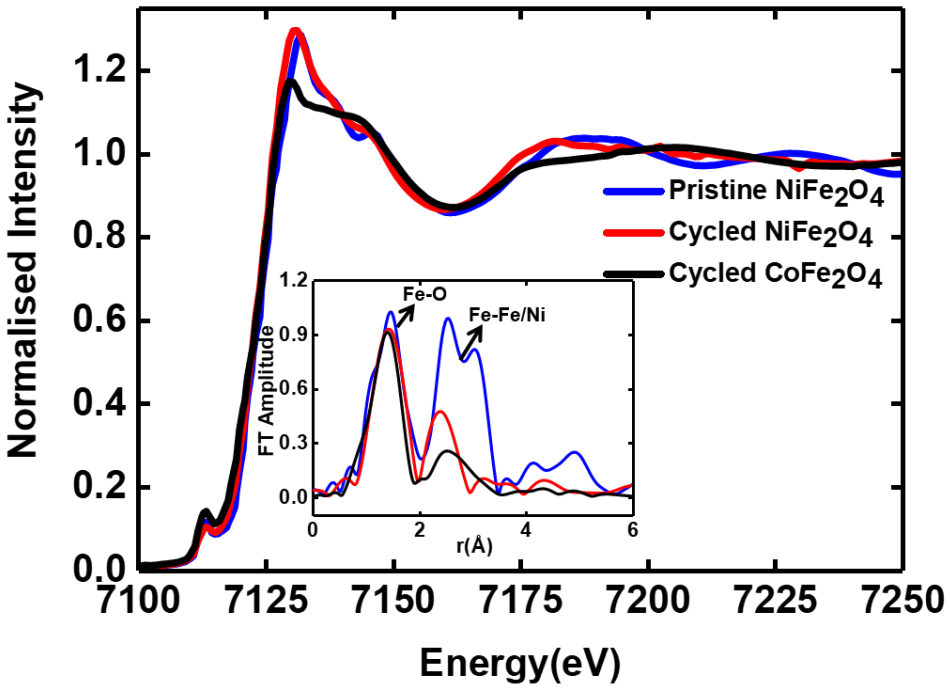


***Figure 40*** *– Fe K edge XANES region of cycled $CoFe_2O_4$ and $NiFe_2O_4$ materials. Inset showing the FT of the cycled materials. XANES as well as the FT of the cycled materials are compared with a pristine $NiFe_2O_4$ sample.*

However, the FT (inset) shows that the second shell, where the metal-metal interaction appears, has almost vanished for the samples after one complete cycle compared to the pristine samples. This conclusively proves that Fe metal formed during the first discharge has completely retransformed into an amorphous or cluster sized oxide phase. By comparing the edge position with the Fe reference material the formal valance of +3 can be assigned to the Fe-oxide formed. In contrast, for both Co and Ni edge, strong differences in the XANES line shapes were observed for both pristine and samples after 1$^{st}$ cycle. For both edges, the XANES

region for the samples after one complete cycle, measured at the inflection point, is closer to those for a Co or Ni metal foil than for CoO or NiO (***Figure 41***).

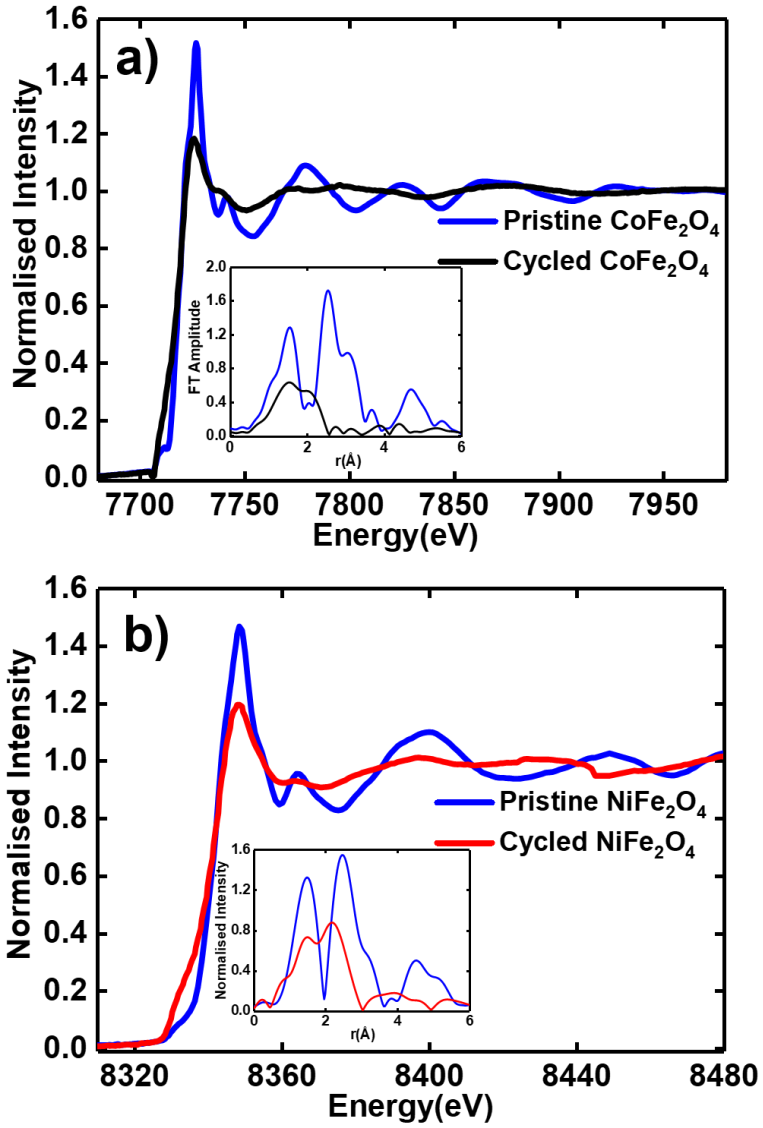


***Figure 41*** *– Co and Ni K edge XANES region of cycled $CoFe_2O_4$ (a) and $NiFe_2O_4$ (b) materials. Inset showing the FT of the cycled material. XANES as well as the FT of the cycled material are compared with those from pristine $CoFe_2O_4$ and $NiFe_2O_4$ samples.*

Similarly, the FT (inset) at both Co and Ni edges for the samples after one complete cycle show dominant peaks around 2.3 Å which can be attributed to the presence of metallic domains. Therefore, it may be concluded that both, metallic Co and Ni formed during the first discharge, are not completely transformed into their corresponding oxides. In order to get some quantitative information about the phase fraction, LCF fitting was done on the cycled

samples at the Co and Ni edges using CoO, Co metal, NiO and Ni metal spectra as references, respectively. From the LCF fitting, about 60% of Co and Ni remained in the metallic phase in the completely cycled $CoFe_2O_4$ sample. LCF fits of the Co and Ni edges are shown in ***Figure 42***

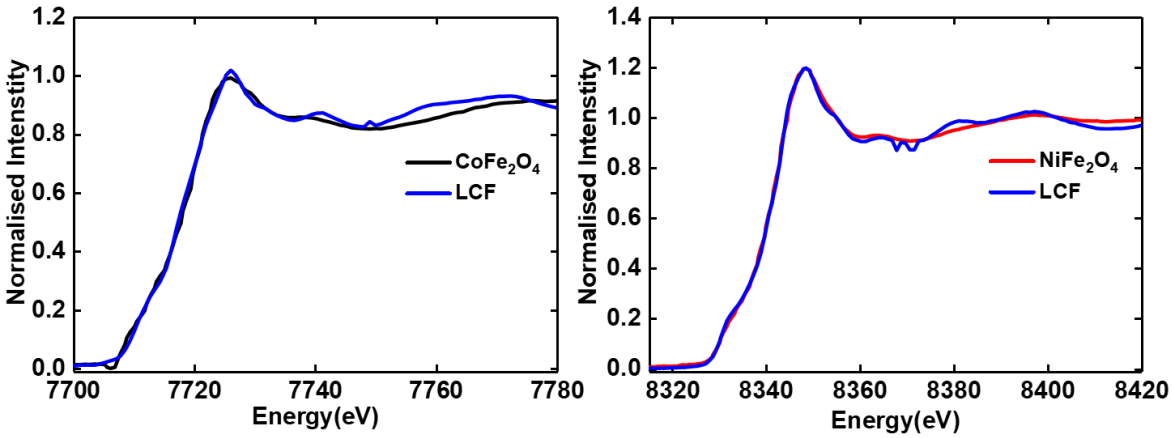


***Figure 42*** *– LCF fitting with CoO, Co metal, NiO and Ni metal spectrum as references for Co and Ni K edge XANES region of cycled $CoFe_2O_4$ (a) and $NiFe_2O_4$ (b) materials.*

This phenomenon could be explained by the fact that the oxidation of Fe takes place already at lower potentials than the oxidation of Co and Ni. Alternatively, the phenomena could also be explained in terms of a kinetic effect, assuming a core-shell model of the metallic domains formed during the reduction process, with a Ni/Co core and Fe shell. It is expected that, during the re-oxidation process, the Fe which is near to the surface is preferentially oxidized compared to the Ni and Co which is in the core. These metallic fractions may remain electrochemically inactive in the subsequent cycle resulting in an overall reduction in the capacity.

## 3.3.2. Discussion

Ternary transition metal ferrites $MFe_2O_4$ ($M$ = Co, Ni) synthesized by inverse co-precipitation were investigated as conversion electrode model systems in Li half cells. *In situ* XAS studies performed at Fe, Co and Ni K edges reveal that during the conversion reaction the ternary

oxides transform into binary metal oxides which are then subsequently reduced to the corresponding metallic states. The EXAFS analysis confirmed that the metallic phases formed are nano-structured. At the end of the first cycle, metallic Fe domains formed during discharge, are completely reoxidized. However, no such complete oxidation was observed for the Co and Ni metallic phases. The reason for the observed behavior can be attributed to a thermodynamically more favoured formation of $Fe_2O_3$ in comparison with NiO or CoO. In addition, a kinetic limitation due to the formation of a core-shell structure with a Ni/Co core and Fe shell could be suspected. The hindered reoxidation of Co and Ni in the applied potential window could be a reason for the observed irreversible capacity loss in the first cycle for both materials. A higher reversible capacity and hence a higher coulombic efficiency especially in the initial cycle would require a complete oxidation of Ni and Co at lower potentials. It is also interesting to mention the findings which were published later on $NiFe_2O_4$[93,94] and $CoFe_2O_4$[95]. These XAS studies on $NiFe_2O_4$ and $CoFe_2O_4$ also support the reduction of both spinels into metallic state during lithiation and re-oxidation during subsequent de-lithiation, although Fe, Co and Ni absorbers behave differently during cycling. Analysis unveiled a partially irreversible conversion of Ni and Co metal to subsequent NiO and CoO and complete oxidation of metallic Fe to $Fe_2O_3$.

The cycling stability as well as coulombic efficiency could be improved by several strategies. These include formation of nanocomposites with different carbon materials thereby enhancing the electrical connectivity as well as forming a stable SEI by establishing a protective layer that prevents the direct contact of active material with electrolyte[96–98]. Another approach is electrode structuring using methods like electrospinning[99,100]. In addition, combining with a suitable polymer binder or alginate binder and subjecting the composite electrodes to heat treatments can also bring out improvements in the electrochemical performance[101,102].

## 3.4. Investigation of initial lithiation mechanism in $CoFe_2O_4$ and $NiFe_2O_4$ using *in situ* SRPD

The investigation of the electrochemical mechanism of conversion oxides with powder diffraction provides only a limited insight into the overall mechanism. However, the initial phase changes occurring in the material are identified very well using diffraction techniques before the amorphization of the material in the later lithiation state. Diffraction studies on $CoFe_2O_4$ and $NiFe_2O_4$ are scarce. Islam *et al.*,[94] reports the initial decrease and further disappearance of Bragg reflections assigned to $NiFe_2O_4$ at different stages of first discharge and clearly distinguishable reflections corresponding to the formation of $Li_2O$ and metallic Fe and Ni. However, the experiment was carried out *ex situ* and only few points during lithiation and de-lithiation were examined.

With the *operando* X-ray diffraction studies on $CoFe_2O_4$[95], a shift of all reflections to smaller 2θ angles until the uptake of 0.5 lithium with an increase of 2% in the unit cell parameter was observed. Further lithiation leads to a decrease in intensity of the spinel phase along with the appearance of a new phase with reflections close to those of the main spinel phase. The newly formed phase was assigned to a rock salt type structure with $Fm\bar{3}m$ space group and the unit cell parameter was found to be about half of that of the original cell. Similar transformation into a rock salt type structure is also observed in $MnFe_2O_4$ and $MgFe_2O_4$[103,104]. After uptake of 2 Li per formula unit, the spinel phase cannot be detected anymore, whereas reflections of the oxidic rock salt phase consisting of either both cations or phase-separated oxides dominate the XRD pattern which slowly disappear further after the intake of 6 lithium and no reflections could be detected thereafter.

It is also interesting to see the intermediate phases identified in binary spinel oxides using powder diffraction. Thackeray et al.[105], reported the structural evolution of the inverse

spinel $Fe_3O_4$ upon the electrochemical insertion of lithium up to a stoichiometry of $Li_2Fe_3O_4$. He suggested the mechanism to be a displacement of tetrahedral 8a $Fe^{3+}$ ions to octahedral 16c sites at a critical lithium ion concentration $x_c$ ($x_c < 1$). Initially the lithium is filled into the vacant 16c sites and further insertion of lithium into the structure involves filling of the tetrahedral 8a sites. Even though there are 64 tetrahedral interstices situated at three non-equivalent positions 8a, 8b and 48f, from electrostatic considerations the occupancy of tetrahedral 8b sites would be energetically less stable than occupancy of 8a sites or those 48f sites having only two Fe next neighbors. The $[Fe_2]_{16d}O_4$ subarray remains intact during the whole process and the spinel $Fd\bar{3}m$ structure is preserved with empty 8a sites. For an intake of more than 2 moles of lithium, disproportionation into $Li_2O$ and elemental Fe is proposed. Recently our co-workers investigated binary oxides such as $Fe_3O_4$, α-$Fe_2O_3$, γ-$Fe_2O_3$, $Co_3O_4$ and CuO and the presence of intermediate metastable phases such as $(Li_xFe)_{16c}[Fe_2]_{16d}O_4$, α-$(Li_{1-x}Fe_{1+x})O_2$, $(Li_xFe)_{16c}[Li_xFe_{1.33}]_{16d}O_4$, $(Li_xCo)_{16c}[Co_2]_{16d}O4$ and $Cu_2O$, respectively, were confirmed by *in situ* SRPD[106]. Therefore, the intermediate phases formed during the initial discharge process of different binary and ternary conversion oxides still are differently explained. Considering the fact that the initial lithiation process is highly important for the subsequent formation of $Li_2O$/metal nanoparticles which leads to further charge-discharge cycles, it is the most relevant step that has to be studied and understood in detail.

Herein, the intermediates formed during the initial lithiation process of $CoFe_2O_4$ and $NiFe_2O_4$, synthesized by an inverse co-precipitation method and annealed at 800 °C (CFO-800 and NFO-800) are investigated by *in situ* SRPD.

Larcher *et al.*,[107] investigated the electrochemical lithiation in normal spinel $Co_3O_4$ using *in situ* diffraction and suggested that the nature of the intermediate is rate/surface dependent. They proposed that the intermediate $Li_xCo_3O_4$ phase is always formed upon

electrochemical reduction of $Co_3O_4$ spinel phase, but its stability is highly dependent on the discharge rate or current density. $Co_3O_4$ with a crystallite size of 100 nm is cycled with different C-rates from C/6 to C/75 until 2 moles of lithium. Additionally, they observed that when the current density is high enough (C/6, C/10, C/12, C/15, C/25) $Li_xCo_3O_4$ remains stable. A spontaneous decomposition into CoO was seen when the current density is reduced or interrupted intermittently. To study the influence of current density on initial lithiation intermediate formation, CFO-800 and NFO-800 were also cycled at two different C-rates of C/10 and C/40.

In the current study, the average particles size was estimated to be 70±21 nm for CFO and 52±19 nm for NFO by SEM analysis (***Figure 22***). CFO-800 crystallizes in a partially inverse cubic spinel structure and the patterns were indexed with the space group $Fd\bar{3}m$. Whereas NFO-800 crystallizes in an inverse cubic spinel structure and the patterns were indexed with the space group $Fd\bar{3}m$. Therefore, in CFO-800 the $Fe^{3+}$ and $Co^{2+}$ partially occupy the tetrahedral sites in the spinel structure whereas in NFO-800 the tetrahedral sites are solely occupied by $Fe^{3+}$. The unit cell parameters obtained from Rietveld refinement based on the observed diffraction data of pristine materials as seen from ***Figure 17*** and ***Figure 18*** is 8.3725(1) Å and 8.3408(1) Å for CFO-800 and NFO-800 samples, respectively.

## 3.4.1. Voltage Profile

CFO-800 and NFO-800 were cycled against Li at a charge discharge rate of C/10 and C/40. ***Figure 43*** shows the voltage versus lithium profile during the first discharge cycle. The potential profile during cycling is separated into two regions, denoted as discharge (black) and charge (red) plots. During the discharge the cell potential drops rapidly to 0.71 V for NFO-800 cycled at C/10 and 0.78 V for the sample cycled at C/40 whereas, at 0.8 V for CFO-

800 cycled at C/10 and 0.9 V for the sample cycled at C/40 followed by a plateau. At the end of the discharge process, the potential is decreased to 0.01 V. For CFO-800 cycled at C/10, the capacity of the whole discharge process amounts to 1195 mAh $g^{-1}$ (theoretical capacity: 914 mAh $g^{-1}$), corresponding to an uptake of 10.45 Li per formula unit.

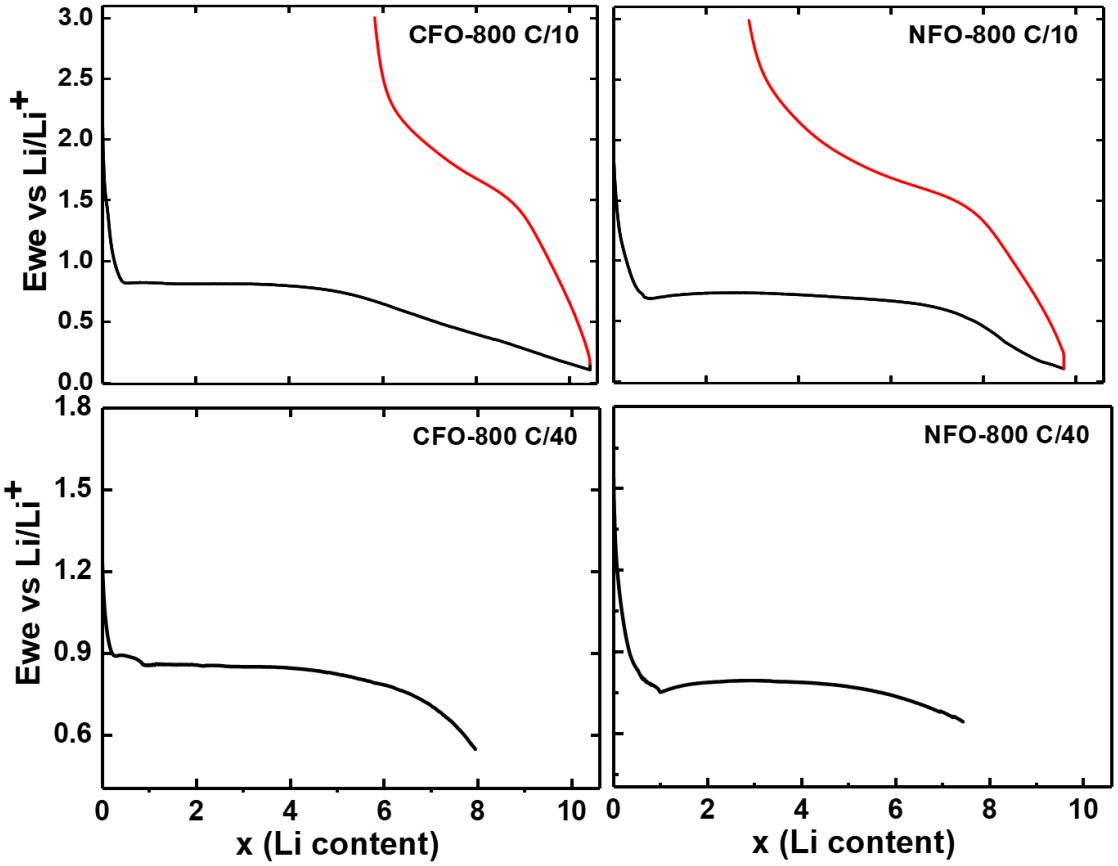


***Figure 43*** *– Discharge profiles with respect to lithium content for CFO-800 and NFO-800 discharged at C/10 and C/40.*

For NFO-800 cycled at C/10, the capacity of the whole discharge process amounts to 1115 mAh $g^{-1}$ (theoretical capacity: 915 mAh $g^{-1}$), corresponding to an uptake of 9 of 9.76 Li per formula unit and the corresponding charge represented by the red curve yields a charge capacity of 780 mAh $g^{-1}$ with an extraction of 6.8 moles of lithium.

## 3.4.2. *In Situ* SRPD of CFO-800 at C/10

*In situ* SRPD was carried out to investigate the structural evolution in CFO-800 during electrochemical cycling at a C/10 rate. *In situ* SRPD recorded for CFO-800 during the initial discharge up to the intake of 2 moles of lithium is presented in

***Figure 44***. In the beginning of the lithiation all reflections shift slightly towards smaller 2θ angles. This behavior was previously reported by Permien *et al.*, for $CoFe_2O_4$[95], rGO-$CoFe_2O_4$[97], $MnFe_2O_4$[103] and $MgFe_2O_4$[104]. At the lithium content x=1, there is clearly a new phase. The intensities of reflections of the new phase increase with further lithiation at the cost of a decreasing intensity of the initial reflections.

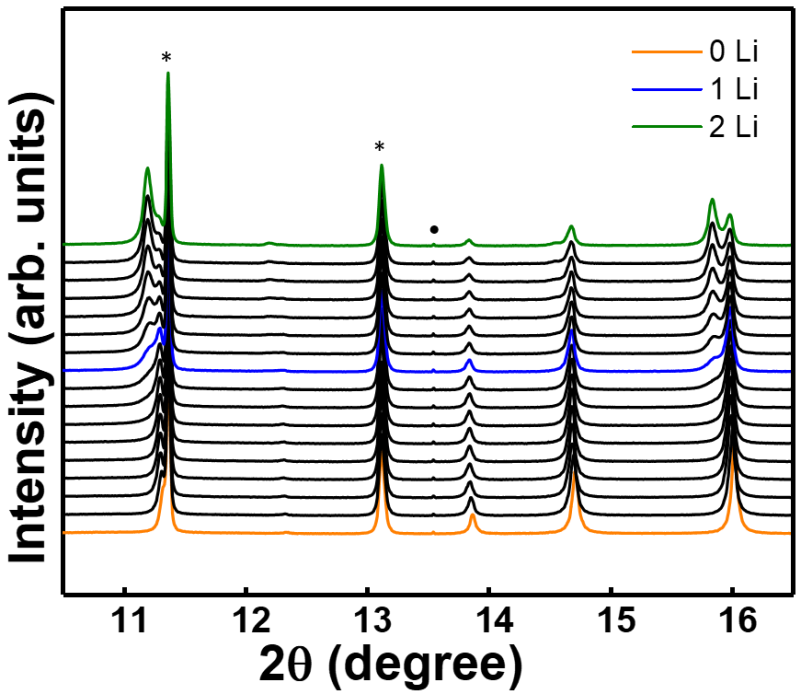


***Figure 44*** *– in situ SRPD of CFO-800 up to the intake of 2moles of lithium discharged at C/10. (• lithium metal reflection and * Copper foil reflection).*

Rietveld refinement based on the observed diffraction data accounts for the presence of a new phase starting from 0.08 moles of lithium intake. The newly formed phase is indexed as a cubic spinel phase ($Fd\bar{3}m$ space group) with empty tetrahedral 8a sites, lithium

displacing the $Co^{2+}$ and $Fe^{3+}$ atoms from the tetrahedral (A) 8a site to the empty octahedral (B) 16c site.

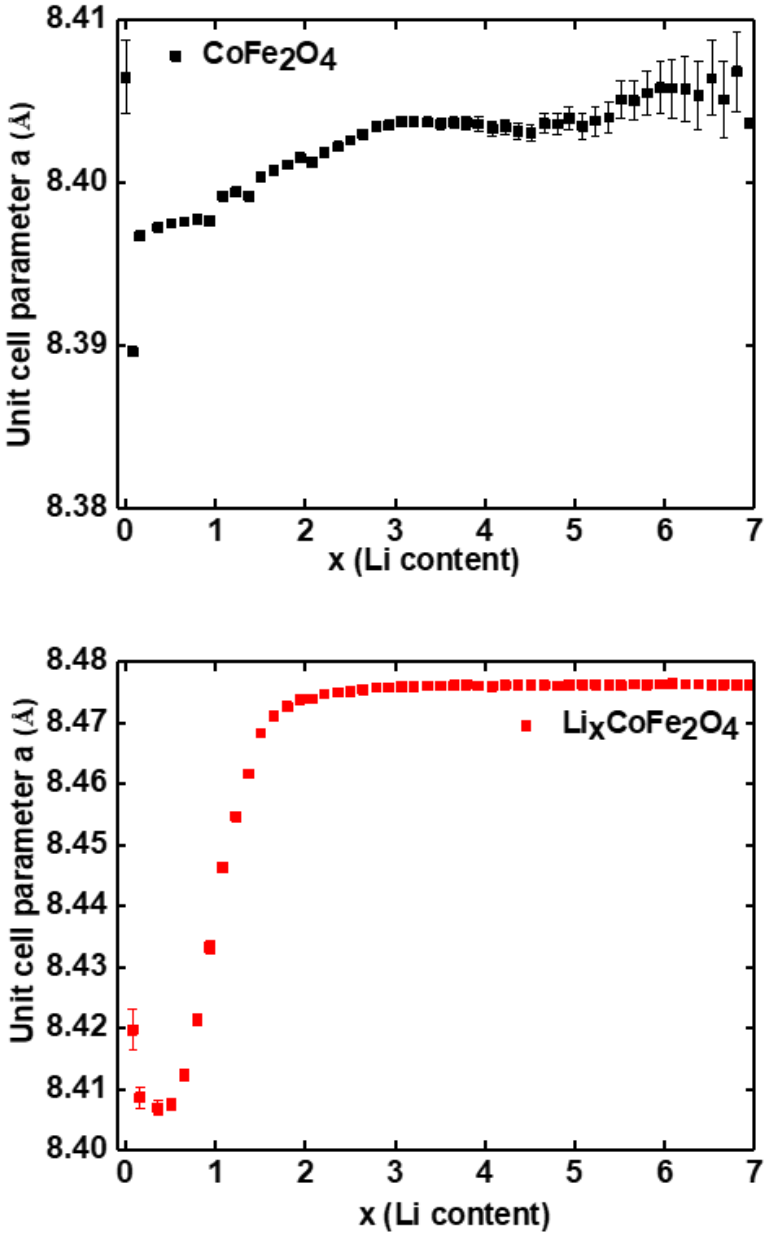


***Figure 45** – Changes in the unit cell parameter as a function of number of moles of lithium (x) for main phase ($CoFe_2O_4$) and additional new lithiated phase ($Li_xCoFe_2O_4$) for CFO-800 discharged at C/10.*

The initial $CoFe_2O_4$ and lithiated $Li_xCoFe_2O_4$ phases are clearly distinguishable with Rietveld refinement based on the powder diffraction patterns due to their difference in lattice parameters. ***Figure 45*** shows the changes in the unit cell parameter as a function of number of moles of lithium (x) intake for the main phase ($CoFe_2O_4$) and the additional lithiated phase

($Li_xCoFe_2O_4$). The lithiated $Li_xCoFe_2O_4$ phase at 0.8 moles of lithium intake has a lattice parameter of 8.419(3) Å. With further lithiation, the lattice parameter gradually increases.

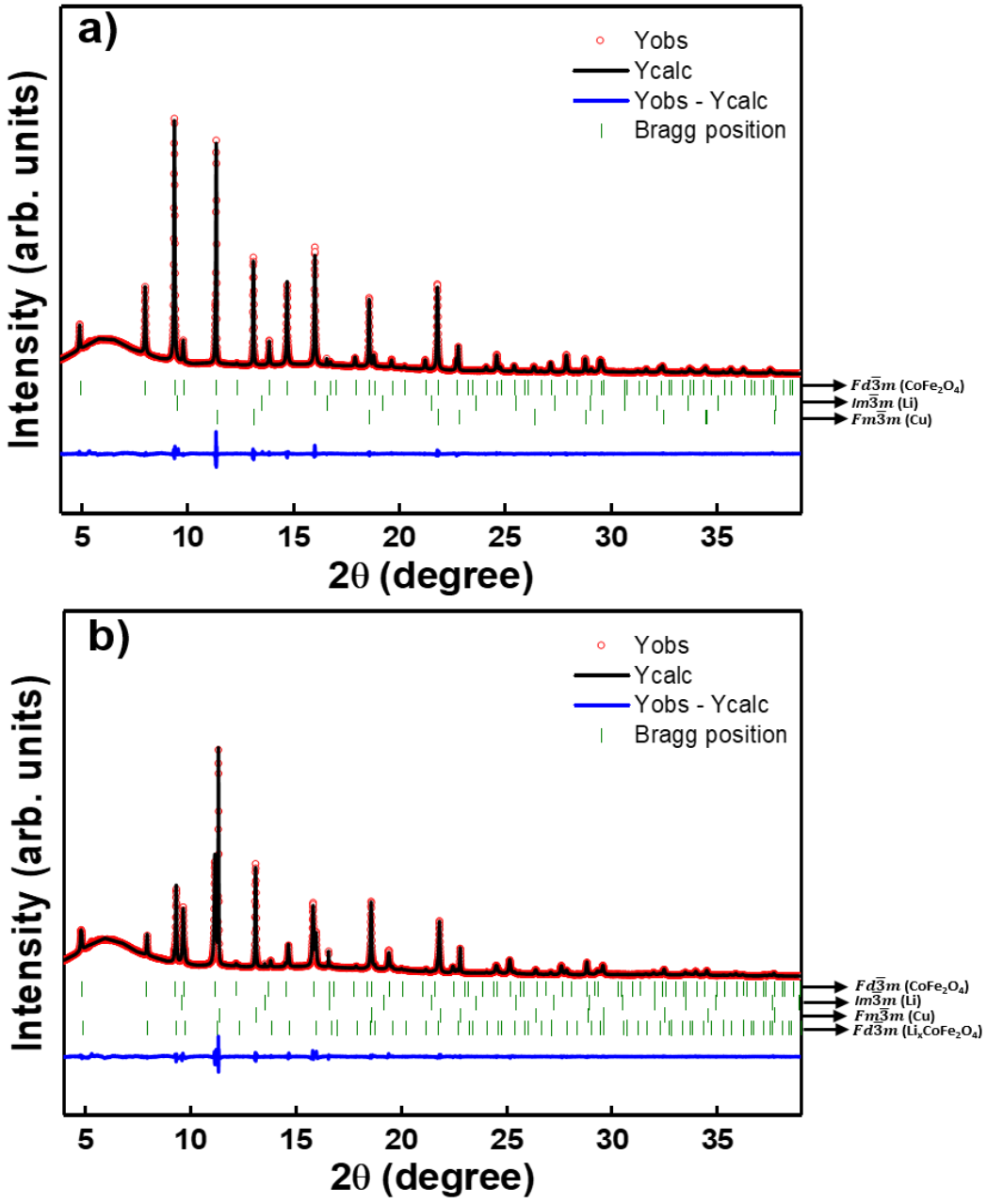


***Figure 46** – Rietveld refinement results for diffraction patterns of CFO-800 observed during the first discharge at lithiation states of x=0 (a) and x=2 (b) moles of lithium, discharged at C/10*

***Figure 46*** shows the Rietveld refinement results during the first discharge process at lithiation states of x=0 (a) and x=2 (b) moles of lithium. As the lithiation proceeds further the

reflections' intensities of the $CoFe_2O_4$ decrease together with a decrease in phase ratio and along with an increase in the intensity of $Li_xCoFe_2O_4$ and corresponding phase ratio as observed from ***Figure 47***.

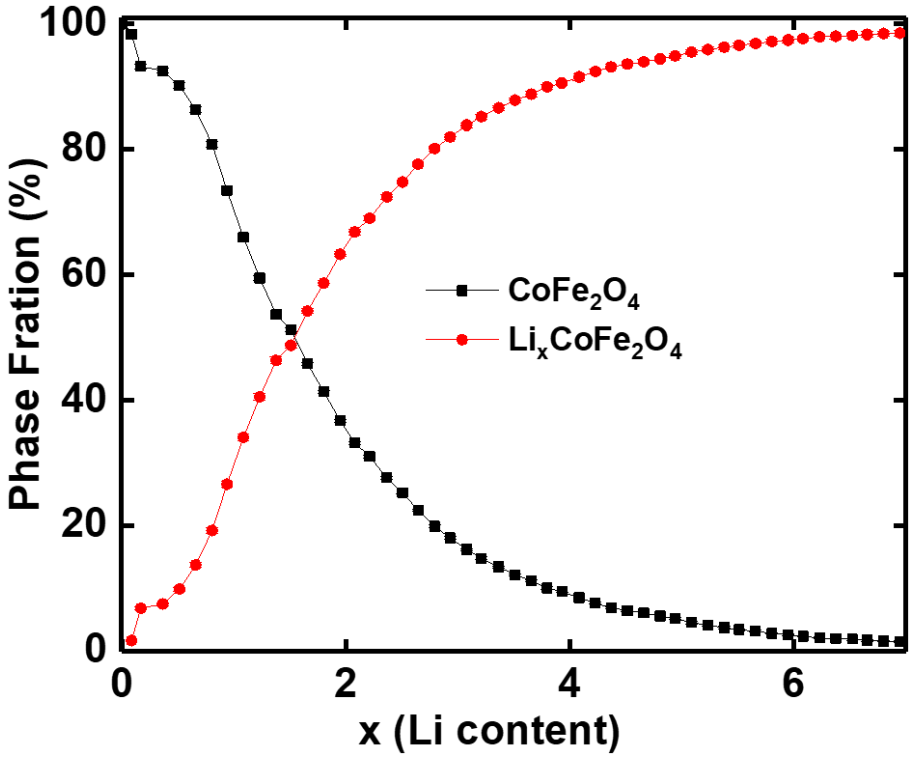


***Figure 47*** *– The phase ratios vs. Li content (moles) of crystalline phases during cycling for CFO-800 discharged at C/10*

Further discharge leads to the destruction of the lithiated phase $Li_xCoFe_2O_4$, which is reflected by a broadening of the reflections. The decomposition of this phase is probably accompanied by the formation of Co and Fe metal nanoparticles in an amorphous matrix of $Li_2O$. However, the nanorange or amorphous end products are not detectable with X-ray diffraction. ***Figure 48*** shows the *in situ* SRPD during the complete cycle. The initial $CoFe_2O_4$ phase completely disappears and the $Li_xCoFe_2O_4$ phase reflections are broadened at the end of discharge, which cannot be analyzed by Rietveld refinement. During the consecutive charge there is a shift in the reflections of the $Li_xCoFe_2O_4$ phase to higher 2θ values. This could be the formation of monoxide either FeO or CoO or both as detected in *ex situ* samples at the end of charge by XAS with nearly the same stoichiometry and a slightly different lattice

parameter. However, the data cannot be investigated further with X-ray diffraction because the monoxides formed are highly amorphous.

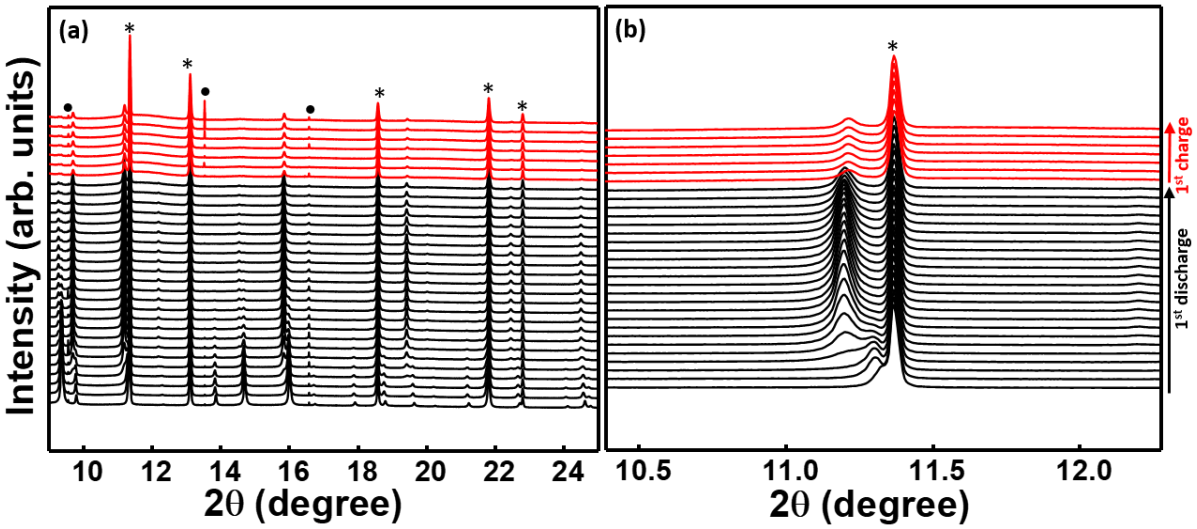


***Figure 48*** *– Selected 2θ [(a) 9-25 2θ and (b) 10.4-12.3 2θ] regions of the in situ SPRD patterns of CFO-800 measured at the MSPD powder diffraction beamline at ALBA during first cycle at C/10. (•lithium metal reflection and * Copper foil reflection).*

The lattice parameter expansion, crystallite size and micro-strain analysis obtained by Rietveld refinement based on observed diffraction data of CFO-800 at various discharge points during *in situ* SRPD are shown in ***Table 11***. The maximum strain is given in the Fullprof microstructural output file as $\frac{\triangle d}{d}$x10$^{-4}$.

***Table 11 - Rietveld refinement results based on observed diffraction data for $Li_xCoFe_2O_4$ at various lithiation states. Lattice parameter expansion, micro-strain analysis and crystallite size are given.***

| Lithium Content (x) | Lattice Parameter and Lattice Parameter Expansion | | Crystallite Size (nm) | Maximum Strain |
|---|---|---|---|---|
| | $Li_xCoFe_2O_4$ | Expansion | $Li_xCoFe_2O_4$ | $Li_xCoFe_2O_4$ |
| **Initial** | 8.419(3) | 0.155 (compared to pristine phase) | 30.25 | 36.73 |
| 1.51 | 8.468(2) | 0.582 | 32.585 | 32.23 |

| | | | | |
|---|---|---|---|---|
| 2.50 | 8.475(1) | 0.665 | 35.16 | 9.55 |
| 3.51 | 8.4760(8) | 0.677 | 42.88 | 7.38 |
| 4.51 | 8.4761(7) | 0.678 | 47.98 | 7.17 |
| 5.51 | 8.4762(7) | 0.679 | 50.01 | 7.69 |
| 6.52 | 8.4762(7) | 0.679 | 50.10 | 8.37 |
| 6.94 | 8.4762(8) | 0.679 | 48.52 | 8.14 |

The lattice parameter of lithiated $Li_xCoFe_2O_4$ shows a 0.17% increase compared to the initial $CoFe_2O_4$ phase. With increasing lithiation the lattice parameter also increases to 8.4762(7) Å after the intercalation of 5.5 moles of lithium.

### 3.4.3. *In Situ* SRPD of CFO-800 at C/40

The CFO-800 was also cycled at a C-rate of C/40 to see if the mechanism of lithiation is influenced by the rate of discharge. The structural evolution during initial discharge for CFO-800 cycled at C/40 is displayed in ***Figure 49*** for selected 2θ regions, where colored lines correspond to a specific lithium stoichiometry in the electrode material. The reflection marked with (•) is from the lithium counter electrode.

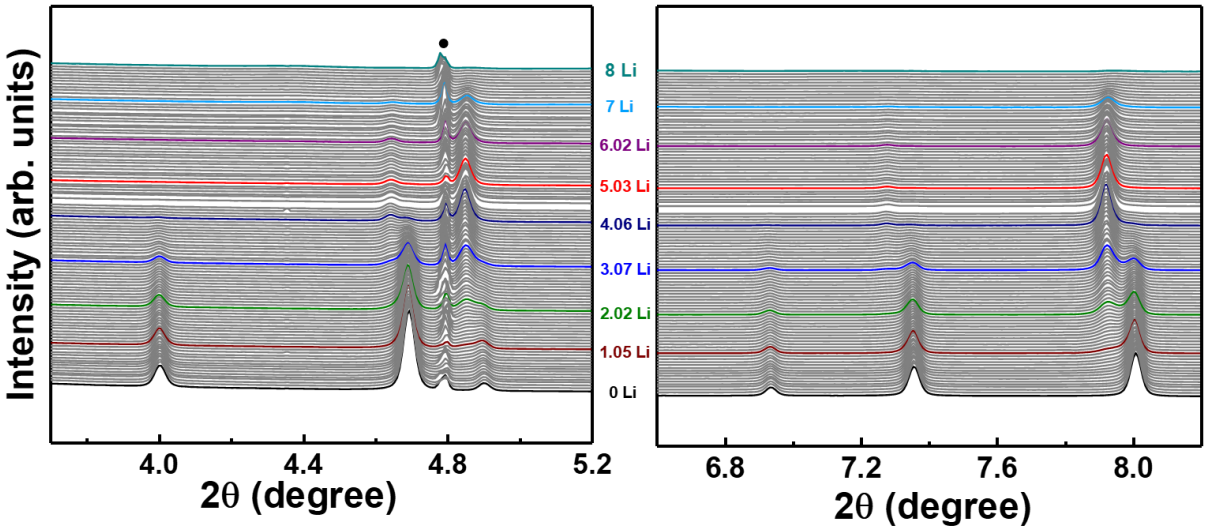


***Figure 49*** *– Selected 2θ [(a) 3.7-5.2 2θ and (b) 6.6-8.2 2θ] regions of in situ SPRD patterns of CFO-800, discharged at C/40 measured at High Resolution Powder Diffraction beamline P02.1, DESY. (•lithium metal reflection).*

When comparing the structural evolution profile of CFO-800 cycled at C/40 to that cycled at C/10, one could see that with a much slower C-rate the new phase starts to appear a bit later. Rietveld refinement confirms the appearance of a new lithiated phase with $Fd\bar{3}m$ space group from 0.8 moles of lithium uptake which is at 0.08 moles of lithium for CFO-800 cycled at C/10. With a comparatively slower cycling rate of C/40, the amorphization is reached at an earlier state of discharge which makes it hard to analyze the XRD patterns with Rietveld refinement.

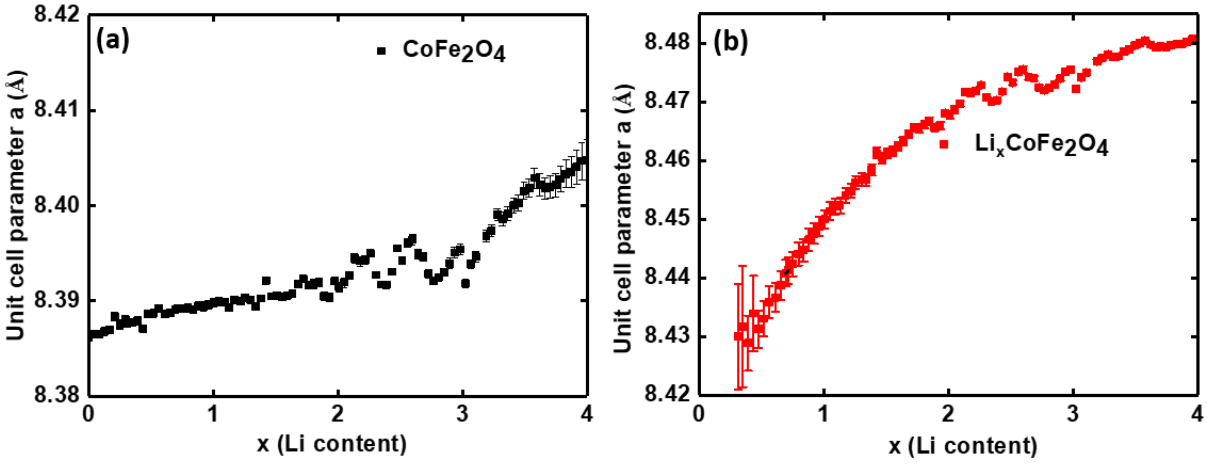


***Figure 50*** *– Changes in the unit cell parameter as a function of number of moles of lithium (x) for main phase ($CoFe_2O_4$) and additional new lithiated phase ($Li_xCoFe_2O_4$) for CFO-800, discharged at C/40.*

***Figure 50*** shows the changes in the unit cell parameter as a function of number of moles of lithium (x) for the main phase ($CoFe_2O_4$) and the additional lithiated phase ($Li_xCoFe_2O_4$) obtained by Rietveld refinement based on the observed diffraction data. The lithium uptake leads to an expansion of the unit cell and thereby an increase in the lattice parameter of the $CoFe_2O_4$ phase from 8.3725(2) to 8.405(8) Å. The lithiated intermediate $Li_xCoFe_2O_4$ phase at 0.8 lithium has a lattice parameter of 8.429(9) Å. With further lithiation the lattice parameter gradually increases to 8.4783(3) Å after the intake of 4.5 lithium. ***Figure 51*** shows the phase ratios versus lithium content for CFO-800 cycled at C/40. A phase ratio of 1:1 for $CoFe_2O_4$ and $Li_xCoFe_2O_4$ phases are reached with an uptake of 2 moles of lithium and with 4.5 moles of lithium the main phase completely disappears.

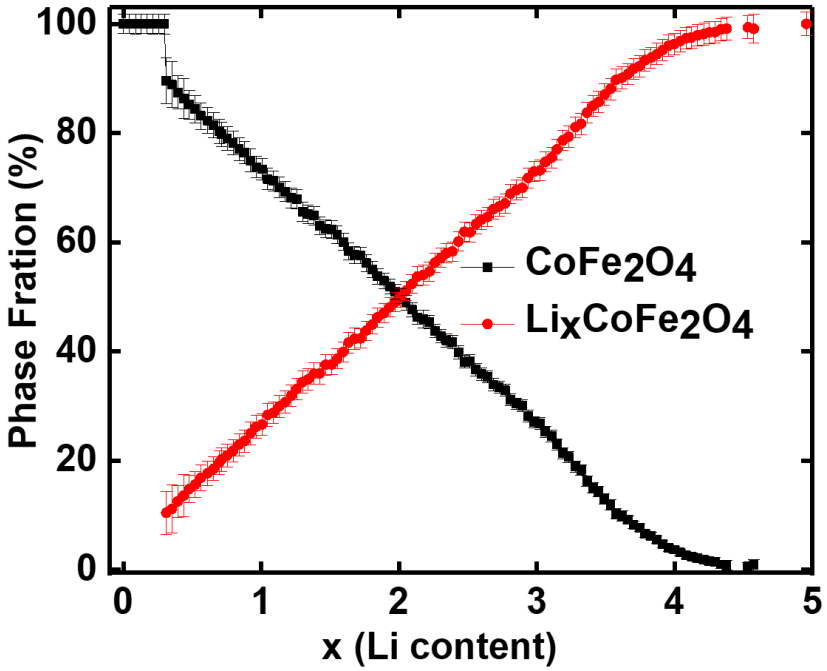


***Figure 51*** *– The phase ratios vs. Li content of crystalline phases during cycling for CFO-800 discharged at C/40.*

The oscillations in lattice parameter as seen from ***Figure 50*** between 2 and 3 lithium might be due to the synchrotron radiation beam instability, as there is no such oscillations seen in the corresponding phase ratio (***Figure 51***). Further discharge results in the complete

amorphisation and no further detection of phases is possible with X-ray diffraction. The lithiated phase is expected to directly transform into metal nanoparticles of Co and Fe in the $Li_2O$ matrix.

### 3.4.4. *In Situ* SRPD of NFO-800 at C/10

In the CFO-800 material, the intermediate phase is identified with *in situ* SRPD as $Li_XCoFe_2O_4$ with $Fd\bar{3}m$ space group with a larger lattice parameter compared to the main phase. However, the Rietveld refinement results confirm the appearance of a new phase with the uptake of 0.08 moles of lithium per formula unit for CFO-800 cycled at C/10 and at 0.8 moles of lithium uptake at C/40 and with 4.5 moles of lithium the main phase completely disappears.

*In situ* SRPD for NFO-800 during the initial discharge at C/10 up to the intake of 5 moles of lithium is presented in ***Figure 52***. Even though there is a visible set of new reflections at lower 2θ angles next to the main phase reflections, after the intake of 3.5 lithium, the increase in the intensity of the newly formed phase is rather slow compared to that in CFO-800 material. The total intensity of the diffraction patterns decreases rather fast which limits the accuracy of refinement.

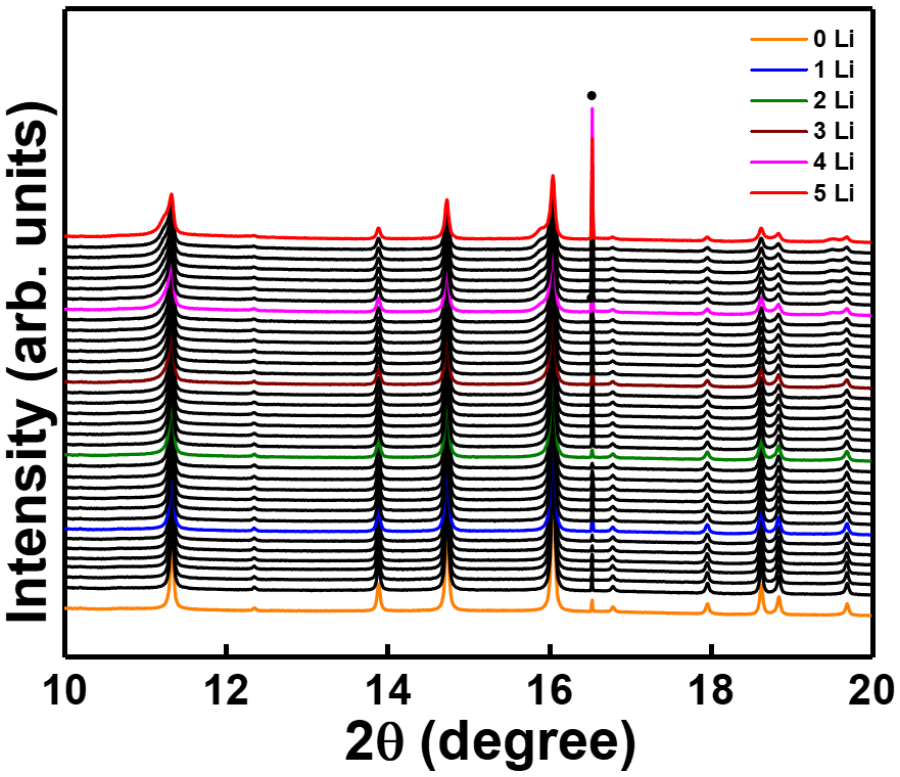


***Figure 52** – in situ SRPD of NFO-800 up to 5 moles of lithium intake, when discharged at C/10. (•lithium metal reflection).*

As in case of the CFO sample, there is a narrow solid solution region in the beginning of the discharge, followed by the appearance of the second phase $Li_xNiFe_2O_4$. Rietveld refinement confirms the presence of a new phase starting from 0.2 moles of lithium which is $Li_xNiFe_2O_4$ in cubic spinel space group $Fd\bar{3}m$ with a structural displacement of atoms from tetrahedral 8a sites to octahedral 16c sites. Nevertheless, clearly visible shoulders on the main phase reflection set is only observed after the uptake of approximately 3.5 moles of lithium. The intensity of $NiFe_2O_4$ main phase decreases and disappears with increasing intensity of $Li_xNiFe_2O_4$ phase during the discharge. ***Figure 53*** shows the Rietveld refinement results based on the observed diffraction data for NFO-800, discharged at C/10 at lithiation states of x=0 (a) and x=5 (b) moles of lithium. The intensity of reflections at x=5 decreases considerably along with a corresponding broadening.

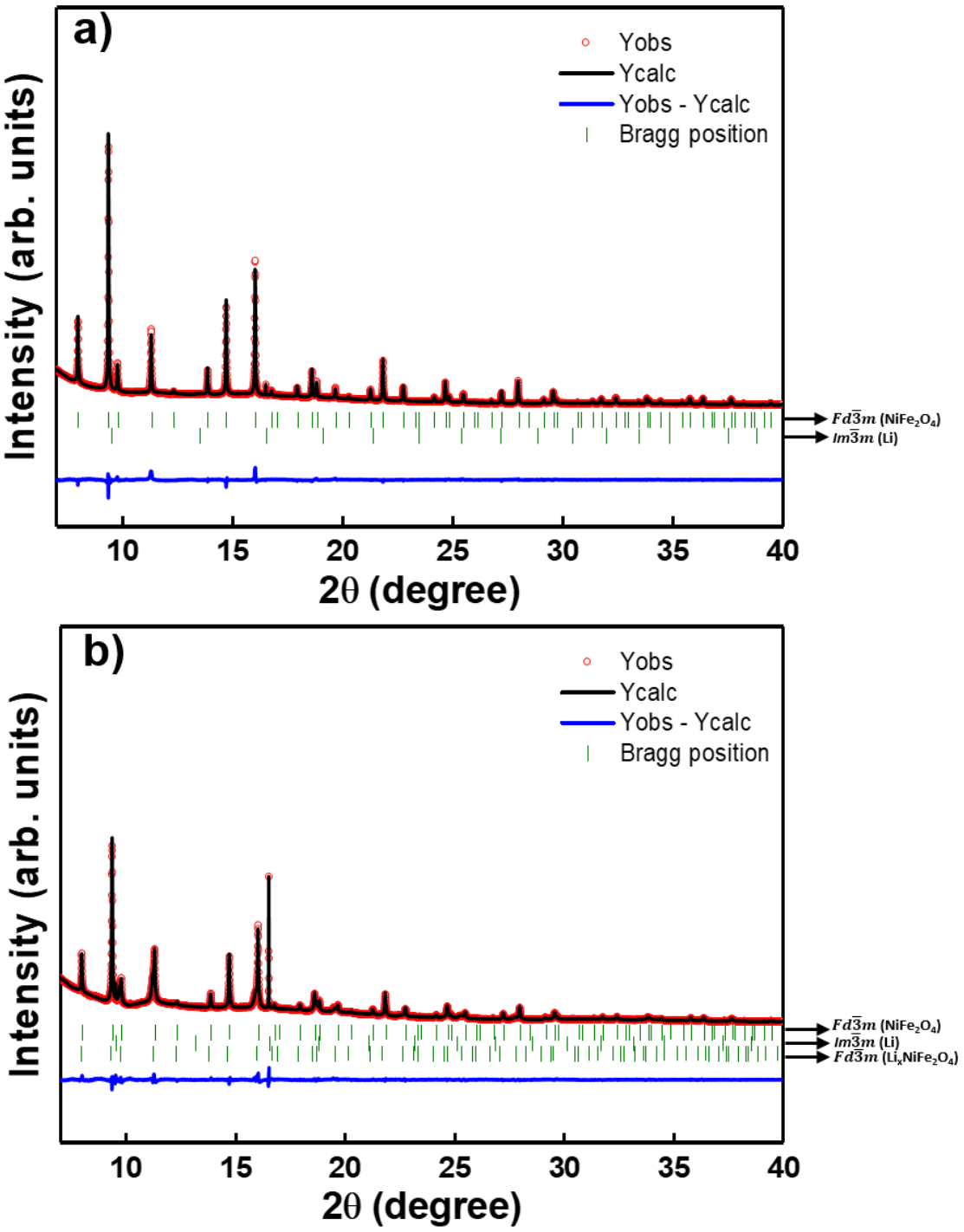


***Figure 53** – Rietveld refinement results based on observed diffraction data for NFO-800 discharged at C/10 at lithiation states of x=0 (a) and x=5 (b) moles of lithium.*

***Figure 54*** shows the *in situ* SRPD of NFO-800 during the first discharge-charge cycle. The decrease of the intensities of the intermediate phase $Li_xNiFe_2O_4$, due to amorphization, begins at lower lithium contents compared to CFO-800. During the charge there is no shift in the reflections of the $Li_xNiFe_2O_4$ phase to a higher 2θ value as observed in CFO-800.

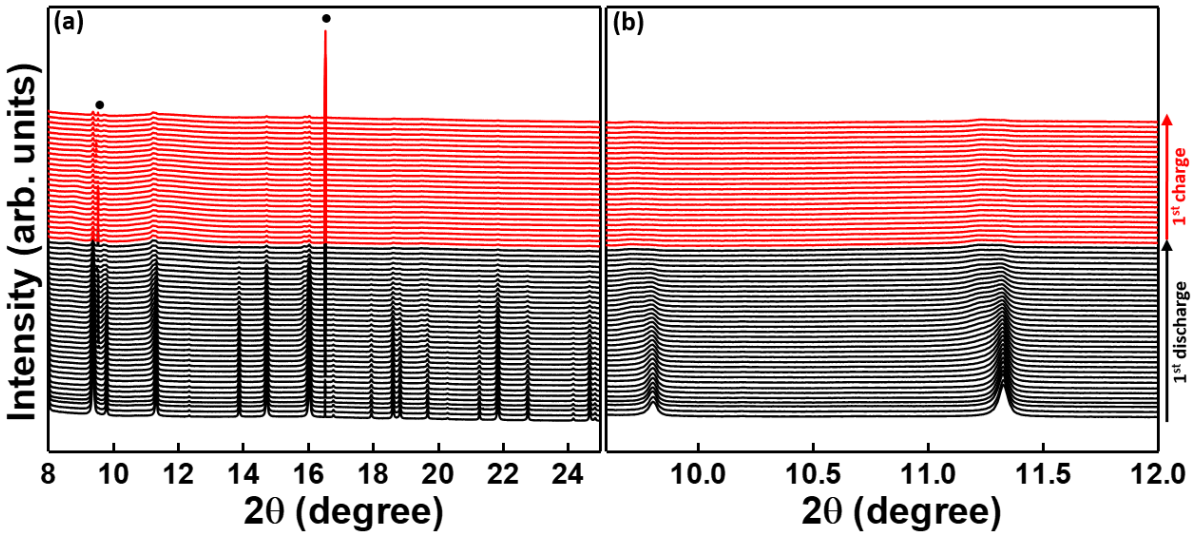


***Figure 54*** *– Selected 2θ [(a) 8-25 2θ and (b) 9.5-12 2θ] regions of in situ SPRD patterns of NFO-800 measured at the MSPD powder diffraction beamline at ALBA during first cycle cycled at C/10. (•lithium metal reflection).*

The lattice parameter received from Rietveld refinement based on the obtained diffraction data for pristine NFO-800 is 8. 3408(1) Å. The lithiation leads to an expansion of the unit cell and thereby an increase in the lattice parameter of the host structure of $NiFe_2O_4$ from 8.3408(1) to 8.3481(3) Å. Permien *et al.*, observed a similar expansion in lattice parameter during initial lithiation[95,103,104]. However, together with an expansion of approximately 0.2%, the reflections shift to lower scattering angles. In the current experiment, only a slight unit cell expansion of approximately 0.007% was observed from the initial state, which might be caused by intercalation of a very small amount of Li into the host structure without the shift in reflections. Instead, a two phase reaction mechanism was observed further on.

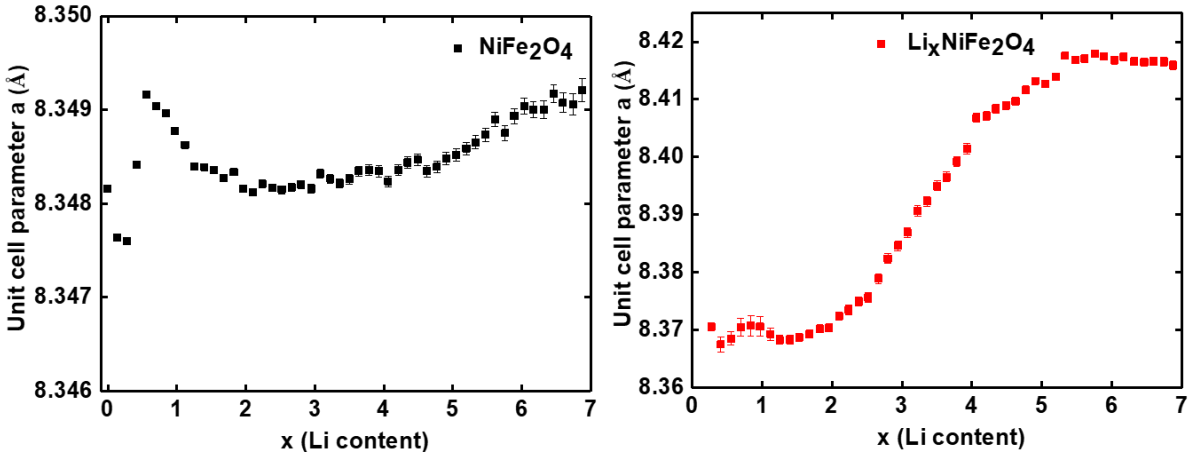


***Figure 55*** *– Changes in the unit cell parameter as a function of number of moles of lithium (x) for main phase ($NiFe_2O_4$) and additional new lithiated phase ($Li_xNiFe_2O_4$) for NFO-800 discharged at C/10*

***Figure 55*** shows the changes in the unit cell parameter as a function of number of moles of lithium (x) for $NiFe_2O_4$ and lithiated $Li_xNiFe_2O_4$. The Freshly formed lithiated $Li_xNiFe_2O_4$ phase at 0.2 moles of lithium intake has a lattice parameter of 8.3705 (7) Å. The lattice parameter remains without much difference until 2 moles of lithium uptake and with further lithiation it gradually increases. Also the information about the phase fraction evolution is extracted by Rietveld refinement based on the obtained diffraction data as seen in ***Figure 56***.

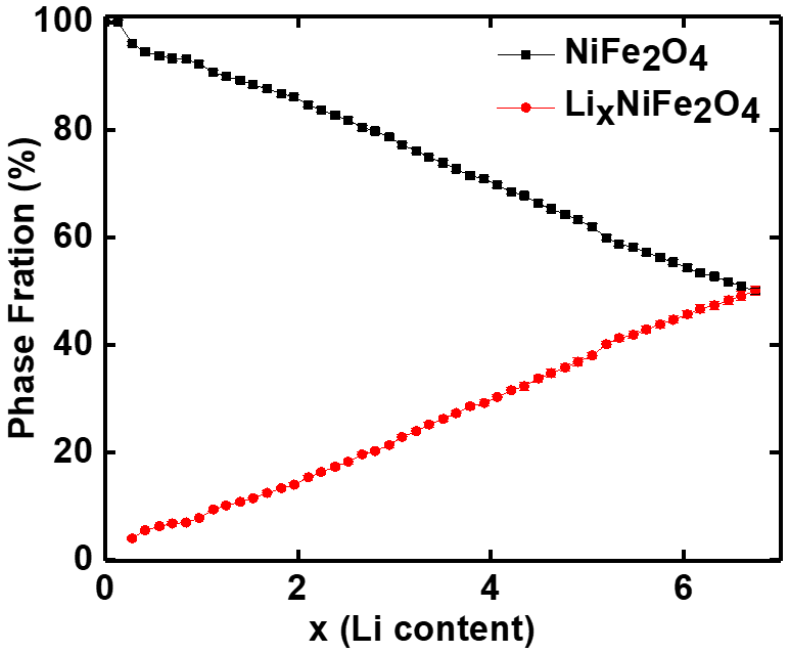


***Figure 56*** *– The phase ratios vs. Li content of crystalline phases during cycling for NFO-800, discharged at C/10.*

The $Li_xNiFe_2O_4$ phase is formed with lithiation of 0.2 moles of lithium. The phase ratio of $NiFe_2O_4$ decreases with increasing phase ratio of $Li_xNiFe_2O_4$. However, the process takes place gradually compared to that for CFO-800 material. Hence, the conversion of newly formed $Li_xNiFe_2O_4$ into Ni and Fe metal nanoparticles in an amorphous matrix of $Li_2O$ at the end of discharge might be incomplete. Moreover, this cannot be proved by X-ray diffraction due to the nanocrystalline or amorphous nature of the end products.

## 3.4.5. *In Situ* SRPD of NFO-800 at C/40

The influence of C-rate over the electrochemical reaction mechanism in ternary transition metal ferrites is further investigated by cycling NFO-800 at a C-rate of C/40. The structural evolution during the initial discharge process for CFO-800 cycled at C/40 is displayed in ***Figure 57*** for selected 2θ regions, where colored lines correspond to the different amounts of lithium uptake. The reflection marked with (•) are from the lithium counter electrode and (*) from copper current collector.

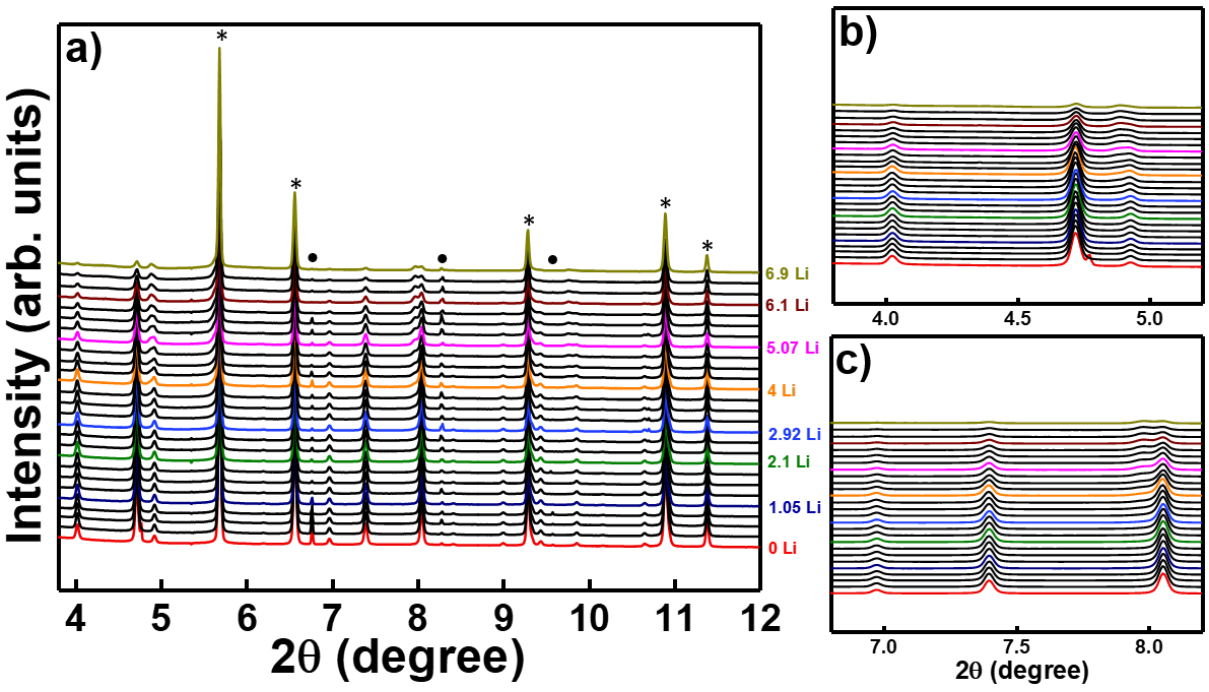

***Figure 57** – Selected 2θ [(a) 3.7-5.2 2θ, (b) 6.6-8.2 2θ) and (c) 6.6-8.2 2θ] regions for in situ SPRD patterns of NFO-800 discharged at C/40 measured at High Resolution Powder Diffraction beamline P02.1, DESY. (•lithium metal reflection and *Copper foil reflection).*

The structural evolution of NFO-800 cycled at C/40 seems to occur in the same manner as that at C/10. However, the new lithiated phase $Li_xNiFe_2O_4$ with $Fd\bar{3}m$ space group appears at a higher degree of lithiation (x = 0.8). With comparatively slower cycling rate of C/40, the amorphization and broadening of reflections can be observed at an earlier state of lithiation which makes Rietveld refinement difficult after 4 moles of lithium uptake.

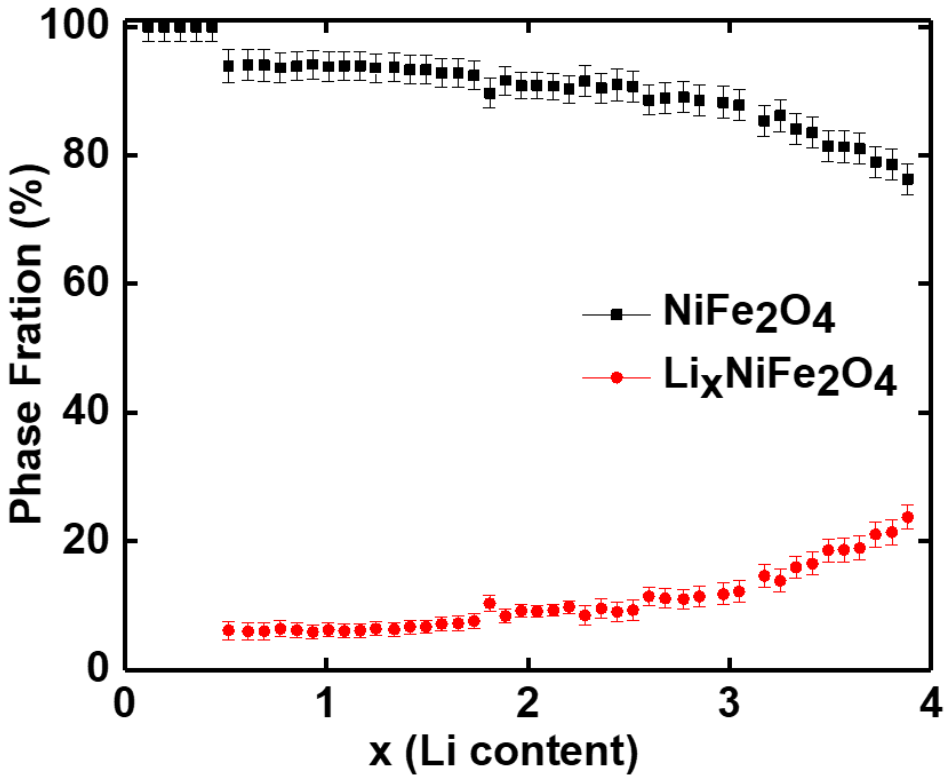


***Figure 58** – The phase ratios vs. Li content of crystalline phases during cycling for NFO-800 discharged at C/40.*

***Figure 58*** shows the phase ratios versus lithium content for NFO-800 cycled at C/40. In CFO, equal amount of $CoFe_2O_4$ and $Li_xCoFe_2O_4$ phases are observed with an uptake of 2 moles of lithium and with 4.5 moles of lithium uptake, the main phase completely disappears whereas in NFO samples cycled at C/10 and C/40 the phase transformation occurs rather slowly.

## 3.4.6. Discussion

Partially inverse CFO-800 and inverse NFO-800 cubic spinels indexed with the space group $Fd\bar{3}m$ are investigated to understand the initial lithiation mechanism during first discharge. To study the influence of the discharge rate on the electrochemical mechanism, we performed the experiments at two current densities: C/10 and C/40, respectively. During the first discharge both, the initial intercalation and later conversion reaction are assumed to have distinct reaction dynamics. Even though the reaction speed of intercalation is much faster, the conversion reaction accommodates more Li ions. As previously reported, the overall electrochemical kinetics is dependent on the applied C-rate, which in turn determines the propagation speed of the interfaces of the different phases during the lithiation and conversion reaction[108]. However, the propagation speed of the intercalation process is about 1 order of magnitude faster than the following conversion reaction[109]. In the current study, the intermediate lithiated phase appears at 0.08 and 0.8 moles of lithium intake for CFO-800 cycled at C/10 and C/40, respectively, whereas at 0.2 and 0.8 moles of lithium uptake for NFO-800 cycled at C/10 and C/40 respectively. Hence, the higher C-rate of the samples results in higher propagation speed of the lithiated phase interface. Therefore, in terms of total lithium insertion capacity, both reactions give important contributions to the overall energy storage rate.

This intermediate lithiated phase was always indexed with the space group $Fd\bar{3}m$. The characteristic feature of this intermediate phase is the rearrangement of the cations within the spinel structure. As reported previously by Thackeray *et al.,*[105] and Adam *et al.,*[106] for binary spinel oxide $Fe_3O_4$, the insertion of lithium into octahedral 16c sites of the spinel causes the migration of the transition metal cations from the tetrahedral 8a sites to octahedral 16c sites. We believe that the same mechanism occurs during the discharge of CFO-800 and NFO-800,

where the intermediate lithiated spinel with empty tetrahedral 8a sites is formed. The cation distribution of the intermediate spinel phase corresponds to $\mathbf{(Li,Me)_{16c}[Me_2]_{16d}O_4}$.

***Table 12 - Changes in lattice parameter for CFO-800 and NFO-800 cycled at C/10 and C/40.***

| Lithium Content (X) | Lattice Parameter of Main Phase | | | | Lattice Parameter of Lithiated Phase | | | |
|---|---|---|---|---|---|---|---|---|
| | CFO-800 C/10 | CFO-800 C/40 | NFO-800 C/10 | NFO-800 C/40 | CFO-800 C/10 | CFO-800 C/40 | NFO-800 C/10 | NFO-800 C/40 |
| 0.5 | 8.39748(7) | 8.3886(3) | 8.34916(2) | 8.3408(2) | 8.4075(9) | 8.433(2) | 8.368(1) | 8.368(3) |
| 1 | 8.3991(1) | 8.3898(4) | 8.34862(3) | 8.3415(4) | 8.4463(8) | 8.449(1) | 8.369(1) | 8.368(3) |
| 1.5 | 8.40035(9) | 8.3905(3) | 8.34835(3) | 8.3415(4) | 8.4682(2) | 8.4612(8) | 8.3687(7) | 8.368(3) |
| 2 | 8.4012(1) | 8.3914(4) | 8.34812(3) | 8.3413(5) | 8.4739(1) | 8.4677(6) | 8.3724(7) | 8.368(3) |
| 2.5 | 8.4025(1) | 8.3942(3) | 8.34814(4) | 8.3415(6) | 8.4751(1) | 8.4732(3) | 8.3756(8) | 8.368(3) |
| 3 | 8.4037(2) | 8.3918(4) | 8.34831(4) | 8.3428(7) | 8.47595(8) | 8.4722(2) | 8.3869(8) | 8.368(3) |
| 3.5 | 8.4036(3) | 8.4015(8) | 8.34825(5) | 8.3418(8) | 8.47608(8) | 8.4796(3) | 8.3950(8) | 8.368(3) |
| 4 | 8.4033(4) | 8.404(2) | 8.34823(5) | 8.3424(7) | 8.47600(8) | 8.4808(3) | 8.4067(7) | 8.368(3) |

In both, initial spinel phase and intermediate spinel phase, the oxygen anions located at the 32e site and iron, cobalt and nickel anions at the 16d site remain intact during the whole process. The changes in the unit cell parameter for the intermediate phases observed for CFO-800 and NFO-800 cycled at C/10 and C/40 is summarized in ***Table 12***. Because of the low scattering factor of lithium, the lithiation degree cannot be directly calculated from the diffracted intensities. However, the lattice parameter expansion is an important indicator of the lithium incorporation into the host structure of the spinel.

***Table 13 - Phase ratio evolution with Li content for CFO-800 and NFO-800 cycled at C/10 and C/40.***

| Lithium Content (X) | Phase Ratio of Main Phase | | | | Phase Ratio of Lithiated Phase | | | |
|---|---|---|---|---|---|---|---|---|
| | CFO-800 C/10 | CFO-800 C/40 | NFO-800 C/10 | NFO-800 C/40 | CFO-800 C/10 | CFO-800 C/40 | NFO-800 C/10 | NFO-800 C/40 |
| 0.5 | 90.17 | 84.38 | 93.76 | 93.88 | 9.83 | 15.62 | 6.24 | 6.12 |
| 1 | 65.96 | 73.38 | 90.64 | 93.81 | 34.04 | 26.62 | 9.36 | 6.19 |
| 1.5 | 51.26 | 62.37 | 88.36 | 93.33 | 48.74 | 37.63 | 11.46 | 6.67 |
| 2 | 33.17 | 50.13 | 84.65 | 90.84 | 66.83 | 49.87 | 15.35 | 9.16 |
| 2.5 | 25.21 | 38.21 | 81.75 | 90.73 | 74.79 | 61.79 | 18.25 | 9.27 |
| 3 | 16.15 | 26.84 | 77.17 | 88.25 | 83.85 | 73.16 | 22.84 | 11.75 |
| 3.5 | 12.12 | 12.99 | 73.82 | 81.36 | 87.88 | 87.01 | 26.18 | 18.64 |
| 4 | 8.45 | 3.71 | 69.72 | 60.31 | 91.55 | 96.29 | 30.28 | 39.69 |

The phase ratio evolution vs. Li content, during initial discharge of CFO-800 and NFO-800 cycled at C/10 and C/40 is summarized in ***Table 13***. As lithiation proceeds, the intensity of the main phase decreases and the weight fraction of the lithiated phase increases. The intermediate lithiated phase is expected to undergo complete structural destruction to form metallic nanoparticles at the end of discharge. In CFO-800 material, the two phase reaction with the formation of the intermediate phase occurs much faster compared to NFO-800. For the cobalt-containing spinel, the initial phase almost completely disappears after the intake of 4 moles lithium regardless of the C-rate. For NFO-800 material, 30% of the initial spinel $NiFe_2O_4$ was still observed at the same state of discharge. This could be a reason for the decrease in specific capacity of NFO-800 material compared to CFO-800 as previously

observed in ***Figure 32***. Therefore, the electrochemical conversion reaction of the Ni spinel phase to metallic nanoparticles may not be complete, leaving behind unreacted spinel phase residues at the end of discharge.

## 3.5. Lithiation-Delithiation Mechanism in $Fe_3O_4$

The first studies on high temperature Li/$Fe_3O_4$ cells were made in the late 1970s and early 1980s, after that the performance of iron-containing spinels ($Fe_3O_4$ and $Fe_2O_3$) as battery materials at room temperature[110] was reported. Thackeray et al. demonstrated the importance of the $[B_2]X_4$ spinel framework as a host electrode structure and the ability to tailor the cell voltage by selection of various B cations[111]. Ever since, $Fe_3O_4$ has been intensely investigated for battery applications[68,77,112–117] owing to its main advantages such as low weight, minimal volume changes, low charging potentials, cost-effectiveness, non-toxicity and high energy density. One formula unit of $Fe_3O_4$ can store about eight lithium ions with a theoretical capacity of 928 mAh $g^{-1}$. Recently, the performance of a full cell battery consisting of a porous carbon $Fe_3O_4$ anode and $Li[Ni_{0.59}Co_{0.16}Mn_{0.25}]O_2$ cathode was reported, which was cycled for over 1000 cycles with capacity retention of 63.8% at high currents[118,119].

Powder diffraction investigation of chemical and electrochemical lithiation in $Fe_3O_4$ has been performed by Thackeray *et al.*,[105] Chen *et al.*,[87] Fontcuberta *et al.*,[120] and Islam *et al.*,[121,122] in early 80's. Thackeray *et al.*, reported the lithium insertion into $Fe_3O_4$ at room temperature both chemically and electrochemically in a compositional range $0<x<2$ for $Li_xFe_3O_4$. The $[Fe_2]O_4$ subarray of the spinel structure remains intact during the lithiation and the tetrahedral A-site $Fe^{3+}$ ions are displaced to empty octahedral 16c positions and the $Li^+$ ions in excess of $x = l$ are located in tetrahedral sites which results in a rock-salt type structure. Chen et al. obtained $LiFe_3O_4$ and $Li_2Fe_3O_4$ phases by chemical lithiation using n-butyllithium

at room temperature and determined their structure by powder X-ray diffraction data. For n-butyllithium: $Fe_3O_4 > 2$, a mixture of $Li_2Fe_3O_4$ and decomposition products were obtained. The lattice parameters and relative X-ray intensities of the lithiated compounds were in good agreement with previously reported results by Thackeray *et al.*,[105]. It is interesting to note that Chen *et al.*, with electrochemical lithiation obtained a mixture of spinel and rock-salt type lithiated phases. Islam *et al.*,[121,122] examined the effect of lithium insertion into $Fe_3O_4$ using theoretical atomistic simulation techniques. These results also support the reaction mechanism in which insertion proceeds with reduction and displacement of the tetrahedrally coordinated $Fe^{3+}$ to produce the ordered rock-salt structured phase, $LiFe_3O_4$. However all these investigations were limited to *ex situ* measurements up to the lithiation of 2 moles lithium.

Takeuchi and his co-workers[123–129] did extensive studies (2013-2017) on $Fe_3O_4$ electrode material. XAS investigation of nanosized $Fe_3O_4$ as a function of crystallite size varying from 7–26 nm exhibited notable differences in the local environment. They observed a substantial increase in discharge capacity with reducing crystallite size. This effect was attributed to an increase of active surface area and to a decrease of the path length for ion and electron transport due to surface oxidation[123]. Further, combined *ex situ* XRD and XAS were used to measure the structural change for a varying crystallite size (8.9–26.2 nm). *Ex situ* XRD at 0.7 and 1.7 electron equivalents confirm the spinel-like local structure with iron in both tetrahedral and octahedral environments. At 2.8 electrons, an intermediate structure and at 4, 6, and 8 electron equivalents rock-salt structure was observed. EXAFS provided experimental evidences indicative of metallic Fe nanoparticle formation at 6.0 and 8.0 electron equivalents[130]. Studies on magnetite carbon composite electrodes suggested that the size and architecture of the electrode over multiple length scales must be considered in

conjunction with the active material to realize the desired electrochemical performance[125]. It is very interesting to mention how the investigation proceeded further. Studies of the atomistic structural evolution in $Fe_3O_4$ using complementary *ex situ* synchrotron X-ray/TEM-EELS techniques and with first-principles calculations revealed that the multiple electron transfer reaction was enabled by the retention of the cubic close packed O-anion framework throughout the whole discharge and charge processes. It is within a robust cubic close packed O-anion framework that local cation displacement/re-ordering occurred in response to the lithium insertion and extraction[126]. Additionally, the most recent simulation studies suggest that during the lithiation of up to 3 electron equivalents, α-$Li_xFe_3O_4$ is formed which is further transformed to β-$Li_4Fe_3O_4$ and further converted to γ-(4 $Li_2O$ + 3 Fe). Also, the simulations for the lithiation of 6 and 32 nm $Fe_3O_4$ suggest that the rate of conversion to γ-(4 $Li_2O$ + 3 Fe) decreases with decreasing crystal size[127]. Therefore, the explanation of the electrochemical mechanism over the past years needs further clarification.

There were two *in situ* TEM[109,131] investigations which were reported very recently. He *et al.*,[109] by comparing the *in situ* STEM results with phase-field simulation, found that the formation of $LiFe_3O_4$ phase is predominant in the early state of lithiation, whereas the conversion reaction initiates immediately afterward and propagates before the complete intercalation, resulting in the coexistence of $Fe_3O_4$, $Li_xFe_3O_4$, and Fe + $Li_2O$ phases due to the competition between the intercalation and conversion reactions. They also concluded that the applied C-rate determines the propagation speed of the interfaces of $Fe_3O_4$/$Li_xFe_3O_4$ and $Li_xFe_3O_4$/Fe+$Li_2O$ which was again confirmed in the current study of CFO-800 and NFO-800 using different C-rates. Su *et al.*,[131] shows that the single-crystalline $Fe_3O_4$ nanowires get converted to Fe nanograins embedded in a $Li_2O$ matrix during first discharge and further gets

converted into FeO nanograins rather than the original $Fe_3O_4$ phase in the corresponding charge process.

In 2000, Poizot *et al.*,[22] reported the electrodes made of nanoparticles of binary transition metal oxides (MO, where M is Co, Ni, Cu or Fe) demonstrating electrochemical capacities of 700mAh/g, with 100% capacity retention for up to 100 cycles and at high recharging rates. Further studies based on iron oxide containing electrode materials showed improved electrochemical performances with mixed composite in various size and morphologies including $Fe_3O_4$/FeO/Fe microcomposite[132] (260 mAh/g after 60 cycles), $Fe_3O_4$/FeO/Fe/C[133,134](600 mAh/g after 60 cycles and 900 mAh/g after 500 cycles), FeO/C[135] (510 mAh/g after 50 cycles), $Fe_3O_4$/FeO/C nanotube[136](1017 mAh/g after 50 cycles), $Fe_3O_4$/Fe[137,138] (540 mAh/g after 100 cycles and 750 mAh/g after 50 cycles) and $Fe_3O_4$/Fe/C nanocomposites[139](600 mAh/g after 40 cycles). Zeng *et al.*,[136] suggested the initial lithiation in $Fe_3O_4$/FeO/C composite for both $Fe_3O_4$ and FeO (equations 3, 4). With the intake of 2 moles of lithium, $Li_xFeO$ is converted into metallic Fe together with the formation of $Li_2O$ amorphous matrix (equation 5). And with further lithiation, $Li_xFe_3O_4$ also gets converted into the same (equation 6).

$$Fe_3O_4 + xLi + xe^- \rightarrow Li_xFe_3O_4 \quad (3)$$

$$FeO + xLi + xe^- \rightarrow Li_xFeO \quad (4)$$

$$Li_xFe_3O_4 + (8\text{-}x)Li^+ + (8\text{-}x)\, e^- \rightarrow 4Li_2O + 3Fe \quad (5)$$

$$Li_xFeO + (2\text{-}x)\, Li^+ + (2\text{-}x)\, e^- \rightarrow Li_2O + Fe \quad (6)$$

However, there was no detailed investigation on the electrochemical mechanism in mixed composite iron oxide materials. To account for a more precise explanation for the overall electrochemical mechanism during the first cycle, *in situ* techniques such as *in situ* X-

ray absorption spectroscopy and *in situ* synchrotron radiation powder diffraction were applied to FO-600 and FO-800. Within the current research we focus on giving a better insight into the electrochemical reaction mechanism of FO-600 and FO-800.

### 3.5.1. *In Situ* SRPD

For *in situ* SRPD measurements, FO-600 and FO-800 were cycled against Li at a charge discharge rate of C/40. ***Figure 59*** shows the voltage versus lithium profile during first discharge up to approximately 5 moles of lithium insertion. Both FO-600 and FO-800 show a similar voltage profile. As seen previously for CFO-800 and NFO-800 materials, during the discharge the cell potential drops rapidly to around 0.7 V which is followed by a voltage plateau.

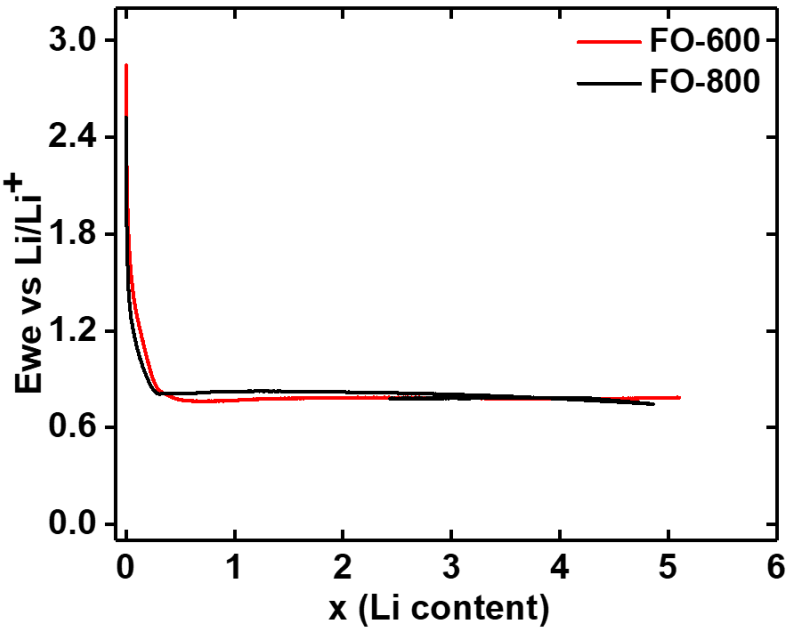


***Figure 59*** *– The x (Li content) versus voltage curve for FO-600 and FO-800 during in situ SRPD measurements at a C-rate of C/40.*

In the current study, pristine FO-600 is phase pure and crystallizes in the inverse spinel $Fe_3O_4$ structure (Lattice parameter = 8.3920(1) Å, space group $Fd\bar{3}m$, ICSD record: 26410) with tetrahedral A sites solely occupied by $Fe^{3+}$ ions and the octahedral B sites occupied by

$Fe^{2+}$ and $Fe^{3+}$ ions[56,57]. FO-800 contains 62.02% FeO (Lattice parameter = 4.3248(3) Å, space group $Fm\bar{3}m$, ICSD record: 31081) and 37.98% $Fe_3O_4$ (Lattice parameter = 8.3930(7) Å, space group $Fd\bar{3}m$, ICSD record: 26410) as seen from ***Figure 20***.

The *in situ* SRPD data during initial discharge up to 5 moles of lithium are shown in ***Figure 60***. High intensity reflections in FO-600 at 5.67° and 8.02° 2θ positions which correspond to the $Fe_3O_4$ phase show an initial shoulder, that increases with further lithiation. This behavior was also observed in CFO-800 and NFO-800 materials. Similar changes were also observed in FO-800 material for the $Fe_3O_4$ phase. However, the decrease in the intensity of the reflections with increasing lithiation is more pronounced in FO-800 material. Rietveld refinement confirms the dominant new phase as lithiated $Fe_3O_4$ starting from 0.1 lithium for FO-600 and from 0.7 lithium for FO-800. In the lithiated cubic spinel phase the atoms occupying 8a tetrahedral sites are displaced to 16c octahedral sites together with the intercalation of lithium into 16c site.

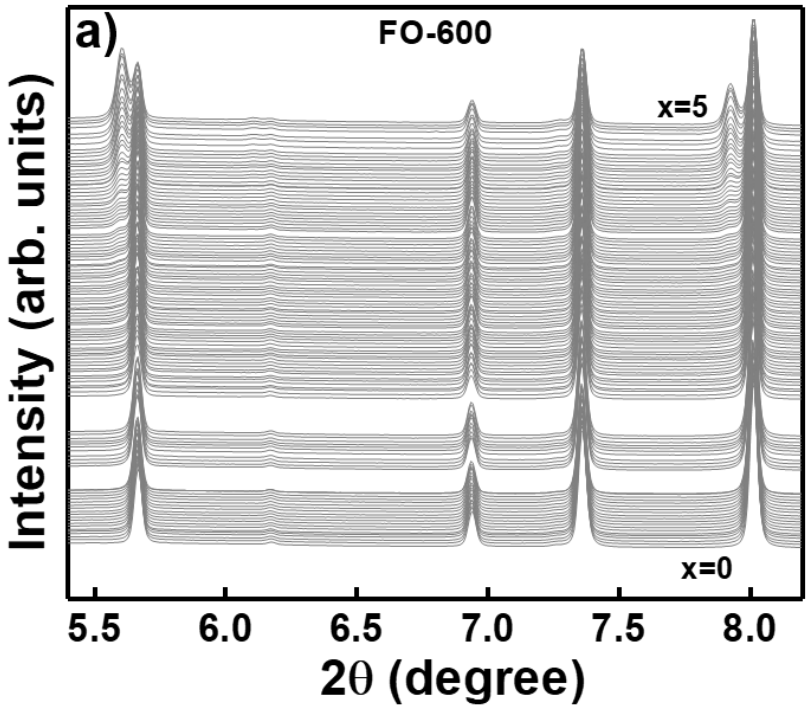

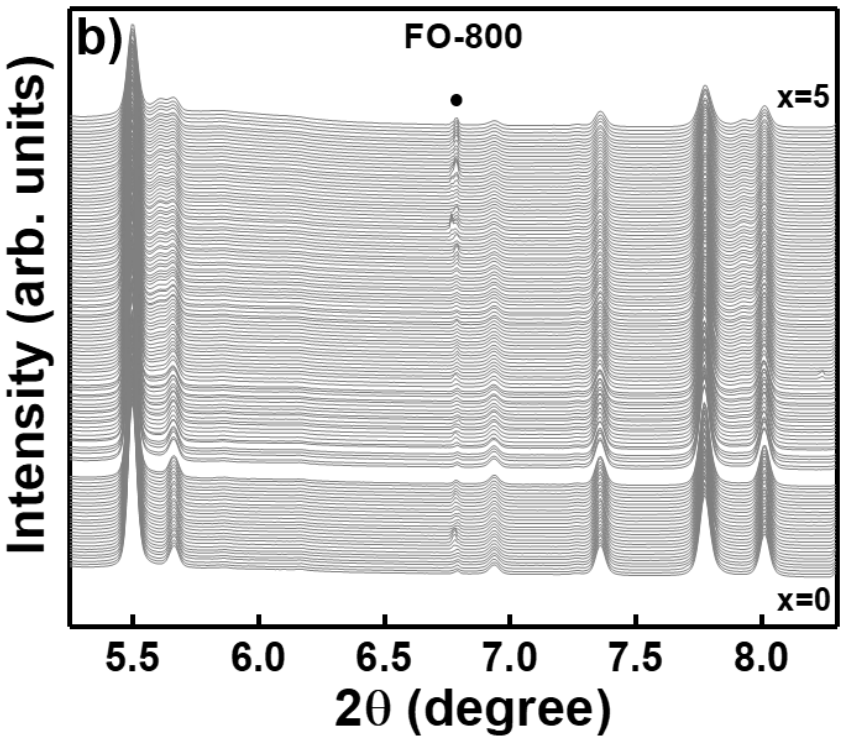


***Figure 60 –*** *Selected 2θ regions for in situ SPRD patterns of FO-600 (**Figure 62a**) and FO-800 (**Figure 62b**) measured during first discharge at a C-rate of C/40. (• lithium metal reflection. The missing XRD patterns are due to beam loss).*

***Figure 61*** shows the changes in the unit cell parameter as a function of number of moles of lithium reacted (x) for the main phase ($Fe_3O_4$) and the lithiated phase ($Li_xFe_3O_4$) for FO-600. The lattice parameter increases 0.058 % in the $Li_xFe_3O_4$ from 8.3961(1) Å to 8.4010(1) Å with lithiation of 5 moles of lithium. The lattice parameter of $Fe_3O_4$ main phase is nearly constant up to lithiation of 5 moles lithium. The sudden deviations and jumps in the data points were from a beam loss and resulting changes occurring in the beam energy and reflection intensity.

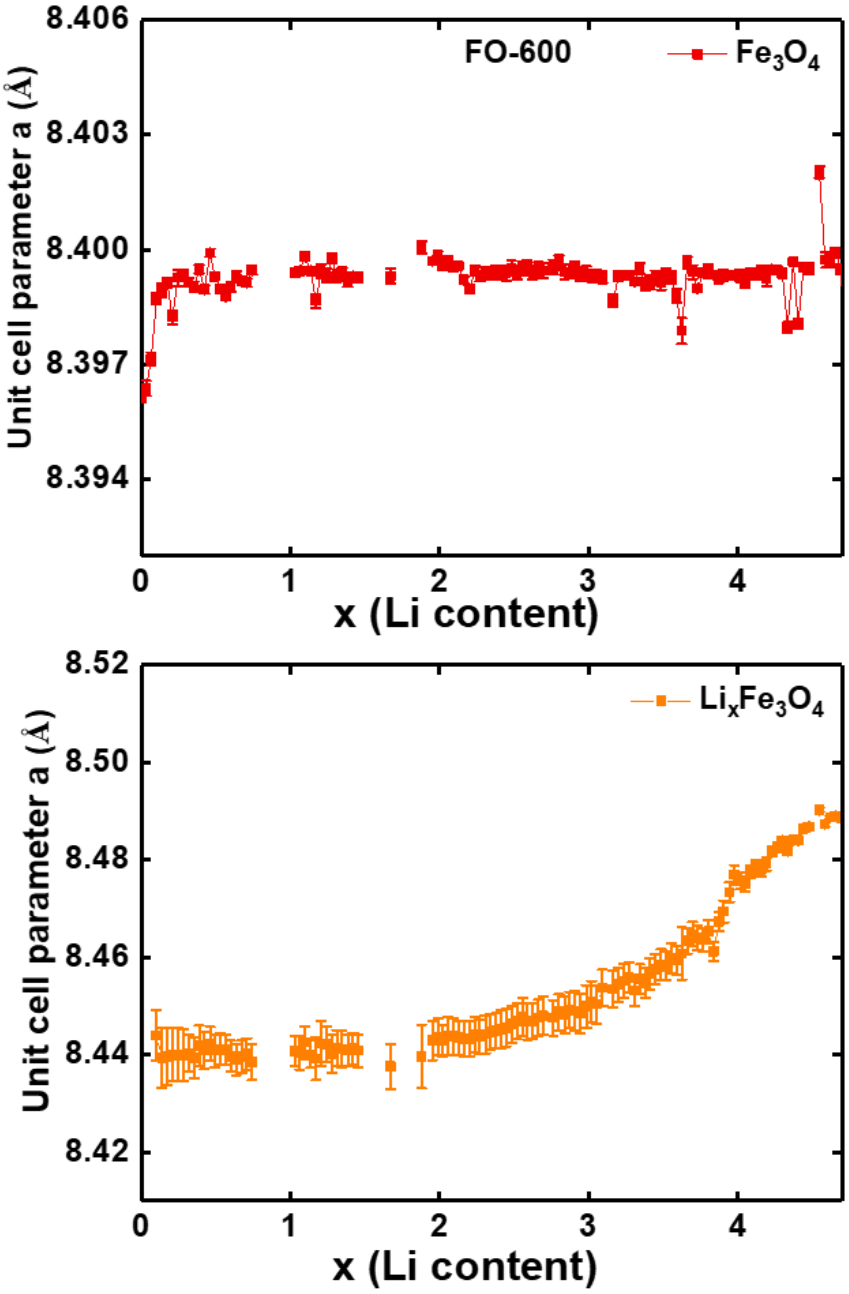


***Figure 61*** *– Changes in the unit cell parameter as a function of number of moles of lithium reacted (x) for main phase ($Fe_3O_4$) and additional new lithiated phase ($Li_xFe_3O_4$) for FO-600 discharged at C/40 (Missing points in the data set are due to beam loss).*

Rietveld refinement results based on the synchrotron diffraction data obtained during the first discharge at lithiation states of x = 0 and x = 5 moles of lithium are shown in ***Figure 62***. The corresponding phases used for Rietveld refinement are marked in the figure.

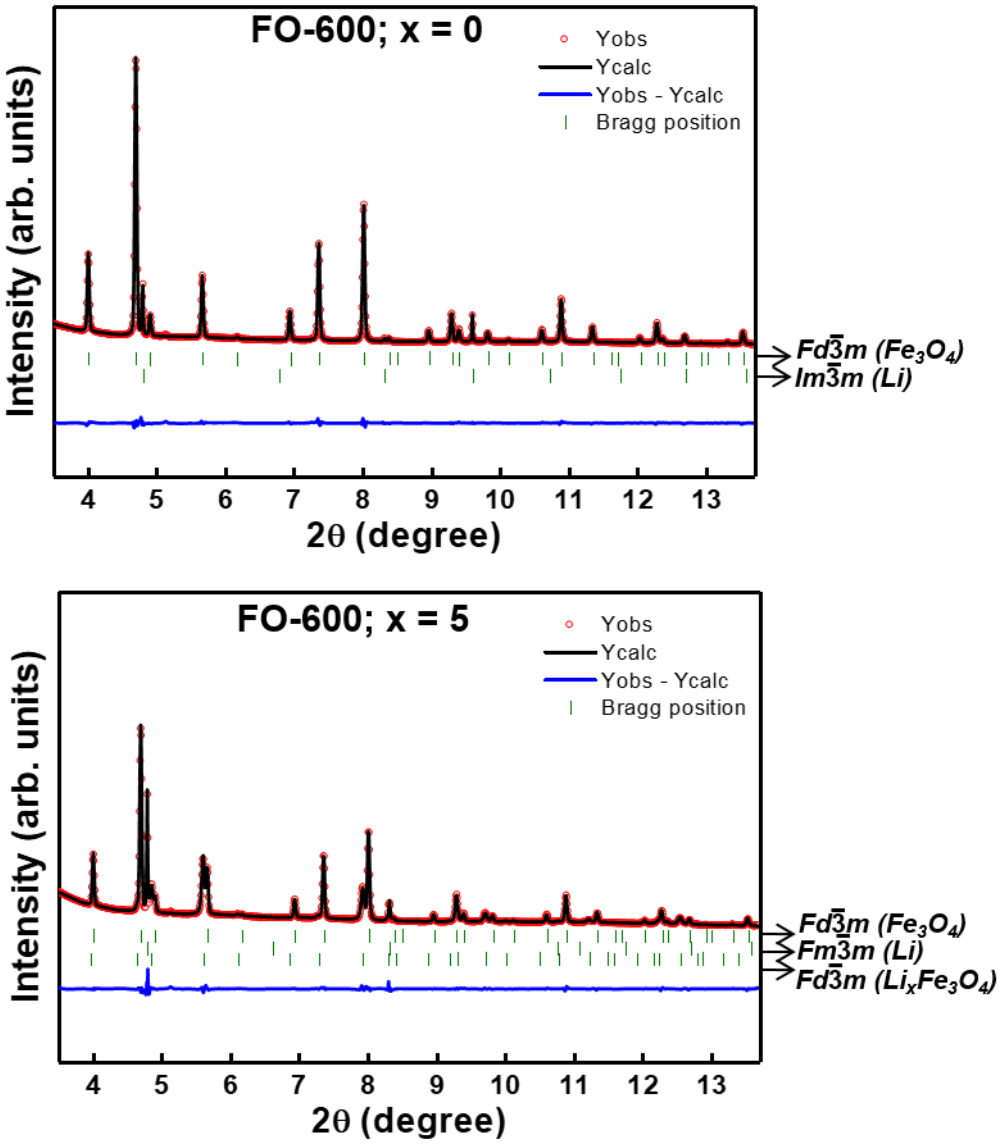


***Figure 62** – Rietveld refinement results based on the synchrotron diffraction data obtained for FO-600 obtained during the first discharging process at lithiation states of x=0 (a) and x=5(b) moles of lithium when discharged at C/40.*

The changes in the unit cell parameter as a function of number of moles of lithium (x) for various phases in FO-800 are shown in ***Figure 63***. The $Fe_3O_4$ phase undergoes lithiation with the formation of $Li_xFe_3O_4$. The lattice parameter of the FeO phase remains almost constant (4.3276(2) Å at x = 0 and 4.3274(1) Å at x = 5). The lattice parameter of the freshly formed lithiated phase $Li_xFe_3O_4$ (8.50(1) Å) increases up to 8.54(1) Å upon insertion of 1 mol Li, however, it decreases again upon insertion of 2 mol of Li and remains constant after that. One of the most interesting findings in the electrochemical mechanism of FO-800 material is

the appearance of a new metallic Fe phase (space group $Im\bar{3}m$, ICSD record: 44863) from 2 moles of lithium. Hence, formed metallic Fe was assumed to be less crystalline nano-sized particles which results in a decrease in intensity and broadening of the reflections as seen in ***Figure 60***.

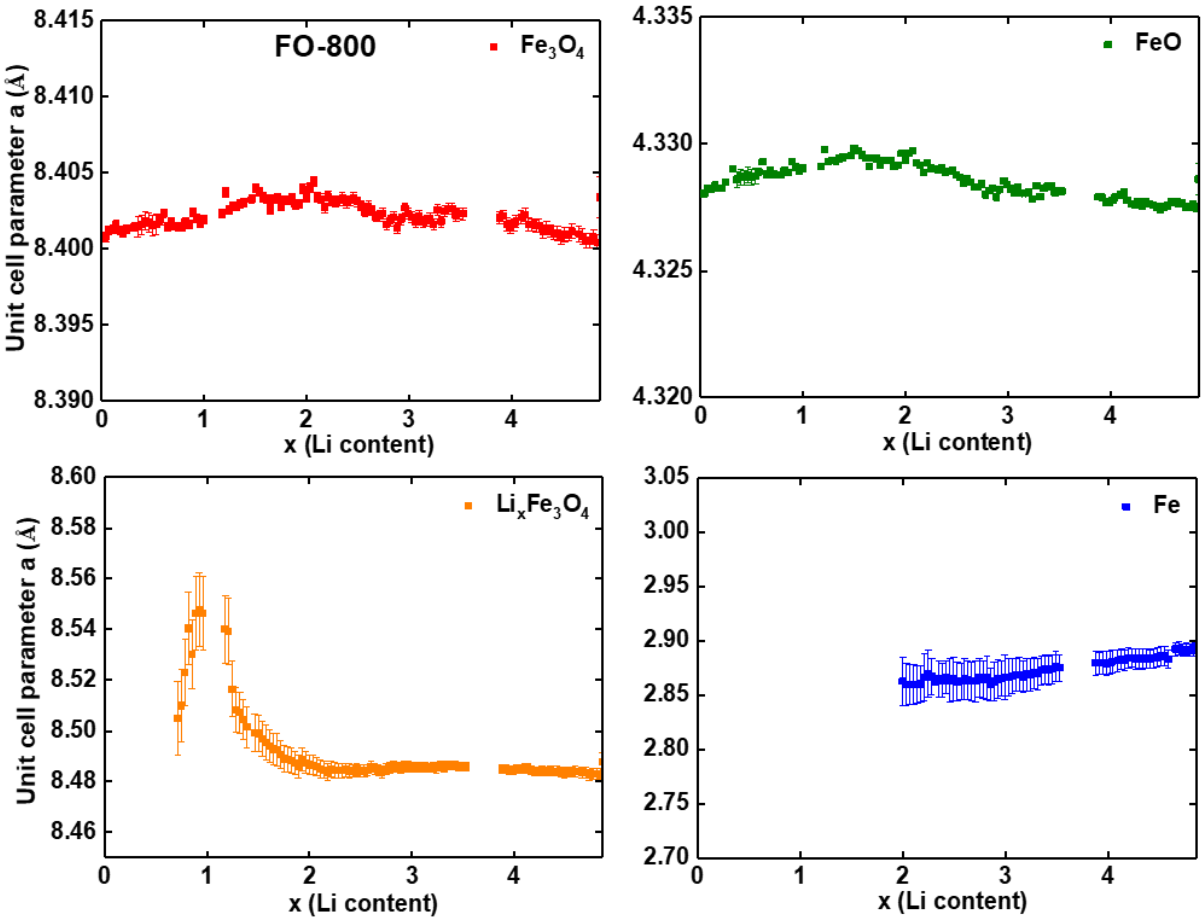


***Figure 63*** *– Changes in the unit cell parameter as a function of number of moles of lithium (x) for $Fe_3O_4$, FeO and newly formed phases, $Li_xFe_3O_4$ and Fe for FO-800 discharged at C/40*

Rietveld refinement based on the synchrotron diffraction data obtained during the first discharge process at lithiation states of x = 0 and x = 5 moles of lithium are shown in ***Figure 64***.

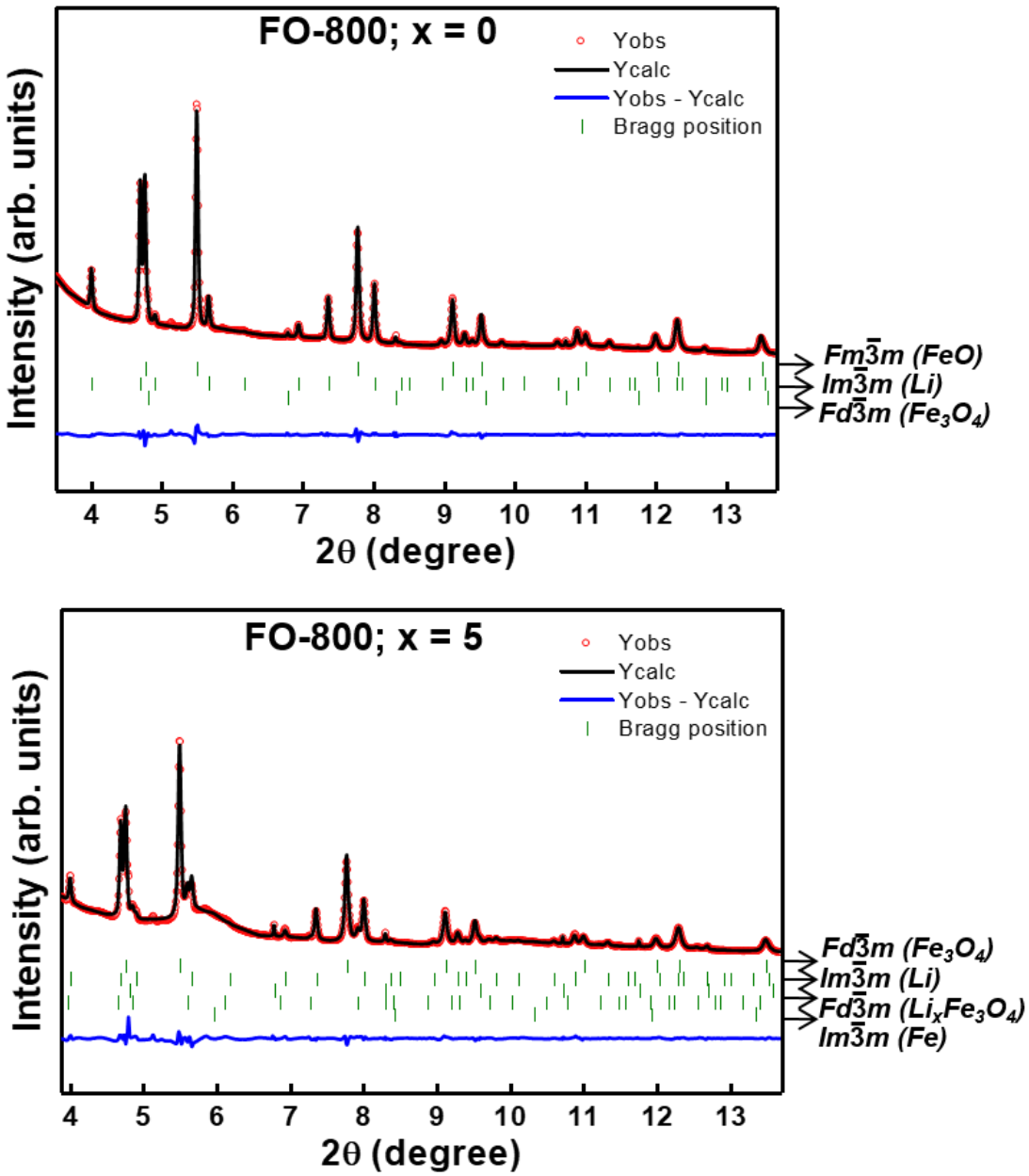


***Figure 64*** *– Rietveld refinement results based on the diffraction patterns obtained for FO-800 during the first discharging process at lithiation states of x=0 (a) and x=5(b) moles of lithium when discharged at C/40.*

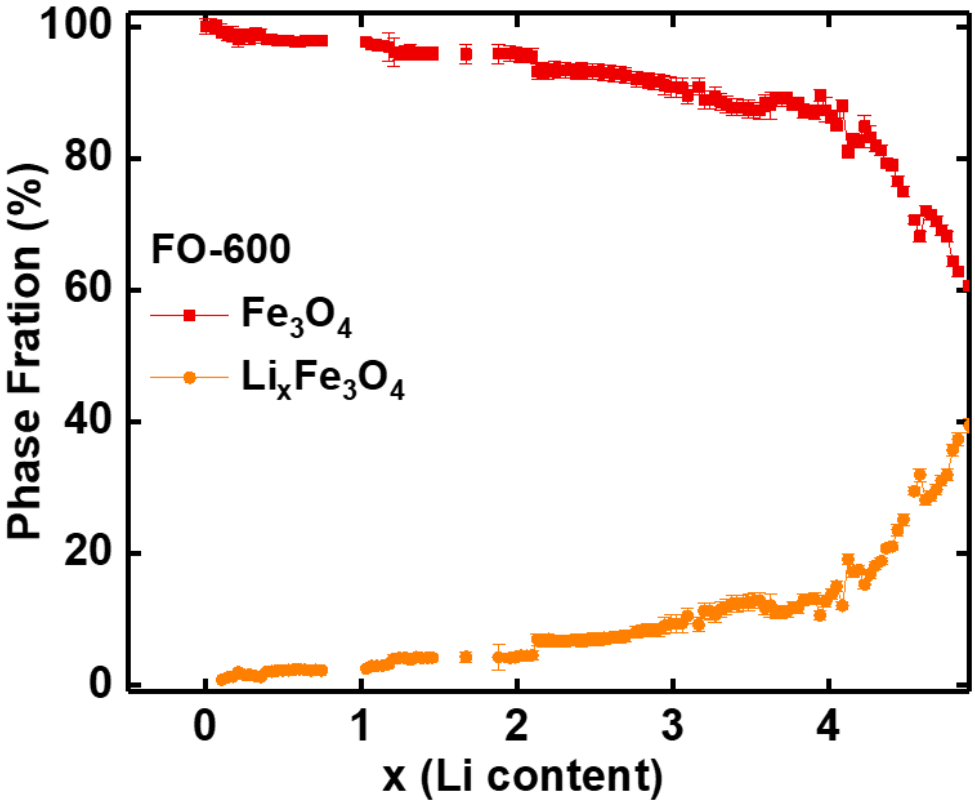


***Figure 65*** *– The phase ratios vs. Li content of crystalline phases during cycling for FO-600 discharged at C/40.*

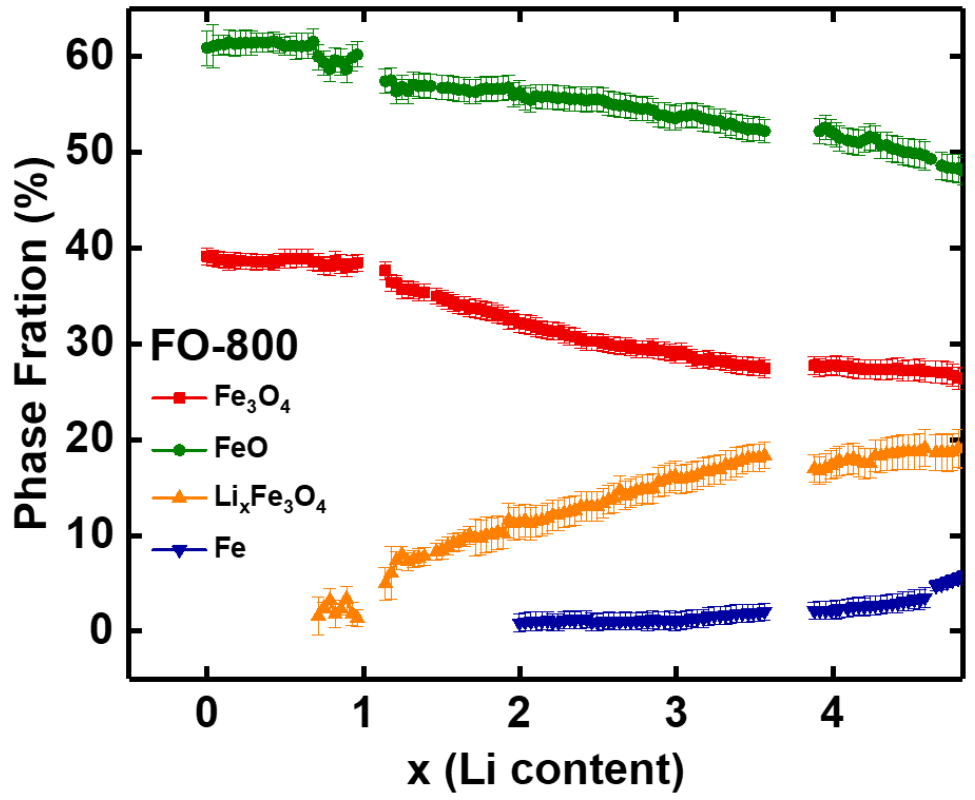

***Figure 66*** *– The phase ratios vs. Li content of crystalline phases during cycling for FO-800 discharged at C/40.*

Rietveld refinement results based on the obtained powder diffraction patterns also show the changes in the phase ratio during lithiation. ***Figure 65*** and ***Figure 66*** show the phase ratios with respect to lithium content for FO-600 and FO-800, respectively. In FO-600, the amount of the $Fe_3O_4$ main phase decreases with increasing amount of lithiated $Li_xFe_3O_4$ phase. Similar trends of these phases were observed in FO-800. Nevertheless, the electrochemical lithiation mechanism proceeds in a more complex way in FO-800. The fraction of the rock salt FeO main phase remains rather unchanged until 1 mole of lithium. However, it decreases with further lithiation, most probably due to transformation of this phase to the metallic Fe.

Deeper discharge above 5 moles of lithium might lead to a partial or even complete destruction of the lithiated $Li_xFe_3O_4$ and FeO phases. The decomposition of these phases is probably accompanied by the formation of Fe metal nanoparticles in an amorphous matrix of $Li_2O$. These severe structural transformations into amorphous state are hard to investigate with XRD and hence were further investigated by XAS.

## 3.5.2. *In Situ* X-Ray Absorption Spectroscopy

Initial delithiation is as crucial as lithiation in understanding the structural changes and electrochemical behavior of iron oxide based electrodes. However, there is only very limited literature regarding this as discussed in the beginning. Herein, *in situ* XAS measurements were carried out on FO-600 and FO-800 materials during the first cycle at a charge-discharge rate of C/10 in a voltage window 0.1-3 V to identify the phases which could not be detected by X-ray diffraction. ***Figure 67*** shows the Li content (x) versus voltage ($E_{we}$) curve for FO-600 cycled against Li. Red and black curves represent the discharge and charge, respectively.

The spike in the voltage curve of FO-600 material (x = 0.26) was due to pausing the cell cycling for a short time.

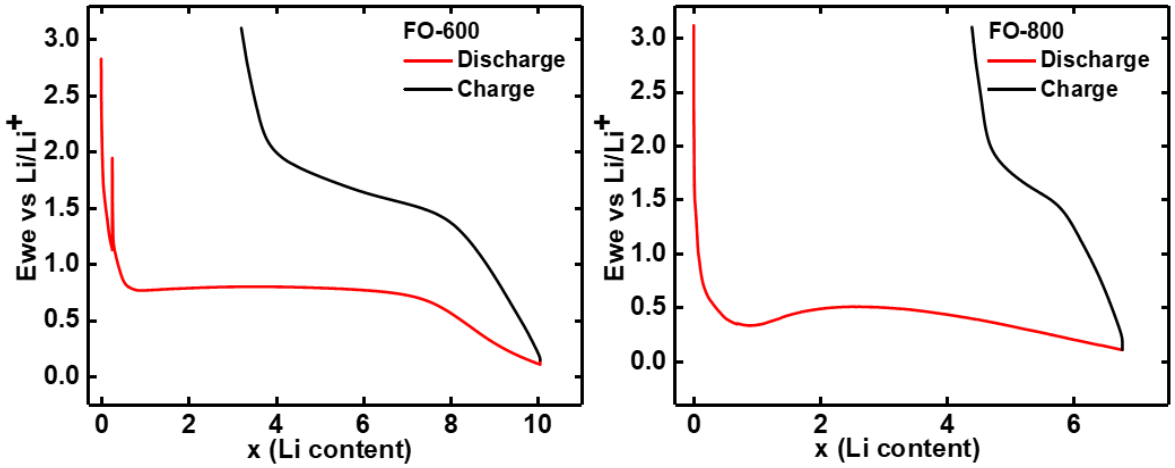


***Figure 67*** *– The x (Li content) versus voltage curve for FO-600 and FO-800 during in situ XAS measurements at a C-rate of C/10.*

The difference in the electrochemical performance of FO-600 and FO-800 is clearly visible in the voltage curve. At the same applied voltage window and C-rate, the electrochemical cells showed different behavior. The lithium uptake of FO-600 with 10 moles of lithium was much higher than that of FO-800 with 7 moles of lithium. In addition, during the consecutive charging, FO-600 delithiates more effectively than FO-800.

To obtain direct information about the oxidation states of Fe and in FO-600 and FO-800, the XANES regions of the XAS spectra at the Fe K edge were compared to the XANES regions of different reference materials such as Fe metal foil, FeO, $Fe_2O_3$ and $Fe_3O_4$ (***Figure 25***). Fe has a formal valence state of $Fe^{3+/2+}$ in FO-600 as it overlaps the edge position of the $Fe_3O_4$ reference material. Whereas, the edge position FO-800 was shifted to lower energy and tend to overlap the edge position of reference FeO spectra where Fe is in +2 oxidation state. This finding is in accordance with the XRD, since $Fe_3O_4$-800 °C is an admixture of $Fe_3O_4$ and FeO (62.02% of FeO and 37.98% $Fe_3O_4$ obtained from Rietveld analysis). The pre-edge feature of the Fe K edge in $Fe_3O_4$-600 °C where Fe occupies both tetrahedral and octahedral sites was

much more pronounced compared to $Fe_3O_4$-800 °C where the majority is FeO with octahedrally coordinated Fe.

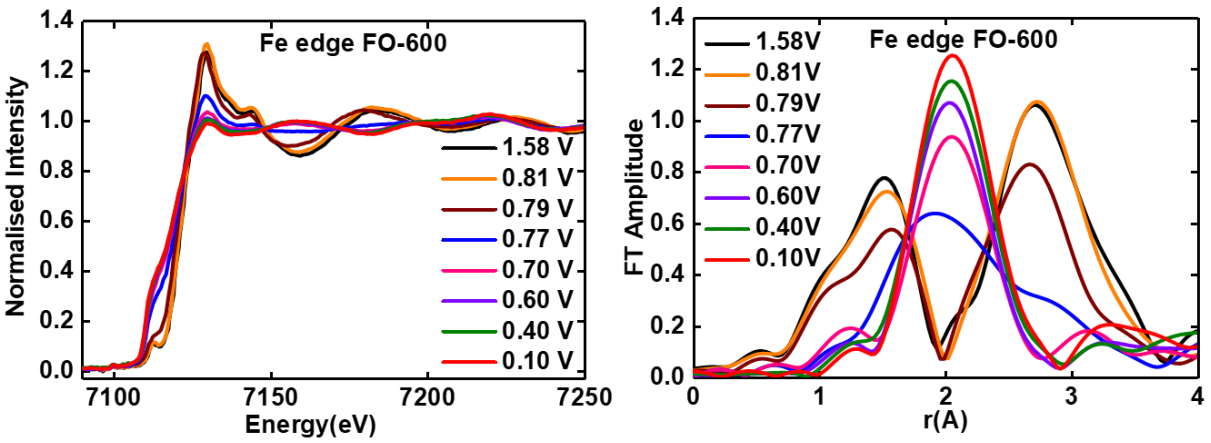


***Figure 68*** *– In situ XANES and corresponding FT region obtained for FO-600 during first discharge.*

During the initial discharge/lithiation, the edge position of the Fe K edge (7119 eV for pristine FO-600) is shifted to lower energy and changes in the XANES line shape as well as intensity were also observed (***Figure 68***). Both changes in edge position as well as line shape clearly indicate a change in oxidation state as well as in the local coordination of the absorbing atom. However, the overall XANES line shape and coordination environment is preserved until 0.79 V which corresponds to 4 moles of lithium uptake. According to Rietveld refinement results based on the *in situ* SRPD data, at this voltage, only two phases exist: the pristine $Fe_3O_4$ phase and lithiated $Li_xFe_3O_4$. As the voltage drops eventually, the edge positions shift continuously to lower energy until the end of discharge (7113 eV at the end of discharge) and the coordination environment shows serious changes. Better understanding of this phenomenon is obtained by the Fourier transformations for the corresponding Fe K edge during first discharge as shown in ***Figure 68***. The FT amplitude and normalized intensity decreases with increasing lithiation up to 0.79 V and until this point there clearly exist two shells corresponding to Fe-O and Fe-Fe bond distances at around 1.5 and 2.7 Å, respectively. After the insertion of 5 moles of lithium i.e., at 0.77 V, the Fourier transform spectrum shows

an intermediate shape between the former and latter spectra. At 0.70 V with the intake of 7 moles of lithium, structural transformation was observed at the FT Fe K edge with the formation of a prominent peak at 2 Å. This peak contributes to the first neighbors shell in metallic Fe as also seen in other $CoFe_2O_4$ and $NiFe_2O_4$ samples. The peak position is sustained and the FT amplitude increases till the end of discharge with an uptake of 10 moles of lithium.

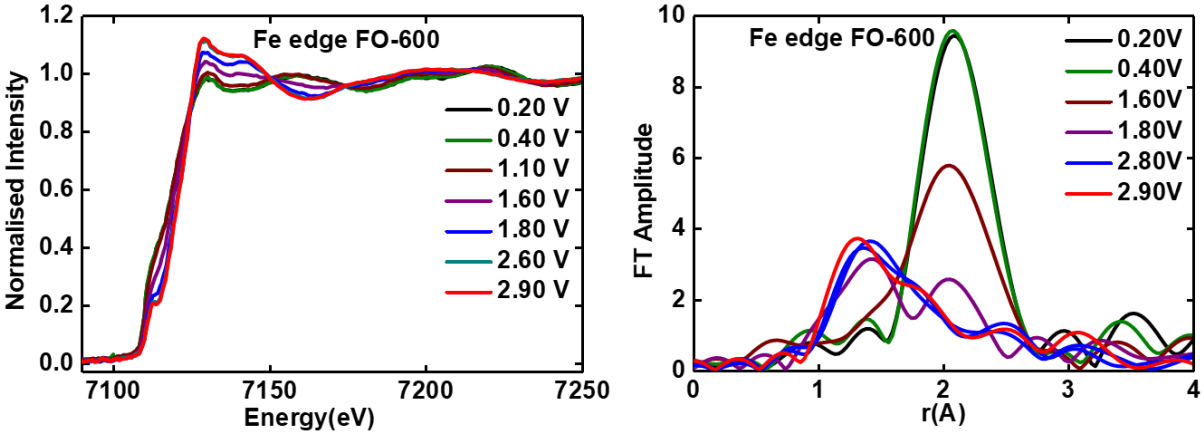


***Figure 69*** *– In situ XANES and corresponding FT region obtained for FO-600 during first charge.*

*In-situ* XANES during charge at the Fe K-edge for the FO-600 electrode until 2.90 V with corresponding Fourier transform spectra is shown in ***Figure 69***. During charging, the Fe K edge position shifts to higher energy from 7113 eV to 7118 eV along with the changes in XANES shape and intensity, which indicates the oxidation of metallic Fe. . However, one could see that the edge position does not go back to the former state but to a slightly lower energy. Therefore, the pristine oxidation state and the oxidation state of the first delithiation product might be different. The corresponding Fourier transform EXAFS data for the Fe K edge suggests that, once the material is fully delithiated at 2.9 V, the peak positions denote the formation of a FeO or $Fe_2O_3$ instead of the initial $Fe_3O_4$. The FT amplitude at 2 Å from metallic Fe decreases gradually during the delithiation and shifts to 1.3 Å. Even though the metallic peak amplitude decreases considerably, there is still a shoulder at 1.8 Å which

suggests the incomplete oxidation of metallic Fe nanoparticles even at the end of delithiation which was also observed in $CoFe_2O_4$ and $NiFe_2O_4$ samples at the end of charge.

FO-800 was also subjected to electrochemical cycling within the same voltage window and C-rate and the *in situ* XAS measurements during cycling are shown in ***Figure 70***. *In situ* XANES shows similar features as seen in FO-600.

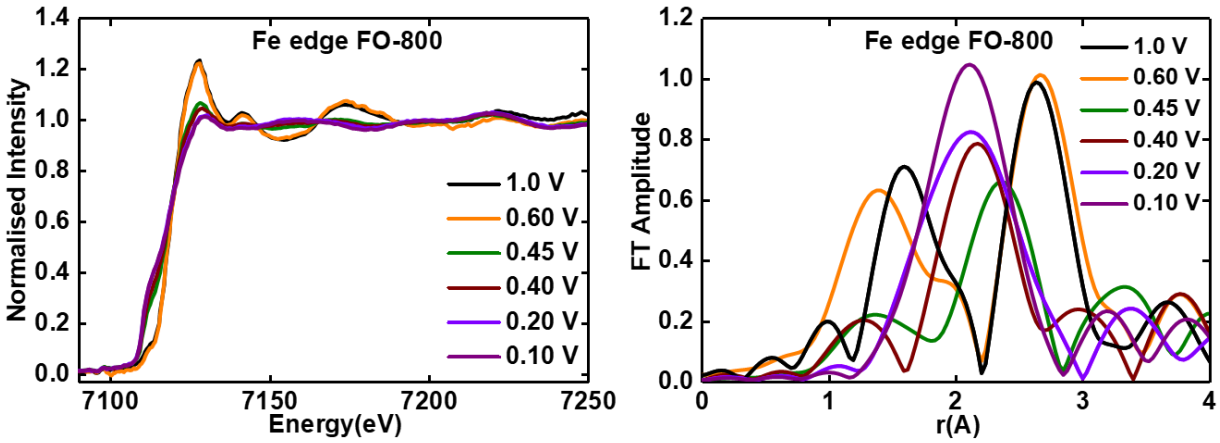


***Figure 70*** *– In situ XANES and corresponding FT region obtained for FO-800 during first discharge.*

The initial edge position at 7117 eV shifts to lower energy (7113 eV) at the end of discharge. Also, the coordination environment changes drastically from 0.45 V. In comparison to the Fourier transform of FO-600, FO-800 shows a prominent single peak at 2.1 Å which is an indication of metallic Fe, however, the formation of this peak was achieved rather slowly and does not follow the same trend as in FO-600. This suggests that the kinetics of the conversion reaction might be different in both materials.

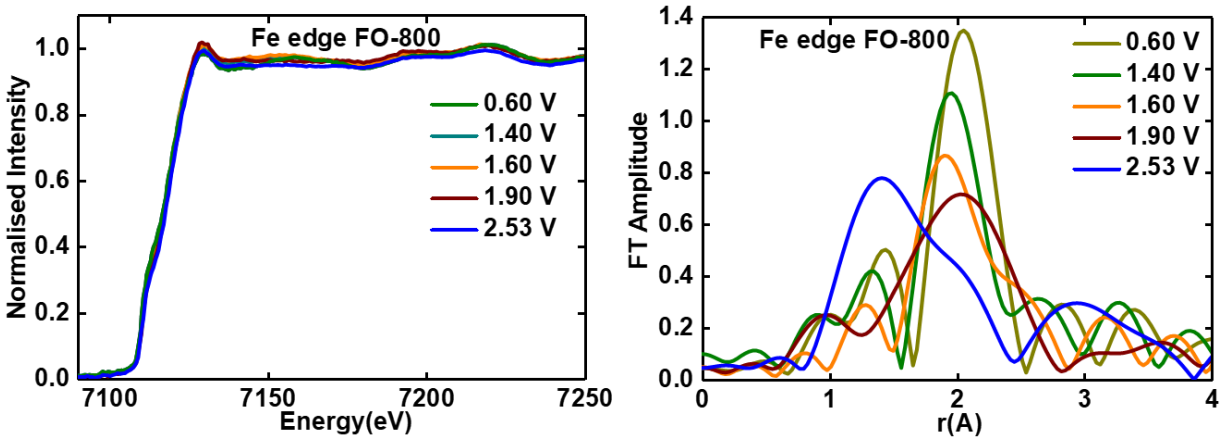


***Figure 71** – In situ XANES and corresponding FT region obtained for FO-800 during first charge.*

*In situ* XANES and Fourier transform upon delithiation of FO-800 material are shown in ***Figure 71***. Voltage profile and lithium content during the electrochemical cycling of FO-800 clearly show a difference in the electrochemical delithiation, in comparison with FO-600. FO-600 delithiates 6.86 moles of lithium while FO-800 only 2.38 moles. This difference in the delithiation profile is also visible in the XAS measurements. *In situ* XANES shows a rather slight shift of the edge position from 7113 eV to 7115 eV during delithiation and the line shape remains the same without much change. The Fourier transform of the EXAFS region also supports this finding. The metallic Fe formed at the end of discharge remains the same without oxidation until 1.90 V, represented by the peak at 2.1 Å, except for the slight shift in the peak position. However, at the end of charge/delithiation the peak shifts to the meatal oxygen position at 1.4 Å with a pronounced shoulder of metal-metal bond distance of around 2 Å.

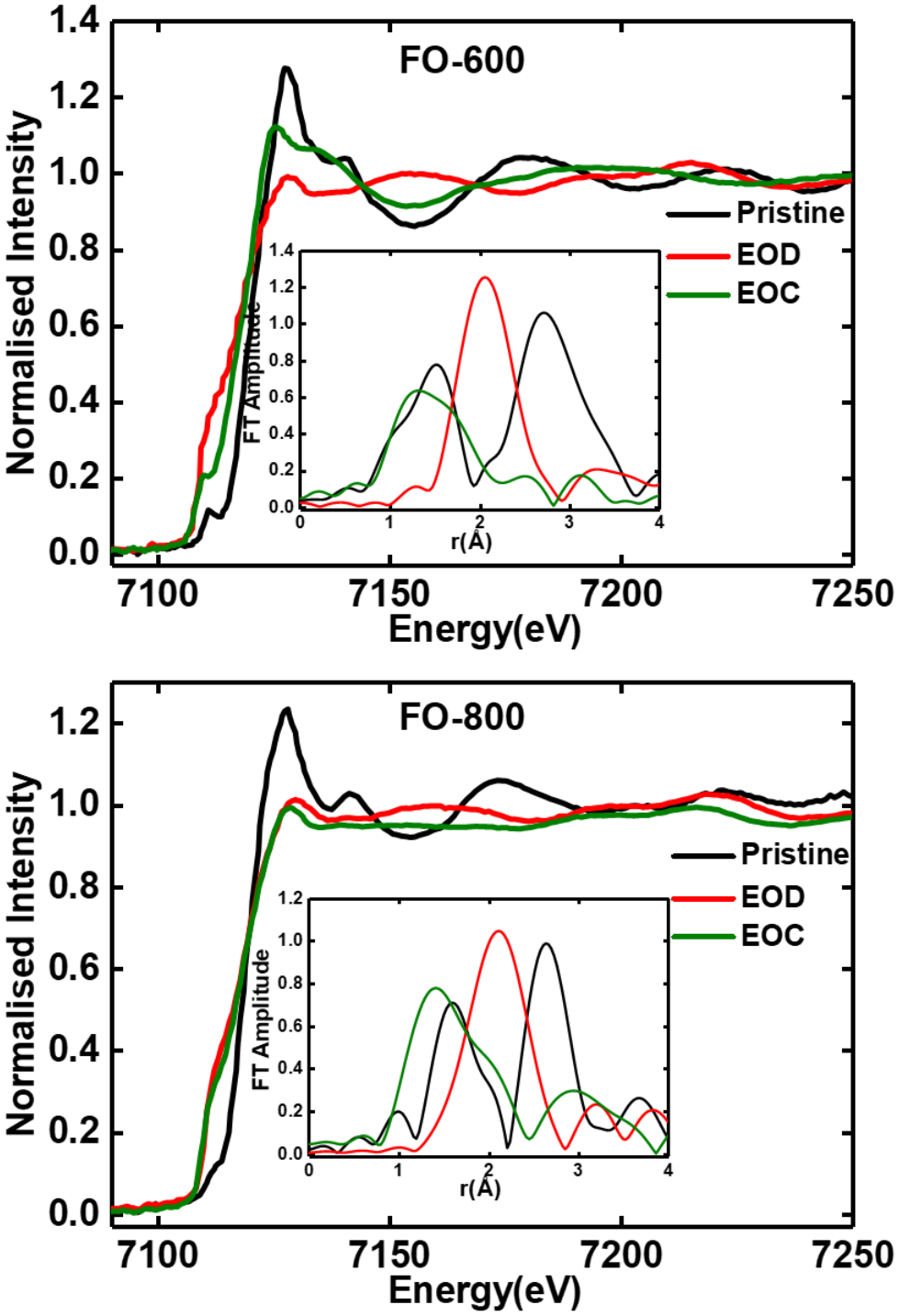


***Figure 72** – Comparison of XANES and the corresponding FT regions obtained for pristine FO-600 and FO-800, at the end of discharge and end of charge.*

For both FO-600 and FO-800 samples, a comparison plot was made; containing the XANES spectra at the pristine, end of discharge and end of charge states, to directly visualize the changes (***Figure 72***). The FT is shown in the inset. It can be seen that the XANES line shape at the Fe K edge of FO-600 for all three states are different. However, at the end of

charge the XANES pre edge feature reappears but does not overlap with that of the pristine. In FO-800 (***Figure 72***), the edge position at the end of discharge and end of charge does not change much; however, the XANES line shape/coordination environment shows slight differences. FT (inset) shows that at the end of charge, the second shell, where the metal-metal interaction appears, is reduced and appears only as a shoulder for the sample after one complete cycle compared to the pristine sample. This conclusively proves that Fe metal formed during the first discharge was re-transformed into an amorphous or cluster sized oxide phase different from the initial material. Also, the metallic Fe formed during the first discharge was not completely transformed into their corresponding oxides.

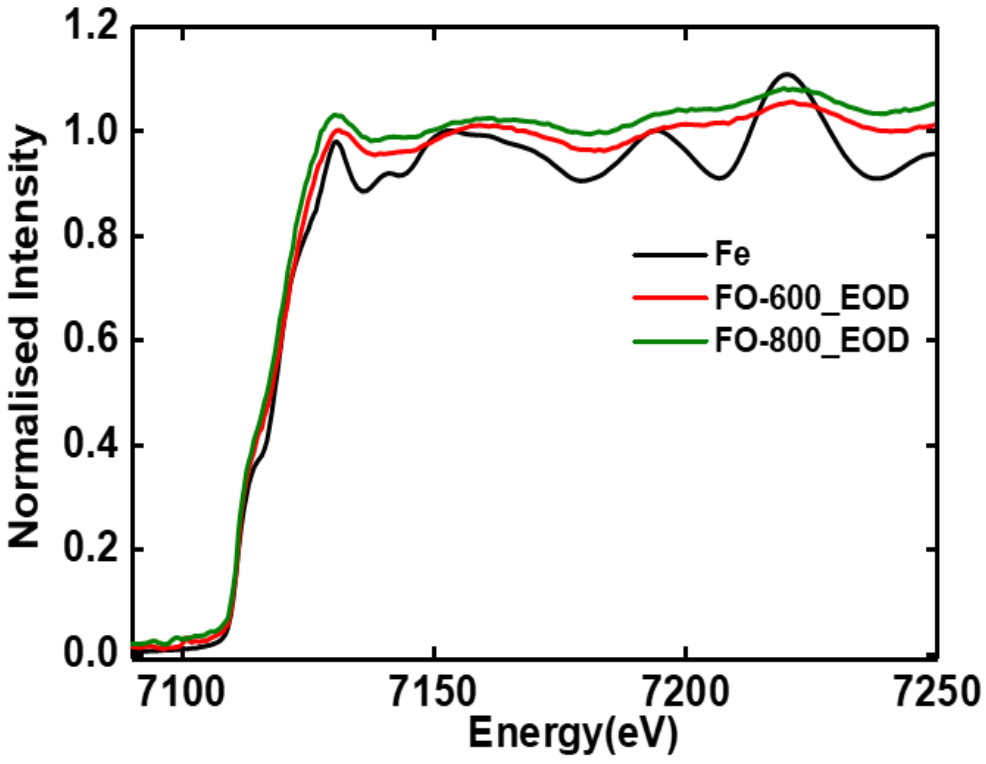


***Figure 73*** *– Fe K edge XANES region of completely lithiated/end of discharge FO-600 and FO-800 compared to metallic Fe reference material.*

Comparing the edge position of lithiated FO-600 and FO-800 with the Fe metal foil reference material (

***Figure 73***) conclusively confirms the formation of metallic Fe at the end of discharge. The bulk reference metal foil has a different coordination environment compared to the Fe nanodomains formed at the end of discharge.

FO-600 and FO-800 at the end of charge were also compared to $Fe_2O_3$ and FeO reference materials (***Figure 74***). By comparing the edge position of FO-600 with the reference materials with a pre-edge feature it tends to overlap with $Fe_2O_3$. In contrast, FO-800 has strong differences in the XANES line shapes after the 1$^{st}$ cycle. The XANES region for the samples after one complete cycle, measured at the inflection point, is closer to that of FeO. The formal valence state of the pristine material cannot be assigned to both Fe-oxides formed.

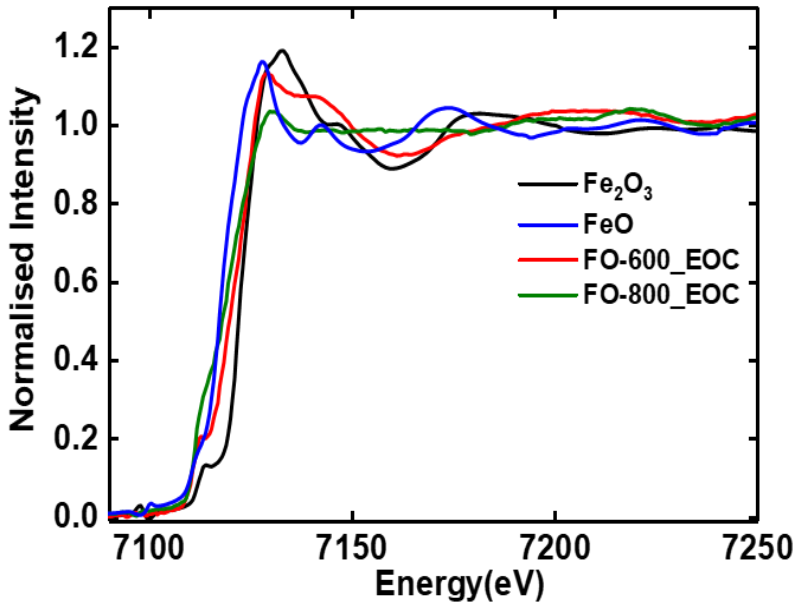


***Figure 74*** *– Fe K edge XANES region of delithiated/end of charge FO-600 and FO-800 compared $Fe_2O_3$ and FeO reference materials.*

In order to get some quantitative information about the phase fraction, LCF fitting was done on the discharged and charged samples at the Fe K edges using the Fe metal, $Fe_2O_3$ and FeO spectra as references. ***Table 14*** shows the LCF fitting results of the Fe K edge XANES spectra at the end of discharge fitted with $Fe_2O_3$, FeO and Fe metal.

*Table 14 - LCF fitting results at Fe K edge for FO-600 and FO-800 at the end of discharge and end of charge. Contribution of each reference material at various state of charge of FO-600 and FO-800 are tabulated (5% error bar).*

| Sample | Potential | Contribution from $Fe_2O_3$ | Contribution from FeO | Contribution from Fe |
|---|---|---|---|---|
| FO-600 | EOD | 0 | 0.06 | 0.94 |
| FO-800 | EOD | 0 | 0.18 | 0.82 |
| FO-600 | EOC | 0.53 | 0.37 | 0.1 |
| FO-800 | EOC | 0.07 | 0.26 | 0.67 |

From the LCF fitting, about 94% FO-600 and 82% FO-800 material was transformed to metallic Fe at the end of discharge. During the consecutive charging, most of the metallic Fe remains unreacted in FO-800 and the rest oxidized to FeO with a negligible amount of $Fe_2O_3$. However, in FO-600 at the end of charge, most of metallic Fe oxidizes to FeO (37%) and $Fe_2O_3$ (53%).

## 3.5.3. Discussion

*In situ* SRPD and *in situ* XAS has shown to be an important combination to obtain detailed understanding of the structural changes occurring in crystalline, nanocrystalline and amorphous phases in iron oxide based electrode materials for lithium ion batteries. With high surface area and electrolyte decomposition on the surface, nanoparticles do not offer long term cycling stability[68] even with good electrochemical conversion kinetics. FO-800 with a $FeO/Fe_3O_4$ mixture after the first cycle still contains unreacted metallic Fe nanoparticles. Nevertheless, the material showed better capacity retention on further cycling. The unreacted

Fe nanoclusters might provide a good conductive network in the electrode during further cycling even though the FeO formed after the first cycle offers lower capacity than $Fe_3O_4$. Therefore, the effect of particle size and annealing temperature for transition metal oxides shows that there is an optimum size for improved capacity which is very likely to be material dependent[66,67].

Using *in situ* SRPD technique, an intermediate lithiated phase ($Li_xFe_3O_4$) was observed during the initial lithiation along with $Fe_3O_4$ as observed previously by Chen *et al.*,[87] which increases with increasing lithiation for both FO-600 and FO-800 materials. For FO-800, the conversion of FeO to metallic Fe starts at an onset of 2 moles of lithium uptake. However, the intermediate lithiated phase was indexed during Rietveld refinement to the cubic spinel phase ($Fd\bar{3}m$ space group), the atoms occupying 8a tetrahedral sites are displaced to 16c octahedral sites together with the intercalation of lithium into 16c[106] and not with a rock salt phase as reported in most of the previous works. Further studies using *in situ* XAS confirm the existence of multiple phases between intercalation and conversion reactions during the first discharge which is in good agreement with the findings by He *et al.*,[109].

Furthermore, the *in situ* XAS data suggest that, the starting material and the metallic Fe nanodomains formed when the material is fully lithiated impact the homogeneity of the iron oxide phase formed during the subsequent delithiation. Lithiation of FO-600 resulting in rather complete conversion into Fe domains favors the formation of both FeO and $Fe_2O_3$ with a higher ratio of $Fe_2O_3$ upon delithiation. However, a complete conversion into iron oxide was not seen in FO-800 and the delithiation kinetics was more favored for the formation of FeO than $Fe_2O_3$.

## 3.6. Electrochemical Reaction mechanism and Alloying in $ZnFe_2O_4$

By replacing one iron atom in $Fe_3O_4$ by zinc the theoretical capacity is enhanced as lithium ions can form a lithium zinc alloy. Ever since the first report of the electrochemical lithiation of $ZnFe_2O_4$ in 2004[140], this compound is considered an interesting candidate for high-capacity anode materials (1072 mAh $g^{-1}$). Recently, much attention has been paid to the modification of $ZnFe_2O_4$ through various approaches ranging from morphological modifications[34,141,142], simple carbon coating[84,143] to doping heteroatoms in the graphene supported hollow $ZnFe_2O_4$ nanosphere[144]; double graphene layer encapsulation[145] and MOF derived ZnO/ $ZnFe_2O_4$ nanostructures[146,147]. These approaches were proposed to improve the reversibility and cycling life, however, the fundamental study of the mechanism of electrochemical conversion in this material is not fully clear and is still under investigation.

In contrast to other transition metal ferrite spinels, $ZnFe_2O_4$ transforms to metallic Fe and Zn which accounts for a total theoretical lithium uptake of 9 moles at the end of discharge: 8 moles for the conversion reaction and one additional electron equivalent for the LiZn alloying at the end of deep discharge starting from around 0.4 V. This has been investigated by Nuli, Guo and Sharma *et al.,*[140–142] by XPS and TEM techniques. Whereas the most recent study by Zhang *et al.,*[148] using combined *in situ* XRD and *ex situ* XAS and PDF characterization found no evidence for the LiZn alloy even at the reduction limit of 0.2 V. How so ever, the reliability of an *ex situ* XAS measurement is questionable considering the fact that zinc can easily get oxidized in particular when present around Fe. Also *in situ* TEM studies by Su *et al.,*[149] only accounts for the formation of metallic Fe and Zn nanograins at the end of discharge.

The overall lithiation process can be summarized as:

$$ZnFe_2O_4 + 8Li^+ + 8\,e^- \rightarrow Zn°/ZnLi + 2Fe° + 4Li_2O \qquad (7)$$

$$Zn + Li^+ + e^- \rightarrow ZnLi \qquad (8)$$

The previous literature reports account for lithium intercalation from the very beginning, were the initial lithiation is assumed to take place through two distinct mechanisms: (i) Either by widely observed lithium intercalation into the main structure, where the lithium is inserted into the main phase up to x = 2 in $Li_xZnFe_2O_4$ which further transforms into a rocksalt structure[84,141,148] followed by the formation of metallic Zn and Fe, (ii) By a two phase mechanism[142], where lithium intercalation results in the formation of a new lithiated phase along with the main phase. Furthermore, a detailed investigation on the phase transformation during the initial intercalation with structural refinement results is still not reported. Nuli *et al.,* even proposed a direct conversion of the main phase into binary oxides[140] (ZnO and FeO).

All the previous studies agree with the formation of Zn and Fe metal at the end of the first lithiation and the consecutive reversible formation of ZnO in the following cycles. Even though Fe shows a comparatively faster oxidation kinetics during charging, discrepancies regarding the binary iron oxides remain unclear. Sharma *et al.,* confirmed the formation FeO after 50 cycles by TEM[142] whereas Guo *et al.,* considered FeO as an intermediate product and suggested that the metallic Fe end product of the first discharge is firstly oxidized to FeO which is further oxidized to $Fe_2O_3$ as the charge voltage increases[141] which is in agreement with the recent *in situ* TEM studies by Su *et al.,*[149].

The first delithiation/reversible reactions:

$$ZnLi/Zn + Li_2O \rightleftarrows ZnO + 2Li+ + 2e^- \qquad (9)$$

$$2Fe + 3Li_2O \rightleftarrows Fe_2O_3/FeO + 6Li+ + 6e^- \qquad (10)$$

Within the current research we focus on answering two important questions:

(i) Whether or not Zn forms LiZn alloy during lithiation in the electrochemical cell.

(ii) Whether the following delithiation of this electrode results in the conversion of metallic Fe formed at the end of discharge to binary FeO or $Fe_2O_3$.

Hence, to account for a more precise explanation for the overall electrochemical mechanism, *in situ* SRPD and *in situ* X-ray absorption spectroscopy were carried out on inverse co-precipitation synthesized ZFO-800 electrodes.

### 3.6.1. *In Situ* Synchrotron Radiation Powder Diffraction

The current study was carried out on ZFO-800 material. ZFO-800 consists of 98.90% inverse spinel $ZnFe_2O_4$ (Space group: $Fd\bar{3}m$) and 1.10% ZnO (Space group: P $6_3$ m c) (***Figure 21***) as observed from the Rietveld analysis with an average particle size 82±35 nm (***Figure 22***). ***Figure 75a*** shows the voltage versus lithium content curves during galvanostatic cycling. After the fast drop of voltage from 3.1 V to 0.75 V a small plateau appears with the insertion of 0.2 $Li^+$. This plateau implies a possible reaction at this voltage. After that a long plateau at 0.78 V until approximately 5.5 $Li^+$ was observed after which metallic Zn and Fe were expected to be formed. The slope region below 0.65 V is attributed to the formation of an SEI film and below 0.4 V the Li Zn alloying reaction is expected to occur with a polymeric gel-type layer formed on LiZn alloy and Fe° nanoparticles upon deep discharge[142,150].

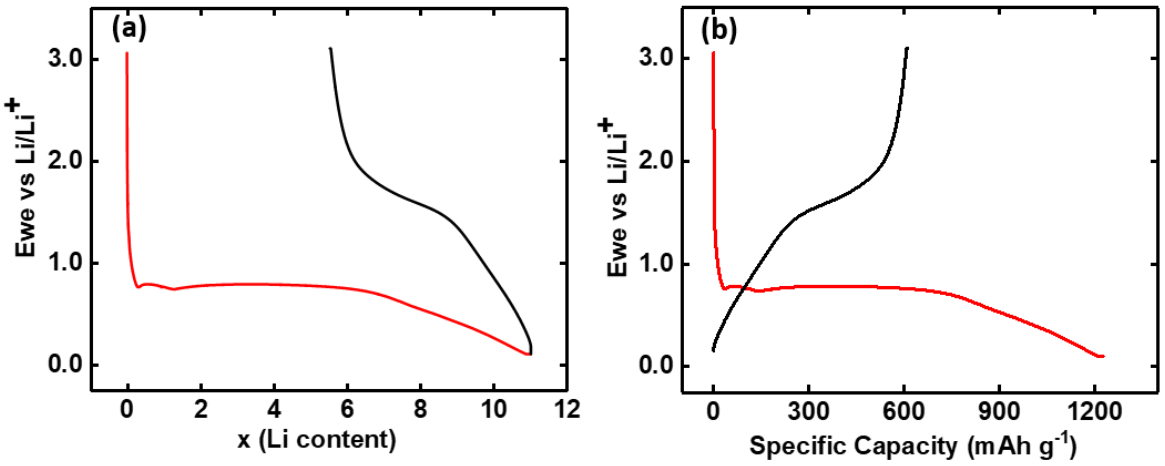


***Figure 75*** *– Discharge (Red line)-charge (Black line) profiles with respect to lithium content (a) and specific capacity (b) of ZFO-800 electrodes.*

The capacity obtained accounts for a total of 11 moles of $Li^+$ (Theoretically 9 moles of $Li^+$) per mole of $ZnFe_2O_4$. The initial discharge capacity of ZFO-800 is 1223 mAh $g^{-1}$ at 11.04 moles $Li^+$. The experimentally observed capacity was significantly higher than the theoretical capacity mainly due to SEI formation and additional $Li^+$ accommodation through reaction with grain boundary phases in nanostructures. In the consecutive charging process, the electrode exhibits a specific charge capacity of 606 mAh $g^{-1}$ with an incomplete extraction of 5.5 moles of $Li^+$ (***Figure 75***).

Herein, the structural evolution and phase identification of ZF0-800 electrode during initial discharge upto 7 $Li^+$ is examined using *in situ* SRPD with Rietveld analysis of the obtained data. ***Figure 76*** displays the structural evolution during first discharge up to 7 moles of $Li^+$ for ZFO-800 material for selected 2θ regions with a discharge rate of C/10 in the voltage range 3.1.-0.1 V. The reflections marked with asterisk (*) are from the lithium counter electrode.

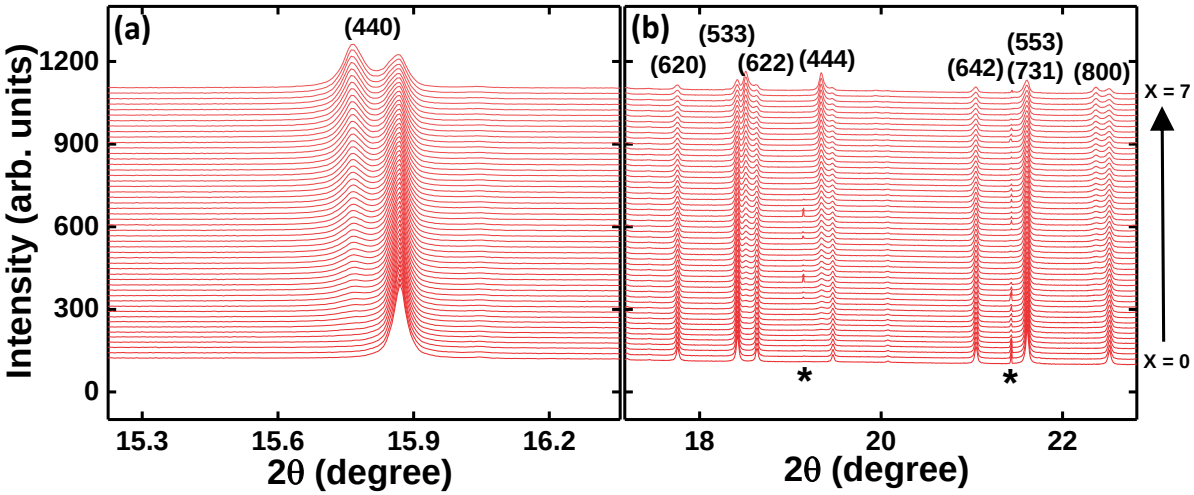


***Figure 76*** *– Selected 2θ ((a)15.2-16.4 2θ and (b) 17.1-22.8 2θ)regions of in situ SPRD patterns of ZFO-800 measured at the MSPD powder diffraction beamline at ALBA during initial discharge up to 7 $Li^+$.*

The evolution of the reflections in ***Figure 76*** during the first discharge is characteristic for a two-phase mechanism as previously observed in FO-600, FO-800, CFO-800 and NFO-800. Therefore, in spite of the difference in the transition metal partial substitution in $Fe_3O_4$ and difference in applied c-rate, all the material showed similar electrochemical lithiation mechanism during initial discharge. ***Figure 77*** shows the Rietveld refinement results for the XRD patterns observed at different lithiation states of 0.145 and 6.942 moles of lithium.

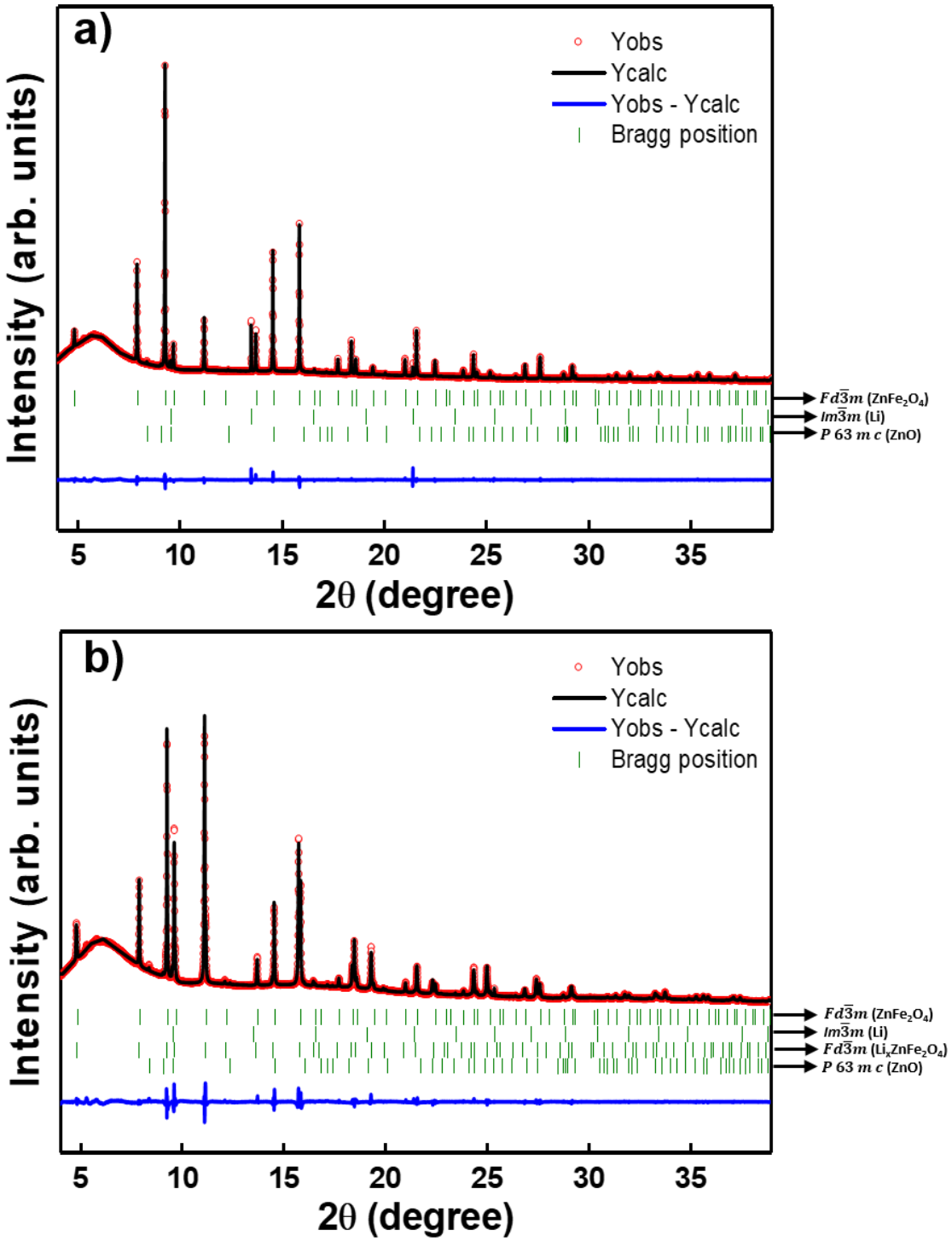


***Figure 77** – Synchrotron diffraction patterns of ZFO-800 observed during the first discharging process at lithiation states of x=0.145 and x=6.942 moles $Li^+$.*

The ZFO-800 material consists of 98.90% $ZnFe_2O_4$ (Space group: $Fd\bar{3}m$) and 1.10% ZnO (Space group: $P\,6_3\,m\,c$) as seen from the Rietveld refinement of the pristine material and up to 0.3 lithium there is no change in the already existing phases except for the lattice

parameter expansion of 0.04 % from 8.445355(9) Å to 8.44872(1) Å. Above the critical concentration of 0.3 lithium a two phase mechanism with the formation of a new phase with the same space group ($Fd\bar{3}m$) as the initial main phase is observed. This newly formed lithiated phase exhibits similar crystal structure with empty 8a sites as previously observed in other materials.

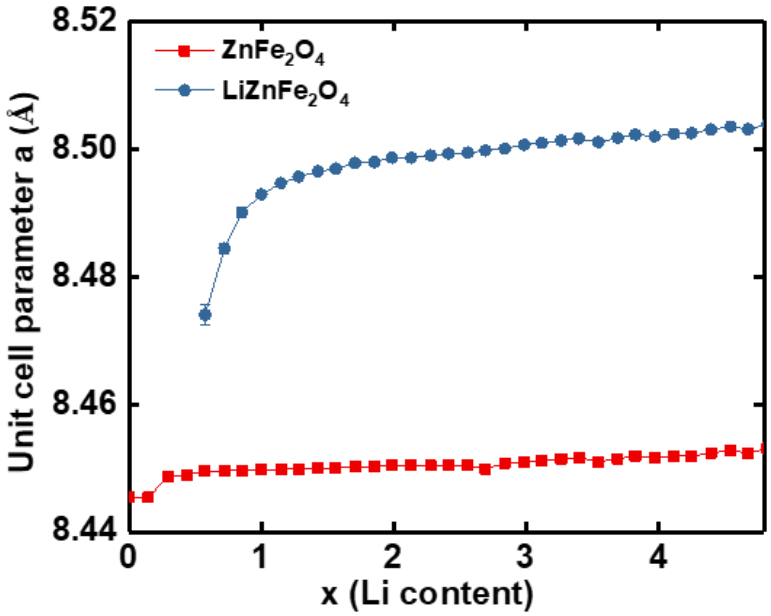


***Figure 78** – Change in the unit cell parameter as a function of number of moles of Li (x) inserted in the structure for ZFO-800.*

The difference in lattice parameter for both phases comprises 0.34 % from 8.445355(9) Å for the main phase to 8.47401(2) Å for the freshly formed lithiated phase. ***Figure 78*** shows the changes in the unit cell parameters of the already existing $ZnFe_2O_4$ phase and the freshly formed $Li_xZnFe_2O_4$ phase during initial discharge.

As the lithiation proceeds further the reflection intensities of the main phase decrease together with the decrease in phase ratio. The phase ratio of the lithiated phase increases as observed from ***Figure 79*** during the voltage plateau observed at 0.8 V. Deeper discharge with the voltage drop leads to the crystal structure destruction of the lithiated phase with the formation of Zn and Fe metal nanoparticles in an amorphous matrix of $Li_2O$.

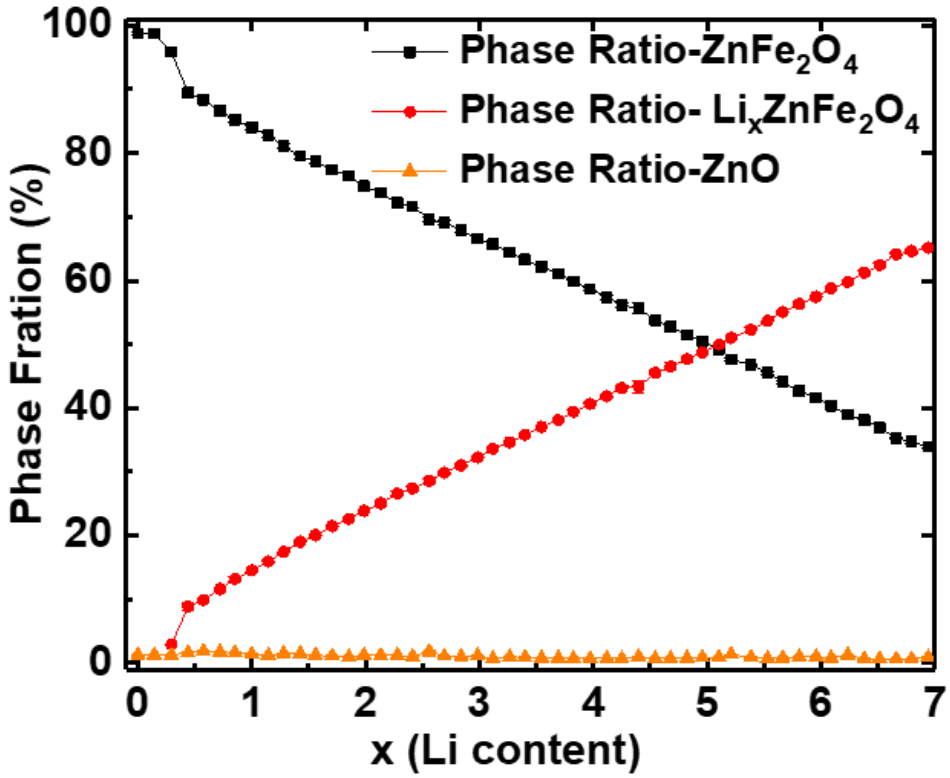


***Figure 79** – The phase ratios vs. Li content of crystalline phases during cycling for ZFO-800.*

However there is no evidence for LiZn alloy formation or metallic Zn using diffraction studies.

***Table 15 - Rietveld refinement results for $ZnFe_2O_4$ and $Li_XZnFe_2O_4$ at various lithiation states. Lattice parameter expansion, micro-strain analysis and crystallite size are given.***

| Lithium Content (X) | Lattice Parameter and Lattice Parameter Expansion | | | | Crystallite Size (nm) | | Maximum Strain | |
|---|---|---|---|---|---|---|---|---|
| | $ZnFe_2O_4$ | Expansion | $Li_XZnFe_2O_4$ | Expansion | $ZnFe_2O_4$ | $Li_XZnFe_2O_4$ | $ZnFe_2O_4$ | $Li_XZnFe_2O_4$ |
| **Initial** | 8.445355(9) | | 8.47401(2) | **0.34** | 115 | 19 | 2.31 | 35.69 |
| 1.56 | 8.449955(8) | 0.054 | 8.4968(1) | 0.27 | 171 | 40 | 5.61 | 28.66 |
| 2.56 | 8.45788(2) | 0.15 | 8.5068(1) | 0.39 | 191 | 48 | 7.16 | 20.29 |
| 3.55 | 8.45100(3) | 0.067 | 8.50106(6) | 0.32 | 195 | 61 | 7.97 | 19.01 |
| 4.55 | 8.45275(3) | 0.088 | 8.50347(5) | 0.35 | 208 | 67 | 9.39 | 15.99 |

| | | | | | | | | |
|---|---|---|---|---|---|---|---|---|
| 5.53 | 8.4595(1) | 0.17 | 8.5107(1) | 0.43 | 237 | 72 | 11.20 | 13.66 |
| 6.52 | 8.46038(9) | 0.18 | 8.51208(9) | 0.45 | 266 | 81 | 13.15 | 11.93 |
| 7.09 | 8.4600(1) | 0.17 | 8.5105(1) | 0.43 | 257 | 89 | 13.47 | 11.38 |

The lattice parameter expansion, crystallite size and micro-strain analysis obtained by Rietveld refinement of ZFO-800 at various discharge points during *in situ* SRPD are shown in ***able 15***. The maximum strain is given in the Fullprof microstructural output file as $\frac{\triangle d}{d}$x$10^{-4}$. The lattice parameter expansion for the freshly formed lithiated phase is 0.34% which further increases to 0.43% by intercalation of 7 moles of lithium. However, there is only a 0.17% increase in the lattice parameter of the main phase during the whole process. Also the lattice strain of the initial phase of $ZnFe_2O_4$ increases with increasing lithiation or decreasing phase ratio and consecutively the freshly formed lithiated phase has higher strain compared to the same phase with the insertion of 7 moles of lithium. The crystallite size of the lithiated phase is much smaller compared to the initial phase which confirms the formation of a nanocrystalline lithiated phase during initial discharge. The metallic Zn and Fe, formed at the end of discharge and not detected by the synchrotron diffraction, are expected to be even smaller in the range of 2-5 nm.

## 3.6.2. *In Situ* X-Ray Absorption Spectroscopy

The *in situ* XAS measurements were carried out on ZFO-800 material during the first cycle at a charge-discharge rate of C/10 in a voltage window 0.1-3 V to identify the phases which could not be detected by X-ray diffraction. However, it has to be emphasised that the quantification of phase fractions well below 5% is extremly difficult by XAS. Also this study aims at observing whether or not LiZn alloy is formed at the end of deep discharge. ***Figure***

***80*** shows the Li content (x) versus voltage ($E_{we}$) curve for ZFO-800 cycled against Li. Red and black curves represent the discharge and charge curves, respectively.

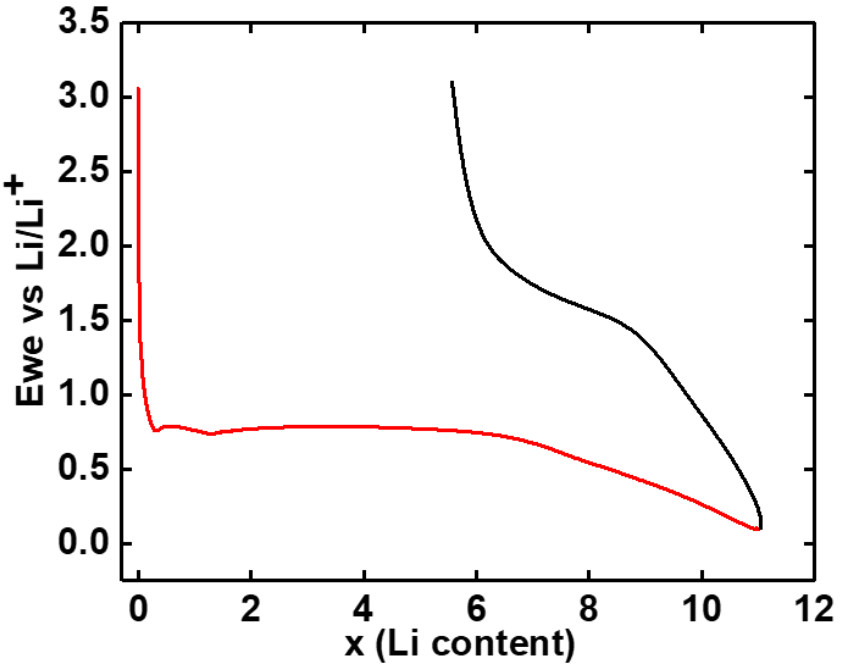


***Figure 80*** *– The x (Li content) versus voltage curve for ZFO-800 for in situ XAS measurements.*

To obtain direct information about the oxidation states of Fe and Zn in ZFO-800, the X-ray absorption near edge structure (XANES) regions of the XAS spectra at Fe and Zn K edges were compared with the XANES regions obtained from XAS spectra of different reference materials.. ***Figure 27a*** and ***b*** show the Fe and Zn K edge XANES regions for pristine ZFO-800 compared to reference materials. The overlapping of edge positions of pristine ZFO-800 with $Fe_2O_3$ and ZnO reference materials was observed. Therefore, Fe exists as $Fe^{3+}$ and Zn as $Zn^{2+}$ in ZFO-800. Rietveld refinement of the diffraction data of pristine ZFO-800 (***Figure 21***) states the existence of 98.90% $ZnFe_2O_4$ (Space group: $Fd\bar{3}m$) and 1.10% ZnO (Space group: P $6_3$ m c).

A pre-edge feature as in in 3d transition metal oxides can also be observed at the Fe K edge of pristine ZFO-800 material at 7110 eV, whereas no pre-edge peak can be observed at the Zn K-edge because of the fully occupied 3d orbitals of Zn. Similar behavior of the pre-

edge was observed in a recent publication where local structural changes of nano-crystalline $ZnFe_2O_4$ during lithiation and de-lithiation are studied by *ex-situ* XAS[151].

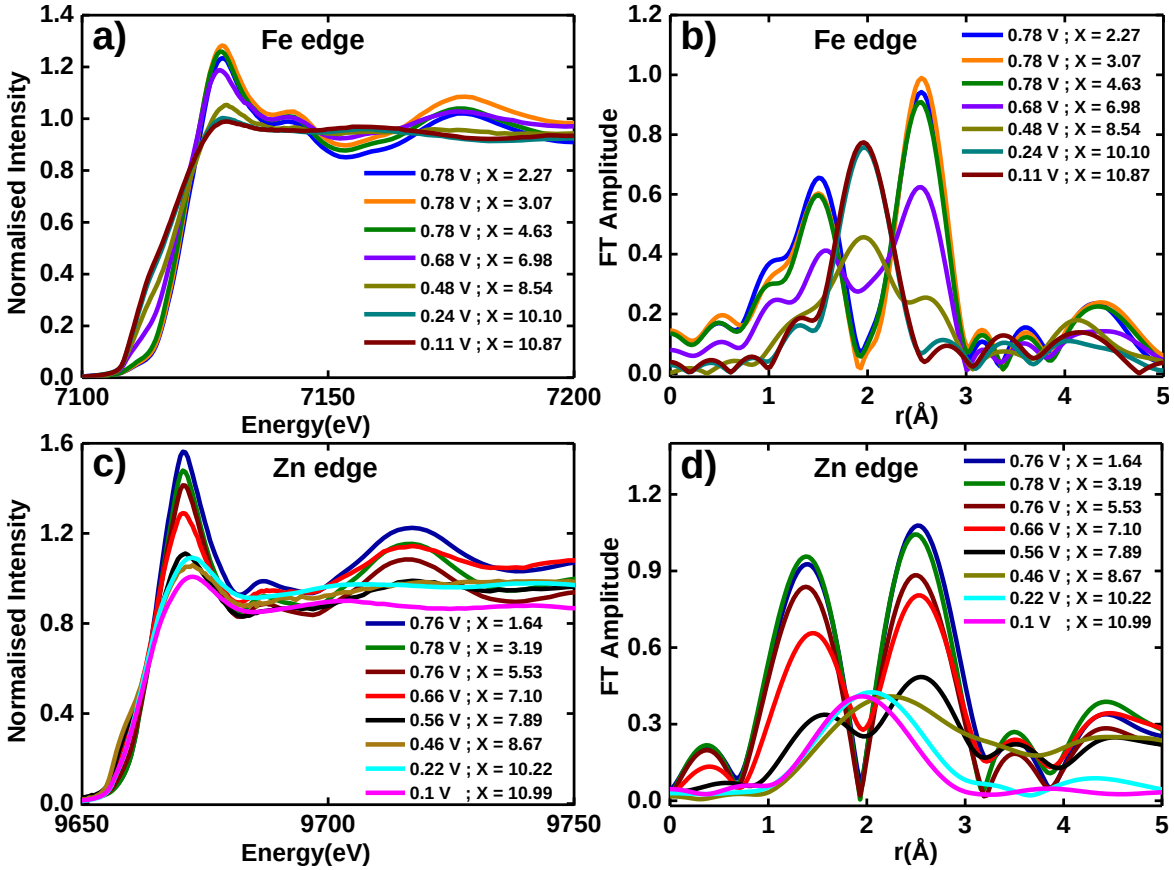


***Figure 81*** *– Normalized in-situ XANES region for the Fe (a) and Zn (c) K-edge of ZFO-800 during first discharge/lithiation until 0.1 V with corresponding Fourier transform spectra obtained for Fe (b) and Zn (d) K-edge.*

During the initial discharge/lithiation, the edge position of both, Fe and Zn K edge, is shifted to lower energy i.e. from 7118 to 7112 eV for Fe K edge and 9660 to 9658 eV for Zn K edge. Furthermore, considerable change in the XANES line shape as well as intensity is also observed (***Figure 81(a)*** and ***(c)***). Both changes in edge position as well as line shape clearly indicate a change in oxidation state as well as a rearrangement in the local coordination of the absorbing atom. By careful analysis it can be seen that up to insertion of approximately 7 Li, along with the edge shift, the intensity of the white line as well as the amplitude of the oscillation is decreased. However, the overall XANES line shape is still preserved during the insertion of 7 lithium. Apparently, at this state two phases coexist: the pristine phase and

lithiated/intercalated ZFO. The Fourier transformations for the corresponding Fe and Zn K edge during first discharge are shown in ***Figure 81(b)*** and ***(d),*** respectively. The FT amplitude and normalized intensity decreases with increasing lithiation. After the insertion of 6 moles of lithium there is a drastic rearrangement and structural transformation at both Fe and Zn K edges. The FT of both Fe and Zn K edge of the parent material is characterized by two dominant peaks approximately at 1.5 Å and 2.5 Å, the former arises from the backscattering of the nearest neighbor shell of oxygen anions in the first coordination shell and the latter peak is due to the second nearest neighbor scattering. It is to be mentioned that the scattering from the tetrahedral as well as octahedral sites cannot be resolved within the second shell due to the low resolution of the data. The low resolution (especially for Zn edge) is partly attributed to low data quality arising from the high absorption of the Cu foil on which the active material is coated. Furthermore, Cu K edge overlap with Zn K edge and the tailing EXAFS region of Cu K edge can distort the Zn K edge.

Reduction of $Fe^{3+}$ to Fe° is achieved before the reduction of $Zn^{2+}$ to Zn°. The shape of the FT amplitude begins to change drastically with the insertion of 6 moles of lithium at the Fe K edge, whereas this occurs with the insertion of 7 moles of lithium at the Zinc K edge. Once the cell is discharged to 0.4 V which corresponds to more than 8 moles of lithium, a prominent peak around 1.96 Å appears which is visible until the end of discharge for Fe K edge spectra. This peak contributes to the first neighbors shell in metallic Fe and was also seen in other compounds. However, the Fe-O contribution doesn't disappear completely, a shoulder still exists at 1.3 Å which corresponds to the existence of some amount of FeO even after the complete discharge.

***Figure 82*** and ***Table 16*** shows the LCF fitting results of the Fe K edge XANES spectra at the end of discharge fitted with $Fe_2O_3$, FeO and Fe metal.

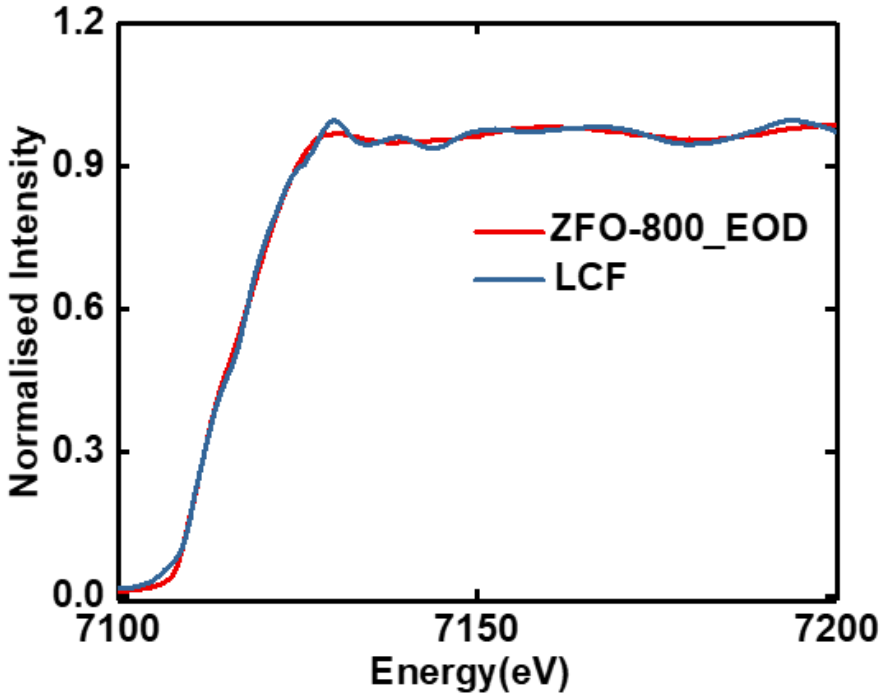


***Figure 82** – LCF fitting with $Fe_2O_3$, FeO and Fe metal as references for Fe K edge XANES region at the end of discharge.*

***Table 16 - LCF fitting results at Fe K edge for ZFO-800 at end of discharge. Contribution of each reference material at different potentials are tabulated (5% error bar).***

| Sample | Potential | Contribution from $Fe_2O_3$ | Contribution from FeO | Contribution from Fe |
|---|---|---|---|---|
| ZFO-800 | 0.11 V | 0.1 | 0.3 | 0.6 |

Therefore, there is a negligible amount of $Fe_2O_3$ whereas Fe metal together with FeO contributes significantly to the spectra. Compared to the Fe K edge FT, the Zn K edge FT is dominated by a single broad peak around 2.2 Å with the intake of 8.67 moles of lithium. This peak shifts further to lower values, 2.05 Å and 1.95 Å with the intake of 10.22 and 10.99 moles of lithium respectively. For the better understanding of the changes observed at the end of discharge, EXAFS analysis at both Fe and Zn was done by fitting theoretical FEFF paths

with experimental paths in r-space. The EXAFS fit results of the completely discharged ZFO-800 electrode at the Fe and Zn K-edge is shown in

***Figure 83*** The fit parameters are listed in ***Table 17***. Amplitude reduction factors were obtained from the EXAFS fitting of the Fe and Zn metal foil spectra and are fixed during the fitting.

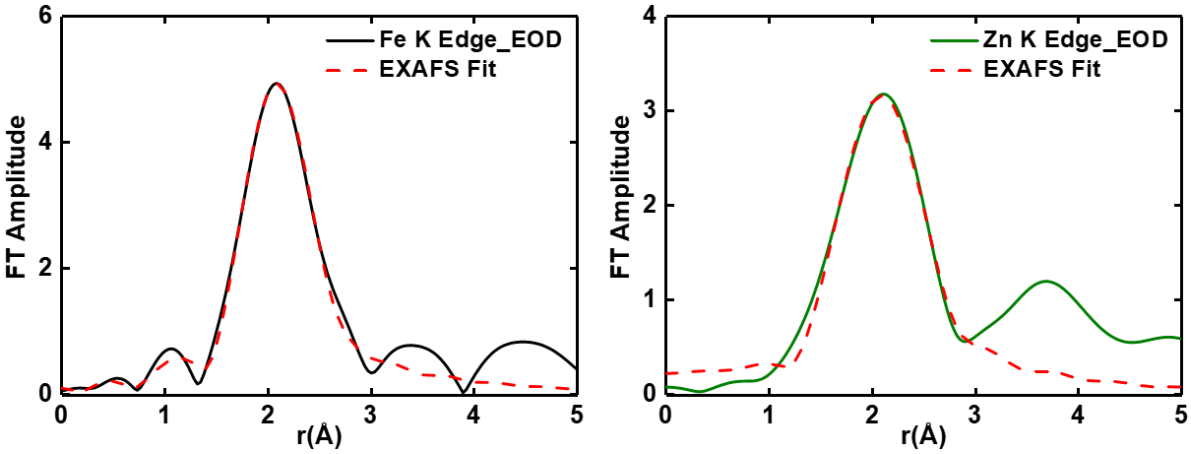


***Figure 83*** *– Comparison of EXAFS fits of Fe and Zn K-edge of ZFO-800 electrode discharged to 0.01 V and pure iron and zinc metal foil.*

A direct explanation about LiZn alloying is difficult due to insufficient resolution in r-space. However, the EXAFS fitting shows a Zn-Zn bond distance distortion or considerable deviation from the expected Zn-Zn bond distance from the bulk (2.66 Å) as shown in ***Table 17***, which could be an indication of alloying. The EXAFS fit result for the Zn K edge at the end of discharge as seen from

***Figure 83*** shows a change in the shoulder at shorter distances. This suggests that the metallic Zn is further converted to $Zn^{-}$ state which is LiZn alloy formation. This behavior was previously observed in an *in-situ* XAFS study of the capacity fading mechanisms in ZnO[152].

| ***Table 17 - EXAFS fitting results at the end of discharge.*** | | | |
|---|---|---|---|
| **Edge** | **Coordination Number (N)** | **Interatomic distance (r Å)** | **Debye Waller factor ($Å^2$)** |

| | | | |
|---|---|---|---|
| Fe | (Fe-Fe ) 2.4 | (Fe-Fe) 2.41(2) | (Fe-Fe) 0.005(2) |
| Zn | (Zn-Zn) 4.3 | (Zn-Zn) 2.44(1) | (Zn-Zn) 0.013(1) |

The EXAFS fit for the Fe K edge with pure Fe metal foil gives a good fit as expected. EXAFS analysis of the pure metal foils yields a higher coordination number whereas at the end of discharge of the ZFO-800 electrode, the coordination numbers of metal–metal shells were considerably lower. This confirms the formation of nano-metallic domains or clusters.

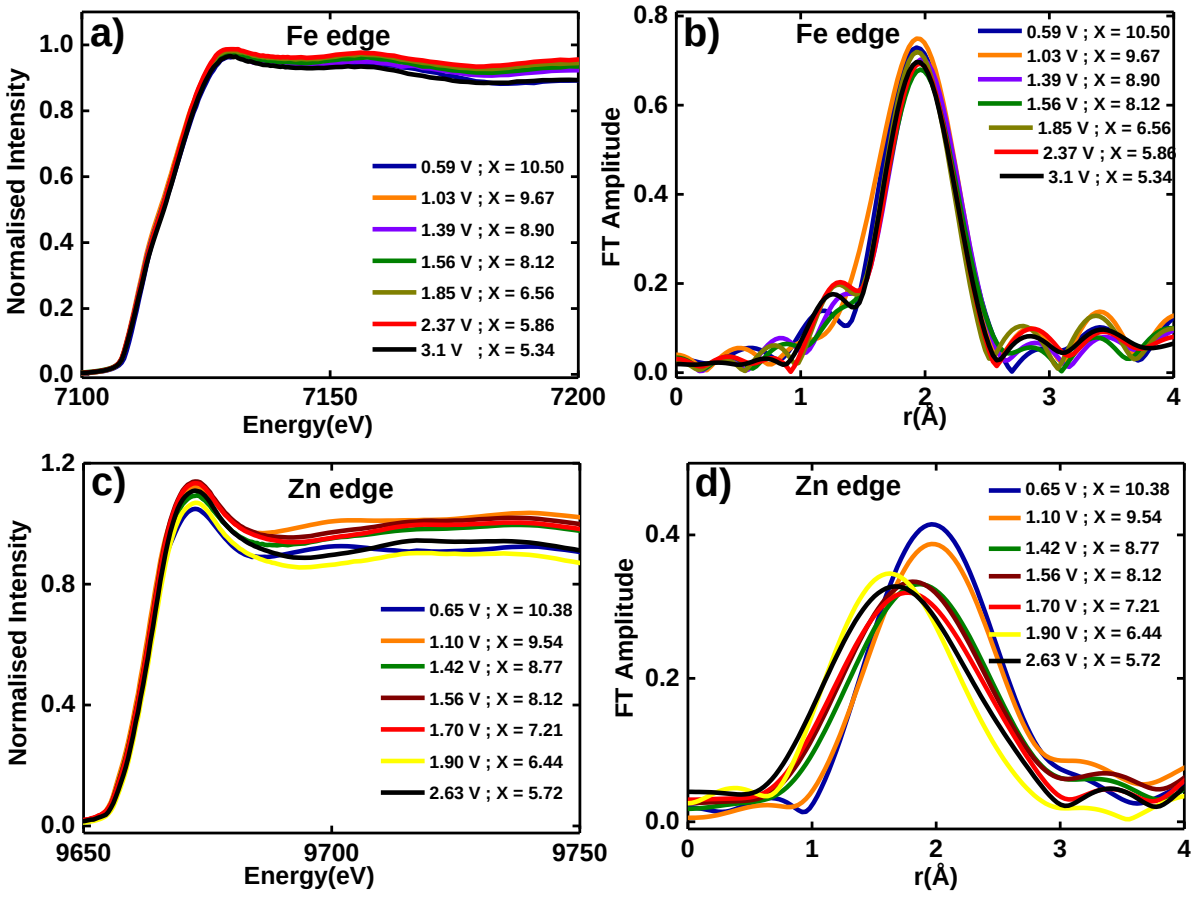


***Figure 84** – Normalized in-situ XANES region for the Fe (a) and Zn (c) K-edge of ZFO-800 during first charge/de-lithiation until 3.1 V with corresponding Fourier transform spectra obtained for Fe (b) and Zn (d) K-edge.*

*In-situ* XANES during the corresponding charge for the Fe and Zn K-edge of ZFO-800 until 3.1 V with the corresponding Fourier transform spectra is shown in ***Figure 84***. No significant changes like XANES peak shape or peak intensity were observed especially for

the Fe K edge. However, the edge position for both Zn and Fe K edge was slightly shifted to higher energy indicating an oxidation of the metallic phase. However, the corresponding Fourier transform EXAFS data for Zn shows more pronounced changes as the Zn/Li alloy peak was further shifted to lower bond distances indicating an oxidation of Zn. From the EXAFS study, it is clear that the Zinc is preferentially oxidized compared to the Fe and large fraction of Fe exists in the metallic form.

### 3.6.3. Discussion

The long and short range structural changes in ZFO-800 electrodes during lithiation-delithiation are studied by *in-situ* SRPD and *in-situ* XAS. In-situ diffraction studies account for a two phase mechanism of the initial lithiation. The main phase of $ZnFe_2O_4$ and additional phase $Li_xZnFe_2O_4$ coexist from the very beginning with the insertion of 0.3 moles of lithium. Both main phase and lithiated phase crystallize in $Fd\bar{3}m$ space group, however, in the lithiated phase the atoms occupying 8a tetrahedral sites are displaced to 16c octahedral sites together with the intercalation of lithium into 16c site. With increasing lithiation the main phase decreases with an increase in the lithiated phase.

Whereas no metallic Zn, Fe or Li-Zn alloys were observed in the diffraction experiment, the Fourier transform of the *in-situ* XANES region for Fe and Zn K edge reveals the formation of metallic nanoparticles along with the formation of LiZn alloy. The reduction in the FT amplitude and normalized intensity confirms that the formation products are amorphous nanoparticles. However, these phases are not completely transformed into corresponding $FeO/Fe_2O_3$ and ZnO upon delithiation. Especially a large fraction of metallic Fe is still found at the end of charge. One major reason for this could be the inaccessibility of Zn and Fe metallic nanoparticles formed at the end of discharge for the corresponding oxidation during

charging. Even then, for the same material, the possibility of improvement in the reversibility of the redox reaction between lithium and transition metal oxides in the 2$^{nd}$ cycle and also the following cycles as observed by Zhou et.al,[151] cannot be completely neglected. The incomplete conversion of the electrode material results in the formation of inactive phases which leads to a decrease in capacity of the electrodes.

# Chapter 4 – Conclusion

In the current work, the electrochemical performance, phase transformation and microstructure development during the first discharge-charge process of transition metal ferrites ($M$Fe$_2$O$_4$, $M$ = Fe, Co, Ni, Cu and Zn) were investigated using combined *in situ* synchrotron powder diffraction and X-ray absorption spectroscopy techniques. The main findings are summarized as followings:

- The electrochemical performance of inverse co-precipitation synthesized $M$Fe$_2$O$_4$, $M$ = Fe, Co, Ni, Cu and Zn shows that the electrochemical composition (binary vs. ternary) and the type of the additional metal in the ternary ferrites have strong impact on the electrochemical performance. In addition, factors such as annealing temperature, electrode composition, electrode pressing and binder also have strong influence on the electrochemical performance. Among the different materials, Binary $Fe_3O_4$ demonstrates a more stable cycling behavior than ternary oxides. Cu and Zn ferrites show less degradation upon cycling in comparison to Co and Ni compounds.
- Investigation of lithium storage mechanism in nano-crystalline Co and Ni ferrites *by in situ* SRPD confirms the formation of a two-phase mechanism of which the newly formed intermediate phase is indexed with the space group $Fd\bar{3}m$. The characteristic feature of this intermediate phase is the rearrangement of the cations within the spinel structure. The insertion of lithium into octahedral 16c sites of the spinel causes the migration of the transition metal cations from the tetrahedral 8a sites to empty octahedral 16c sites. The cation distribution of the intermediate spinel phase corresponds to $\mathbf{(Li,Me)_{16c}[Me_2]_{16d}O_4}$. Therefore, the traditional description of the loss of the initial microstructure upon the conversion process to form rock salt type structure has to be re-considered.

- *In situ* XAS studies performed on $CoFe_2O_4$ and $NiFe_2O_4$ at Fe, Co and Ni K edges revealed the formation of metallic nanoparticles at the end of first discharge. During the subsequent charging, metallic Fe domains completely reoxidized, whereas no such complete oxidation was observed for the Co and Ni metallic phases. This could be attributed to a thermodynamically more favoured formation of $Fe_2O_3$ in comparison with NiO or CoO. The hindered reoxidation of Co and Ni in the applied potential window could be a reason for the observed irreversible capacity loss in the first cycle for both materials. A higher reversible capacity and hence a higher coulombic efficiency especially in the initial cycle would require a complete oxidation of Ni and Co at lower potentials.
- During the first discharge, both initial intercalation and later conversion reactions are assumed to have distinct reaction dynamics. In the current study, the intermediate lithiated phase appears at 0.08 and 0.8 moles of lithium intake for CFO-800 cycled at C/10 and C/40, respectively, whereas at 0.2 and 0.8 moles of lithium uptake for NFO-800 cycled at C/10 and C/40, respectively. Hence, the higher C-rate of the samples results in higher propagation speed of the lithiated phase interface.
- Nanocrystalline phase pure FO-600($Fe_3O_4$) and microcrystalline FO-800 containing a FeO/$Fe_3O_4$ mixture shows that, with high surface area and electrolyte decomposition on the surface, FO-600 nanoparticles do not offer long term cycling stability even with good electrochemical conversion kinetics whereas FO-800 microcrystalline particles shows excellent electrochemical cycling stability. Using *in situ* SRPD technique, an intermediate lithiated phase ($Li_xFe_3O_4$, $Fd\bar{3}m$ space group) was observed during the initial lithiation along with $Fe_3O_4$ which increases with increasing lithiation for both FO-600 and FO-800 materials. For FO-800 the conversion of FeO to metallic Fe starts at an onset of 2 moles of lithium uptake. FO-800 with FeO/$Fe_3O_4$ mixture after the first cycle still contains

unreacted metallic Fe nanoparticles. Nevertheless, the material showed better capacity retention on further cycling. Furthermore, the *in situ* XAS data suggest that, the starting material and the metallic Fe nanodomains formed when the material is fully lithiated impact the homogeneity of the iron oxide phase formed during the subsequent delithiation. Lithiation of FO-600 resulting in a rather complete conversion into Fe domains favors the formation of both FeO and $Fe_2O_3$ with a higher ratio of $Fe_2O_3$ upon delithiation. However, a complete conversion into iron oxide was not seen in FO-800 and the delithiation kinetics was more favored for the formation of FeO than $Fe_2O_3$.

- In $ZnFe_2O_4$ anode material, *in situ* diffraction studies account for a two-phase mechanism during first discharge as observed in other materials. At the end of first discharge, a mixture of metallic Fe and Zn, ZnO, LiZn and $Li_2O$ phases co exists. These phases were not completely transformed into the corresponding FeO/$Fe_2O_3$ and ZnO upon delithiation. The incomplete conversion of the electrode material results in the formation of inactive phases which leads to a decreasing capacity of the electrodes.

Therefore, this thesis work provides the first detailed comparative study on the influence of the electrochemical performance and reaction mechanism of $Fe_3O_4$ with a partial substitution of Fe using different 3d-cations (Co, Ni, Cu and Zn). It also adds in-depth insight into the existing knowledge of particle size and c-rate dependent reaction mechanisms. The information obtained from these findings can help to further improve the electrochemical performance of conversion type ferrite anode materials for their potential energy storage applications in LIBs.

# Bibliography


1. C. M. Hayner, X. Zhao & H. H. Kung, *'Materials for Rechargeable Lithium-Ion Batteries',* Annu. Rev. Chem. Biomol. Eng., 3, 445–471 (2012).

2. M. S. Whittingham, *'Electrical Energy Storage and Intercalation Chemistry'*, Science, 192, 1126 -1127 (1976).

3. K. Mizushima, P. C. Jones, P. J. Wiseman & J. B. Goodenough, *'$Li_xCoO_2$ ($0<x\leqslant1$): A new cathode material for batteries of high energy density'*, Solid State Ionics, 15, 783–89 (1980).

4. M. M. Thackeray, W. I. F. David, P. G. Bruce & J. B. Goodenough, *'Lithium insertion into manganese spinels'*, Mater. Res. Bull., 18, 461–472 (1983).

5. F. Schipper, & D. Aurbach, *'A brief review: Past, present and future of lithium ion batteries',* Russ. J. Electrochem., 52, 1095–1121 (2016).

6. J. M. Tarascon & M. Armand, *'Issues and challenges facing rechargeable lithium batteries'*, Nature, 414, 359–367 (2001).

7. D. Aurbach, E. Zinigrad, Y. Cohen & H. Teller, *'A short review of failure mechanisms of lithium metal and lithiated graphite anodes in liquid electrolyte solutions',* Solid State Ionics, 148, 405–416 (2002).

8. S. Basu, C. Zeller, P. J. Flanders, C. D. Fuerst, W. D. Johnson & J. E. Fischer *'Synthesis and properties of lithium-graphite intercalation compounds',* Mater. Sci. Eng., 38, 275–283 (1979).

9. J. O. Besenhard & G. Eichinger, *'High energy density lithium cells: Part I. Electrolytes and anodes',* J. Electroanal. Chem. Interfacial Electrochem., 68, 1–18 (1976).

10. R. Yazami & P. Touzain, *'A reversible graphite-lithium negative electrode for electrochemical generators',* J. Power Sources, 9, 365–371 (1983).

11. N. A. Kaskhedikar & J. Maier, *'Lithium Storage in Carbon Nanostructures',* Adv. Mater., 21, 2664–2680 (2009).

12. A. Yoshino, *'The Birth of the Lithium-Ion Battery',* Angew. Chemie Int. Ed., 51, 5798–

5800 (2012).

13. K. Persson, V. A. Sethuraman, L. J. Hardwick, Y. Hinuma, Y. S. Meng, A. V. D. Ven, V. Srinivasan, R. Kostecki & G. Ceder *'Lithium Diffusion in Graphitic Carbon',* J. Phys. Chem. Lett., 1, 1176–1180 (2010).

14. K. Sato, M. Noguchi, A. Demachi, N. Oki & M. Endo, *'A Mechanism of Lithium Storage in Disordered Carbons',* Science., 264, 556–558 (1994).

15. U. Kasavajjula, C. Wang & A. J. Appleby, *'Nano- and bulk-silicon-based insertion anodes for lithium-ion secondary cells',* J. Power Sources, 163, 1003–1039 (2007).

16. S. Goriparti, E. Miele, F. D. Angelis, E. D. Fabrizio, R. P. Zaccaria & C. Capiglia *'Review on recent progress of nanostructured anode materials for Li-ion batteries',* J. Power Sources, 257, 421–443 (2014).

17. P. Poizot, S. Laruelle, S. Grugeon, , L. Dupont, & J.-M. Tarascon, *'From the vanadates to 3d-metal oxides negative electrodes',* Ionics, 6, 321–330 (2000).

18. J. Cabana, L. Monconduit, D. Larcher & M. R. Palacín, *'Beyond intercalation-based Li-ion batteries: The state of the art and challenges of electrode materials reacting through conversion reactions',* Adv. Mater., 22, 170–192 (2010).

19. R. Malini, U. Uma, T. Sheela & M. Ganesan, *'Conversion reactions : a new pathway to realise energy in lithium-ion battery — review',* Ionics, 15, 301–307 (2009).

20. J.-M. Tarascon, S. Grugeon, M. Morcrette, S. Laruelle, P. Rozier, & P. Poizot, *'New concepts for the search of better electrode materials for rechargeable lithium batteries',* Comptes Rendus Chim., 8, 9–15 (2005).

21. F. Wang, R. Robert, N. A. Chernova, N. Pereira, F. Omenya, F. Badway, X. Hua, M. Ruotolo, R. Zhang, L. Wu, V. Volkov, D. Su, M. S. Whittingham, C. P. Grey, G. G. Amatucci, Y. Zhu, & J. Graetz, *'Conversion Reaction Mechanisms in Lithium Ion Batteries: Study of the Binary Metal Fluoride Electrodes Conversion Reaction Mechanisms in Lithium Ion Batteries : Study of the Binary Metal Fluoride Electrodes',* J. Am. Chem.Soc., 133, 18828–18836 (2011).

22. P.Poizot, S. Laruelle, S. Grugeon, L. Dupont & J.-M. Tarascon, *'Nano-sized transition-metal oxides as negative-electrode materials for lithium-ion batteries', Nature*, 407, 496–499 (2000).

23. I. Plitz, F. Badway, J. Al-Sharab, A. DuPasquier, F. Cosandey & G. G. Amatucci, *'Structure and Electrochemistry of Carbon-Metal Fluoride Nanocomposites Fabricated by Solid-State Redox Conversion Reaction',* J. Electrochem. Soc., 152, A307-A315 (2005).

24. N. Pereira, L. C. Klein & G. G. Amatucci, *'The Electrochemistry of $Zn_3N_2$ and LiZnN',* J. Electrochem. Soc., 149, A262-A271 (2002).

25. N. Pereira, L. Dupont, J-M. Tarascon, L. C. Klein, & G. G. Amatucci, *'Electrochemistry of $Cu_3N$ with Lithium',* J. Electrochem. Soc., 150, A1273-A1280 (2003).

26. N. Pereira, F. Badway, M. Wartelsky, S. Gunn & G. G. Amatucci, *'Iron Oxyfluorides as High Capacity Cathode Materials for Lithium Batteries',* J. Electrochem. Soc., 156, A407-A416 (2009).

27. Y. Oumellal, A. Rougier, G. A. Nazri, J.-M. Tarascon & L. Aymard, *'Metal hydrides for lithium-ion batteries',* Nat. Mater., 7, 916–921 (2008).

28. F. Badway, N. Pereira, F. Cosandey & G. G. Amatucci, *'Carbon-Metal Fluoride Nanocomposites',* J. Electrochem. Soc., 150, A1209-A1218 (2003).

29. P. P. R. M. L. Harks, F. M. Mulder & P. H. L. Notten, *'In situ methods for Li-ion battery research: A review of recent developments',* J. Power Sources, 288, 92–105 (2015).

30. S-H. Yu, S. H. Lee, D. J. Lee, Y-E. Sung & T. Hyeon, *'Conversion Reaction-Based Oxide Nanomaterials for Lithium Ion Battery Anodes', Small,* 12, 2146–2172 (2016).

31. J. Jiang, Y. Li, J. Liu, X. Huang, C. Yuan, & X. W. Lou, *'Recent advances in metal oxide-based electrode architecture design for electrochemical energy storage',* Adv. Mater., 24, 5166–5180 (2012).

32. P. Meister, H. Jia, J. Li, R. Kloepsch, M. Winter, & T. Placke, *'Best Practice: Performance and Cost Evaluation of Lithium Ion Battery Active Materials with Special Emphasis on Energy Efficiency',* Chem. Mater., 28, 7203–7217 (2016).

33. M. Salavati-Niasari, T. Mahmoudi, M. Sabet, S. M. Hosseinpour-Mashkani, F. Soofivand & F. Tavakoli, *'Synthesis and Characterization of Copper Ferrite Nanocrystals via Coprecipitation',* J. Clust. Sci., 23, 1003–1010 (2012).

34. Z. Xing, Z. Ju, J. Yang, H. Xu & Y. Qian, *'One-step hydrothermal synthesis of $ZnFe_2O_4$ nano-octahedrons as a high capacity anode material for Li-ion batteries',* Nano Res., 5, 477–485 (2012).

35. P. Lavela & J. L. Tirado, *'$CoFe_2O_4$ and $NiFe_2O_4$ synthesized by sol-gel procedures for their use as anode materials for Li ion batteries',* J. Power Sources, 172, 379–387 (2007).

36. P. Preetham, S. Mohapatra, S. V. Nair, D. Santhanagopalan & A. K. Rai, *'Ultrafast pyro-synthesis of $NiFe_2O_4$ nanoparticles within a full carbon network as a high-rate and cycle-stable anode material for lithium ion batteries',* Rsc Adv., 6, 38064–38070 (2016).

37. D. Wadewitz, W. Gruner, M. Herklotz, M. Klose, L. Giebeler, A. Voß, J. Thomas, T. Gemming, J. Eckert & H. Ehrenberg, *'Investigation of Copper-Cobalt-Oxides as Model Systems for Composite Interactions in Conversion-Type Electrodes for Lithium-Ion Batteries',* J. Electrochem. Soc., 160, A1333–A1339 (2013).

38. W. Gruner, J. Thomas, L. Giebeler, H. Ehrenberg & D. Wadewitz, *'Interactions of Copper and Iron in Conversion Reactions of Nanosized Oxides with Large Variations in Iron-Copper Ratio',* J. Electrochem. Soc., 158, A1383-A1392 (2011).

39. S. A. Hassanzadeh-Tabrizi, & E. Taheri-Nassaj, *'Synthesis of high surface area $Al_2O_3$-$CeO_2$ composite nanopowder via inverse co-precipitation method',* Ceram. Int., 37, 1251–1257 (2011).

40. P. G. Bruce, B. Scrosati & J-M. Tarascon, *'Nanomaterials for rechargeable lithium batteries',* Angew. Chem. Int. Ed. Engl., 47, 2930–2946 (2008).

41. M. Herklotz, F. Scheiba, M. Hinterstein, K. Nikolowski, M. Knapp, A-C. Dippel, L. Giebeler, J. Eckert & H. Ehrenberg, *'Advances in in situ powder diffraction of battery materials: A case study of the new beamline P02.1 at DESY, Hamburg',* J. Appl. Crystallogr., 46, 1117–1127 (2013).

42. M. Herklotz, J. Weiß, E. Ahrens, M. Yavuz, L. Mereacre, N. Kiziltas-Yavuz, C. Dräger, H. Ehrenberg, J. Eckert, F. Fauth, L. Giebler & M. Knapp, *'A novel high-throughput setup for in situ powder diffraction on coin cell batteries',* J. Appl. Crystallogr., 49, 340–345 (2016).

43. T. Roisnel & J. Rodríguez-Carvajal. *'WinPLOTR: a Windows tool for powder diffraction patterns analysis',* Materials Science Forum, Proceedings of the Seventh European Powder Diffraction Conference, 378-381, 118-123 (2000).

44. F. Fauth, I. Peral, C. Popescu & M. Knapp, *'The new Material Science Powder Diffraction beamline at ALBA Synchrotron',* Powder Diffr., 28, S360–S370 (2013).

45. A. P. Hammersley, S. O. Svensson, M. Hanfland, A. N. Fitch & D. Hausermann, *'Two-dimensional detector software: From real detector to idealised image or two-theta scan',* High Press. Res., 14, 235–248 (1996).

46. B. Ravel, & M. Newville, *'ATHENA, ARTEMIS, HEPHAESTUS: Data analysis for X-ray absorption spectroscopy using IFEFFIT',* J. Synchrotron Radiat., 12, 537–541 (2005).

47. S. Bhuvaneswari, M. P. Pratheeksha, S. Anandan, D. Rangappa, R. Gopalan & N. T. Rao, *'Efficient reduced graphene oxide grafted porous $Fe_3O_4$ composite as a high performance anode material for Li-ion batteries',* Phys. Chem., 16, 5284-5294 (2014).

48. A. Bhaskar, S. Krueger, V. Siozios, J. Li, S. Nowak & M. Winter, *'Synthesis and characterization of high-energy, high-power spinel-layered composite cathode materials for lithium-ion batteries',* Adv. Energy Mater., 5, 1–12 (2015).

49. L. Zhou, Q. Fu, D. Zhou, F. Xue, & Y. Tian, *'Solvothermal synthesis of $CoFe_2O_4$ submicron compact spheres and tunable coercivity induced via low-temperature thermal treatment',* J. Magn. Mater., 392, 22–26 (2015).

50. L. Liu, A. Han, M. Ye & W. Feng, *'The evaluation of thermal performance of cool coatings colored with high near-infrared reflective nano-brown inorganic pigments: Magnesium doped $ZnFe_2O_4$ compounds',* Sol. Energy, 113, 48–56 (2015).

51. N. H. Li, S. L. Lo, C. Y. Hu, C. H. Hsieh & C. L. Chen, *'Stabilization and phase transformation of $CuFe_2O_4$ sintered from simulated copper-laden sludge',* J. Hazard. Mater., 190, 597–603 (2011).

52. H. S. C. O'Neill & A. Navrotsky, *'Cation Distributions and Thermodynamic Properties of Binary Spinel Solid Solutions',* Am. Mineral., 69, 733–753 (1984).

53. H. S. C. O'Neill, & A. Navrotsky, *'Simple spinels: crystallographic parameters, cation radii, lattice energies, and cation distribution',* Am. Mineral., 68, 181–194 (1983).

54. Y. H. Hou, Y. J. Zhao, Z. W. Liu, H. Y. Yu, X. C. Zhong, W. Q. Qiu, D. C. Zeng & L. S. Wen, *'Structural, electronic and magnetic properties of partially inverse spinel $CoFe_2O_4$ : a first-principles study',* J. Phys. D. Appl. Phys., 43, 445003-445012 (2010).

55. R. Adam, D. Wadewitz, W. Gruner, V. Klemm, H. Ehrenberg & D. Rafaja, *'Phase and Microstructure Development in the Conversion Type Electrodes for Li-Ion Batteries Based on the Cu-Fe-O System',* J. Electrochem. Soc., 160, A1594–A1603 (2013).

56. H. S. C. O'Neill & W. A. Dollase, *'Crystal structures and cation distributions in simple spinels from powder XRD structural refinements: $MgCr_2O_4$, $ZnCr_2O_4$, $Fe_3O_4$ and the temperature dependence of the cation distribution in $ZnAl_2O_4$',* Phys. Chem. Miner., 20, 541–555 (1994).

57. C. G. Shull, E. O. Wollan & W. C. Koehler, *'Neutron scattering and polarization by ferromagnetic materials',* Phys. Rev., 84, 912–921 (1951).

58. J. K. Kim, W. D. Moon, K. S. Lee & K. Jung, *'Formation of a highly oriented FeO thin film by phase transition of $Fe_3O_4$ and Fe nanocrystallines',* Thin Solid Films, 360, 118–121 (2000).

59. S. J. A. Figueroa, S. J. Stewart, T. Rueda, A. Hernando & P. De La Presa, *'Thermal evolution of Pt-rich FePt/$Fe_3O_4$ heterodimers studied using x-ray absorption near-edge spectroscopy',* J. Phys. Chem., 115, 5500–5508 (2011).

60. S. Ayyappan, G. Panneerselvam, M. P. Antony, N. V. Rama Rao, N. Thirumurugan, A. Bharathi & J. Philip, *'Effect of initial particle size on phase transformation temperature of surfactant capped $Fe_3O_4$ nanoparticles',* J. Appl. Phys., 109, 084303, 1-8 (2011).

61. D. Makovec, A. Kodre, I. Arčon & M. Drofenik, *'The structure of compositionally constrained zinc-ferrite spinel nanoparticles',* J. Nanoparticle Res., 13, 1781–1790 (2011).

62. T. Kamiyama, K. Haneda, T. Sato, S. Ikeda & H. Asano *'Cation Distribution in $ZnFe_2O_4$ fine particles studied by neutron powder diffraction',* Solid State Commun., 81, 563–566 (1992).

63. M. H. Nilsen, C. Nordhei, A. L. Ramstad & D. G. Nicholson, *'XAS (XANES and EXAFS) investigations of nanoparticulate ferrites synthesized continuously in near critical and supercritical water',* J. Phys. Chem., 111, 6252–6262 (2007).

64. M. Keppeler & M. Srinivasan, *'Interfacial Phenomena/Capacities Beyond Conversion Reaction Occurring in Nano-sized Transition-Metal-Oxide-Based Negative Electrodes in Lithium-Ion Batteries: A Review',* ChemElectroChem, 4, 2727–2754 (2017).

65. M. Bijelić, X. Liu, Q. Sun, A. B. Djurišić, M. H. Xie, A. M. C. Ng, C. Suchomski, I. Djerdj, Z. Skoko & J. Popović, *'Long cycle life of $CoMn_2O_4$ lithium ion battery anodes with high crystallinity',* J. Mater. Chem., 1, 14759–14767 (2015).

66. S. Grugeon, S. Laruelle, R. Herrera-Urbina, L. Dupont, P. Poizot, & J-M. Tarascon, *'Particle Size Effects on the Electrochemical Performance of Copper Oxides toward Lithium',* J. Electrochem. Soc., 148, A285-A292 (2001).

67. F. M. Courtel, H. Duncan, Y. Abu-Lebdeh & I. J. Davidson, *'High capacity anode materials for Li-ion batteries based on spinel metal oxides $AMn_2O_4$ (A = Co, Ni, and Zn)',* J. Mater. Chem., 21, 10206–10218 (2011).

68. Y. X. Chen, L. H. He, P. J. Shang, Q. L. Tang, Z. Q. Liu, H. B. Liu & L. P. Zhou, *'Micro-sized and Nano-sized $Fe_3O_4$ Particles as Anode Materials for Lithium-ion Batteries',* J. Mater. Sci. Technol., 27, 41–45 (2011).

69. H. Buqa, M. Holzapfel, F. Krumeich, C. Veit & P. Novák, *'Study of styrene butadiene rubber and sodium methyl cellulose as binder for negative electrodes in lithium-ion batteries',* J. Power Sources, 161, 617–622 (2006).

70. J.-P. Yen, C.-C. Chang, Y.-R. Lin, S.-T. Shen & J.-L. Hong, *'Effects of Styrene-Butadiene Rubber/Carboxymethylcellulose (SBR/CMC) and Polyvinylidene Difluoride (PVDF) Binders on Low Temperature Lithium Ion Batteries',* J. Electrochem. Soc., 160, A1811–A1818 (2013).

71. R. Zhang, Xu. Yang, D. Zhang, H. Qiu, Q. Fu, H. Na, Z. Guo, F. Du, G. Chen & Y. Wei, *'Water soluble styrene butadiene rubber and sodium carboxyl methyl cellulose binder for $ZnFe_2O_4$ anode electrodes in lithium ion batteries',* J. Power Sources, 285, 227–234 (2015).

72. P. Zeng, X. Wang, M. Ye, Q. Ma, J. Li, W. Wang, B. Geng & Z. Fang, *'Excellent lithium ion storage property of porous $MnCo_2O_4$ nanorods',* RSC Adv., 6, 23074–23084 (2016).

73. R. Indhrajothi, I. Prakash, M. Venkateswarlu & N. Satyanarayana, *'Binder effect on the battery performance of mesoporous copper ferrite nanoparticles with grain boundaries as anode materials',* RSC Adv., 4, 44089–44099 (2014).

74. P. R. Kumar & S. Mitra, *'Nickel ferrite as a stable, high capacity and high rate anode for Li-ion battery applications',* RSC Adv., 3, 25058–25064 (2013).

75. C. He, S. Wu, N. Zhao, C. Shi, E. Liu & J. Li, *'Carbon-encapsulated $Fe_3O_4$ nanoparticles as a high-rate lithium ion battery anode material',* ACS Nano, 7, 4459–4469 (2013).

76. Z. Yang, J. Shen & L. A. Archer, *'An in situ method of creating metal oxide–carbon composites and their application as anode materials for lithium-ion batteries',* J. Mater. Chem., 21, 11092-11097 (2011).

77. Y. Piao, H. S. Kim, Y-E. Sung & T. Hyeon, *'Facile scalable synthesis of magnetitenanocrystals embedded in carbon matrix as superior anode materials for lithium-ion batteries',* Chem. Commun., 46, 118–120 (2010).

78. T. Zhu, J. S. Chen & X. W. Lou, *'Glucose-assisted one-pot synthesis of FeOOH nanorods and their transformation to $Fe_3O_4$@carbon nanorods for application in lithium ion batteries',* J. Phys. Chem., 115, 9814–9820 (2011).

79. L. Ji, Z. Tan, T. R. Kuykendall, S. Aloni, S. Xun, E. Lin, V. Battaglia & Y. Zhang, *'$Fe_3O_4$ nanoparticle-integrated graphene sheets for high-performance half and full lithium ion cells',* Phys. Chem., 13, 7170–7177 (2011).

80. F-X. Ma, P-P. Wang, C-Y. Xu, Jing. Yu, H-T. Fang & L. Zhen, *'Synthesis of self-stacked $CuFe_2O_4$–$Fe_2O_3$ porous nanosheets as a high performance Li-ion battery anode',* J. Mater. Chem., 2, 19330–19337 (2014).

81. S. Peng, L. Li & M. Srinivasan, *'Electrospun $CuFe_2O_4$ nanotubes as anodes for high-performance lithium-ion batteries',* J. Energy Chem., 23, 301–307 (2014).

82. Y. Ding, Y. Yang & H. Shao, *'Synthesis and characterization of nanostructured $CuFe_2O_4$ anode material for lithium ion battery',* Solid State Ionics, 217, 27–33 (2012).

83. L. Jin, Y. Qiu, H. Deng, W. Li, H. Li & S. Yang, *'Hollow $CuFe_2O_4$ spheres encapsulated in carbon shells as an anode material for rechargeable lithium-ion batteries',* Electrochim. Acta, 56, 9127–9132 (2011).

84. D. Bresser, E. Paillard, R. Kloepsch, S. Krueger, M. Fiedler, R. Schmitz, D. Baither, M. Winter & S. Passerini, *'Carbon Coated $ZnFe_2O_4$ Nanoparticles for Advanced Lithium-Ion Anodes',* Adv. Energy Mater., 3, 513–523 (2013).

85. A. S. Hameed, H. Bahiraej, M. V. Reddy, M. Z. Shoushtari, J. J. Vittal, C. K. Ong & B. V. R. Chowdari, *'Lithium Storage Properties of Pristine and (Mg, Cu) Codoped $ZnFe_2O_4$ Nanoparticles',* J. Phys. Chem., 6, 10744-10753 (2014).

86. Li, H., Y. Wei, Y. Zhang, F. Yin, C. Zhang, G. Wang & Z.Bakenov, *'Synthesis and electrochemical investigation of highly dispersed ZnO nanoparticles as anode material for lithium-ion batteries',* Ionics., 22, 1387–1393 (2016).

87. C. J. Chen, M. Greenblatt & J. V. Waszczak, *'Lithium insertion into spinel ferrites',* Solid State Ionics, 18–19, 838–846 (1986).

88. R. Alcántara, M. Jaraba, P. Lavela, J. L. Tirado, J. C. Jumas & J. Olivier-Fourcade, *'Changes in oxidation state and magnetic order of iron atoms during the electrochemical reaction of lithium with $NiFe_2O_4$',* Electrochem. commun., 5, 16–21 (2003).

89. P. Lavela, J. L. Tirado, M. Womes, & J. C. Jumas, *'Elucidation of Capacity Fading on $CoFe_2O_4$ Conversion Electrodes for Lithium Batteries Based on Fe-57 Mossbauer Spectroscopy',* J. Electrochem. Soc., 156, A589–A594 (2009).

90. C. Vidal-Abarca, P. Lavela & J. L. Tirado *'On the role of faradaic and capacitive contributions in the electrochemical performance of $CoFe_2O_4$ as conversion anode for Li-ion cells',* Solid State Ionics, 181, 616–622 (2010).

91. C. Vidal-Abarca, P. Lavela & J. L. Tirado, *'A $^{57}Fe$ Mössbauer spectroscopy study of cobalt ferrite conversion electrodes for Li-ion batteries',* J. Power Sources, 196, 6978–6981 (2011).

92. C. Vidal-Abarca, P. Lavela & J. L. Tirado, *'The Origin of Capacity Fading in $NiFe_2O_4$ Conversion Electrodes for Lithium Ion Batteries Unfolded by $^{57}Fe$ Mössbauer Spectroscopy',* J. Phys. Chem., 114, 12828–12832 (2010).

93. D. Zhou, S. Permian, J. Rana, M. Krengel, F. Sun, G. Schumacher, W. Bensch & J. Banhart, *'Investigation of electronic and local structural changes during lithium uptake and release of nano-crystalline $NiFe_2O_4$ by X-ray absorption spectroscopy',* J. Power Sources, 342, 56–63 (2017).

94. M. Islam, G. Ali, M-G. Jeong, W. Choi, K. Y. Chung, & H-G. Jung, *'Study on the Electrochemical Reaction Mechanism of $NiFe_2O_4$ as a High-Performance Anode for Li-Ion Batteries',* ACS Appl. Mater. Interfaces, 9, 14833-14843 (2017).

95. S. Permien, S. Indris, U. Schürmann, L. Kienle, S. Zander, S. Doyle & W. Bensch, *'What Happens Structurally and Electronically during the Li Conversion Reaction of $CoFe_2O_4$ Nanoparticles: An Operando XAS and XRD Investigation',* Chem. Mater., 28, 434–444 (2016).

96. P. Zhu, S. Liu, J. Xie, S. Zhang, G. Cao & X. Zhao, *'Facile Synthesis of $NiFe_2O_4$/Reduced Graphene Oxide Hybrid with Enhanced Electrochemical Lithium Storage Performance',* J. Mater. Sci. Technol., 30, 1078–1083 (2014).

97. S. Permien, S. Indris, G. Neubüser, A. Fiedler, L. Kienle, S. Zander, S. Doyle, B. Richter & W. Bensch, *'The Role of Reduced Graphite Oxide in Transition Metal Oxide Nanocomposites Used as Li Anode Material: An Operando Study on $CoFe_2O_4$ /rGO',* Chem. Eur. J., 22, 16929–16938 (2016).

98. L. Wu, Q. Xiao, Z. Li, G. Lei, P. Zhang & L. Wang, *'$CoFe_2O_4$/C composite fibers as anode materials for lithium-ion batteries with stable and high electrochemical performance',* Solid State Ionics, 215, 24–28 (2012).

99. S. Nilmoung, P. Kidkhunthod, S. Pinitsoontorn, S. Rujirawat, R. Yimnirum & S. Maensiri, *'Fabrication, structure, and magnetic properties of electrospun carbon/cobalt ferrite ($C/CoFe_2O_4$) composite nanofibers',* Appl. Phys. A Mater. Sci. Process., 119, 141–154 (2015).

100. T. Dong, G. Wang & P. Yang, *'Electrospun $NiFe_2O_4$@C fibers as high-performance anode for lithium-ion batteries',* Diam. Relat. Mater., 73, 210–217 (2017).

101. P. R. Kumar, P. Kollu, C. Santhosh, K. E. V. Rao, D. K. Kim & A. N. Grace, *'Enhanced properties of porous $CoFe_2O_4$ –reduced graphene oxide composites with alginate binders for Li-ion battery applications',* New J. Chem., 38, 3654–3661 (2014).

102. P. R. Kumar & S. Mitra, *'Nickel ferrite as a stable, high capacity and high rate anode for Li-ion battery applications',* RSC Adv., 3, 25058–25064 (2013).

103. S. Permien, H. Hain, M. Scheuermann, S. Mangold, V. Mereacre, A. K. Powell, S. Indris, U. Schürmann, L. Kienle, V. Duppel, S. Harm & W. Bensch, *'Electrochemical insertion of Li into nanocrystalline $MnFe_2O_4$: a study of the reaction mechanism',* RSC Adv., 3, 23001-23014 (2013).

104. S. Permien, S. Indris, M. Scheuermann, U. Schürmann, V. Mereacre, A. K. Powell, L. Kienle & W. Bensch, *'Is there a universal reaction mechanism of Li insertion into oxidic spinels: a case study using $MgFe_2O_4$',* J. Mater. Chem., 3, 1549–1561 (2015).

105. M. M. Thackeray, W. I. F. David & J. B. Goodenough, *'Structural characterization of the lithiated iron oxides $LixFe_3O_4$ and $LixFe_2O_3$ ($0 < x < 2$)',* Mat. Res. Bull., 17, 785–793 (1982).

106. R. Adam, M. Lepple, N. A. Mayer, D. M. Cupid, Y. Qian, P. Niehoff, F. M. Schappacher, D. Wadewitz, G. Balachandran, A. Bhaskar, N. Bramnik, V. Klemm, E. Ahrens, L. Giebler, F. Fauth, C. A. Popescu, H. J. Seifert, M. Winter, H. Ehrenberg, & D. Rafaja, *'Coexistence of conversion and intercalation mechanisms in lithium ion batteries: Consequences for microstructure and interaction between the active material and electrolyte',* Int. J. Mater. Res., 108, 1–13 (2017).

107. D.Larcher, G.Sudant, J.-B. Leriche, Y. Chabre & J.-M. Tarascon, *'The Electrochemical Reduction of $Co_3O_4$ in a Lithium Cell',* J. Electrochem. Soc., 149, A234-A241 (2002).

108. K. He, H. L. Xin, K. Zhao, X. Yu, D. Nordlund, T.-C. Weng, J. Li, Y. Jiang, C. A. Cadigan, R. M. Richards, M. M. Doeff, X.-Q. Yang, E. A. Stach, J. Li, F. Lin & D. Su, *'Transitions from near-surface to interior redox upon lithiation in conversion electrode materials',* Nano Lett., 15, 1437–1444 (2015).

109. K. He, S. Zhang, J. Li, X. Yu, Q. Meng, Y. Zhu, E. Hu, K. Sun, H. Yun, X.-Q. Yang, Y. Zhu, H. Gan, Y. Mo, E. A. Stach, C. B. Murray & D. Su, *'Visualizing non-equilibrium lithiation of spinel oxide via in situ transmission electron microscopy',* Nat. Commun., 7, 11441, 1-9 (2016).

110. N. A. Godshall, I. D. Raistrick & R. A. Huggins, *'Relationships among Electrochemical, Thermodynamic, and Oxygen Potential Quantities in Lithium-Transition Metal-Oxygen Molten Salt Cells',* J. Electrochem. Soc., 131, 543-549 (1984).

111. M. M. Thackeray, *'Spinel Electrodes for Lithium Batteries',* J. Am. Ceram. Soc., 82, 3347–3354 (1999).

112. P. L. Taberna, S. Mitra, P. Poizot, P. Simon & J.-M. Tarascon, *'High rate capabilities $Fe_3O_4$-based Cu nano-architectured electrodes for lithium-ion battery applications',* Nat. Mater., 5, 567–573 (2006).

113. J. Liu, H. Feng, X. Wang, D. Qian, J. Jiang, J. Li, S. Peng, M. Deng & Y. Liu, *'Self-assembly of nano/micro-structured $Fe_3O_4$ microspheres among 3D rGO/CNTs hierarchical networks with superior lithium storage performances',* Nanotechnology, 25, 225401, 1-8 (2014).

114. S. Hariharan, K. Saravanan, V. Ramar & P. Balaya, *'A rationally designed dual role anode material for lithium-ion and sodium-ion batteries: case study of eco-friendly $Fe_3O_4$',* Phys. Chem., 15, 2945-2953 (2013).

115. Q. Xiong, J. Tu, Y. Lu, J. Chen, Y. Yu, X. Wang & C. Gu, *'Three-dimensional porous nano-Ni/$Fe_3O_4$ composite film: enhanced electrochemical performance for lithium-ion batteries',* J. Mater. Chem., 22, 18639-18645 (2012).

116. L. Su, Y. Zhong & Z. Zhou, *'Role of transition metal nanoparticles in the extra lithium storage capacity of transition metal oxides: a case study of hierarchical core–shell $Fe_3O_4$@C and Fe@C microspheres',* J. Mater. Chem. A, 1, 15158-15166 (2013).

117. Y. Zhu, Y.-J. Bai, F.-D. Han, Y.-X. Qi, N. Lun, B. Yao & J.-X. Zhang, *'One-step preparation of six-armed $Fe_3O_4$ dendrites with carbon coating applicable for anode material of lithium-ion battery',* Mater. Lett., 65, 3157–3159 (2011).

118. J. Ming, W. J. Kwak, S. J. Youn, H. Ming, J. Hassoun & Y.-K. Sun, *'Lithiation of an Iron Oxide-Based Anode for Stable, High-Capacity Lithium-Ion Batteries of Porous Carbon-$Fe_3O_4$/$Li[Ni_{0.59}Co_{0.16}Mn_{0.25}]O_2$',* Energy Technol., 2, 778–785 (2014).

119. H. Ming, J. Ming, W.-J. Kwak, W. Yang, Q. Zhou, J. Zheng, & Y.-K. Sun, *'Fluorine-doped porous carbon-decorated $Fe_3O_4$-$FeF_2$ composite versus $LiNi_{0.5}Mn_{1.5}O_4$ towards a full battery with robust capability',* Electrochim. Acta, 169, 291–299 (2015).

120. J. Fontcuberta, J. Rodríguez, M. Pernet, G. Longworth & J. B. Goodenough, *'Structural and magnetic characterization of the lithiated iron oxide $Li_xFe_3O_4$',* J. Appl. Phys., 59, 1918–1926 (1986).

121. M. S. Islam, *'Simulation Studies of lithium intercalation in transition metal oxides',* Philos. Mag. A, 68, 667–675 (1992).

122. M. S. Islam & C. R. A. Catlow, *'Lithium Insertion into $Fe_3O_4$',* J. Solid State Chem., 77, 180–189 (1988).

123. M. C. Menard, A. C. Marschilok, K. J. Takeuchi & E. S. Takeuchi, *'Variation in the iron oxidation states of magnetite nanocrystals as a function of crystallite size: The impact on electrochemical capacity',* Electrochim. Acta, 94, 320–326 (2013).

124. M. C. Menard, K. J. Takeuchi, A. C. Marschilok & E. S. Takeuchi, *'Electrochemical discharge of nanocrystalline magnetite: structure analysis using X-ray diffraction and X-ray absorption spectroscopy',* Phys. Chem. Chem. Phys., 15, 18539-18548 (2013).

125. D. C. Bock, C. J. Pelliccione, W. Zhang, J. Wang, K. W. Knehr, J. Wang, F. Wang, A. C. West, A. C. Marschilok, K. J. Takeuchi, & E. S. Takeuchi, *'Dispersion of Nanocrystalline $Fe_3O_4$ within Composite Electrodes: Insights on Battery-Related*

*Electrochemistry',* ACS Appl. Mater. Interfaces, 8, 11418–11430 (2016).

126. W. Zhang, D. C. Bock, C. J. Pelliccione, Y. Li, L. Wu, Y. Zhu, A. C. Marschilok, E. S. Takeuchi, K. J. Takeuchi & F. Wang, *'Insights into ionic transport and structural changes in magnetite during multiple-electron transfer reactions',* Adv. Energy Mater., 6, 1–11 (2016).

127. K. W. Knehr, K. W. Knehra, C. A. Camab, N. W. Bradya, A. C. Marschilokb, K. J. Takeuchib, E. S. Takeuchib, & A. C. Westa, *'Simulations of Lithium-Magnetite Electrodes Incorporating Phase Change',* Electrochim. Acta, 238, 384–396 (2017).

128. A. M. Bruck, C. A. Cama, C. N. Gannett, A. C. Marschilok, E. S. Takeuchi & K. J. Takeuchi, *'Nanocrystalline iron oxide based electroactive materials in lithium ion batteries: the critical role of crystallite size, morphology, and electrode heterostructure on battery relevant electrochemistry',* Inorg. Chem. Front., 3, 26–40 (2016).

129. D. C. Bock, C. J. Pelliccione, W. Zhang, J. Timoshenko, K. W. Knehr, A. C. West, F. Wang, Y. Li, A. I. Frenkel, E. S. Takeuchi, K. J. Takeuchi & A. C. Marschilok ,*'Size dependent behavior of $Fe_3O_4$ crystals during electrochemical (de)lithiation: an in situ X-ray diffraction, ex situ X-ray absorption spectroscopy, transmission electron microscopy and theoretical investigation',* Phys. Chem. Chem. Phys., 19, 20867–20880 (2017).

130. M. C. Menard, K. J. Takeuchi, A. C. Marschilok & E. S. Takeuchi, *'Electrochemical discharge of nanocrystalline magnetite: structure analysis using X-ray diffraction and X-ray absorption spectroscopy',* Phys. Chem. Chem. Phys., 15, 18539–48 (2013).

131. Q. Su, S. Wang, Y. Xiao, L. Yao, G. Du, H. Ye, & Y. Fang, *'Lithiation Behavior of Individual Carbon-Coated $Fe_3O_4$ Nanowire Observed by in Situ TEM',* J. Phys. Chem., C 121, 3295–3303 (2017).

132. J. Du, Y. Ding, L. Guo, L. Wang, Z. Fu, C. Qin, F. Wang & X. Tao, *'Micro-tube biotemplate synthesis of $Fe_3O_4$/C composite as anode material for lithium-ion batteries',* Appl. Surf. Sci., 425, 164–169 (2017).

133. X. Zhao, D. Xia & K. Zheng, *'An $Fe_3O_4$–FeO–Fe@C composite and its application as anode for lithium-ion battery',* J. Alloys Compd., 513, 460–465 (2012).

134. D. Li, K. Wang, H. Tao, X. Hu, S. Chenga & K. Jiang, *'Facile synthesis of an $Fe_3O_4$/FeO/Fe/C composite as a high-performance anode for lithium-ion batteries',* RSC Adv., 6, 89715–89720 (2016).

135. M. Gao, P. Zhou, P. Wang, J. Wang, C. Liang, J. Zhang & Y. Liu, *'FeO/C anode materials of high capacity and cycle stability for lithium-ion batteries synthesized by carbothermal reduction',* J. Alloys Compd., 565, 97–103 (2013).

136. Z. Zeng, H. Zhao, P. Lv, Z. Zhang, J. Wang & Q. Xia, *'Electrochemical properties of iron oxides/carbon nanotubes as anode material for lithium ion batteries',* J. Power Sources, 274, 1091–1099 (2015).

137. G.-H. Lee, J.-G. Park, Y.-M. Sung, K. Y. Chung, W. I. Cho & D.-W. Kim, *'Enhanced cycling performance of an $Fe^0/Fe_3O_4$ nanocomposite electrode for lithium-ion batteries',* Nanotechnology, 20, 295205, 1-5 (2009).

138. H.-S. Kim, S. H. Baek, M.-W. Jang, Y.-K. Sun & C. S. Yoon, *'Fe-$Fe_3O_4$ Composite Electrode for Lithium Secondary Batteries',* J. Electrochem. Soc., 159159, 325–329 (2012).

139. X. Zhao, D. Xia, & K. Zheng, *'$Fe_3O_4$/Fe/carbon composite and its application as anode material for lithium-ion batteries',* ACS Appl. Mater. Interfaces, 4, 1350–1356 (2012).

140. Y. Nuli, Y. Chu, & Q. Qin, *'Nanocrystalline $ZnFe_2O_4$ and Ag-Doped $ZnFe_2O_4$ Films Used as New Anode Materials for Li-Ion Batteries',* Journal of The Electrochemical Society, 151, A1077–A1083 (2004).

141. X. Guo, X. Lu, X. Fang, Y. Mao, Z. Wang, L. Chen, X. Xu, H. Yang & Y. Liu *'Lithium storage in hollow spherical $ZnFe_2O_4$ as anode materials for lithium ion batteries',* Electrochem. commun., 12, 847–850 (2010).

142. Y. Sharma, N. Sharma, G. V. S. Rao & B. V. R. Chowdari, *'Li-storage and cyclability of urea combustion derived $ZnFe_2O_4$ as anode for Li-ion batteries',* Electrochim. Acta, 53, 2380–2385 (2008).

143. B. Jiang, C. Han, B. Li, Y. He & Z. Lin, *'In-Situ Crafting of $ZnFe_2O_4$ Nanoparticles Impregnated within Continuous Carbon Network as Advanced Anode Materials',* ACS Nano, 10, 2728−2735 (2016).

144. M. Wang, M. Wang, Y. Huang, X. Chen, K. Wang, H. Wu, N. Zhang & H. Fu, *'Synthesis of nitrogen and sulfur co-doped graphene supported hollow $ZnFe_2O_4$ nanosphere composites for application in lithium-ion batteries',* J. Alloys Compd., 691, 407–415 (2017).

145. L. Zhang, T. Wei, J. Yue, L. Sheng, Z. Jiang, D. Yang, L. Yuana & Z. Fan, *'Ultra-small and highly crystallized $ZnFe_2O_4$ nanoparticles within double graphene networks for super-long life lithium-ion batteries',* J. Mater. Chem. A, 5, 11188–11196 (2017).

146. H. Cao, S. Zhu, C. Yang, R. Bao, L. Tong, L. Hou, X. Zhang & C. Yuan, *'Metal-organic-framework-derived two- dimensional ultrathin mesoporous hetero-$ZnFe_2O_4$/ZnO nanosheets with enhanced lithium storage properties for Li-ion batteries',* Nanotechnology, 27, 465402, 1-9 (2016).

147. D. Cai, H. Zhan & T. Wang, *'MOF-derived porous ZnO/$ZnFe_2O_4$ hybrid nanostructures as advanced anode materials for lithium ion batteries',* Mater. Lett., 197, 241–244 (2017).

148. Y. Zhang, C. J. Pelliccione, A. B. Brady, H. Guo, P. F. Smith, P. Liu, A. C. Marschilok, K. J. Takeuchi & E. S. Takeuchi *'Probing the Li Insertion Mechanism of $ZnFe_2O_4$ in Li-Ion Batteries: A Combined X - Ray Di ff raction, Extended X - Ray Absorption Fine Structure, and Density Functional Theory Study',* Chem. Mater., 29, 4282−4292 (2017).

149. Q. Su, S. Wang, L. Yao, H. Li, G. Du, H. Ye & Y. Fang, *'Study on the Electrochemical Reaction Mechanism of $ZnFe_2O_4$ by In Situ Transmission Electron Microscopy',* Nat. Sci. Rep., 6:28197, (2016).

150. D. Larcher, C. Masqueliera, D. Bonninb, Y. Chabrec, V. Massona, J.-B. Lerichea & J.-M. Tarascon, *'Effect of Particle Size on Lithium Intercalation into α-$Fe_2O_3$',* J. Electrochem. Soc., 150, A133-A139 (2003).

151. D. Zhou, H. Jiab, J. Ranaa, T. Plackeb, T. Scherba, R. Kloepschb, G. Schumachera, M. Winter, & J. Banhart, *'Local structural changes of nano-crystalline $ZnFe_2O_4$ during lithiation and de-lithiation studied by X-ray absorption spectroscopy',* Electrochim. Acta, 246, 699–706 (2017).

152. C. J. Pelliccione, Y. Ding, E. V. Timofeeva & C. U. Segre, *'In Situ XAFS Study of the Capacity Fading Mechanisms in ZnO Anodes for Lithium-Ion Batteries',* J. Electrochem. Soc., 162, A1935–A1939 (2015).

# Acknowledgement

The presented study was accomplished at the Institute of Applied Materials-Energy Storage Systems (IAM-ESS), Karlsruhe Institute of Technology, Karlsruhe. Financial support from DFG, within the Research Priority Program SPP 1473, “Materials with new design for improved Li ion batteries-WeNDeLIB” under grant no EH183/16-2, is gratefully acknowledged.

First and foremost, I thank my supervisor Prof. Dr. Helmut Ehrenberg who gave me a chance to work at IAM-ESS and accepting me as a PhD student. During my PhD work, he granted me intellectual freedom to work independently, encouraged original thinking and supported initiatives. I would like to extend my sincere gratitude to Prof. Dr. Horst Hahn, for his kindness and support to allow me to officially defend my PhD work at Materials Science and Engineering department at TU Darmstadt under his supervision.

My thesis would be incomplete without the support of my co-supervisors, Dr. Natalia Bramnik and Dr. Aiswarya Bhaskar, who guided me throughout the journey of my thesis. I thank them for their extensive support and motivation which helped me gain knowledge on novel science, techniques and methodologies. They helped me find a way to go during each stage of my research and it is also noteworthy to mention their endless efforts during the thesis correction.

I would like to thank Dr. Ditty Dixon for introducing me to the X-ray absorption spectroscopy technique and his guidance and effort during my PhD work. Dr. Michael Knapp and Dr. Murat Yavuz, for their guidance on better understanding the X-ray diffraction technique. Work place might be boring without a humorous colleague like Dr. Angelina

Sarapulova. I am thankful to her for being a wonderful person to seek help and willing to discuss any problems and questions regarding XAS and XRD data analysis. Also, I thank all of them for their support during the experiments at synchrotron facilities and making the hard times into fun and learning science in an interesting way. Dr. Lukas Pfaffmann for his help with scanning electron microscopy and Liuda Mereacre for her support in the laboratory is gratefully acknowledged.

My project collaborators, Mr. Robert Adam, Mr. Nicolas Mayer, and Dr. Damian Cupid, were wonderful people to collaborate with and discuss the project. I would like to thank them for the good times during our project meetings and to count on for both scientific and social support whenever needed.

This PhD work has been benefitted from the beam times allocated by P02.1 beamline, PETRA III and P65 beamline, PETRA III EXTENSION at Hamburg, ANKA, Karlsruhe and MSPD and CLAESS beamlines at ALBA, Barcelona. Beam line scientists, Dr. Martin Etter and Dr. Alexander Schökel (P02.1, PETRA III), Dr. Stefan Mangold (ANKA), Dr. Edmund Welter and Dr. Roman Chernikov (P65, PETRA III EXTENSION) and Dr. Francois Fauth (MSPD, ALBA) and Dr. Marta Avila (CLAESS, ALBA) are gratefully acknowledged.

I thank my colleagues at the Institute of Applied Materials-Energy Storage Systems for playing a vital role in setting up a positive energy prevailing in the group and their help during this PhD thesis work. I felt home and we were definitely a big family and I could not have asked for more. Finally, I would like to express my gratitude to my friends and family for being with me always and their great support and love.

# Curriculum Vitae

## Personal Information

| | | |
|---|---|---|
| **Name** | **:** | Geethu |
| **Surname** | **:** | Balachandran |
| **Date of Birth** | **:** | March 25, 1990 |
| **Place of Birth** | **:** | Nilambur, India |
| **Nationality** | **:** | Indian |
| **Marital Status** | **:** | Single |

## Education

**Aug 2008-Feb 2014** **Integrated Master of Technology in Nanotechnology**, Amity Institute of Nanotechnology, **Amity University**, Noida, India

## Work Experience

| | | |
|---|---|---|
| **Dec 2017-Present** | **Project Manager** | EU-VRi - European Virtual Institute for Integrated Risk Management, **Steinbeis**, Stuttgart, Germany |
| **May 2014-Oct 2017** | **Research Associate** | Institute of Applied Materials-Energy Storage Systems (IAM-ESS)), **Karlsruhe Institute of Technology (KIT)**, Karlsruhe, Germany |
| **Jul 2013-Mar 2014** | **Student Research Assistant** | Institute of Nanotechnology, **Karlsruhe Institute of Technology (KIT)**, Karlsruhe, Germany |

## Publications

**2018** G. Tian, F. Scheiba, L. Pfaffmann, A. Fiedler, V. S. K. Chakravadhanula, G. Balachandran, Z. Zhao & H. Ehrenberg, *'Electrostatic self-assembly of $LiFePO_4$ cathodes on a three-*

*dimensional substrate for lithium ion batteries',* Electrochim. Acta, 283, 1375-1383 (2018).

**2017** R. Adam, M. Lepple, N. A. Mayer, D. M. Cupid, Y. Qian, P. Niehoff, F. M. Schappacher, D. Wadewitz, G. Balachandran, A. Bhaskar, N. Bramnik, V. Klemm, E. Ahrens, L. Giebler, F. Fauth, C. A. Popescu, H. J. Seifert, M. Winter, H. Ehrenberg, & D. Rafaja, *'Coexistence of conversion and intercalation mechanisms in lithium ion batteries: Consequences for microstructure and interaction between the active material and electrolyte',* Int. J. Mater. Res., 108, 1–13 (2017)

**2015** G. Balachandran, D. Dixon, N. Bramnik, A. Bhaskar, M. Yavuz, L. Pfaffmann, F. Scheiba, S. Mangold & H. Ehrenberg, *'Elucidation of the Electrochemical Reaction Mechanism in $MFe_2O_4$ (M=Ni, Co) Conversion-Type Negative Electrode Systems by using In Situ X-ray Absorption Spectroscopy',* ChemElectroChem, 2, 1510-1518 (2015)

# Awards, Talks and Conference Contributions

**2017** Invited talk at 2017 DESY Photon Science Users' Meeting at Deutsches Elektronen-Synchrotron (DESY), Hamburg, Germany

**2016** Recipient of `Networking Grant´ awarded for highly competitive PhD students to visit international research groups. As a part of this worked at University of California, Berkeley and Argonne National Laboratory, Illinois, USA

**2016** Poster presentation at 18th International Meeting on Lithium Batteries (IMLB), Chicago, USA

**2016** Oral and poster presentation at the 29th Electrochemical Society (ECS) meeting, San Diego, USA

**2016** Poster presentation at conference on analysis of diffraction data in real space, Grenoble, France

**2015** Poster presentation at 7th Lithium Battery Discussions (LIBD), Arcachon, France.

**2014** International student research assistant fellowship for master thesis from Karlsruhe Institute of Technology, Karlsruhe, Germany.